
POLITECNICO DI MILANO
DEPARTMENT OF ENERGY
DOCTORAL PROGRAMME IN ENERGY AND NUCLEAR SCIENCE AND TECHNOLOGY

# NUMERICAL AND EXPERIMENTAL STUDIES OF PLASMA-MATERIAL INTERACTION IN LINEAR PLASMA DEVICES

Doctoral Dissertation of:
**Michele Sala**

Supervisor:
**Prof. Matteo Passoni, Dr. Andrea Uccello**

Tutor:
**Prof. Luigi Pietro Maria Colombo**

The Chair of the Doctoral Program:
**Prof. Vincenzo Dossena**

2020 – XXXIII

# Abstract

PLASMA-Material Interaction (PMI) is a fundamental subject to be addressed for the success of the Magnetic Nuclear Fusion programme. Research in this field led to the choice of tungsten (W) for the most critical components of the first wall (FW) of the ITER tokamak, due to its attractive thermophysical properties, such as high melting point, good thermal conductivity and low sputtering yield. However, since present-day tokamaks cannot reach the plasma parameters and conditions currently foreseen for the first-wall (FW) of ITER, there is the need to use both simulations and experiments to address PMI in ITER-relevant conditions. As regards simulations, advanced computational models have been developed in order to interpret and predict the plasma parameters in the edge of present-day tokamaks. Similar codes also exists for predicting the materials modifications due to plasma particle bombardment. From the experimental side, PMI studies in ITER-relevant conditions are usually carried on in Linear Plasma Devices (LPDs), simpler and cost-effective devices with respect to tokamaks, which are nevertheless able to produce plasmas of interest for PMI research. However, while simulations codes have been extensively applied in tokamaks, much less attention has been paid to the modelling of LPDs.

The main goal of the present Ph.D. work consists in performing an integrated numerical and experimental study of PMI in LPDs. To this end, the edge-plasma code SOLPS-ITER was selected for the plasma modelling.

Since this code has never been applied for plasma modelling in LPDs, a detailed analysis and interpretation of the code equations in linear geometry was carried on for the first time in this Ph.D. work. Next, a sensitivity scan on code free parameters was performed, aiming to compare simulations results with experimentally available plasma parameters measured in the LPD GyM of Istituto di Scienza e Tecnologia dei Plasmi (ISTP) - CNR. For the material side of the PMI problem, the ERO2.0 code was chosen, due to its recently-developed capabilities of simulating materials modifications down to the nanoscale. A detailed comparison of the ERO2.0 morphology evolution module with literature models was performed for the first time in this Ph.D. work. For the experimental part, the Ph.D. activites focused on the exposures of fusion-relevant $\mathrm{W}$ samples to $\mathrm{D}$ and $\mathrm{He}$ plasmas of the LPD GyM. The $\mathrm{W}$ samples were produced by Pulsed Laser Deposition and characterised before and after the exposures. The morphological modifications induced after plasma exposures are thoroughly discussed and compared with dedicated ERO2.0 numerical simulations.

# Sommario

L'INTERAZIONE Plasma-Materia (PMI, in breve) è un ambito di ricerca di centrale importanza per il successo della fusione a confinamento magnetico. La ricerca in quest'ultimo ambito ha portato ad identificare il tungsteno (W) come materiale di riferimento per la realizzazione delle componenti più critiche del tokamak ITER, per via delle sue eccellenti proprietà termofisiche, come l'elevata temperatura di fusione, ottima conduttività termica e bassa resa di erosione. Tuttavia, dal momento che i tokamak attuali non sono in grado di raggiungere condizioni del plasma simili a quelle previste per la prima parete di ITER, vi è la necessità di fare uso sia di simulazioni che di esperimenti allo scopo di capire l'impatto della PMI in condizioni rilevanti per ITER. Per quanto riguarda le simulazioni, sono stati sviluppati modelli computazionali avanzati allo scopo di interpretare e predire le proprietà del plasma nella regione più esterna del tokamak. Allo stesso modo, sono stati sviluppati anche codici per lo studio delle modifiche indotte sui materiali per via della loro esposizione al plasma. Per quanto concerne l'ambito sperimentale, la PMI in condizioni rilevanti per ITER viene solitamente effettata nelle macchine lineari, per via della loro maggiore semplicità e minor costo, dove è possibile raggiungere parametri di plasma di interesse per le ricerche sulla PMI. Tuttavia, mentre i codici numerici di cui si faceva menzione poco sopra sono stati estensivamente applicati per i tokamak, è emerso dallo studio di letteratura come essi siano stati scarsamente utilizzati allo scopo di modellizzare le macchine lineari. Lo

scopo principale di questo progetto di dottorato, consiste nell'effettuare un indagine combinata numerica e sperimentale della PMI in macchine lineari. A questo proposito, si è utilizzato il codice di bordo plasma SOLPS-ITER per modellizare il plasma. Dal momento che questa versione del codice non è mai stata applicata prima d'ora per la modellizzazione del plasma in macchine lineari, è stata effettuata per la prima volta in questo lavoro di Dottorato una preliminare analisi di interpretazione delle equazioni del codice in macchine lineari. Una volta completato questo primo passo, si è effettuata un'analisi di sensitività su alcuni dei parametri liberi del codice, allo scopo di effettuare un confronto tra l'output delle simulazioni ed profili di plasma misurati sperimentale nella macchina lineare GyM dell'Istituto di Scienza e Tecnologia dei Plasma (ISTP)-CNR. Per il lato materiale della PMI, si è scelto di fare uso del codice recentemente sviluppato ERO2.0, per via della sua capacità di modellizzare l'evoluzione della morfologia superficiale dei materiali a seguito dell'irraggiamento di plasmi. A questo proposito, è stato effettuato per la prima volta in questo lavoro di Dottorato un confronto con il modello di evoluzione morfologica correntemente implementato in ERO2.0 e altri modelli disponibili in letteratura. Per quanto riguarda le attività sperimentali, si è effettuata l'espozione di film di W a plasmi di deuterio ed elio generati nella macchina lineare GyM. Questi campioni di W sono stati prodotti facendo uso della tecnica di deposizione a laser pulsato e sono stati approfonditamente analizzati sia prima che dopo la loro esposizione. Si sono evidenziate modifiche morfologiche indotte per effetto dell'espozione al plasma, le quali sono state approfonditamente discusse e confrontate con gli output di simulazioni dedicate effettuate con il codice ERO2.0.

# Contents

# Introduction and Thesis goals

ENERGY is one of the most important aspects of a developing society. Over 15 terawatts of electricity are consumed every year by human beings and this requirement is undoubtedly doomed to increase since more and more people have access to technological innovations. Nowadays, most of our electricity is coming from chemical reactions which involves the burning fossil fuels. As a combustion process dealing with carbon-based materials, this leads unavoidably to the production of carbon dioxide, which is know to be one of the greatest contributor to the greenhouse effect. Fossil fuels are also a limited resource and, moreover, they are present only in some location on Earth. This latter result in geopolitical conflicts for gaining control over energy resources.

Due to these issues, over the last decades, a great interest has been spent in order to increase the use of renewable sources, such as hydroelectric, solar and wind. However, unfortunately all the aforementioned resources suffer either from a limited availability (e.g. hydroelectric power plant can be built only if a water basin is present) or from their limited capacity factor (wind and solar can operate only if Sun or wind are present). Nuclear energy seems to be one of the most promising candidate for solving the Energy problem. From one side, since its intrinsic energy production mechanism is not based on a conventional chemical reaction but rather on nuclear one, it does not produce any carbon dioxide. Moreover, since nuclear is based on the interaction between atomic nuclei, rather then that between electrons,

the energy density is much grater, over a factor of a million with respect to that of conventional energy sources. Furthermore, the fuel availability is widespread all across the surface of the Earth and not, as it happens for fossil fuels, located only in limited regions.
But, what do we mean with nuclear energy? There are two ways by which one can extract energy from a nucleus: fission and fusion. Fission involves the use of heavy nuclei and it is based, as the same name suggestion, on their separation (split) in order to reach a more stable (energy-favorable) configuration. Nowadays, all the nuclear energy in the world is based upon this very mechanism. While all the aforementioned advantages of nuclear applies for fission, there are undoubtedly some drawbacks. Fission-based power plant have become quite infamous due to the two major incidents of Chernobyl (1986) and Fukushima (2011). Indeed, the the release of a huge amount of radioactivity as a consequence of these incidents, has drawn the public opinions against it. Furthermore, there is still the problem of how to deal with the spent fuel extracted from the core of a fission reactor. Even though promising ideas have been put forward, no definitive solution is nowadays available to the spent fuel problem. For all these reasons, nuclear fusion is drawing an increasing amount of attention. In contrast to fission, fusion involves the union of light nuclei to reach a more stable configuration, with the corresponding release of huge amount of energy. This mechanism is indeed the one which is ultimately powers stars (such as our Sun), counteracting the inward pressure exerted by gravity.
Starting from the end of the Second World War, scientists have been trying to understand how to replicate the same mechanism which is naturally occurring in stars on Earth, in a controlled fashion. It is common to hear that we are trying to put the ”the Sun in a box”. Differently to stars, however, achieving and controlling these fusion reactions is extremely challenging. Indeed, fusion reactions requires very high temperatures (of the order of ten million of degrees). This is due to the fact that, one has to overcome the inherent repulsion of the two, positively-charged, nuclei. Heating-up matter to these temperatures one obtains a plasma, which is commonly known as the fourth state of matter. Moreover, one has to find a way to confine this plasma and, of course, one cannot use the pressure driven by gravity. Fortunately, however, plasmas can interact with magnetic fields through the Lorentz force. Therefore, one can think of using suitably-engineered magnetic fields to bound the plasma in a limited region of space. This is, indeed, the idea behind the so-called *Magnetic Nuclear Fusion*, which constitute the framework under which this Ph.D. thesis was developed. Since the end of the Second World War, two different devices have been put for-

ward to achieve these confinement through magnetic fields: *tokamaks* and *stellarators*. The former is nowadays considered as the most promising candidate for the construction of a commercial fusion power plant. This device was put forward by two Russian physicists, Tamm and Sakharov, and the word literally means ***to****roidal'naya* ***ka****mera s* ***ma****gnitnymi* ***k****atushkami*, that is toroidal chamber with magnetic fields.
In a tokamak, suitably-designed magnetic fields allow the plasma to be confined in a bounded region of space, thus finding a successful alternative for gravity in a star. However, this confinement is not perfect. Indeed, mostly as a consequence of **turbulence-related** phenomena, particle as well as energy escape, leading to an unavoidable touch between the hot plasma and the vessel of the machine. The interaction between plasmas and materials goes under the name of **Plasma-Material Interaction** (PMI) and it is, nowadays, one of the most important topic in the field of Magnetic Nuclear Fusion. The reasons for this are multiple and are due to the complex and interrelated phenomena typical of PMI. For example, energetic plasma particles which leaks through the confined region can impinge on the vessel wall, leading to a material-removal process known as *physical sputtering*. The latter results in a progressive erosion of vessel wall, limiting its overall lifetime. Moreover, the eroded walls' atom can migrate into the plasma, finding their way into the confined region. Here, they can be ionised, giving rise to energy losses, related to line radiation and Bremsstrahlung. This leads to a plasma cool down and, hence, to a degradation of the performance of the device. It emerges thus, even from this simple picture, that the materials to be used for the vessel wall facing the plasma (the so-called *first-wall*, FW) are of crucial importance. Due to its favourable thermophysical properties, such as high resistance towards sputtering and high melting point, tungsten (W) has gained a growing attention for the most critical component of the FW. Indeed, W has been chosen as the reference material for the most critical components of the ITER tokamak, which is currently being built in France. ITER will have the important task of proving the scientific feasibility of fusion, bridging the gap between present-day tokamak experiments and future demonstrative power plant. The high particle and energy loads to which W is exposed can lead, however, to unavoidable modifications of W at the micro/nano-scale. Since, however, present-day tokamak experiments cannot reach the operative conditions foreseen in ITER, the behaviour of W and, in general, of plasma-facing materials cannot be addressed. For this reason, both numerical and experimental tools are needed. Numerical codes aim, from one side, to predict the plasma parameters in the outermost region of the tokamak, the so-called *edge plasma*. From the

other, they also provide insight on how PFM are eroded and transported into the plasma, or allow to understand the impact of non-trivial morphology on the erosion process. Tokamaks are intrinsically complex devices and plasma conditions between discharges change. Therefore, is quite difficult to pinpoint a material modifications to a given plasma parameter. Thus, to address PMI in ITER-relevant conditions one needs a different strategy. Linear Plasma Devices (LPDs) are simple and cost-effective machines which can help to shed light on PMI. Their cylindrical vacuum vessel is surrounded by coils, producing an almost axial magnetic field, confining the plasma in the radial direction. In spite of their importance for PMI studies, only a scarce attention has been paid on the applications of numerical codes, commonly employed to tokamaks, also to LPDs. This application is of great relevance, since it allows from one side to test codes in simpler geometry and, from the other, also to interpret experiments carried on in these devices.
This Ph.D. work falls within the framework just outlined. In particular, it aims to extend the application of numerical codes also to LPDs and, more precisely, to the LPD GyM of Istituto di Scienza e Tecnologia dei Plasmi (ISTP) - CNR. After a thorough literature research the edge plasma code SOLPS (and, particularly, its latest release version SOLPS-ITER) was identified as the best candidate to perform simulations in the linear geometry of LPDs. Similarly, the materials evolution modelling was performed using the recently-develop ERO2.0, which allow to understand transport in complex geometries as well as to understand the feedback existing between erosion processes and the morphology of the irradiated materials. This numerical activity is always accompanied by dedicated experiments in GyM. The latter involves the exposures of opportunely-tailored fusion-relevant W coatings, having unconventional morphology, structure and composition with respect to policrystalline W. The W-based coatings are produced thanks to the use of the Pulsed Laser Deposition technique, a PVD process, which allows film morphology, structure and composition control by suitably tuning its main operational parameters. Morphological modifications induced after plasma exposures are thoroughly analysed by means of a combined used of Atomic Force Microscopy and Scanning Electron Microscopy. These last are also used to generate synthetic surfaces, which are given as an input to the material transport and migration code ERO2.0. Simulations results are compared to the experimental measurements.
All the research activities reported in this Thesis work were developed within the framework of the Nuclear and Energy Science and Technology (STEN) Ph.D. program and it was carried on at the Micro and Nanostruc-

tured materials Laboratory of Politecnico di Milano (Italy). Modelling, as well as experimental activities, were also developed in collaboration with the Istituto di Scienza e Tecnologia dei Plasmi (ISTP) - CNR. Part of the work has also received funding from the EUROfusion WP EDU, WP MST1 and WP PFC research projects. The Thesis work is divided into the following chapters:

- **Chapter 1** aims to give a brief introduction to the basic principles of nuclear fusion. After introducing the most important reactions, the attention is shifted on how to obtained a net power output from them. Particular emphasis is given to the underlying principles of magnetic nuclear fusion. The tokamak concept is then presented and the main features of the ITER project are highlighted.
- **Chapter 2** introduces the issues of Plasma-Material Interaction in magnetic confinement fusion devices, which constitutes the main framework of this Ph.D. work. We also illustrate here the importance of simulations code for interpreting and predicting plasma and material behaviour in present-day tokamaks, as well as future fusion devices. Chapter 2 also discusses the relevance of Linear Plasma Devices for lab-scale investigations of PMI.
- **Chapter 3** starts with the description of the main Thesis goals. The relevant numerical and experimental methods employed to achieve them are next illustrated. In particular, the edge plasma code SOLPS-ITER is first presented, focusing on the main physical model as well as the presentation of the main necessary input to perform a simulation. The material transport code ERO2.0 is similarly described. We also present in this Chapter the Linear Plasma Device GyM of ISTP-CNR.
- **Chapter 4** presents the results of the SOLPS-ITER simulations of GyM $\mathrm{Ar}$ plasmas. In particular, we give here a detailed discussion of how LPDs are seen by edge plasma code and illustrate how the relevant model equations are interpreted when modelling of $\mathrm{Ar}$ plasmas in linear geometries is performed. Next, we present the results of dedicated SOLPS-ITER GyM simulations in $\mathrm{Ar}$ plasmas, by varying several code input, thus performing a sensitivity scan and we perform comparison with experimentally-available plasma profiles in GyM. We conclude the Chapter, by showing preliminary results related to the attempt of building a Neural Network for radial profiles prediction starting from SOLPS-ITER simulations.
- **Chapter 5** starts by giving a general overview of the literature models

concerning morphological modifications under ion irradiations. We focus here, in particular, on a model recently proposed by Škereň et al., due to its great similarity with the surface evolution module in ERO2.0. Next, we compare the results of the Škereň's model and ERO2.0 on both numerically-generated surfaces as well as realistic surfaces, obtained by AFM measurements of W coatings deposited in the framework of this Ph.D. Thesis. We conclude the Chapter by performing a comparison between simulations and experiments.

- **Chapter 6** aims to present the experimental result of this Thesis. We start the Chapter by presenting the main W-based coatings produced during the Ph.D. with the PLD apparatus. We then move on and illustrate the results of the exposures performed in the LPD GyM during this Thesis to D and He plasmas. Particular emphasis is given on the post-exposure characterisation of the W samples.

- **Chapter 7** presents the conclusion of the Ph.D. work and illustrates possible future perspectives.

The contributions summarised in this Thesis work have been published in the following papers

- **M. Sala**, E. Tonello, A. Uccello, X. Bonnin, D. Ricci, D. Dellasega, G. Granucci and M. Passoni, *Simulations of Argon plasmas in the linear plasma device GyM with the SOLPS-ITER code*, Plasma Physics and Controlled Fusion, (2020) 62 055005.

- **M. Sala**, A. Uccello, D. Dellasega, M. Pedroni, E. Vassallo and M. Passoni, *Exposures of bulk W and nanostructured W coatings to medium flux D plasmas*, Nuclear Materials and Energy, (2020) *In press*.

- A. Eksaeva, D. Borodin, J. Romazanov, A. Kreter, A. Pospieszczyk, S. Dickheuer, S. Moeller, B. Goeths, M. Rasinski, U. Knoche, A Terra, A Kirschner, I. Borodkina, M. Eichler, B. Unterberg, S. Brezinsek, Ch. Linsmeier, E. Vassallo, M. Pedroni, M. Passoni, D Dellasega, **M. Sala**, F. Romeo, S. Henderson, M. O Mullane, H. Summers, D. Tskhakaya, K. Schmid, *ERO2.0 modelling of the effects of surface roughness on molybdenum erosion and redeposition in the PSI-2 linear plasma device*, Physica Scripta 2020 (T171), 014057.

- G. Alberti, **M. Sala**, J. Romazanov, A. Uccello, D. Dellasega and M. Passoni, *ERO2.0 modelling of nanoscale surface morphology evolution*, Manuscript in preparation.

In addition, part of the contents of this Thesis have been presented at the following national and international conferences:

- **M. Sala**, E. Tonello, A. Uccello, X. Bonnin, D. Ricci, D. Dellasega, G. Granucci and M. Passoni, *SOLPS-ITER simulations of the GyM Linear Plasma Device*. $46^{th}$ Eureopean Physical Society Conference on Plasma Physics, July 2019, Milan, Italy (poster contribution).
- **M. Sala**, D. Dellasega, A. Uccello, M. Pedroni, E. Vassallo, M. Passoni, *Exposures of bulk W and nanostructured W coatings to medium flux D plasmas*. $17^{th}$ International Conference on Plasma-Facing Materials and Components, May 2019, Eindhoven, Netherland (poster contribution).
- D. Dellasega, **M. Sala**, A. Uccello, E. Besozzi and M. Passoni, *Synthesis of porous and nano W, W-O-N, WN x and W-O coatings for plasma surface interaction studies*. $23^{rd}$ International Conference on Plasma Surface Interactions in Controlled Fusion Devices (PSI-23), June 2018, Princetion (NJ), USA (poster contribution).
- **M. Sala**, *Interaction between fusion-like boundary plasmas and nanostructured tungsten*. Oral presentation at ISTP-CNR.

Finally, during the Ph.D. I have the occasion to participate at the following workshop/training courses:

- SOLPS-ITER workshop, *2D Edge Modelling Training Session*, May 2019.
- SOLPS-ITER workshop, *Edge Modelling training courses*, October 2018.
- Workshop on *Joint SOL and PSI modelling activity*, April 2018, Marseille, France.

CHAPTER 1

# Basic principles of magnetic nuclear fusion

THIS introductory Chapter aims to introduce the basic concept of nuclear fusion. Starting from the well-known binding energy (cfr. § 1.1) per nucleon curve, we naturally introduce the two ways in which the strong nuclear interaction can be exploited to obtain a net release of energy: fission and fusion. The notion of plasmas is then presented in § 1.2 and some examples of physical environments were they can be found are briefly discussed in § 1.3. We move on from here and, following the well-known work of Lawson, derive in § 1.4 a criterion for a self-sustained nuclear fusion reaction. We shift next the attention to the issues of plasma confinement. In particular, the inertial (cfr. § 1.5) and magnetic (cfr. § 1.6) confinement strategies are presented, focusing more on the latter since it constitutes the framework of the present Ph.D. work. The concepts of tokamaks and stellarator are introduced in § 1.6. The final section of the Chapter is devoted to give a brief description of tokamak devices in § 1.7. We introduce the important concept of plasma edge and plasma facing components in § 1.7.2 and conclude the Chapter by briefly presenting the ITER and

DTT projects in § 1.7.3 and § 1.7.4 respectively.

## 1.1 The energy inside a nucleus

Nuclear physics deals with the comprehension of the properties of nuclei. A nucleus consists of A sub-constituents, that is protons and neutrons. The latter can interact among each other both with attractive and repulsive forces. Repulsion occurs due to electromagnetic forces between the positively charged protons. Without the introduction of an attractive interaction between its constituents, a nucleus cannot exists. This interaction has the peculiarity of acting equally, that is irrespectively, of the charge and goes under the name of **strong nuclear force**. For this reason, the constituents of the nucleus are called **nucleons**. A nucleus can be in several quantum state, distinguished by its respective value of the energy. Nucleons always arrange themselves in the condition which minimise the overall energy content.
If one measures the mass of the different nuclei, one finds that it is systematically lower than that of its constituents. For this reason, one can write the mass of a generic nucleus as:

$$M_{\text{nucl}} = ZM_p + (A - Z)\, M_n - \Delta \tag{1.1}$$

where $Z, A$ denote respectively the charge and mass number, $M_p, M_n$ the mass of the proton and neutron, and $\Delta$ is the so-called **mass defect**. The origin of this mass defect can be explained using the well-known relation between energy and mass. Therefore, if we denote with $V$ the overall energy content of the nucleus, then we can write:

$$V = M_{\text{nucl}}c^2 \tag{1.2}$$

By combining (1.1) and (1.2), we can introduce the so-called **binding energy** as:

$$B = ZM_pc^2 + (A - Z)\, M_nc^2 - V = c^2\Delta \tag{1.3}$$

This binding energy is nothing more than the energy one needs to spend to separate the nucleus into its own constituents. One can think of adding on nucleus after the other and plot the energy of the system per nucleon added (the so-called *binding energy*) per nucleon, as shown in figure 1.1 One sees that, for $A < 56$, there is a net gain in energy if we increase the mass number of the system. On the contrary, for $A > 56$ there is a gain in energy if we move from an heavier nucleus to a light one. There are hence two different ways by which one can extract energy from the nucleus, either fusing two

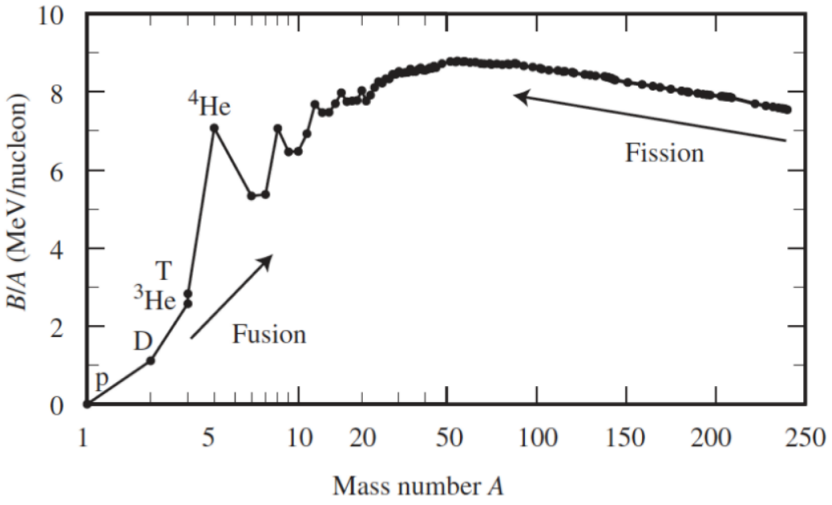


**Figure 1.1:** *Binding energy per nucleon as a function of the mass number.*

light elements or separating an heavy one into two, lighter, fragments. The latter process is called **nuclear fission** while the former **nuclear fusion**.
As the name suggsts, nuclear fission is a process in which an heavy nucleus undergoes a separation process, thus breaking into two lighter fragments. This separation is usually triggered thanks to the use of neutrons. Indeed, due to their lack of electric charge, neutron can easily penetrate the nucleus and promote nuclear reactions. For this reason, the probability of occurrence of a fission reaction (the so-called **cross-section**, measured in **barns**) can be very high, even when the energy of the neutron promoting the reaction is low. This is shown in figure 1.2a, which reports the neutron-induced fission cross-section for several heavy nuclei as a function of energy. It can be seen that even for vanishingly low energies of the incoming neutron, the cross-section can be really high.
Exactly the opposite process occurs in fusion reactions. In this case, if two light nuclei come sufficiently close (in the range of $1\,\mathrm{fm}$), then the strong nuclear force can overcome the Coulomb repulsion among the two positively charge nuclei. However, as mentioned, for this to occur the two interacting partner must be brought to extremely small distances which, in turn, means that the energy must be sufficiently high. One can be more precise simply by using a classical mechanics argument. If we denote the distance at which the nuclear force starts to act with $r_{\mathrm{cr}}$, then for fusion to occur the particles energy must be greater then the electrostatic potential

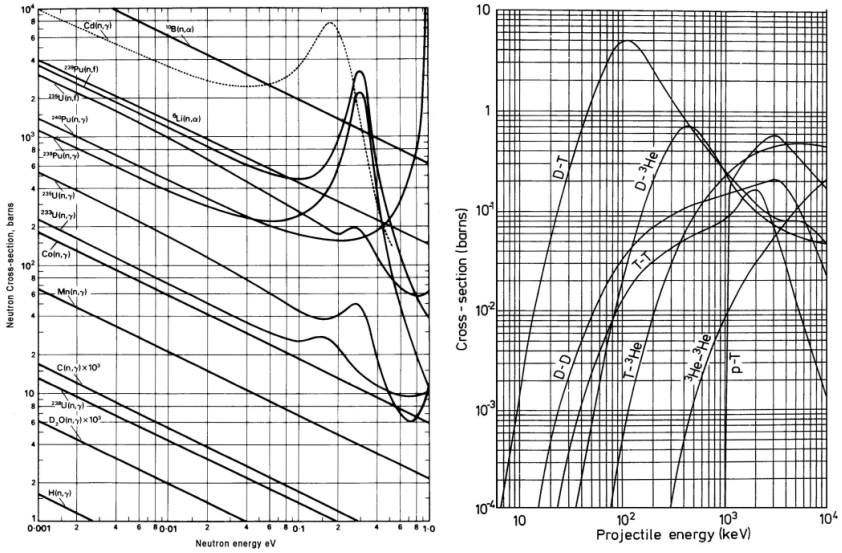


**(a)** *Fission reaction cross-section* **(b)** *Fusion reaction cross-section*

**Figure 1.2:** *Fission and fusion cross-sections as a function of the centre-of-mass energy.*

evaluated at $r_{\mathrm{cr}}$, that is:

$$V = k\frac{Z_1 Z_2 e^2}{r_{\mathrm{cr}}} \simeq \frac{Z_1 Z_2 e^2}{A_1^{1/3} + A_2^{1/3}} \tag{1.4}$$

where we used the fact that $r_{\mathrm{cr}} = 1.44 \times 10^{-15}\left(A_1^{1/3} + A_2^{1/3}\right)$ fm and $k$ is a proportionality constant. The typical value of $V$ evaluated at the critical radius is of the order of some MeV. From (1.4) one can immediately see that the repulsion is stronger for high Z elements. This is the reason why one is interested in light (low-Z) nuclei for fusion reactions on Earth. Quantum mechanical effects can help to reduce the minimum energy requirements imposed by the classical mechanics estimate [95]. Indeed, a particle can penetrate through a potential barrier thanks to quantum tunneling. Considering these aspects, one can write the cross-section for nuclear fusion reactions as:

$$\sigma\left(E\right) \simeq \frac{1}{E} S\left(E\right) \exp\left[-2G\left(E\right)\right] \tag{1.5}$$

where $S$ is the so-called **astrophysical factor**, related to the cross-section for Coulomb repulsion between charged particles, $G$ is the **Gamow factor**, and $E$ the energy in the centre-of-mass of the two colliding partners. The

exponential suppression of the cross-section is the true peculiarity of fusion reactions and it is due, ultimately, to the Coulomb repulsion. Furthermore, one can show that $G \propto Z_1 Z_2 e^2$, where $e$ is the fundamental charge of the electron and $Z_1, Z_2$ denote respectively the atomic numbers of the two interacting particles. In figure 1.2b, we show the fusion cross-section as a function of the centre-of-mass energy for different hydrogen isotopes, currently investigated in fusion researches. They concern, in particular, the use of deuterium (D) and tritium (T) as a nuclear fuel and are described by the following reactions:

$$\begin{aligned} \mathrm{D} + \mathrm{D} &\rightarrow \begin{cases} {}^3\mathrm{He} + n + 3.27\,\mathrm{MeV}, & b = 50\% \\ \mathrm{T} + \mathrm{H} + 4.03\,\mathrm{MeV}, & b = 50\% \end{cases} \\ \mathrm{D} + {}^3\mathrm{He} &\rightarrow {}^4\mathrm{He} + \mathrm{H} + 18.3\,\mathrm{MeV} \\ \mathrm{D} + \mathrm{T} &\rightarrow n + {}^4\mathrm{He} + 17.6\,\mathrm{MeV} \end{aligned} \tag{1.6}$$

Figure 1.2b, one sees that the D-T reaction is the one characterised by the highest cross-section even at the lowest energy. Furthermore, this reaction is also characterised by the highest energy output (the reaction $Q$ value) among those reported in (1.6). In applications, one is not actually involved with just two particles, but rather one has an ensamble of particles each having an energy distributions. If we denote with $i$ and $j$ the two interacting species, then one can define the reaction rate as:

$$\langle \sigma v \rangle_{ij} = \frac{1}{n_i n_j} \int_{\mathbb{R}^6} \sigma\left(v\right) v f_i\left(\mathbf{v}_i\right) f_j\left(\mathbf{v}_j\right) \mathrm{d}\mathbf{v}_i \mathrm{d}\mathbf{v}_j \tag{1.7}$$

where $n_i, n_j$ denote the number density of the two species $i, j$, $v := |\mathbf{v}_i - \mathbf{v}_j|$ the relative velocity, and $f_i, f_j$ the distribution functions of species $i$ and $j$. Therefore, we can write the average number of reaction per unit volume per unit time as:

$$f = n_i n_j \langle \sigma\left(v\right) v \rangle \tag{1.8}$$

It is common to perform the average in (1.7) using a Maxwellian energy distribution for both species. The corresponding reaction rates, sometimes called Maxwellian reaction rates, for the fusion reactions reported in (1.6) are shown in figure 1.3. From this figure, one can again appreciate the fact that the reaction rate of the D-T reaction is the highest. For these reasons, the first generation of nuclear fusion power plant will be based on this reaction. However, it has some drawbacks. First of all, almost all the $Q-$value is related to the kinetic energy of the neutron (i.e. $14.1\,\mathrm{MeV}$). These high-energy neutrons are related with several issues, such as radiation damage

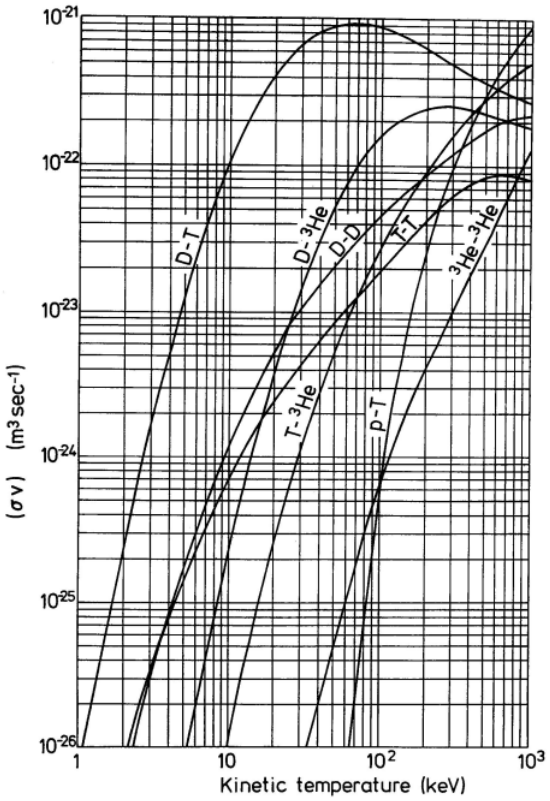


**Figure 1.3:** *Maxwellian reaction rates for the fusion reactions reported in equation* (1.6)*.*

and neutronic activation of the reactor components. Furthermore, it involves T which is radioactive with an half-life of $\simeq 12$ years, which means that it is not available (or, better, available only in trace amounts) in nature and thus it need to be produced. A possible solution is to exploit the neutron flux generated by the fusion reactions to trigger the following reactions with lithium:

$$\begin{aligned} {}^6\mathrm{Li} + n &\rightarrow {}^4\,\mathrm{He} + T + 4.8\,\mathrm{MeV} \\ {}^7\mathrm{Li} + n &\rightarrow {}^4\,\mathrm{He} + T + n - 2.5\,\mathrm{MeV} \end{aligned} \tag{1.9}$$

It is important to notice that ${}^6\mathrm{Li}$ and ${}^7\mathrm{Li}$ have a $7.5\%$ and $92.5\%$ isotopic concentration respectively. Both of these reactions can happen; the first is exothermic while the second one is endothermic.

## 1.2 What is a Plasma?

The word plasmas is often associated with research on magnetic nuclear fusion. However, we shall here briefly see with few examples that this is not the sole case where plasmas show up. Indeed, plasmas are extremely common in nature, since more than $99\%$ of the overall matter in our universe is in the plasma state. Implicitly, by saying "plasma state" we have already defined a plasma as a state of aggregation of the matter. But, what does differentiate a plasma from the others, namely solid, liquid and gases? And, more importantly, is a plasma fundamentally different to a common gas?
To answer these questions, one can consider the following thought experiment. Imagine having a gas, say nitrogen, filling a region of space. If we let the temperature raise in this room then due to thermal motion the collision between the nitrogen atoms can become energetic enough to strip one (or more) electrons, that is ionisation have occurred in our system. One can compute the amount of ionisation to be expected in a gas due to the thermal collision of electrons with neutral atoms using the Saha equation:

$$\frac{n_i}{n_n} \simeq 2.4 \times 10^{21} \frac{T^{3/2}}{n_i} \exp -\frac{U_i}{k_B T} \tag{1.10}$$

In this expression, $n_i$ and $n_n$ denotes the number density of ionised neutrals and neutral atoms respectively, $T$ is the temperature, $k_B$ is the Boltzmann constant and $U_i$ is the ionisation energy of the gas. The ionisation energy $U_i$ is, generally, of the order of some $\mathrm{eVs}$, so that at room temperature the degree of ionisation is extremely low, due to the presence of the exponential factor in equation (1.10). However, if we keep raising the temperature to sufficiently high values, collisions between neutral atoms occurs more often, so that from the original nitrogen gas we have now a system made of nitrogen ions and electrons.
This thought experiment allows us to give a more precise definition of a plasma. We can say that a plasma is a collection of ions and electrons, globally neutral when looked at a distance. This last statement can be made more precise by introducing the concept of **quasi-neutrality**. Consider a two-component plasma made of ions and electrons. We denote with $n_i$ and $n_e$ their respective number densities. Suppose now that we put a point particle of charge $q$ at the origin. We wish to compute the spatial distribution of the electrostatic potential within the plasma. The latter can be obtained by solving the Poisson equation:

$$-\epsilon_0 \Delta\phi = -e\left(n_i - n_e\right) + q\delta\left(\mathbf{x}\right) \tag{1.11}$$

where $\Delta$ is the Laplacian, $e$ the fundamental charge, $\delta$ the Dirac delta function and we assumed for simplicity $Z = 1$. Due to their larger mass, ions will respond to the added charge slower then the electrons. We can therefore assume that their density is unperturbed and set it equal to $n_i = n_\infty$. As for the electrons, the density can be computed once their distribution functions is known. In steady-state conditions, the latter can be computed by solving the Vlasov equation, that is:

$$\boldsymbol{\xi} \cdot \nabla_{\mathbf{x}} f_e - \frac{1}{m} \nabla_{\mathbf{x}} \phi \cdot \nabla_{\boldsymbol{\xi}} k f_e = 0 \tag{1.12}$$

where $k$ is the Boltzmann constant. It can be shown that the solution of this equation is given by:

$$f_e = A \exp\left[ -\frac{\left(\frac{1}{2} m \left|\boldsymbol{\xi}\right|^2 - \phi\right)}{T} \right] \tag{1.13}$$

By integrating this expression over the velocity variable and noting that, for $\phi \to 0$ then $n_e \to n_\infty$, one obtains for the electron density:

$$n_e = n_\infty \exp\left(\frac{e\phi}{kT_e}\right) \tag{1.14}$$

Thus, substituting this expression in (1.11):

$$-\epsilon_0 \Delta\phi = e n_\infty \left[ \exp\left(\frac{e\phi}{kT_e}\right) - 1 \right] + q\delta\left(\mathbf{x}\right) \tag{1.15}$$

In the region of space where $|e\phi/kT_e| \ll 1$, we can expand the exponential in power series, retaining only first order terms (that is, linear in $\phi$). One obtains:

$$-\epsilon_0 \Delta\phi = \frac{e^2 n_\infty}{kT_e} \phi + q\delta\left(\mathbf{x}\right) \tag{1.16}$$

The solution of this equation, which can be obtained by Fourier transform, is:

$$\phi\left(\mathbf{x}\right) = \frac{q}{|\mathbf{x}|} \exp\left(-\frac{|\mathbf{x}|}{\lambda_D}\right) \tag{1.17}$$

where

$$\lambda_D = \sqrt{\frac{\epsilon_0 k T_e}{n_\infty e^2}} \tag{1.18}$$

is the so-called **Debye Length**. This expression shows that, within a plasma, the electrostatic potential does not follow the usual $1/r$ expression, but

rather is shielded through the exponential factor. The Debye length thus express the length by which electrostatic perturbation are shielded in the plasma. This results can be explained by a simple physical argument. The point charge, $q$, inserted into the plasma generate a potential. If we assume that $q$ is positive, then the electron moves towards this charge and try to balance it. In absence of thermal motion this shielding would be perfect. However, since $T$ is finite, there always exist electrons with energy sufficiently high to escape the electrostatic potential well. The potentials that leaks into the plasma can be estimated by equating the thermal $kT_e$ to the electrostatic energy, thus $\phi \simeq kT_e/e$.

## 1.3 Plasmas in nature

As stated in the previous section, plasmas are the most common state of aggregation of matter in the Universe. In this section, we shall briefly discuss applications or physical environments were they can be found. Plasmas can be characterised using two parameters, namely the plasma density, $n$, and its temperature, $kT$. We shall see in the following that these two parameters can take values which span several order of magnitude. As is common in plasma literature we should also measure the temperature in energy units, thus $kT \to T$.

Historically, the first encounter with plasmas came through the study of electrical discharges in gas tubes. These experiments date back to the work of M. Faraday on the so-called **dark discharges** in gases. Starting from the first half of 1800, numerous scientists contributed to comprehension of the property of electric discharges. Among these, pioneering contribution have been performed by Langmuir, Tonks and their collaborators in the $1920s$. It is interesting to note that the word plasma was coined for the first time by I. Langmuir. Indeed, he noticed that the electrically-balanced part of the discharge acted as a substratum able to carry high-velocity electrons, molecules and ions of gas impurities, similarly to what happens in the blood plasma, which transports red and white cells, proteins, hormones and germs. Researches of these type were performed with weakly ionised glow discharges in glass tubes. Typical ranges of plasma density and electron temperature were $T_e \simeq 2\,\mathrm{eV}$ and $n_e \simeq 10^{14} \div 10^{18}\,\mathrm{m}^{-3}$.

Another important contribution to the comprehension of the properties of plasmas comes from the study of astrophysical phenomena. For example, the Sun itself is an important source of plasmas. Indeed, a flow of plasma, called the **solar wind**, is ejected from its surface into the interplanetary space. Near the Earth, typical winds velocity range from $250$ to

$700\,\mathrm{km/s}$, while the electron density and temperature are $n \simeq 5 \times 10^6\,\mathrm{m}^{-3}$ and $T_e \simeq 50\,\mathrm{eV}$. The solar wind collides with the Earth magnetic field, leading to the formation of the so-called **magnetosphere**. The magnetosphere provides an effective shield against the potentially dangerous, high-energy, particles of the solar wind, since the Earth's magnetic field effectively shield this radiation. The Sun has a region containing the solar atmosphere called the **chromosphere** ($\sim 2000\,\mathrm{km}$ in depth). It is a plasma characterised by an average electron density of $10^{16}$ to $10^{17}\,\mathrm{m}^{-3}$ and temperature $\sim 6000\,\mathrm{K}$. Above the chromosphere there extends a large region of corona, whose plasma parameters such as the electron density, depend considerably on the distance from the solar surface. For example, at $10^5\,\mathrm{km}$, the density and temperature are estimated approximately as $10^{14}\,\mathrm{m}^{-3}$ and $10^6\,\mathrm{K}$. At $10^6\,\mathrm{km}$, they are $\sim 10^{12}\,\mathrm{m}^{-3}$ and $\sim 10^6\,\mathrm{K}$ respectively. Finally, within the Sun core (and stars in general), the temperature induced by the gravitational pressure is high enough to promote fusion reactions. The temperature of the Sun's core is estimated to be around $2\,\mathrm{keV}$.
In astrophysics, one can encounter other more exotic examples of plasmas, such as the interior of white dwarfs. Here, the plasma density and temperature are in the range $n \simeq 10^{31} \div 10^{38}\,\mathrm{m}^{-3}$ and $T \simeq 1 \div 10\,\mathrm{keV}$. In this case, the density is so high that one must take into account quantum mechanical effects, related to the Pauli exclusion principle.

## 1.4 The Lawson criterion

In this section, we shall derive a criterion for a self-sustaining nuclear fusion reactor, that is a reactor which is able to sustain itself only using energy coming from the results of the reaction itself. Of course, this is a purely idealised scenario and some energy will still be needed for providing the necessary magnetic field to confine the plasma. The following discussion is based on the paper originally published by Lawson in 1957 [129].
First of all, we consider the energy released by fusion reactions themselves, which can be written as (cfr. § 1.1):

$$P_{\mathrm{F}} = n_1 n_2 \langle \sigma v \rangle E \tag{1.19}$$

where $n_1, n_2$ denotes the (number) density of the two fusion reactants, $\langle \sigma v \rangle$ is the reaction rate averaged over the distribution functions of the two nuclei, and $E$ is the energy released by the reactions itself. For the $\mathrm{D}-\mathrm{D}$ fusion reactions, one can write the product $n_1 n_2$ simply as $n^2/2$. The energy $E$ which appears in this expression should be evaluated carefully. Indeed, not all the energy released in a fusion reactions can be assumed to

be available. In the case of $\mathrm{D}-\mathrm{D}$ fusion, neutron keep most of the energy and being electrically neutral they easily escape the system. Therefore, $E$ is simply equal to the energy carried by the $\alpha$ particles released in the reaction, that is $E = E_\alpha$.
The next step consists in evaluating the energy loss mechanisms for our system. There are two different processes which must be considered:

- **Radiatiave losses**: at sufficiently high temperatures, one can assume that all the nuclei of the system are completely ionised. Under these conditions, radiative losses are entirely due to Bremsstrahlung and therefore:

$$P_{\mathrm{R}} = c_B Z_{\mathrm{eff}}^2 n^2 \sqrt{T} \tag{1.20}$$

  where $c_B$ is the Bremsstrahlung constant ($c_B \simeq 10^{-34}\,\mathrm{W/cm^2}$), $T$ is the temperature and $Z_{\mathrm{eff}}$ is the effective charge of the system. In an idealised scenario, only the reactants itself are present in the system, therefore $Z_{\mathrm{eff}} = 1$ if the fusion occur between hydrogen isotopes. However, as we shall see in the following Chapter, impurities are unavoidable and the latter increase the value of $Z_{\mathrm{eff}}$, which is particularly troublesome due to the square dependence on this quantity in (1.20).

- **Conduction losses**: Losses due to leak of energy from the system are mostly due to transport processes. If we denote with $W$ the overall energy content of the system, then the conduction losses can be evaluated as:

$$P_Q = \frac{W}{\tau_E} \tag{1.21}$$

  where $\tau_E$ is the *energy confinement time*. The mean energy content of the system can be further evaluated under the following assumption:

  - the system temperature is sufficiently high so that matter is in the plasma state.
  - the electron and ion temperature are equal

  In this case, one can write $W = 3nT$, where $n$ and $T$ are the density and temperature of the plasma.

In an idealised case, the power produced by the fusion reactions themselves is sufficient to sustain the overall energy balance of the system. Therefore, assuming stady-state conditions, one can write:

$$P_{\mathrm{F}} = P_{\mathrm{Q}} + P_{\mathrm{R}} \tag{1.22}$$

or

$$c_B Z_{\text{eff}}^2 n^2 \sqrt{T} + \frac{3nT}{\tau_E} = \frac{n^2}{4} \langle \sigma v \rangle E \tag{1.23}$$

If we assume that the conduction losses can be neglected, then equation (1.23) can be rewritten as

$$T_{\text{id}} = \frac{\langle \sigma v \rangle^2 E^2}{16 c_{\text{B}}^2 Z_{\text{eff}}^4} \tag{1.24}$$

where $T_{\text{id}}$ is the **ideal ignition temperature**. This last formula can be used as a first figure-of-merite to compare different reactions. Of course, to exploit fusion for energy production purposes one is interested in having the smallest possible value of $T_{\text{id}}$. For example, if one compares the value of $T_{\text{id}}$ for hydrogenic-based fusion reactions, one sees that that involving D and T is the most promising one, since $T_{\text{id}}^{\text{D-T}} = 4.3\,\text{keV}$ while $T_{\text{id}}^{\text{D-D}} = 15\,\text{keV}$. However, in order to make more quantitative considerations, one has to take into account also the inevitable transport losses $P_{\text{Q}}$. In this case, one obtains a simple relation for a self-sustaining nuclear fusion reaction:

$$n\tau_{\text{E}} \geq \frac{12T}{E \langle \sigma v \rangle - 4 c_{\text{B}} Z_{\text{eff}}^2 \sqrt{T}} \tag{1.25}$$

which is known as the **Lawson criterion**. This inequality tells us that, for ignition to occur, the product of the density and the energy confinement time should be greater or equal that a quantity which is a function of temperature. Thus, one can evaluate which is the minimum value for which the inequality reported above is satisfied. For a $\text{D} - \text{T}$ reaction, one gets:

$$n\tau_{\text{E}} \geq 2 \times 10^{20}\,\text{m}^{-3}\text{s} \tag{1.26}$$

Inequality (1.26) shows that the ignition condition can be obtained both using a very dense plasma confined for a small time or viceversa. This leads quite naturally to the introduction of two strategies in order to achieve ignition:

- **Inertial confinement fusion (ICF)**: exploits the first term in equation (1.26), that is it aims at producing an high density plasma and to confine it for a small amount of time, using the very same target inertia. In intertial confinement experiments, usually a solid cryogenic $\text{D} - \text{T}$ spherical target is used. Superintense lasers are then focused onto aiming to obtain a high density plasma.
- **Magnetic confinement fusion (MCF)**: exploits rather the second term in equation (1.26), by using as the same name suggests magnetic

fields. The focus here is thus not on the achievement of extremely high density. The idea behing magnetic confinement is that if the magnetic fields are suitably shaped then one can hope to bound the plasma, in a confined region of space.

In the following two sections, we shall discuss these two mechanisms in more details. We will only touch upon the main principles of ICF and focus more on MCF, since it constitutes the main framework of the present Thesis work.

## 1.5 Inertial Confinement Fusion

As stated before, ICF aims to achieve ignition conditions by producing a high-density plasma (of the order $\simeq 10^{24}\,\mathrm{cm}^{-3}$ and confining it using the same system inertia. This means that the confinement time are extremely short, of the order $\tau \simeq 10^{-9}\,\mathrm{s}$. This high density plasma environments can be produced in laboratories thanks to the use of lasers. It is no surprise therefore that the research on ICF is intimately connected with the development of high power lasers. The original schema to achieve fusion in a controlled fashion using lasers was first put forward by Nuckolls in 1972 [52]. A simplified illustration of the process is illustrated in figure 1.4. As can be seen, two different approaches for ICF are possible: direct and indirect drive. In both cases the target consists of a cryogenic solid $\mathrm{D}-\mathrm{T}$ spherical shell covered by a low-Z material called the **ablator** containing a $\mathrm{D}-\mathrm{T}$ gas mixture in thermal equilibrium. In direct drive, the high-power lasers directly impinge on the target, while in indirect drive lasers are firstly shot onto a high-Z material enclosure called the **holhraum**, resulting in the production of high-intensity X-rays ultimately responsible for the core compression. In both direct and indirect drive ICF, this compression occur due to the so-called **rocket force** exerted by the ablation of the ablator onto the cryogenic target. Within the latter, the plasma inertia confines the plasma pressure long enough for the thermonuclear burn to produce high amounts of fusion reactions. This process of target compression is schematised in figure 1.4. In order to get an order-of-magnitude estimate of the density and time scale characteristic of ICF one can employ the Lawson criterion, rewritten however in terms of the target dimensions and mass density. In order to perform such conversion, we first notice that to achieve ignition conditions the confinement time, $\tau_E$, must be greater than the reaction time, $\tau_R$. The confinement time can be evaluated as [5]:

$$\tau_E = \frac{R}{c_s} \tag{1.27}$$

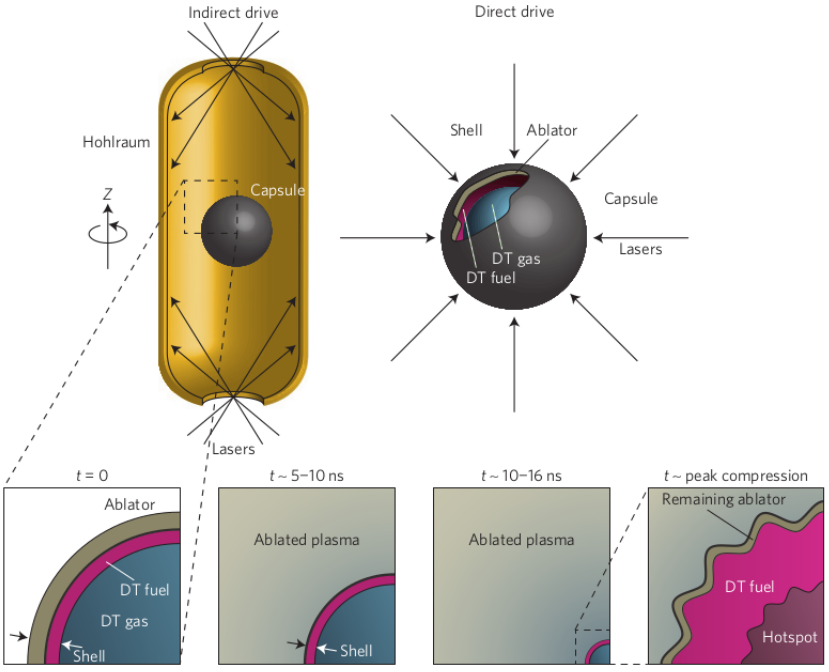


**Figure 1.4:** *Schematic representation of ICF in its two currently mostly developed concept: indirect drive (left) and direct drive (right). In either case, a spherical capsule, is prepared at* $t = 0$ *with a layer of* $\mathrm{D}-\mathrm{T}$ *fuel on its inside surface. As the capsule surface absorbs energy and ablates, the pressure accelerates the shell of remaining ablator and* $\mathrm{D}-\mathrm{T}$ *fuel inwards, resulting in an implosion process. When the shell reaches almost* $1/5$ *of its original radius, it is travelling at a speed of hundreds of* $\mathrm{km/s}$*. When the implosion reaches the minimum radius, a hotspot of* $\mathrm{D}-\mathrm{T}$ *has formed, surrounded by colder and denser* $\mathrm{D}-\mathrm{T}$ *fuel. From [9].*

where $R$ is the sphere characteristic radius and $c_s$ the plasma sound velocity. The reaction time is instead given by:

$$\tau_R \simeq \frac{m_i}{\rho \langle \sigma v \rangle} \tag{1.28}$$

where $\rho$ is the mass density and $m_i$ the ion mass. One can therefore rewrite the Lawson criterion as:

$$\rho R \geq \frac{c_s m_i}{\langle \sigma v \rangle} \tag{1.29}$$

From this expression, it follows that, for the $\mathrm{D}-\mathrm{T}$ reaction, the areal density $\rho R$ should be at least $2 \div 3\,\mathrm{g\,cm^{-2}}$. However, one should note that the laser heating process is explosive in nature, thus only few $\mathrm{mg}$ of fuel can be exploited in order to contain the energy of the explosion. For example,

if we consider a target made of $3\,\mathrm{mg}$ of fuel, then the Lawson criterion 1.29 requires a density of $\rho \geq 100\,\mathrm{g\,cm^{-3}}$. With these densities values, hydrodynamic instabilities are usually responsible for the quenching of the ignition process [9].
Nowadays, the most advanced facility which is investigating ICF is the **National Ignition Facility** [13] (NIF) at Lawrence Livermore National Laboratories (USA), which exploit the indirect drive approach. Although, at the moment, reaching ignition conditions remains an elusive goal, in 2014 scientist at NIF reported for the first time a fusion yield exceeding the total energy (both thermal and kinetic) of the $\mathrm{D}-\mathrm{T}$ fuel [82]. In addition to the indirect drive efforts at NIF, the US laser-fusion programme also relies on the direct drive approach, mostly developed on the **OMEGA laser** [10] located at the University of Rochester.

## 1.6 Magnetic Confinement Fusion

As stated before, the first goal to be achieve in MCF is the confinement of a sufficiently hot and dense plasma for a time scale of several seconds. This requirement is better specified by the Lawson criterion. As the name suggests, in magnetic fusion the idea is to use strong and suitably shaped magnetic fields to confine the hot plasma in a bounded region of space. Indeed, plasmas are made of charged particles (ions and electrons) which can thus interact with externally imposed magnetic fields due to the Lorentz force. Thus, for a particle of charge $q = Ze$, one can write the equation of motion as:

$$m\dot{\mathbf{v}} = Ze\left(\mathbf{E} + \mathbf{v} \times \mathbf{B}\right) \tag{1.30}$$

where $m$ is the particle mass, $\mathbf{E}, \mathbf{B}$ the electric and magnetic field, and $\mathbf{v}$ the particle velocity. In order to understand the most basic principles of magnetic confinement, we consider the motion in the presence of a constant and uniform magnetic field. In this case, it is known [121] that the particle perform a fast gyration motion across the magnetic field direction, with a frequency given by:

$$\Omega = \frac{eZB}{m} \tag{1.31}$$

which is known as the **Larmor frequency**. Thus, if we denote with $v_\perp$ the velocity of the particle across the magnetic field, then the radius of the particle orbit can be estimated as:

$$\rho = \frac{v_\perp}{\Omega} \tag{1.32}$$

called the **Larmor radius**. Therefore, in a uniform and constant magnetic field a charged particle is confined in the direction orthogonal to the magnetic field, but it is otherwise unbounded parallel to it. So, even in the single particle picture in order to obtain confinement, one needs a inhomogeneous and curved magnetic field.

Single particle motion in an inhomogeneous magnetic can be quite complex. In order to get physical insight on the basic principles of magnetic plasma confinement, one can nevertheless use equation (1.30) and simplify it. Indeed, we already observed that a charged particle in a uniform magnetic field perform a fast gyration motion, which we might be however not interested in solving. We can therefore introduce the quantity

$$\mathbf{R} := \mathbf{x} - \frac{1}{\Omega}\mathbf{b} \times \mathbf{v} \tag{1.33}$$

called the **guiding centre**, and hope to find a simplified evolution equation for it. To this end, we suppose that the magnetic field vary slowly in space and time. That is we require that the quantities:

$$L_B := |\nabla \log \mathbf{B}|^{-1}, \tau_B := |\partial_t \log \mathbf{B}|^{-1} \tag{1.34}$$

are long compared to the gyroradius and gyrofrequency, i.e.

$$\frac{\rho}{L_B} \ll 1, \quad \Omega\tau_B \gg 1 \tag{1.35}$$

or, equivalently, that

$$\delta := \max\left(\frac{\rho}{L_B}, \frac{1}{\Omega\tau_B}\right) \ll 1 \tag{1.36}$$

If this condition is satisfied then, following the procedure outlined e.g. in [121], one can obtain an evolution equation for the guiding centre parallel velocity

$$m\dot{v}_\parallel \mathbf{b} = Ze\left(\mathbf{E} + \dot{\mathbf{R}} \times \mathbf{B}\right) - \mu\nabla B - mv_\parallel^2 \boldsymbol{\kappa}, \quad \mathbf{b} := \frac{\mathbf{B}}{B} \tag{1.37}$$

where $\boldsymbol{\kappa}$ is the curvature of the magnetic field lines and $\mu = mv_\perp^2/2B$ is the magnetic moment. In particular, if we take the dot product with $\mathbf{b}$ we obtain:

$$m\dot{v}_\parallel = ZeE_\parallel - \mu\nabla_\parallel B \tag{1.38}$$

The last term in this equation is the so-called **mirror force**. Indeed, it reflects charged particles trying to enter region of strong magnetic fields.

This phenomenon was historically employed for the construction of the very first magnetic fusion devices, which were therefore called **magnetic mirrors**. To illustrate the basic working principles of this device, in figure 1.5 we show the motion of a charged particle projected in the $(x, y)$ plane in a magnetic mirror. This figure was obtained by direct numerical

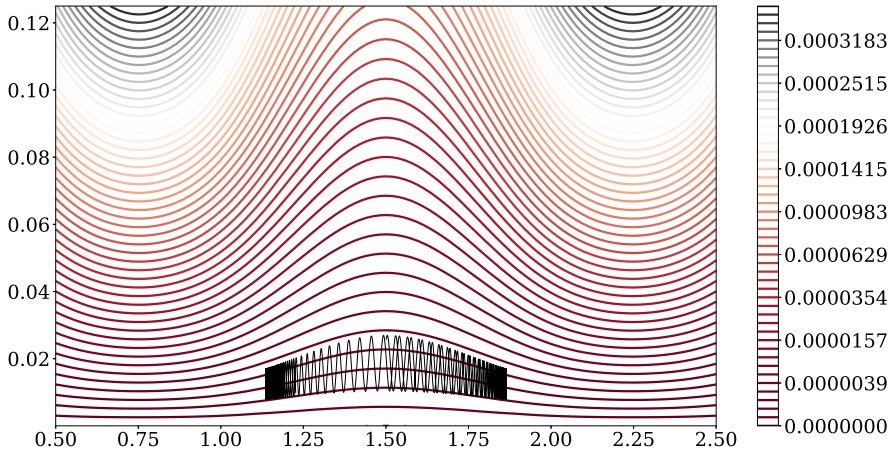


**Figure 1.5:** *Charged particle trajectory (in black) in a magnetic mirror device. The contour lines of the magnetic field are showed in a red-grey colormap. The particle starts its journey from a region of low magnetic field and is reflected back and forth when it reaches the "wells", that is regions of high magnetic field.*

solution of equation 1.30 using an ad-hoc developed Python code. Not all the charged particles in a mirror devices are however trapped. Indeed, it can be shown that for trapping to occur the following condition (e.g. [121]) must be satisfied:

$$\frac{B}{B_{\max}} \leq \frac{v_\perp^2}{v^2} \leq \frac{B}{B_{\min}} \tag{1.39}$$

that is, in magnetic mirrors there always exists a **loss cone**, which must be plugged by some means.

The most natural idea would consists in bending the open field lines characteristic of a mirror devices and let them close on themselves. Closed magnetic field lines are necessarily confined in a bound region of space. The field lines may wander indefinitely through the bounded region in which it is confined, before closing on itself after an infinite journey. An inescapable consequence of this topology is the fact that such a line densely fills some region of the domain in which it is confined; that is, it passes arbitrarily

close to any point of this region. The latter may be the whole domain or some three-dimensional subdomain; finally, the region densely covered by field lines may be a two-dimensional surface. A Theorem of topology guarantees that, if the magnetic field $\mathbf{B}$ never vanishes on this surface and, moreover, this surface does not have any edge, then it must be a toroid [4]. This type of topology is used in most fusion machines such as the **tokamaks** or the **stellarators**, which will be briefly discussed in the following. One can be more quantitative about what has been said so far. Let $\psi(\mathbf{x})$ denote a real, sufficiently regular, function; then the level-set,

$$\psi(\mathbf{x}) = \psi, \tag{1.40}$$

of $\psi$ defines a surface. One can take the function $\psi(\mathbf{x})$ in such a way that the surface is a toroid [8]. Moreover, by varying the real number $\psi$, then the condition (1.40) represent a family of nested toroids, as shown schematically in figure 1.6. One can further assume that the magnetic field

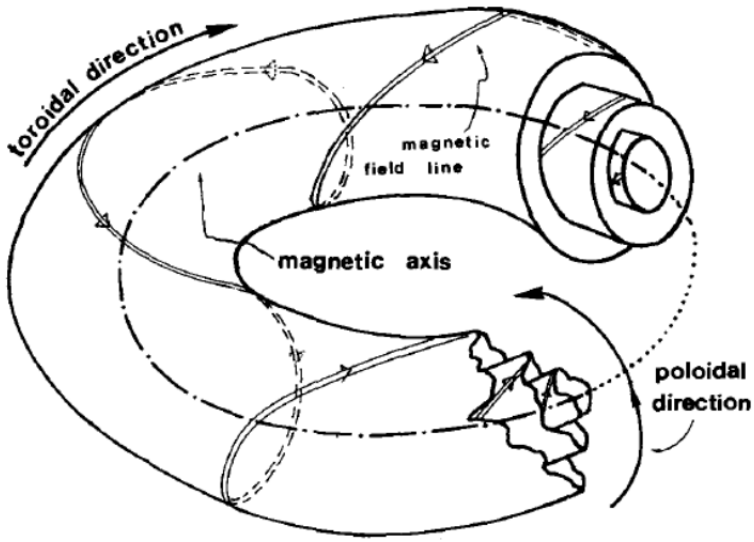


**Figure 1.6:** *Family of nested toroidal magnetic surfaces. The magnetic, indicated with a dashed line, is a degenerate toroidal magnetic surface. The magnetic field lines twist onto the magnetic surfaces. From [8].*

of interest is such that each one of its field lines lies on some surface of the family (1.40). This condition can be expressed as:

$$\mathbf{B}(\mathbf{x}) \cdot \nabla\psi(\mathbf{x}) = 0 \tag{1.41}$$

The surfaces $\psi(\mathbf{x}) = \psi$ having this property are called *magnetic surfaces*. Up to now, nothing has been said about the explicit form of the magnetic field $\mathbf{B}$. However, starting from equation (1.41), one can show [8] that the magnetic field $\mathbf{B}$ must be necessarily of the following form (cfr. figure 1.6):

$$\mathbf{B} = B_\theta \mathbf{g}_\theta + B_\varphi \mathbf{g}_\varphi, \tag{1.42}$$

where $\mathbf{g}_\theta$ and $\mathbf{g}_\varphi$ denote two versors in the poloidal and toroidal direction respectively. One can show that the only presence of a toroidal magnetic field is not enough to guarantee confinement of plasma particles in a bounded region of space. Indeed, in these conditions the magnetic field curvature and gradient would originate a vertical drift [121] which is in opposite direction for ions and electrons. The resulting electric field causes an outward $\mathbf{E} \times \mathbf{B}$ drift of the whole plasma and hence such a simple magnetic field configuration will be unstable. Therefore, to avoid the charge separation it is necessary to twist the magnetic field lines, that is the poloidal component $B_\theta$ of the magnetic field cannot vanish. This brings about the question on how one can generate a non-vanishing $B_\theta$ and hence obtaining the required twisting of the magnetic field lines. Here we shall concentrate only on tokamaks and stellarators:

- the tokamak approach was proposed by two Russian physicists, Tamm and Sakharov, in 1950 [146]. The toroidal magnetic field is provided by simple magnets and the necessary twist is produced by the plasma itself, by means of an electric current in the plasma which gives rise to the component $B_\theta$ of the magnetic field, as shown in figure 1.7. This current flowing in the toroidal direction is produced by induction, the plasma acting as the secondary circuit of a transformer.
- the stellarator approach was proposed in 1951 by Spitzer [125]. In a stellarator the twist of the magnetic field lines is created by external coils wound around the plasma torus, as shown in figure 1.7. These external coils have the advantage that the current can be controlled from outside and can flow continuously, differently to what happens in tokamaks, which are pulsed devices. However, from figure 1.7 one can appreciate the complexity of the magnetic coils which are needed in stellarators.

## 1.7 Tokamaks

As stated at the end of the previous section, tokamaks were first proposed in Soviet Union 1950, by A. D. Sakharov and I. E. Tamm. They formu-

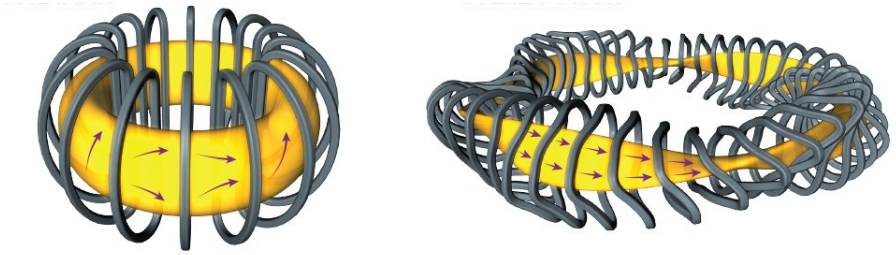

**Figure 1.7:** *Schematic design of a stellarator (left) tokamak (right). In a tokamak, the twisting of the magnetic field lines is provided by the combination of external coils and the plasma current flowing into the plasma. In a stellarator, the twisting is provided by external coils only.*

lated the most basic principles of magnetic confinement of high temperature plasma and performed the first estimations of a possible thermonuclear reactor. In a tokamak, the plasma is contained withing a toroidal vacuum chamber and is confined, as stated in the previous section, by means of toroidal and poloidal magnetic fields. Reaching ignition conditions in such a device is, however, non-trivial and several components need to be optimised. Here, we will briefly touch upon to the most basic aspect concerning tokamak devices will be discussed.

### 1.7.1 Plasma heating

In a tokamak, the poloidal component of the magnetic field necessary to provide the twisting of magnetic field lines is provided by the current, $I_P$, flowing into the plasma. The latter is, in turn, induced by means of the transformer principle. In order to increase the energy and thus the temperature of the plasma, the most basic source of heating is provided by the same plasma current. This occurs thanks to the principle of **Ohmic heating**, thus:

$$P_{\text{Ohm}} = R_P I_P^2 \tag{1.43}$$

where $R_P$ denote the plasma electrical resistance. From this expression, one can think of achieving ignition conditions simply by increasing the plasma current. This is however not possible. Indeed, increasing $I_P$ over certain values leads to plasma instabilities which can destroy the plasma confinement. Moreover, the plasma resistance is not constant. Indeed, it can be shown that the plasma conductivity, $\sigma_{\|}$, is given by [121]:

$$\sigma_{\|} = \frac{12\pi^{3/2}}{\sqrt{2}} \frac{T_e^{3/2}\epsilon_0^2}{Ze^2\sqrt{m_e}\log\Lambda} L_{11} \tag{1.44}$$

where $T_e$ is the electron temperature, $Z$ the atomic number, $m_e$ the electron mass, $\log \Lambda$ the Coulomb logarithm and $L_{11}$ a numerical constant. From this expression, one can see that the conductivity (the inverse of the resistivity) increases with increasing temperature and, consequently, the Ohmic power decreases. Other heating mechanism become thus necessary in order to reach ignition conditions. Here we shall list some of this so-called **additional heating** mechanism which have been studied in tokamaks since the 1970s with the T-10 installation [149]. One possible solution consists in using a high-energy neutral particle beam injector. The mechanism which is ultimately responsible of plasma heating is ultimately due to **charge-exchange** reaction, that is a reaction of the form:

$$\mathrm{D}^+ + \mathrm{D} \rightarrow \mathrm{D} + \mathrm{D}^+ \tag{1.45}$$

where $\mathrm{D}$ denotes the deuterium atom. In this process, the high-energy neutral transfer its energy(and charge) to the low-energy ion.
Additional heating mechanism are, instead, based on the fact that a plasma, being composed by electrons and ions, can interact with electromagnetic waves. The latter, under some circumstances, can be effectively absorbed into the plasma, damping their energy into it (resonances). Several of such radiofrequency-based heating mechanism are possible, but the most common ones usually involve the coupling of the electromagnetic wave at the cyclotron resonance of the ions or the electrons. The corresponding heating mechanism are, for this reason, called **Electron Cyclotron Resonance** (ECR) heating and **Ion Cyclotron Resonance** (ICR) heating.

### 1.7.2 Plasma Facing Components

Up to now, the discussion have been limited to the description of how to confine the plasma in a bounded region of space through magnetic fields. However, this confinement is not perfect and some of the power and particle leaks through the magnetic field, leading to an unavoidable interaction between the plasma and the vacuum vessel wall, which in turn leads to the issue of the so-called **Plasma-Material Interaction** (PMI). As we shall see in the forthcoming Chapter, this PMI results in important consequences for both plasmas and materials. We should limit here to observe that even in the very first tokamak installation (the T-1 tokamak), it was noted that the energy power balance was entirely dominated by radiative losses, resulting from impurity vacuum vessel materials migrating into the plasma [149]. The materials directly facing the plasma, called the **Plasma Facing Materials** (PFCs), play a pivotal role in magnetic fusion research and they are

the dowels of the so-called First Wall (FW). Indeed, since they are directly exposed to the plasma they are subjected to extreme operative conditions, in terms of both particle and energy loads. In addition, they must be able to maintain their functional properties during all the operation history. In order to mitigate the coupled effect on both plasmas and materials of PMI, one possible strategy is to let this interaction to occur only on a limited portion of the first wall. Two different strategies have been devised to this end: the **limiter** and the **divertor** configuration, which are shown schematically in figure 1.8. As the name suggests, the limiter consists simply in a protrusion

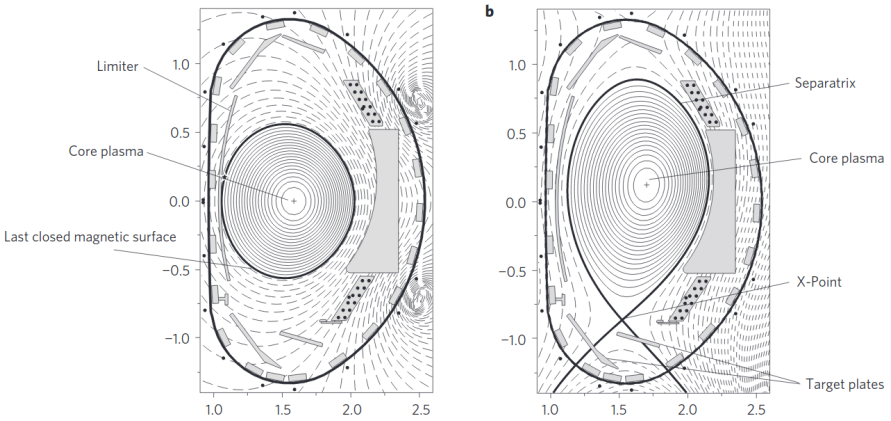


**Figure 1.8:** *The limiter (left) and the divertor (right) configuration. From [53].*

of the FW inside the plasma. The action of the limiter is thus apparent: it allows to protect the vessel main chamber from the interaction with the hot plasma. In spite of being the most obvious solution for preventing PMI, the limiter has major drawbacks. The direct interaction between the hot plasma and the limiter surface can produce too high power loads, resulting in hot spots and thus generating large erosion problems of the limiter surface and difficult impurity control [151]. A possible way out of these drawbacks, is to let a current flowing in an external conductor in the same direction as the plasma current. This allow to create a point, called the **X-point**, where the poloidal component, $B_\theta$, of the magnetic field vanishes. In this way, the plasma is effectively diverted (hence the name **divertor configuration**) from its confined hot region, through the **separatrix**. In both the divertor and limiter configurations, one can distinguish between a region of closed and open field lines. For this reason, one can identify the so-called **Last Closed Flux Surface** (LCFS), beyon which magnetic field lines are open. The thin annular plasma that extend beyond the LCFS is called **scrape-off**

**layer** (SOL) and the plasma properties in this region are those ultimately impacting the PMI. A distinction is usually made between the **plasma edge** and the SOL; the former includes the SOL but also extended some distance inside the LCMS into the main plasma

### 1.7.3 ITER

We have outlined what are the most basic ingredients of a tokamak device. Here, we shall discuss one of the most important machines of this kind, which is being built in Cadarache (France). It is called the **ITER** project. ITER (which literally means *the way* in latin) has the main objective of proving the scientific feasibility of fusion as an alternative source of energy. The original design of the ITER project officially began in 2006 as a joint venture of seven member entities, that is EU, India, China, Japan, Russia, South Korea and the US. The major aim of the ITER project will consists in providing a thermonuclear burning $\mathrm{D}-\mathrm{T}$ plasma with a gain factor $Q = 10$ and an expected fusion power of $\simeq 500\,\mathrm{MW}$. As mentioned, the tokamak is currently under construction. In more details, the tokamak complex surrounding construction will be finished in 2021, while the tokamak assembly in 2025. At the end of the 2025, the first non-nuclear phase will begin, employing firstly $\mathrm{He}$ and $\mathrm{D}$ plasmas. It is not before $2035$ that the first $\mathrm{D}-\mathrm{T}$ should be expected.
A schematic representation of the ITER tokamak is shown in figure 1.9. This machine will confine a volume of plasma of about $\simeq 840\,\mathrm{m}^3$, with a major radius of $R = 6.3,\mathrm{m}$, using a toroidal field at the machine axis of about $6\,\mathrm{T}$. The latter will be provided by superconductive field coils. Thanks to the latter, it will be possible to achieve a quasi-steady state regime. Neutral beam injection and radiofrequency heating will be employed, for an a total external input power of $73\,\mathrm{MW}$. The plasma current will be around $15\,\mathrm{MA}$. The FW plasma facing materials will be based on beryllium (Be) for the main chamber and tungsten (W), exploited for the divertor components, where the most extreme conditions are expected.

### 1.7.4 DTT

Undoubtedly, the ITER project should and would mark an important step towards the successful construction of a demonstrative power plant based on fusion reactions, **DEMO**, which is scheduled to be completed by 2050. One of the main challenges in the roadmap is, however, the development of a reliable solution for the daunting task of heat and power exhaust system able to withstand the large loads to be expected at the divertor region

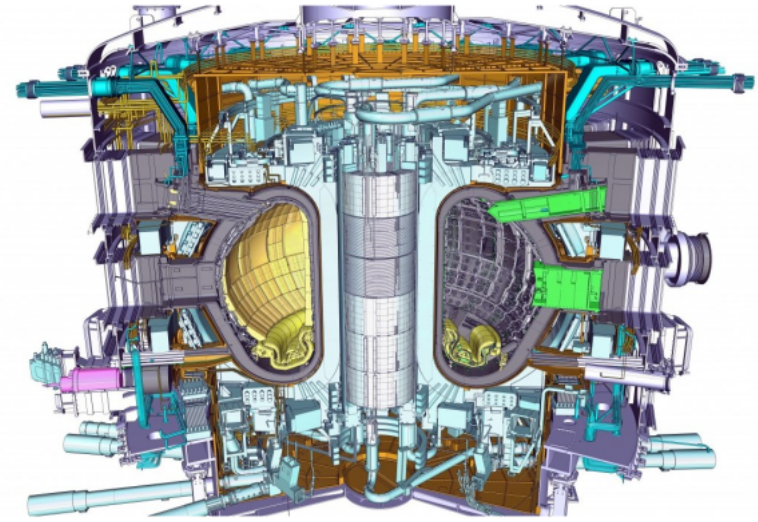

**Figure 1.9:** *Schematic representation of the ITER tokamak. From [1].*

of a fusion power plant. For this reason, in parallel with the ITER project, the EUROfusion consortium has initiated a dedicated project which aims at studying alternative solutions for power exhaust in a DEMO-like machine. The latter will be carried on in a new machine, called the **Divertor Tokamak Test** facility (DTT) [87]. DTT will have to operate in a range of possible scenario, with significant power loads, alternative plasma configuration plasma edge and bulk conditions approaching, in as much as possible, those planned for DEMO. An optimal balance between these requirements and the need to realise the new tokamak accomplishing the DEMO timescale, led to the choice of the following machine parameter: major radius $R = 2.1\,\mathrm{m}$, minor radius $a = 0.65\,\mathrm{m}$, toroidal field at the machine axis $B_\varphi = 6\,\mathrm{T}$, plasma current of $I_p = 5.5\,\mathrm{MA}$ and a pulse duration of $90 \div 100\,\mathrm{s}$. The overall additional power for plasma heating will be $P_{\mathrm{ext}} = 45\,\mathrm{MW}$. In addition to different plasma scenarios, DTT will have also the possibility of testing various plasma facing components (such as tungsten and liquid metals) up to an overall power flux of about $20\,\mathrm{MW/m^2}$. The final target of the DTT experiment is the realisation of an integrated solution (bulk and edge plasma) for the power exhaust in view of DEMO.

CHAPTER 2

# The issue of Plasma-Material Interaction

In this Chapter, we will briefly present the most important topics of Plasma-Material Interaction (PMI). We start in § 2.1 with a broad discussion related to the interaction between plasma ions and solid matter. We distinguish here between thermal (cfr. § 2.1.2) and particle (cfr. § 2.1.1) effects. We then move on and in § 2.2 analyse the impact that PMI has on the tokamaks operation. We shall see that, for example, that due to sputtering the eroded material can migrate into the plasma, leading to complex phenomena such as plasma cooling and PFC materials re-deposition. In light of the PMI and its issue on tokamak operation, we then consider in § 2.3 the best candidate materials for the tokamak first-wall and discuss in some details the advantage of W as a first-wall material. We proceed by summarising the PMI effects (cfr. § 2.4) that have been observed in literature after the exposures of W to deuterium, § 2.4.1, and helium, § 2.4.2 plasmas. We then move on and discuss in § 2.5 some details the necessity of modelling efforts for PMI mitigation and control in both present-day and future devices. We focus, in particular, on both the plasma (cfr. § 2.5.1 and

the material side (cfr. § 2.5.2) of the PMI modelling. The necessity for the lab-scale investigations of PMI in fusion-relevant environment is then introduced in § 2.6. We focus here in particular on the pivotal role of Linear Plasma Devices (LPDs) in the PMI field § 2.6.1 and on the possibility of mimicking fusion-relevant coatings with material science techniques (cfr. § 2.6.2). We conclude the Chapter with the discussion of the specific aims of the Ph.D. work.

## 2.1 Plasma interaction with matter

When discussing the basic principles of MCF (cfr. § 1.6), nothing as being said about the faith of particles which leave the confined region. Indeed, the confinement provided by the twisting of field lines in a toroidal device is not perfect and, more strikingly, it should not be so. The reason for this last, apparently contradictory, statement is the following. In a thermonuclear plasma, the $\mathrm{He}$ ions which are produced initially have a very high energy, $\simeq 3.5\,\mathrm{MeV}$. This high-energy population of ions quickly thermalise with the background plasma ions, through Coulomb collisions. However, once this process has terminated, the $\mathrm{He}$ ions no longer contribute to the fusion process and will, if not pumped away from the system, results in fuel dilution. That is, the plasma will no longer produce fusion reaction at a sufficiently high rate. In addition to this, even if $\mathrm{He}$ ashes were not the problem, as already stated, one should note that confinement in a toroidal device is not perfect. This means that the plasma unavoidably interact with the vacuum vessel of the reactor. Even if we let this interaction to occur only in a remote region of the tokamak discharge chamber (say by employing a diverted configuration), the interaction of two such different states of the matter (solid and plasma) have dramatic consequences on both. These effects, which collectively go under the name of **Plasma-Material Interaction** (PMI), occur on time and length scale which span from nanoseconds to years and from nanometers to millimeters, respectively. In addition to this multi-scale nature of the PMI problem, the plasma and the material side must be studied in a coupled manner. Said otherwise, PMI is a **multiscale and coupled** problem. A summary of the various PMI process is schematically presented in figure 2.1. In the remaining of this Section, we shall discuss in some details the type of effect that can be expected due to the PMI. Collectively, we shall distinguish between **particle** and **thermal** effects. The latter are due to the power that must be exhausted from the plasma, while the former are related to the effected induced onto the PFCs related to particle bombardment.

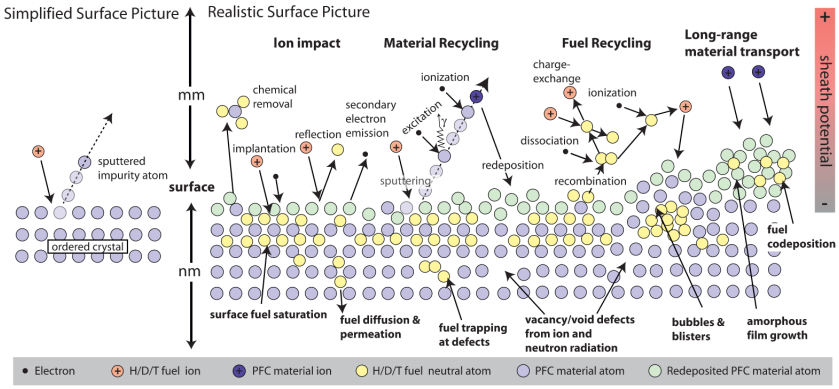


**Figure 2.1:** *Schematic illustration of the various PMI processes. From [158].*

### 2.1.1 Particle effects

Plasma particles are released due to transport from the confinement region of tokamak devices. The interaction of these particles with the PFCs results in important particle-induced effects. Furthermore, in addition to plasma particle, in $D-T$ thermonuclear plasma also a flux of high-energy neutrons is produced as well as $He$ ashes. Whenever an energetic particle interact with a solid material, it can transfer part of its kinetic energy to the **primary knock-out atom** which in turn can collide with other lattice atoms. This process, repeated over many collisions, results in the so-called **collisional cascade**. The latter is shown in figure 2.2. During the collisional cascade, some atoms are displaced from the lattice, leading to the formation of defects, such as vacancies and interstitials. The type of the radiation damage experienced by the PFMs depend on the type of impinging particle, its energy and, furthermore, on its chemical affinity with the FW materials.

Undoubtedly, one of the most important results of the collisional cascade is the process known as **physical sputtering**. The theory of physical sputtering has been original put forward by Sigmund [147], who first used transport theory to compute the amount of sputtered target atoms per incident ions, a quantities which is called **sputtering yield**. Sigmund computed this quantity by considering amorphous (i.e. random) targets. In such a case, one can give a qualitative picture of the sputtering process as follows. An ion impinging onto a given target undergoes a series of collisions slowing down into the target itself. In this process, atoms which recoil with a sufficiently high energy can undergo secondary collisions, thereby generating other recoiling atoms. Both the ion itself and the energetic recoiling atoms

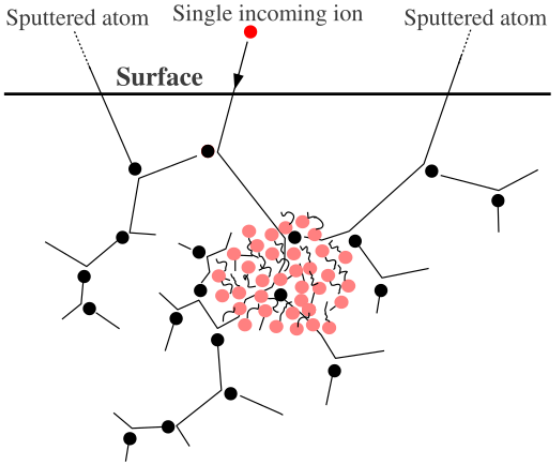


**Figure 2.2:** *Illustration of the physics of the collision cascade. At high kinetic energies ($\geq 1\,\mathrm{keV}$) an incoming ion and the recoils (shown in black) collide only occasionally and travel in almost straight paths in between collisions. They loose energy during the collision continuously due to electronic friction. This initial phase can be successfully described using the binary-collision approximation and mostly leads to the formation of point defects and single atom sputtering. When they have slow down sufficiently, a dense region of many-body collisions known as a heat spike can form. From [59].*

have the possibility of getting scattered back through a series of collisions. It should be noted that the back-scattered ion and the energetic recoiling atoms only account for a minor portion of the overall number of the sputtered atoms, while they constitute most of the sputtered energy. Indeed, the energy distribution of the sputtered atoms is given by [17]:

$$f(E) = \frac{E}{(E + E_s)^{3+2m}} \tag{2.1}$$

where $E$ denotes the energy of the sputtered atom, $E_s$ is the so-called **surface binding energy** and $m$ is a parameter which ultimately depends on the type of the interaction potential. It can be shown that the maximum of the distribution, $f(E)$, is given by $E_{\max} = E_s/(2-2m)$. Now, since $E_s$ is usually of the order of some $\mathrm{eVs}$, then the peak atom energy is small. This results can be explained by noting that most of the sputtered atoms are due to high-order recoiling atoms, which are characterised by a low energy [147].

One of the most important property of physical sputtering is that is characterised by a threshold value of the impinging ion energy below which sputtering cannot take place. Indeed, the recoiling atoms put in motion through

the collisional cascade must have energies sufficiently high to overcome the surface binding energy, $E_s$. In particular, for light ions impinging on heavy materials the threshold energy can be computed as [16]:

$$E_{\mathrm{th}} = \frac{(M_1 + M_2)}{4M_1M_2\left(M_1 - M_2\right)^2} E_s \tag{2.2}$$

where $M_1$ and $M_2$ denote the incident particle and target mass respectively. Up to now, nothing has been said about the energy dependence of the sputtering yield. One could expect that the higher the impinging ion energy, the higher will be the sputtering yield. However, this is not the case. Indeed, if the impinging ion has a high energy, it will penetrate deeply into the target material and, thus, most of the collisional cascade will far away from the surface. Indeed, the energy dependence of the sputtering yield, $Y$, at normal incidence can be described by the following expression [16]:

$$Y\left(E\right) = QS_n\left(E\right)\left(1 - \frac{E_{th}}{E}\right)^2\left[1 - \left(\frac{E_{th}}{E}\right)^{2/3}\right] \tag{2.3}$$

where $S_n\left(E\right)$ is a function for the energy dependence of the energy deposited in elastic collision, while $E_{th}$ and $Q$ are fitting parameters, which depend on the ion-target combination. In figure 2.3, we show the sputtering yield behaviour of several ion-target combination. As it is seen from this figure, the sputtering yield strongly depend on the mass of ion-target masses combination. This means that heavier and, thus, high-Z materials are much more difficult to be sputtered from low-Z light elements. This is the case of $\mathrm{W}$, which is sputtered from impinging $\mathrm{D}$ ions only above $\simeq 200\,\mathrm{eV}$. In figure 2.3, we reported also the sputtering yield of $\mathrm{D}$ on $\mathrm{C}$. Quite interestingly this curve does not show any energy threshold, that is even thermal particle can lead to a substantial sputtering of $\mathrm{C}$. This constitutes an example of another type of sputtering mechanism which goes under the name of **chemical sputtering**. In this case, material removal is the results of a chemical bonding process of the plasma ion with the solid material.

As stated at the beginning of this section, in a thermonuclear $\mathrm{D} - \mathrm{T}$ plasma one need also to account for the interaction of $\mathrm{He}$ ashes and neutrons with the PFCs. In particular, fusion-produced neutrons are characterised by a high energy ($14.1\,\mathrm{MeV}$). Furthermore, neutrons are electrically neutral and can thus penetrate deeply into the the material, inducing bulk damages by collisional cascade and, furthermore, nuclear transmutations of target atoms. As a result of the collisional cascade, the structure of the PFM

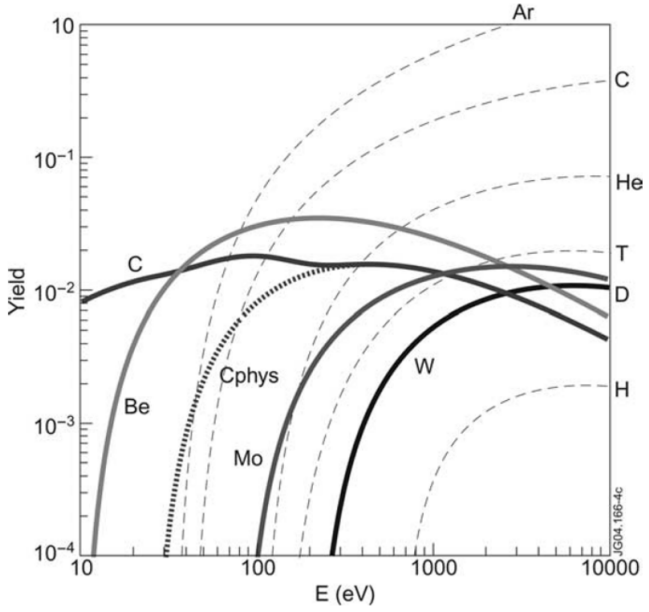


**Figure 2.3:** *Physical sputtering yield for different fusion relevant materials bombarded with* D *(solid lines). The dashed lines denote the sputtering yield of* W *bombarded with different, fusion-relevant, atoms.*

changes dramatically. Particularly, $(n, \alpha)$ reactions can lead to **swelling** phenomena, due to the generation of voids and $\mathrm{He}$ bubbles in the lattice vacancies. In addition to this, nuclear transmutations can result in the formation of multi-component alloys with thermodynamic and transport properties which might differ substantially from that of the unirradiated material. As regards the $\mathrm{He}$, the latter can lead to important phenomena when interacting with solid PFCs. Indeed, the surface of PFCs can be deeply affected by the exposure to energetic $\mathrm{He}$ that can results, in addition to sputtering phenomena, to the growth of surface nanostructures (such as the **fuzzy** structure), and implantation phenomena.

### 2.1.2 Thermal effects

The plasma that leaks through the confined region of a toroidal magnetic device finds itself on the open field lines characteristic of the scrape-off layer region. Undoubtedly, one of the most striking properties of plasmas in a magnetic field consists in the fact that transport processes are deeply anisotropic. In particular, plasma transport occurs much faster in the parallel-to-B ($\parallel$) direction then in the orthogonal one ($\perp$), which leads

to the fact that the plasma-wetted area is usually much smaller with respect to the overall area of the tokamak vessel wall. In order to be more precise as regards the last statement, one needs to introduce the concept of **SOL width**. The latter is usually defined as the perpendicular distance from the magnetic separatrix over which the plasma thermodynamic and transport quantities are spread onto the open field lines which defines the SOL itself. In principle, one can introduce a different SOL width for each specifying plasma and transport quantities. However, since we are here interested in thermal effects, we shall limit to the discuss the power SOL width. The latter can then be estimated using the following argument. Once the plasma coming from the core plasma reaches a limiter or a divertor target, it has spent as much time traveling trough the SOL in the $\parallel$ as in the $\perp$ direction, that is:

$$\tau_{\parallel} = \tau_{\perp} \tag{2.4}$$

This last equality can be rephrased in terms of distances and velocities as follows:

$$\frac{L_{\parallel}}{v_{\parallel}} = \frac{\lambda_{\mathrm{SOL}}}{v_{\perp}} \tag{2.5}$$

where $L_{\parallel}$ denotes the so-called parallel connection length [151], $\lambda_{\mathrm{SOL}}$ is the SOL width, $v_{\parallel}$ and $v_{\perp}$ are the velocities in the $\parallel$ and $\perp$ with respect to $B$ direction, respectively. Thus, in order to estimate $\lambda_{\mathrm{SOL}}$ one needs first to obtain an expression for $v_{\perp}$, which however turns out to be extremely challenging. A successful model which has been recently proposed is the so-called **heuristic drift model** [118]. Using this model, one obtains the following scaling for the power SOL width $\lambda_q$:

$$\lambda_q \propto \frac{a}{R}\frac{1}{B_{\theta}} \tag{2.6}$$

This expression shows that $\lambda_q$ is inversely proportional to the poloidal magnetic field which, in turn, is related to the plasma current $I_p$. Particularly interesting is the evaluation of equation (2.6) using the parameter $a, R$ and $B_{\theta}$ of the ITER device. One obtains $\lambda_q \simeq 2\,\mathrm{mm}$. This shows that, due to transport anisotropies, the thickness of the SOL can be extremely small. In turns, this also means that all the power either injected into the plasma or produced by $\alpha$-heating must be exhausted in an extremely thin channel, which results in very high $\simeq 50\,\mathrm{MW/m^2}$ [76], intolerable, heat fluxes onto the targets, in the case of ITER.

In addition to these average heat loads, one must take into account also transient heat loads that might occur in a tokamak. Such transient loads

may occur as a results of off-normal events, such as a **disruption**. The latter can lead to power densities of $\mathrm{GW/m^2}$ delivered within a millisecond time scale. Tokamaks are also characterised by burst of energy and particle released periodically from the plasma onto the targets. These are the **Edge Localised Modes** (ELMs). The latter are instabilities at the plasma edge, which appear above a certain pressure gradient. They partly expel the edge plasma energy content within less than a millisecond.

## 2.2 PMI impact on tokamaks operation

In the last two Sections, a brief overview of the PMI was given. Up to now however, nothing has been said on the impact of PMI on the tokamak operations.

As regards the particle effects, we shall start by considering the effect of sputtering. As mentioned in the previous Section, the interaction of the plasma ions with the PFCs can result in the release of target atoms. Once eroded, these **impurity** ions can migrate into the plasma, leading to potentially serious issue for the tokamak operation. Indeed, it was noted since the beginning of the experimental research on tokamak, that most of the heating power was lost by radiation due to impurities [149]. It is important to stress that we are actually here speaking of a peculiar type of radiation loss, namely **line radiation**, which occurs as a results of electron being excited from their energy levels in a partially ionised atom. It is clear, therefore, that line radiation is more severe for those atoms characterised by a large amount of electrons in their shells, i.e. for the high-Z atoms. In addition to these radiative power loss issues, there is also the problem of **fuel dilution**. This arise because impurity atoms produce many electrons and, for a given plasma pressure, these electrons take the place of fuel particles. Therefore, at high concentration, impurities prevent the plasma to be effectively heated. Furthermore, impurities can also lead to disruptions as a result of cooling with correspondent modification of the current profile. In addition to these sputter-produced impurities, there are also those which are naturally present in any system, namely oxygen or water and carbon monoxide molecules, which are absorbed in the PFCs. These species can be desorbed thermally or through the interaction with the plasma ions. Since the tokamak is a closed system, the impurity atom that find their way into the plasma must inevitably **redeposit** onto the PFCs. The type of redeposition process depend both on the impurity atom as well as on the plasma parameters, such as the electron density and temperature. Usually, for sufficiently high density, the ionisation mean free path is small and, therefore, impurity

redeposit close from where they are originally produced, giving rise to the so-called **prompt redepositon**. In another circumstances, impurities might migrate into remote region of the tokamak. Eroded particles which redeposit onto the PFC lead to the formation of thick layer which develop on top of the pristine FW. These coatings are usually composed by the various elements present in the machine, that is they are characterised by a complex composition. In addition, they also show morphology and structures which might differ completely from that of the original FW materials. In figure 2.4, we show an example of a W redeposit found in JET-ILW. It can

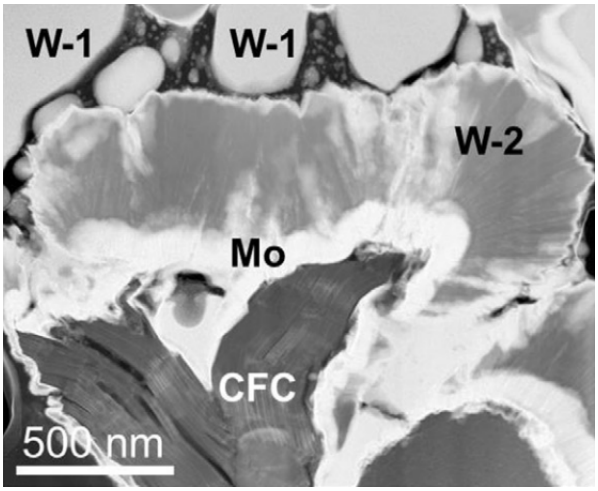


**Figure 2.4:** *Structure and composition of a* W *redeposit found in JET-ILW.* $W-1$ *and* $W-2$ *stand for amorphous and crystalline phase of* W *respectively. From [20].*

be seen that its structure can be really complex, with coexistence of different crystalline W phases. Their unconventional structure can be potentially dangerous for tokamaks operation. Indeed, they can co-deposit with the hydrogen isotopes which constitutes the main ions in the plasma, or with other gas impurities, such as nitrogen or oxygen, thus forming oxide and nitride layers. Particularly, the trapping with hydrogenic species is a concern. Indeed, when operated with $D-T$ mixtures, one needs to pay attention to the problem of **tritium inventory** in the tokamak. Since T is a radioactive element, its overall content must be below a threshold value, which for ITER is about $700\,g$ [55].
In $D-T$ burning plasma with significant He production an additional effect can occur on plasma-exposed metallic PFCs, such as W. Indeed, when W surfaces are exposed to He under certain conditions (e.g. [7,99,126]) the formation of a fiber-form structure, called **fuzzy-**W, has bee observed. This

particular structure (shown in figure 6.3) has been widely studied, mainly due to concerns on its mechanical and heat integrity under plasma exposures. We shall now consider the impact of thermal effects on the tokamak

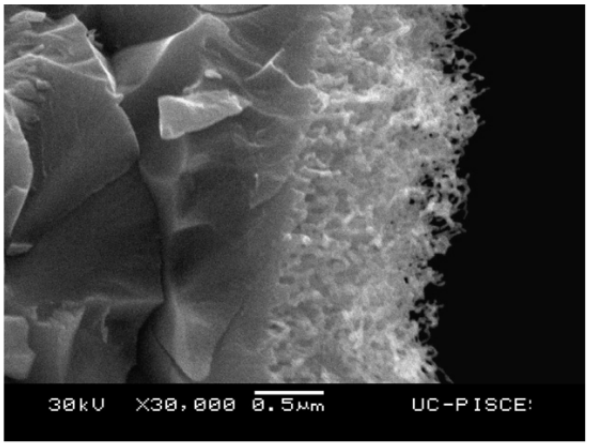


**Figure 2.5:** *Example of fuzz formed on a* He*-exposed* W *surface. From [136].*

operation. In § 2.1.2, we showed that due to the anisotropy of plasma transport, the power SOL width can be very small, which results in high power fluxes onto the PFCs and, in particular, onto the divertor targets. Recalling the discussion made there, if we take as an example the ITER case, then the power fluxes in the divertor region can be as high as $\simeq 50\,\mathrm{MW/m^2}$. This value is well above the maximum tolerable value of $10 \div 15\,\mathrm{MW/m^2}$ which is set by the choice of the materials [76, 86] by preserving their integrity. However, it might occur that, during off-normal events, power densities as high as tens of $\mathrm{GW/m^2}$ can be achieved, usually in a time scale of some $\mathrm{ms}$. These off-normal events can lead to a substantial modification of the materials properties. Due to power fluxes of such an high intensities, the surface temperature can easily overcome the **recrystallisation temperature** of the materials, which is usually taken as a criterion to limit the peak heat fluxes onto the divertor targets [86]. Above this temperature, the surface morphology and crystalline structure of the materials can be deeply modified. In addition, the surface temperature can reach values above the **melting** temperature, which can result in droplet being released into the main plasma, with potentially hazardous impact on the overall tokamak operation.

## 2.3 First Wall materials candidates

In light of the complex phenomena related to plasma-surface interaction, § 2.1, and their impact on the tokamaks operation, § 2.2, it emerges that the selection of materials for PFCs in a magnetic confinement fusion device is a complex process that usually involves numerous trade-offs. In general, this selection is heavily weighted according to specific design objectives or constraints, and it is difficult to make broad statements regarding the properties of good versus bad materials. For example, there are requirements which are dictated by plasma performance (as, for examples, the necessity to minimise impurity contamination of the main plasma), requirements of engineering integrity and component lifetime (e.g. to withstand thermal stresses, to have acceptable erosion) and requirements of safety (minimise the tritium and radioactive dust inventories). A good plasma-facing material should have the following properties [135]:

- low sputter yield (both phyisical and chemical);
- low thermal erosion during off-normal heat loads such as disruptions and ELMs;
- low atomic number to avoid excessive radiation cooling of the main plasma;
- compatibility with hydrogen isotopes, that is low chemical interaction, low trapping probability, low permeability and, therefore, low tritium retention and inventory;
- high melting point;
- low vapour pressure;
- high thermal conductivity;
- high strength;
- low elastic module;
- high fracture stress;
- high thermal shock resistance;
- low activation by neutrons;

and many others. It is clear that no single material can satisfy all the above listed requisites. However, since the first days of magnetic confinement fusion, several different materials have been considered. The remaining of

this section is therefore dedicated to the illustration of advantages and disadvantages of different materials that have been tested in tokamaks.
As already mentioned, even at the dawn of the fusion research it was realised that most of the input heating power was radiated by impurities present in the plasma [149]. The first wall of these devices was made of middle-$Z$ elements, such as iron and nickel, which are characterised by good mechanical properties but rather high sputtering yields. Only by covering the most critical elements of the vessel, like the divertor targets or limiters, with low $Z$ materials, such as carbon, led to further progress in fusion research [135]. Carbon has excellent thermophysical properties, shows no melting, has high thermal shock resistance, and preserves its shape even under extreme temperature excursion. Moreover it can withstand, at least to some degree, off normal events such as disruptions and ELMs [135]. The weak point of carbon is that it suffers from high chemical sputtering due to the interaction with hydrogen leading to the formation of hydrocarbons and their radicals. Thick layers of hydrogenated carbon films could deposit on all plasma facing components, but also on components in remote areas. These layers contain large amounts of hydrogen isotopes and, therefore, the ability to retain tritium could prevent the use of carbon in future fusion reactors. The problem of $\mathrm{T}$ retention in a full-$\mathrm{C}$ device is evidenced in figure 2.6, where we show the tritium inventory foreseen in ITER for different PFMs choices after exposures to plasma discharges with different particles fluxes and baseline temperatures. Beryllium is another low-$Z$ element which has promising features as plasma-facing material. In particular, it is non reactive with hydrogenic species and it is a good thermal conductor. Its low atomic number makes it compatible with plasma operation, since it reduces the radiative effects in case of plasma contamination by armour erosion. However, its low melting temperature (1560 K) and the relatively high sputtering yield prevent its application as a divertor material and, therefore, can only be used for the protection of vessel main chamber. In spite of these positive features, the heat load at the first wall of future reactors (like DEMO) will prevent the use of Be even at the main chamber. High-$Z$ materials, such as tungsten, feature a very low erosion yield and, moreover, do not suffer from chemical sputtering; however their radiation capability is particularly high, due to line emission phenomena. In spite of this, the development of plasma scenarios with a rather cold plasma edge brought high-$Z$ materials such as tungsten under consideration. In particular, having plasma temperatures in front of the target plates in the few-eV region, allows to suppress the erosion yield due to their high threshold energies for physical sputtering. In particular, no notable erosion is observed

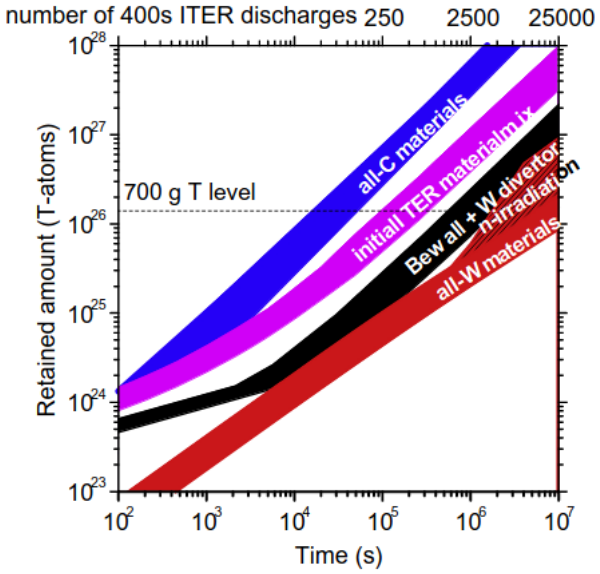


**Figure 2.6:** *tritium inventory foreseen in ITER for different PFMs choices after exposures to plasma discharges with different particles fluxes and baseline temperatures. From [55].*

for tungsten up to a plasma temperature of about $20\,\mathrm{eV}$. Moreover, the probability of prompt redeposition is relatively small due to its high mass and, therefore, large Larmor radius. The problems are the high heat load and off-normal events such as disruptions and ELMs which can cause significant melting of tungsten and a possible loss of the molten layer [135]. From the discussion made so far, since different conditions exist at different positions of the wall, for example, high heat and particle fluxes at the divertor targets and limiters, and less demanding conditions with fluxes of charge-exchange neutrals at the baffles and main chamber elements, one can think to adopt different materials for the PFCs. This is, in fact, the strategy that is adopted for the ITER PFCs, as can be appreciated from figure 2.7. Carbon Fiber Composite (CFC) was initially chosen for the divertor targets as a result of its high thermal shock resistance owing to its lack of a melting phase at the interested pressures, making it extremely resistant under the strong transient heat load expected during ITER plasma instabilities. However, carbon (C) has a significant hydrogen retention and, since the nuclear license limits the T-inventory in ITER to $700\,\mathrm{g}$ for safety reasons [55], removal techniques should have been employed to recover the trapped tritium. Moreover, CFC materials endure severe degradation of

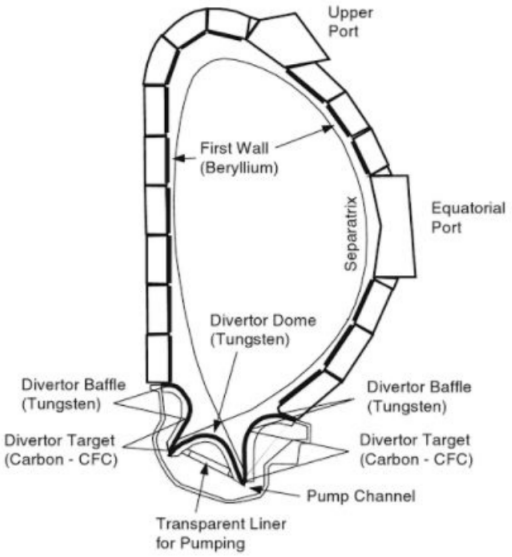


**Figure 2.7:** *Cross-section of ITER with PFCs (prior to 2013) including the main chamber, the V-shaped divertor slots with the divertor targets, baffles, and the divertor dome. From [135].*

their thermo-mechanical properties under high fluence neutrons irradiation at typical neutron fusion energies. These concerns, together with budget issues, brought the ITER Council during the $13^{\text{th}}$ meeting at Saint Paul-lez-Durance (France), on 20-21 November 2013, to the choice of a full-W divertor for ITER [1].

## 2.4 PMI effect on W

In ITER, the W divertor is expected to work from day 1, that is from the non-nuclear to the $\mathrm{D}-\mathrm{T}$ nuclear phase, when the milestone $Q = 10$ gain factor will be achieved. However, the multitude of the PMI phenomena will unavoidably lead to some modifications of the W surfaces, even in the non-nuclear phase. These modifications can lead to substantially modifications of the pristine W which can jeopardise its capabilities to withstand high thermal and particle fluxes. It is the scope of this section to briefly summarise the literature results concerning the W modifications induced by plasma exposures which have been reported in literature. Being the present Ph.D. Thesis work mostly concerned with the particle-induced effects (cfr. § 2.1.1), in what follows we limit ourselves to their impact on W surfaces.

### 2.4.1 Deuterium-induced modifications

The most common and currently most studied fusion reactions for magnetic confinement fusion applications involve hydrogenic species. Therefore, the first concern is related to the understanding of how tungsten surfaces react when exposed to hydrogenic plasmas. Since T is a radioactive element, it turns out to be quite difficult to be used as the main plasma species for these type of studies. In addition, it is widely considered that, from the point of view of PMI, D and T behave similarly. Therefore, full D plasmas are employed in order to understand PMI interaction with a W surface.
As regard sputtering, the contribution to the erosion of the W surfaces by interaction with D is usually considered to be negligible, at least in the divertor region of both present-day tokamaks and ITER. This is due to the fact that the D sputtering yield of W is very small (cfr. figure 2.3), since the threshold energy for this process to occur is as high as $\simeq 200\,\mathrm{eVs}$ [152]. Such high energies are not expected to occur in normal conditions at the divertor targets in ITER, where typical electron temperatures, $T_e$, should be $T_e \leq 10\,\mathrm{eVs}$ [76]. However, there can be portion of the FW of tokamaks which might be subjected to high-energy fluxes of D. Indeed, charge-exchange interaction (cfr. equation (1.45)) can lead to the production of high energy D *atoms* which, being neutral, can easily escape from the confinement region of the device. The energy can reach values easily above $\simeq 100\,\mathrm{eV}$ (e.g. [79, 88, 109]). Anyway, even low energy D can have important effect when interacting with W surfaces. Indeed, it is known (e.g. [108, 120]) that hydrogenic atoms have a very low solid solubility, but high mobility into W. When interacting with W surfaces, D atoms penetrate few nanometres with the material, since they are low energy. However, their high mobility implies that D can diffuse deep into the bulk of the material. Hydrogen isotopes can then be easily immobilised by impurity atoms present in the lattice, on the surface of grain boundaries, at dislocations and voids, or by other lattice imperfections which can act as trapping sites. The accumulation of D can lead to important modifications of the material mechanical and transport properties, which might hinder the integrity of the W surfaces exposed to D plasmas in the tokamak environment. The trapped D can additionally lead to the formation of blisters on the W surfaces. An example of such a modification is shown in figure 6.10 The formation of micrometric-sized bubbles can be clearly seen on the W surface. The mechanism which is ultimately responsible for the formation of D blisters is still unclear, but it is generally believed that it is due to the accumulation of D at trap sites, which results in the mecha-

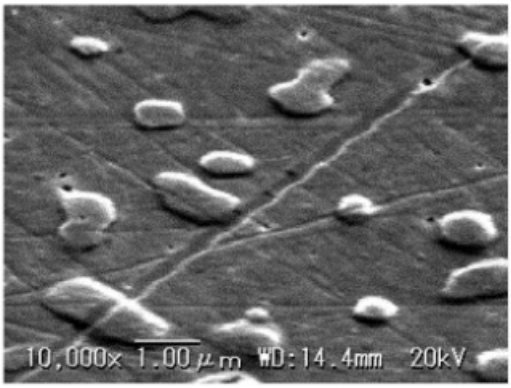


**Figure 2.8:** *Example of blisters observed on a* D*-exposed* W *surface. From [116].*

nism of crack growth and loop punching. During the implantation of low energy deuterium ions, if the incident flux is higher than the rate of D diffusion out of the implantation range, combined with the low solubility of D in W, then a high D concentration (supersaturation) in the near surface results. This leads to stresses that are relaxed by blistering [157]. Blistering after fusion-relevant D exposures has been investigated in depth with respect to both the impinging ion energy, fluence, surface temperature and roughness [27, 60, 77, 85, 103, 157]. For example, the ion energy alone is found to influence the blister dimension: smaller blister are favoured by low energy [60]. In addition, the surface properties (roughness or surface mechanical imperfections) are found to strongly favour or suppress blistering [27]. The formation of such structures can be potentially dangerous for the tokamak operation. Indeed, blisters formation on W surfaces can lead to an increase of D retention of plasma-exposed surfaces [49]. In addition, blisters can burst leading to the release of impurities within the plasma [75]. Blistering is not the only surface modifications which have been reported in literature. Indeed, at smaller scale (i.e. at the nanometer range) **surface nanostructures** have been reported in literature [49, 50, 111, 112, 154]. An example of W surface nanostructuring is reported in figure 2.9. The formation of surface nanostructures is an important aspect to be considered for tokamaks operation. Indeed, as reported by [154], surface morphology changes at the nanoscale can lead to a degradation of material properties as well as to enhanced erosion. Furthermore, it has been shown that surface modifications can lead to enhanced hydrogen retention [68].

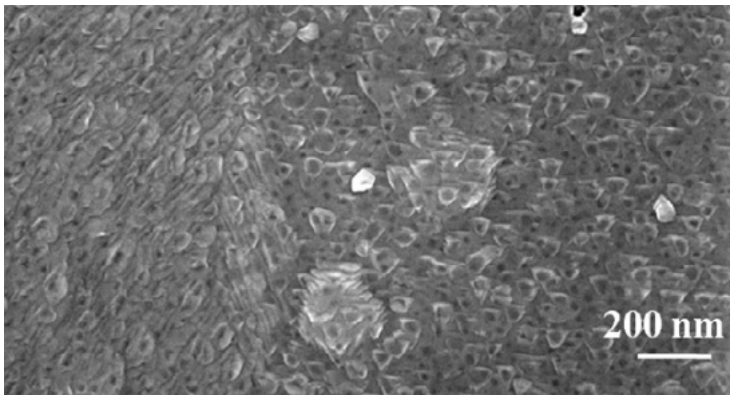


**Figure 2.9:** *Scanning Electron Microscope images showing the nanostructures developed on a* W *surface after* D *plasma exposures. From [50].*

### 2.4.2 Helium-induced modifications

Since the most promising fusion reactions to be employed in MCF is the one involving D and T, it is not difficult to understand why great attention has been paid in literature to the understanding of He-induced modifications in W surfaces. Furthermore, the first experimental campaign in ITER will be performed in He plasmas.
Literature studies concerning He plasma exposures are very wide. Indeed, the latter can lead to substantial surface modifications (such as formation of nanostructures and blisters), which are found to be deeply depend on the plasma exposure conditions (He flux and fluence, incident ion energy and surface temperature). Similarly to what happens for D, also He shows a very low solubility in solid and a high mobility [120]. Thus, by diffusing into W, it can be trapped at defects and accumulate at vacancy clusters. The subsequent formation and coalescence of He bubbles can lead to significant morphology changes, which strongly depend on the exposure temperature. In figure 2.10 we report a summary of the possible He-induced modifications as a function of the temperature. At low surface temperature, that is below $T_{\mathrm{surf}} < 900 \div 1000\,\mathrm{K}$, nanometric-sized bubbles develop on the surface [61, 70, 92]. In particular, a He energy threshold for bubbles formation has been identified at $\simeq 9\,\mathrm{eV}$. Furthermore, a fluence threshold of $\simeq 0.5 \div 1 \times 10^{24}\,\mathrm{He/m^2}$ has been identified for bubbles saturation. If the fluence is increase above this value, a network of stepped structures appears on the surface. These are reported in figure 2.11 The direction of the undulation, their interval and type are found to strongly depend on the crystalline orientation. A detailed explanation for the development of such

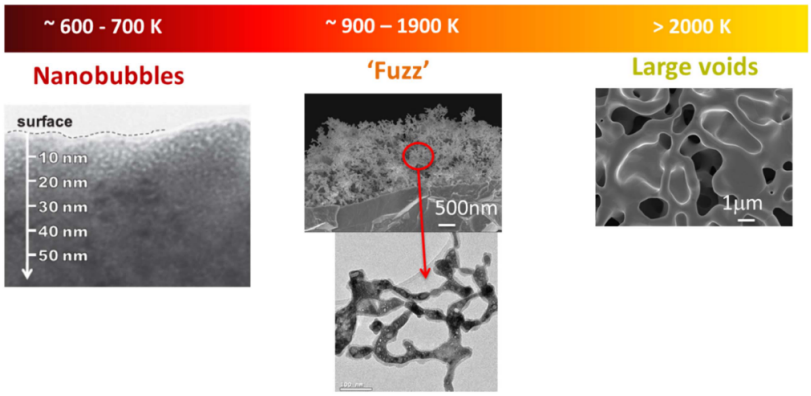


**Figure 2.10:** *Synthetic overview of the possible* W *morphology change after* He *irradiation at low energies. At temperatures below* $\sim 900\,\mathrm{K}$ *the formation of small nanobubbles is observed (left). At* $T > 2000\,\mathrm{K}$ *large voids appear on the surface (right), while the fuzzy-*W *nanostructures develop in the range* $900 \div 1900\,\mathrm{K}$. *From [115].*

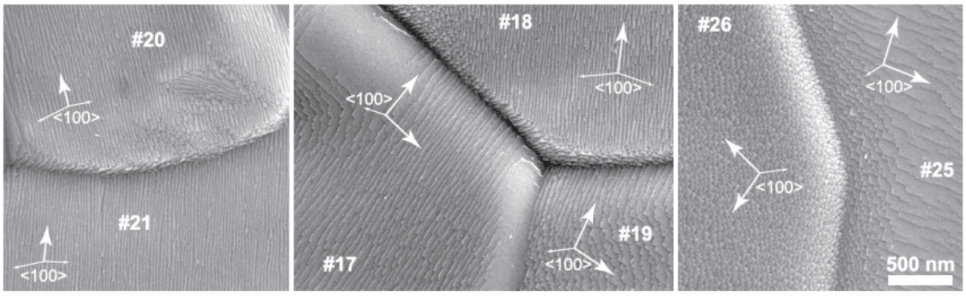


**Figure 2.11:** *Scanning Electron Microscope images showing the formation of stepped structures on the* W *surface exposed at* $473\,\mathrm{K}$ *with an incident ion energy of* $75\,\mathrm{eV}$ *and at a fluence of* $1 \times 10^{26}\,\mathrm{He/m^2}$. *From [92].*

structures is still missing. Possible hypothesis are related to the dislocation loop punching phenomenon, induced by the He bubbles pressure [80]. Also sputtering [150] could explain the formation of such structures. However, ripples are also observed to developed below the sputtering threshold of W when bombarded with He, as reported by [92].
When the surface temperature reaches values in the range $900 \div 1000\,\mathrm{K}$ and for $E_{\mathrm{ion}} > 20 \div 30\,\mathrm{eV}$, the formation of the fuzzy-W has been widely observed in literature [7, 99, 126]. An example of such structure is reported in figure 6.3. Fuzz formation has been widely studied in literature, since it raises particular concern about its mechanical and thermal integrity under plasma exposures. Furhtermore, the conditions for fuzz formation to occur

are expected to be reached in the ITER divertor regione [115] and W fuzz has been observed in nowadays tokamaks [45]. Fuzzy-W shows a rather precise interval of temperature, energy and fluence in which it develops on the surface of pristine W [96, 100]. In particular, an incubation fluence of around $\simeq 10^{24}\,\mathrm{He/m^2}$ has been reported to be necessary for its formation, while the impinging He energy should be in the range $20 \div 30\,\mathrm{eV}$ [115]. As regards the temperature, it has been observed that for fuzz formation to occur $T_{\mathrm{surf}} > 0.25 T_{\mathrm{melt}}$, where $T_{\mathrm{melt}}$ is the melting temperature [98].
When the surface temperature is further increased beyond this limit, i.e. $T_{\mathrm{melt}} > 2000\,\mathrm{K}$, fuzz growth is reduced. This phenomenon is possibly due to the thermally enhanced desorption of He, leading to the formation of large voids [115].

## 2.5 Modelling efforts for PMI mitigation and control

In § 2.1, we discussed in some details the main physical effect of PMI. In light of these, we showed how the tokamaks operation can be impacted (cfr. § 2.2). We then analysed the various FW materials (cfr. § 2.3) which have been tested in the tokamak, and discussed the pivotal role which W is playing in present-day and future devices, due to its favourable thermophysical properties. A brief discussion was also given (cfr. § 2.4) on the impact of PMI on W surfaces exposed to fusion-relevant D and He plasmas.
As said in § 2.1, PMI is a coupled problem, involving both palsmas and materials. The detailed comprehension of all the physical processes characteristic of PMI require the use of ad-hoc physical models and, therefore, computational tools. The latter can be subdivided into two macro categories. Indeed, the usual tactics to study PMI computationally is to subdivide the problem, and studying separately plasmas and materials. It is therefore the aim of the present Section to provide a broad overview of the most important, currently employed, codes in these two categories.

### 2.5.1 Edge plasma modelling

Computational edge plasma models have been developed with the main aim to understand the complicated plasma phenomena which occurs at the edge of magnetic confinement fusion devices and thus being able to extract useful information, such as heat and particle fluxes onto the PFCs foreseen in future experiments. The edge region of MCF devices is characterised by several peculiarities, which ultimately determines challenges to be addressed when solving numerically the physical model. Indeed, as al-

ready mentioned in § 2.1.2, magnetised plasmas are characterised by strong anisotropies in their transport properties. That is, plasma transport occurs much faster parallel to the magnetic field lines than perpendicular to it. Particularly in tokamak devices, toroidal symmetry can usually be assumed, which reduces the computational burden from three spatial dimension to just two. The edge plasma region is also often characterised by the simultaneous presence of the main plasma ions (say D) as well as impurities. The latter can either be due to atoms sputtered from the FW of the device, or injected into it for the scope of radiating away part of the power which enter the SOL by cross-field transport. These impurities might be high-$Z$ atoms (for example, W) which thus would require in principle the tracking of each charge states as an individual species. In addition to accounting for plasma ions, edge plasma models need to take into consideration also atomic processes. The reason for this can be easily understood if we consider the divertor region of tokamak devices. In this region, one is interested in having the lowest possible electron temperature (say below $T_e \leq 10\,\mathrm{eV}$), in order to minimise heat fluxes to the divertor region. In this temperature range, atomic processes such as line radiation, charge-exchange reaction, ionisation and recombination, cannot be neglected, but instead do play a major role in determining the local divertor conditions.
Up to now, nothing has been said about the physical model that can be employed for the description of the plasma edge. In principle, the most detailed model for a plasma in the edge fusion devices is a kinetic one, where both the plasma and the atomic species are treated kinetically, that is one should solve the following model [16]:

$$\begin{aligned}
&\partial_t f_j + \xi_j \cdot \nabla_{\mathbf{x}_j} f_j = \sum_{i=1}^{n_s} Q_i\left(f_i, f_j\right) + \sum_{\alpha=1}^{n} Q_\alpha\left(f_\alpha, f_j\right) \\
&\partial_t f_\alpha + \xi_\alpha \cdot \nabla_{\mathbf{x}_\alpha} f_\alpha + \frac{eZ_\alpha}{m_\alpha}\left[\mathbf{E} + \xi \times \mathbf{B}\right] \cdot \nabla_{\xi_\alpha} f_\alpha = \sum_{\beta=1}^{n} Q_\beta\left(f_\alpha, f_\beta\right) + \sum_{j=1}^{n_s} Q_j\left(f_j, f_\alpha\right)
\end{aligned} \tag{2.7}$$

In this expression, $f$ denotes the one-particle distribution function (e.g. [14]), $\xi, \mathbf{x}$ are the phase-space coordinates (velocity and space) and $\mathbf{E}, \mathbf{B}$ the electric and magnetic fields. The greek subscript refers to the charge particles, while the latin ones to the neutral atoms or molecules. Finally, $Q_\alpha$ and $Q_j$ account for charged particles and neutral collisions respectively. In plasma physics, the former is also called the **Landau collision operator** [121,139]. In spite of being the most complete possible description of edge plasmas, it is clear that (2.7) cannot be realistically solved in the full complexity

which is typical of the outermost region of tokamak devices. Luckily however edge plasma are usually sufficiently collisional [16, 151] (see also Appendix A), that is the $Q_\alpha$ collisional operator can be consider the largest contribution in (2.7) for the charged particles. In such cases, one can reduced the complexity of the kinetic model by moving to a fluid description, that is by taken moments of the kinetic equation [16, 121, 143]. The corresponding plasma fluid equations are called **Braginskii equations** [8, 12]. The general form of the plasma fluid equations can be written as (assuming here a simple quasi-neutral two-species electron-ion plasma)

$$\frac{\partial n}{\partial t} + \nabla \cdot (n\mathbf{v}_i) = \sum_m S_m \left[f_i\right] \tag{2.8}$$

$$\begin{aligned}
\frac{\partial}{\partial t}\left(m_i n \mathbf{v}_i\right) + \nabla \cdot \left(m_i n \mathbf{v}_i \otimes \mathbf{v}_i + \pi_i\right) &= \sum_m \mathbf{S}_m \left[m_i \xi f_i\right] - \nabla p_i + \\
&+ ne\left(-\nabla\phi + \frac{\mathbf{v}_i}{c} \times \mathbf{B}\right) - \mathbf{R}_{ei} \\
0 = \sum_m \mathbf{S}_m \left[m_e \xi f_e\right] \mathbf{S}_{m_e} - \nabla p_e - ne\left(-\nabla\phi + \frac{\mathbf{v}_e}{c} \times \mathbf{B}\right) + \mathbf{R}_{ei}
\end{aligned} \tag{2.9}$$

$$\begin{aligned}
\frac{\partial}{\partial t}\left(\frac{3}{2} n T_i\right) + \nabla \cdot \left(\frac{5}{2} n T_i \mathbf{v}_i + \mathbf{q}_i\right) &= \mathbf{v}_i \cdot \nabla p_i + \sum_m S_m \left[\frac{m_i}{2} \xi^2 f_i\right] - \\
&- \pi_i : \nabla \mathbf{v}_i + Q_\Delta \\
\frac{\partial}{\partial t}\left(\frac{3}{2} n T_e\right) + \nabla \cdot \left(\frac{5}{2} n T_e \mathbf{v}_e + \mathbf{q}_e\right) &= \mathbf{v}_e \cdot \nabla p_e + \sum_m S_m \left[\frac{m_e}{2} \xi^2 f_e\right] - \\
&- \pi_e : \nabla \mathbf{v}_e - Q_\Delta
\end{aligned} \tag{2.10}$$

Notice that charge neutrality has been assumed, that is $n_e \simeq n_i = n$ (cfr. § 1.2). The latter, in turn, imposes a constraint for the electrical current which must be divergence-free, that is $\nabla \cdot \mathbf{j} = 0$. Furthermore, the electron inertia and electron viscous stress tensor have been neglected [148]. Moreover, $Q_\Delta$ denotes the electron-ion energy exchange term, given by:

$$Q_\Delta = -Q_{ei} + \mathbf{R}_{ei} \cdot (\mathbf{v}_e - \mathbf{v}_i) \tag{2.11}$$

where $\mathbf{R}_{ei}$ is the electron-ion friction force [12, 16, 121]. The set of plasma fluid equations reported above need to be completed with appropriate expression of the transport quantities, such as the electron and ion heat fluxes and viscous stress tensor. This task was first performed by Braginskii

in [12], by considering a simple two-component hydrogenic plasma made of electrons and ions. Subsequent refinement of these expressions were derived by Balescu [8]. Both these two treatments are based on the **trace impurity approximation**. That is, it is assumed that the plasma is dominated by a hydrogenic specie. Possible plasma impurities are accounted for since they change the local value of the effective atomic number, $Z_{\text{eff}}$, of the plasma. However, recently Zhdanov in [160] derived the full expression of the transport fluxes in a multi-component plasma without resorting to the trace impurity assumption.
The quantities $S_m\left[f\right]$, $\mathbf{S}_m\left[m\xi f\right]$ and $S_m\left[m\xi^2/2 f\right]$ in the plasma fluid equations reported above denote the source related to plasma-neutrals interactions. Differently from plasma particles, neutrals (i.e. atoms and molecules) are treated at a kinetic level, due to their larger mean-free paths [16]. Moreover, only Monte Carlo methods (such as those implemented in the Eirene [128] and Eunomia [89] codes) can handle the wide ranges of surfaces geometries, reflection models and support complex atomic and molecular processes that occur in real fusion edge plasmas. Therefore, computational edge plasma models that are commonly employed are usually based on a coupled fluid+Monte Carlo description of the plasma, where only neutral particles are treated kinetically.
A satisfactory description of the charged species in the plasma edge has to include both the effects of transport perpendicular to the magnetic surfaces (largely dominated by turbulence), and parallel transport toward the material boundaries in the scrape-off layer. This description must therefore be at least two-dimensional. 2D models (such as B2.5 [102, 105], UEDGE [141], SOLEDGE2D [46, 47]) of the plasma SOL are based on the assumed toroidal axysymmetry geometry of tokamaks, resulting in a two-dimensional edge models which describes the plasma parameters in a poloidal cross-section of the torus. Three-dimensional edge fluid codes have also been developed. Example of these are the EMC3 [159] and SOLEDGE3D [48] codes. Their applications to tokamak devices is scarcer with respect to the widespread 2D codes. At present, however, the above-mentioned codes are somewhat limited, because at least one important ingredient, the turbulent plasma transport across the magnetic field is not understood completely (e.g. [121]). A common employed strategy consist in substituting turbulent-driven radial flows with an effective diffusion coefficient (e.g. [47]). This procedure is based on the observation that the turbulent flows are characterised by time scales which are much faster with respect to the typical transport ones. This allows, therefore, to perform a decomposition of the fluid quantities (such as the plasma density, for exam-

ple) into an average and a fluctuating component, the average being taken over spatial and time scale much longer than the typical turbulent ones. We can be more concrete about what has been said so far, by applying the decomposition procedure to the plasma continuity equation. By writing $n = \langle n \rangle + \tilde{n}$, one obtains:

$$\partial_t \langle n \rangle + \nabla \cdot (\langle n \rangle \langle \mathbf{v} \rangle + \langle \tilde{n} \tilde{\mathbf{v}} \rangle) = \langle S_n \rangle \tag{2.12}$$

where $S_n := \sum_m S_m [f_i]$. The flux due to the fluctuating component $\langle \tilde{n} \tilde{\mathbf{v}} \rangle$ is treated as a diffusive flux, i.e. $\langle \tilde{n} \tilde{\mathbf{v}} \rangle = -D_\perp \nabla_\perp \langle n \rangle$. Recently, however, there have been some attempts to derive self-consistent expression for the radial transport coefficients, by iteratively coupling a mean-field transport code (i.e. a code solving for averaged quantities) and a turbulence code, as explained in details [38].
Therefore, the goal of present mean field edge plasma code is to treat all the other, predictable, physical components of the corresponding model accurately [16]. This applies, in particular, to the atomic, molecular and surface processes, which largely control the plasma flow and plasma energy content in the important near divertor targets region. If this degree of accuracy can be achieved, then the unknown anomalous cross-field transport can be separated and isolated computationally, and determined experimentally.
This particular strategy is the one adopted in SOLPS (Scrape-Off Layer Plasma Simulation) [93], which consists of two coupled codes: B2.5 and Eirene, and it constitutes the main numerical tool employed in the present Ph.D. Thesis work. For this reason, additional details on the code structure will be provided in Chapter 3.

### 2.5.2 Materials modelling

In the previous section, we highlighted in some details the main tools that have been developed for the modelling of edge plasmas. Here, we will focus instead on the modelling of materials under fusion-relevant irradiation. Studying the effect of irradiation on materials is an extremely challenging task to be performed. Indeed, it constitutes a classic example of an inherently multiscale phenomenon. The relevant processes range from the atomic nucleus to the structural components length scales, that is spanning more than 10 orders of magnitude, while time scales bridge more than 22. Furthermore, a wide range of variables controls the mix of nano/microstructural features formed and the corresponding degradation of physical and mechanical properties. This multiscale nature of phenomena is quite well illustrated in figure 2.12. Due to the existence of such vast length and time

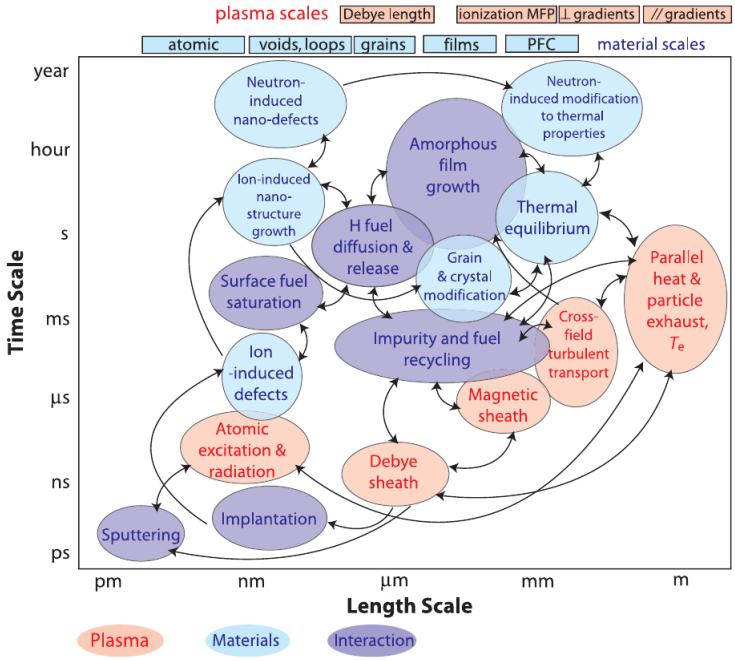


**Figure 2.12:** *Graphical representation of the multiple time and length scale involved in the coupled processes characteristics of PMI. In the figure, processes occurring in the plasma are highlighted in red; those in the near-surface or bulk of materials in light blue. Finally, those due to the interaction between solids and plasma in purple. From [158].*

scales, it is clear that no single modelling tool can be used to understand materials modifications under plasma irradiation. Therefore, one has to select the best code to study a specific effect. In what follows, we shall give a brief overview of the type of modelling approaches that can be used to study radiation damage in materials. We shall only limit to give some insight on the binary-collision approximation codes, basing our discussion on [59] and refer to this Review for additional details on other materials modelling methods.

Binary-Collision approximation (BCA) is undoubtedly the oldest simulation approach for the calculation of the motion of ions in solids. As the name suggests, in this approach an ion is propagated into a given material by means of a sequence of independent binary collisions, solving the scattering integral starting from a repulsive interatomic potential. One of the best-known example of such an approach is the TRIM/SRIM code [51]. It uses a Monte Carlo algorithm to select the impact parameter of the next

colliding atom as well as its type. Due to the randomness of the collision partner, it can describe fairly well only amorphous materials. However, the BCA method has several limitations, since it cannot distinguish when a cascade goes from the linear to the heat spike regime. Due to its high efficiency, the BCA method is of great interest for the fusion community. Indeed, it can be easily coupled with plasma simulations codes, such as SOLPS (cfr. § 2.5.1). In addition to this, BCA codes can be used to track material mixing due to ion implantation and surface composition changes due to preferential sputtering. A particularly interesting refinement of the TRIM code is SDTrimSP [107], designed for atomic collisions in amorphous targets to calculate ranges, reflection coefficients and sputtering yields, as well as more detailed information as depths distribution of implanted ions and energy distributions of backscattered and sputtered atoms. Quite interesting is the dynamic mode of operation of the code, which allows for target modifications (changes in the composition) due to ion irradiation. Recently a further upgrade of the code has been provided, which allows to track materials modification in 2D. That is, the target is resolved in two dimensions, allowing to account for effect of roughness on the scattering and sputtering and to model dynamical morphological changes [3]. The SDTRIMSP and SDTRIMSP-2D codes has been extensively applied also for tackling material modifications in magnetic confinement fusion [28, 65, 84, 94]. Recently, however, a new addition to the realm of materials modelling codes has been introduced, namely ERO2.0. Strictly speaking, ERO [39] is an erosion and transport code, developed with the aim of studying impurity transport in magnetic confinement fusion devices, so that it does not account directly for radiation damage effects on materials. Rather, ERO is coupled to more material-specific code, such as for example SDTRIMSP or ERO for the computation e.g. of the sputtering yields. Anyway, the newly developed ERO2.0 has recently introduced also the capability of accounting for materials morphological changes under plasma irradiation [19, 24]. The ERO2.0 code constitutes one of the main numerical tool employed in the framework of this Thesis. Additional details on the code structure will be therefore given in Chapter 3.

## 2.6 Lab-scale investigations of PMI

As discussed in § 2.3, W is currently considered as one of the most promising candidate PFCs for the most critical region of the ITER tokamak, namely the divertor targets. Since W is a high-Z element, its erosion must be considered carefully, in order to avoid possible limitations in the lifetime of

PFCs and also to minimise radiative losses. Due to its importance, it is not a surprise that great efforts have been spent by researchers in order to understand and control PMI with W surfaces. From the experimental point of view, there is however a difficulty in present-day tokamaks in the exploration of the relevant plasma regimes expected in ITER. Indeed, current devices are not able to achieve the extremely highly particle fluxes, $\simeq 10^{24}\,\mathrm{m}^{-2}\mathrm{s}^{-1}$, and fluences, $\simeq 10^{26}\,\mathrm{m}^{-2}$, expected at the divertor region of ITER [140]. So, if from one side tokamaks are of fundamental importance to study the impact of PMI on the overall performance of the machine, they are not able to fully asses PFCs modifications in plasma conditions relevant for ITER or future fusion power plants. In addition to this, PMI in tokamaks is usually the results of integrated tokamak campaigns, in which the plasma conditions from discharge to discharge might differ considerably. Thus, it can be difficult to pinpoint a peculiar material modification to a precise plasma parameter.
The issue just outlined above justify the search for additional, complementary, lab-scale approaches, which can help in the investigation of PMI impact on PFCs. We shall see in § 2.6.1, that in the so-called Linear Plasma Devices (LPDs) it is possible to reach plasma conditions expected in different portion of the FW of ITER and, thus, also at the divertor targets. In addition to this, one can use suitable deposition techniques, such as the Pulsed Laser Deposition (PLD), in order to produce fusion-relevant coatings that can mimic co/re-deposits layer found in tokamak. More details of this technique will be given in § 2.6.2. We shall see, in particular, that thanks to the versatility of the PLD, the coating properties (e.g. the structure, morphology and composition) can be finely tuned during deposition in order to mimic different tokamak coating scenarios.

### 2.6.1 Linear Plasma Devices

Linear Plasma Devices offer the possibility to bridge the gap which is currently present in the field of PMI research in ITER-relevant conditions at a moderate cost. Indeed, they are unique facilities capable of producing stable, steady-state and multispecies plasmas. Furthermore, the materials of choice can be exposed to well-precised and finely-tunable pre-selected conditions. In addition to this benefit, LPDs can also study the impact of synergistic effects (e.g. sputtering and heat fluxes) onto exposed-materials, which would otherwise require separate and specific facilities. In any case, it should be noted that LPDs do not provide the full answer to the PMI mitigation and control in future fusion devices. Indeed, once testing on

these facilities is performed, one needs also to proceed to perform experiments also in more complicated and expensive toroidal confinement facilities. Thus, PMI research in LPDs and tokamaks should be considered to be complementary. LPDs are characterised however by some advantages with respect to present-day tokamaks [29]:

- in some of the present-day LPDs, ion fluxes and fluences relevant for the ITER divertor can be reached, while in present-day tokamaks the fluences are one or two order of magnitude lower;
- as already mentioned, the PMI studies in LPDs are characterised by a fine control and reproducibility of the exposure parameters. This means that independent parameter variations and their impact onto a specific modification can be assessed.
- PMI research in LPDs is far more cost effective with respect to that in tokamaks

Even though there exists a large variety of LPDs all across the world, the general setup for a PMI experiment in a LPD is quite common. Indeed, LPDs are constituted by a cylindrical vacuum chamber surrounded by magnetic field coils in the azimuthal direction. Flowing current in the coils produce an almost axial magnetic field. An example of such a device is reported in figure 2.13. Most of the LPDs employ water-cooled copper

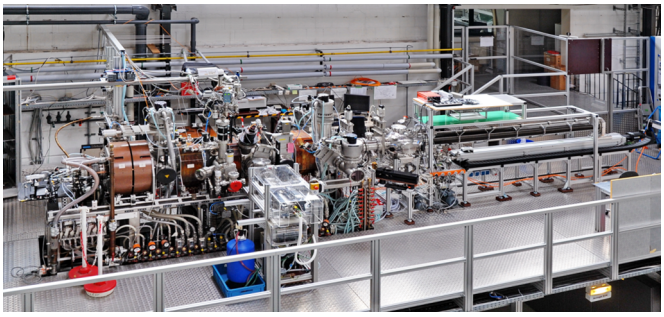

**Figure 2.13:** *The PSI-2 linear plasma device at Forschungzentrum Julich. From [2].*

coils capable of producing a steady state magnetic field of $0.1\,\mathrm{T}$. The vacuum chamber is usually subdivided into several regions. For example, the source region is responsible for the generation of the plasma column with a diameter usually of $\simeq 1 \div 10\,\mathrm{cm}$. The plasma then expands along the magnetic filed lines through a buffer region, reaching finally the target exposure region. The buffer and exposure regions can be separated by a vacuum diaphragm to allow for the differential pumping of the gas introduced into

the plasma source. This buffer region is sometimes needed in order to provide different gas pressure in the target and source regions, which might be needed to taylorthe ionisation degree of the plasma in the former [29]. In the exposure region, the plasma parameters are monitored, e.g. by Langmuir Probes (LPs) or by Thomson scattering. Analogously, the exposure region is usually observed by various spectroscopic methods, e.g. allowing to measure the amount of eroded materials.
In table 2.1 we summarise the main operational parameters of a selection of LPDs, which are routinely employed in PMI studies. We report also for comparison the condition expected at the ITER divertor. Even though in a LPD the target exposure parameters cannot completely match those of boundary plasma in a tokamak, PMI-relevant parameters of material exposures can come quite close to the conditions expected at the ITER divertor. The lower particle flux of several LPDs is lower with respect to that foreseen in ITER. However, it can be compensated by the possibility to operate in a continuous manner, thus reaching the same fluences expected in one ITER pulse. In LPDs, the incident ion energy can be controlled simply by properly negative biasing of the samples holder. This leads to an almost monoenergetic energy distribution of the incident ions. This bias acceleration can moreover result in a distribution of incidence angles narrowly peaked towards the normal, which is ideal for studying the impact of different ion angles on the exposed surfaces.
Experimental investigations of PMI in LPDs has been performed by several researchers. For example, almost all the results that we briefly summarised in § 2.4 have been obtained after plasma exposures in LPDs. These researches contributed significantly to the understanding of the behaviour of ITER-relevant FW materials (such as W). In spite of the fact that studies on LPDs are usually experimental, there is a growing attention in the PMI field towards the modelling of these facilities. Numerical simulations are necessary for the interpretation and comparison of results coming from different devices. In addition, simulation models can be benchmarked against experimental findings in LPDs much more easily than it routinely occurs in tokamaks devices again, mostly, due to their simplified structure and geometry. Several numerical codes which are commonly applied for the modelling of tokamaks, including edge plasma codes like SOLPS (cfr. § 2.5.1) and or Monte Carlo material transport code such as ERO (cfr. § 2.5.2), have also been applied to the linear geometry of LPDs.
In literature, edge plasma codes simulations of LPDs dealt with both interpretative and predictive studies [54,57,58,63,64,66,78,127]. In particular, Kastelewicz et al. [127] are the first that applied SOLPS4.0 to a linear ge-

| | PISCES-B (UCSD, USA) | PISCES-A (UCSD, USA)/TPE (INL, USA) | NAGDIS-II (Nagoya University, Japan) | PSI-2 (FZJ, Germany) | Pilot-PSI (FOM-Differ, The Neatherlands) | Magnum-PSI (FOM-Differ, The Neatherlands) | ITER-divertor ($Q_{\mathrm{D-T}} = 10$ |
|---|---|---|---|---|---|---|---|
| Discharge Type | Reflex arc | Reflex arc | Cusp arc | Arc with cylindrical cathode | Cascaded arc | Cascaded arc | Tokamak |
| $B$ [T] | 0.04 | 0.1 | 0.25 | 0.1 | 0.4-1.6 | 0.43-1.73/3 | 5 |
| $T_e$ [eV] | 3-50 | 3-20 | 0.1-10 | 1-40 | 0.1-5 | 0.1-4/0.1-10 | 1-10 |
| $n_e$ $\left[\mathrm{m}^{-3}\right]$ | $10^{16} \div 10^{19}$ | $10^{16} \div 10^{19}$ | up to $10^{20}$ | $10^{16} \div 10^{19}$ | up to $10^{21}$ | $10^{19} \div 10^{21}$ | $10^{20} \div 10^{21}$ |
| $\Gamma$ $\left[\mathrm{m}^{-2}\mathrm{s}^{-1}\right]$ | $10^{20} \div 10^{23}$ | $10^{20} \div 10^{22}$ | up to $10^{23}$ | $10^{20} \div 10^{23}$ | $10^{25}$ | $10^{23} \div 10^{25}$ | $10^{24} \div 10^{25}$ |
| $\Phi$ $\left[\mathrm{m}^{-2}\right]$ | $10^{28}$ | $10^{27}$ | $10^{27}$ | $10^{27}$ | $10^{27}$ | $10^{27} \div 10^{28}$ | $10^{26} \div 10^{27}$ per 400 s pulse |
| $E_{\mathrm{ion}}$ (target bias) [eV] | $10 \div 300$ | $10 \div 200$ | $10 \div 200$ | $10 \div 300$ | $1 \div 100$ | $1 \div 300$ | $\simeq 10 \div 100$ |
| Pulse length [s] | Steady-state | Steady-state | Steady-state | Steady-state | $3 \div 10$ | steady state when superconducting | $300 \div 500$ |
| Plasma diameter [cm] | 5 | 5 | 2 | 6 | 1.5 | 2.5/10 | n/a |

**Table 2.1:** *Main PMI-relevant plasma parameters that can be achieved in PMI devices available worldwide. For comparison, we report also the parameters at the ITER divertor. From [29].*

ometry. The same SOLPS version was used in [66] for predicting the main plasma parameters in MAGNUM-PSI. More recent works used SOLPS5.0 to simulate plasma transport in MAGPIE [63] and PROTO-MPEX [64, 78]. In particular, Rapp et al. [54] were the first to describe how to model radio-frequency heated LPDs with SOLPS. The SOLEDGE2D-EIRENE code was applied to PILOT-PSI to understand the effects of different atomic physics models [57]. Effects of pumping efficiency and radial transport coefficients were studied [58] and a quantitative analysis of the importance of transport and atomic processes, based on the two-point model [151], was performed.
In addition to plasma modelling of LPDs via edge codes, also the 3D Monte Carlo code ERO have been used for simulation of experiments in in PISCES-B, Pilot-PSI and PSI-2 [22, 34, 35, 41]. More recently, also the ERO2.0 code have been used for interpretative modelling of experiments in PSI-2. The newly-developed capabilities of ERO2.0 of surface evolution modelling under plasma irradiation have been applied for understanding surface roughness effects on Mo physical sputtering and redeposition.

### 2.6.2 Mimicking W coating in tokamaks through Pulsed Laser Deposition

As discussed in § 2.2, the process of W transport and redeposition on different region of the FW of tokamak devices can be quite complex. Indeed, to summarise, W redeposits with different morphology, structures and compositions can be found in different machines. Studying the properties of these layers (such as their behaviour when exposed to fusion-relevant plasmas) can be quite non-trivial. In fact, as mentioned in the previous paragraph, tokamak can be quite complex environments. Furthermore, one is usually able to retrieve FW samples from these devices only at the end of the experimental campaigns. For this reason, it is clear that having a lab-scale tool to mimic the complexity of such W re/co-deposits can be of great interest. In the framework of the present Thesis work, we employed the **Pulsed Laser Deposition** technique. The latter constitutes an example of a physical vapour deposition technique, were the materials to be deposited are brought to the vapour phase thanks to a laser ablation process. The PLD was chosen since it has proven to be extremely versatile in tailoring the structure of the deposits in its morphology and composition down to the nanoscale [36]. In particular, fusion-relevant W coatings have been routinely produced with these technique and have attracted the attention of the fusion community (e.g. [30, 73, 83, 91]). The presence of a background as

during the deposition strongly affects the expansion dynamic of the plume. Indeed, due to collision processes between the ablated species and the background gas atoms, the former slow down and thus reach the substrates with lower energy. Of course, the higher the background gas pressure the lower will be the energy of the deposited species. As a consequence, one can finely tailor the coating morphology, structure and composition. In particular, for low energy of the background gas the ablated species are sufficiently energetic and the deposition occur atom-by-atom, which results in turn in **compact films**. The opposite occur if the background pressure is high. In this case, the plume is more confined and the deposition occur through cluster formation, resulting in **porous coatings**. Furthermore, reactive gases, such as $N_2$ and $O_2$, can be used in the PLD setup to promote chemical reactions and bond formation with the ablated species. In addition to the gas parameter, it should be pointed out that the coating is also influenced by the laser parameters, such as wavelength, energy-per-pulse, fluence and so on. From the results coming from various experimental campaigns in tokamaks (cfr. § 2.2), the co/redeposit layers show various morphology, changing from compact to porous, different structure, from amorphous to crystalline, and various elemental composition with presence of gas impurities. By taking the advantage of the high versatility of the PLD, one can therefore easily mimic these fusion-relevant $W$ coatings and study their property in a controlled fashion. In addition, one can also expose these coatings in fusion-relevant environment in LPDs.

CHAPTER 3

# Thesis goals and methods

THIS Chapter aims to present the main goals of the present Ph.D. work as well as illustrating the main numerical and experimental tools employed in order to reach them. In particular, the specific goals of the Thesis are illustrated in § 3.1. Next we present the numerical tools, considering first edge plasma modelling with the SOLPS code § 3.2, focusing more on its latest release SOLPS-ITER. After giving a brief overview of the model implemented into the code, we proceed by presenting some technical tools necessary to perform simulations with this code. We present next, in a similar fashion, the erosion and transport code ERO § 3.3, focusing in particular on the ERO2.0 version.
We consider next, § 3.4, the main experimental tools which have been employed in the Thesis for the production (cfr. § 3.4.1) and characterisation (cfr. § 3.4.2) of the W and Mo based coatings produced in the framework of this Thesis. We conclude the Chapter, by giving in § 3.4.3 some details of the LPD GyM of ISTP-CNR, were the exposures of the W-based samples to different D and He have been performed.

## 3.1 Specific goals of the Thesis

At this point, all the necessary elements to understand the motivations and goals of this Ph.D. work have been introduced. Before proceeding, let us briefly summarised what has been said so far. In Chapter 1, the main aspects of nuclear fusion and magnetic confinement have been addressed. Chapter 2 dealt with the complex issue of PMI in fusion devices. We highlighted here the complexity of the involved phenomena for both plasmas and materials, discussing in particular their coupled and multi-scale nature. The necessity to use numerical codes as well as lab-scale investigations of PMI has then been naturally presented and the pivotal role of LPDs in this field has been highlighted. Furthermore, we stressed the dependence of the plasma-induced modifications to the ion species, which prompt the needs to extend numerical and experimental investigations in the PMI field also to other plasmas, such as pure $\mathrm{He}$ and $\mathrm{Ar}$ plasmas.
The activities carried on during this Ph.D. starts from here, that is from the complex and important field of PMI research in LPDs. Due to their central role in this field, the numerical and experimental investigation of PMI in LPD is of pivotal importance, and a first step in this direction has been performed during this Ph.D. work. The motivations behind the present Ph.D. work come from the observation that, in MCF literature, there are only a handful of studies related to the modelling of PMI in LPDs, both using edge plasma (e.g. SOLPS) and material-specific (e.g. ERO/ERO2.0) codes. Applying these modelling tools also to LPDs is of great interest, since they allow for the interpretation of the outcomes of dedicated experiments carried on in these facilities. In addition, from the experimental point of view, the behaviour of $\mathrm{W}$ coatings having unconventional structure, morphology and composition, produced via material science techniques, when exposed to fusion-relevant plasmas has not been studied in depth in literature.
For these reasons, thanks to the numerical tools and the experimental facilities, we investigated in details both numerical and experimental aspects of PMI in LPDs. Specifically, concerning the former, we addressed the following questions:

- Can edge plasma codes be applied to LPDs with suitable adaptations?
- Can we reproduce experimentally-measured plasma parameters in GyM?
- What are the most relevant terms in the SOLPS equations that determine the GyM parameters in its current configuration?
- Can we simulate numerically the surface morphology evolution via

ERO2.0 and compare the results with experimental measurements?

Concerning the latter:

- What is the behaviour of nanostructured W samples when exposed to the GyM plasma?
- What are the qualitative features of the plasma-induced modifications on these specimen and how do they relate to those of bulk W?

In more details:

- The **numerical activities** focus on the adaptation and application of the edge plasma code SOLPS (specifically, its most recent version SOLPS-ITER) to the GyM device and, in general, to LPDs. Since the code was written having in mind the typical toroidal geometry of tokamaks, the applications to LPDs is not straightforward and requires some care. For this reason, a preliminary study of the relevant literature was first necessary, in order to better understand the physical model implemented in SOLPS. Next, the geometrical features of the code were interpreted from the point of view of the simplified cylindrical structure typical of LPD. In this way, it was possible to understand which relevant terms in the model equations are active when modelling of LPDs is performed. Once this task was terminated, we started carrying on modelling activities with SOLPS of the LPD GyM, particularly focusing on Ar plasmas, which have never been done in literature before. The choice to consider pure Ar plasma is unusual for simulations with edge transport codes, where hydrogen (H) or deuterium (D) are commonly the main plasma species. Indeed, in tokamaks, Ar impurities are present in trace in the plasma as seeding for power dissipation purposes [25, 62]. In PMI studies performed in LPDs, instead, Ar is often selected as the main plasma species [23,42]. A dedicated sensitivity study of the code was, for this reason, carried on aiming to understand the impact of the simulations input on experimentally-measurable radial profile (i.e. electron density, temperature, and plasma potential) and a preliminary comparison with experimentally-measured plasma profile was performed. These sensitivity scans were then interpreted quantitatively by analysing which terms in the equation model are the dominant ones when modelling GyM Ar plasmas.
  The material side of PMI was numerically investigated through the ERO code and, specifically, with its newest version ERO2.0, applying its newly-developed capabilities for the modelling of materials mor-

phology evolution at the micro/nano-scale level. To this end, a dedicated literature studies was first necessary in order to understand what are the physical model that are commonly employed to describe material morphology evolution under ion irradiation. It should be noted that this literature lies outside the world of PMI in MCF devices. Thus, knowledge of materials modelling outside the fusion world was acquired. The latter was in turn employed in order to interpret physically the surface evolution module currently implemented in ERO2.0. We found, in particular, a great similiarity between it and the physical model put forward by Škereň in [101]. We next implemented this model in the FreeFem++ framework and checked its correct numerical implementation by replicating the results of [101]. Finally, we performed dedicated comparison with the ERO2.0 code on both numerically-generated and experimentally-retrieved surfaces, simulating their morphological modifications after exposures to different plasmas and ion beams.

- The **experimental activities** focus instead on the production, via material science techniques (using the Pulsed Laser Deposition), of samples, having different morphology, structure, composition and roughness with respect to that of conventional bulk materials. The activity of coating production dealt mostly with W. From previous knowledge acquired available at the NanoLab laboratory of Politecnico di Milano, it was possible to deposit W coatings with different morphology, composition and structure. After a detailed characterisation of these coatings, a selection of them have been exposed to fusion-relevant plasmas in the GyM LPD facility of ISTP-CNR, as well as in other LPDs under the activities coordinated by the EUROfusion program. In particular, two different experimental campaigns, in D and He plasmas, were carried on. Samples were next thoroughly characterised after the exposures and the observed plasma-induced modifications were discussed and compared to literature results.

All the numerical and experimental activities were mostly carried on at the NanoLab laboratory (Politecnico di Milano). The production of W-based samples via the Pulsed Laser Deposition apparatus was also carried on under the activities supervisied by the EUROfusion program. Some of these samples were exposed, as already mentioned, in the GyM device of ISTP-CNR.

## 3.2 Modelling of edge plasmas with SOLPS-ITER

In this section we shall describe the SOLPS-ITER code, that is the latest release of the SOLPS code package developed by the ITER Organisation (IO), which couples the most recent parallelised version of the Monte Carlo Eirene with the B2.5 fluid plasma solver. We start first by providing a brief description of the physical models implemented into the B2.5 (cfr. § 3.2.1) and the Eirene (cfr. § 3.2.2) part of SOLPS, which constitutes the two most important module of this code package. The structure of the SOLPS-ITER code repository is the briefly outlined in § 3.2.3. We present here, in addition, the main subpackages which are needed to perform a simulation.

### 3.2.1 B2.5 physical model

This section aims to present the physical model which is currently implemented in the B2.5 module of the SOLPS code. The idea behind it has already been briefly discussed in § 2.5.1. The starting point is the set of conservation equation for the plasma density, $n$, the electron and ion temperatures, $T_e$ and $T_i$, and the parallel ion velocity, $v$. This set of conservation equation is closed thanks to the quasi-neutrality conditions, which imply that the electric current, $\mathbf{j}$, is divergence-free, that is $\nabla \cdot \mathbf{j} = 0$.
Since B2.5 is a 2D code, this set of equations are specified in a suitable reference frame, where the toroidal coordinate can be ignored, in the sense that partial derivatives in this direction vanish identically. This reflect the assumed toroidal symmetry of tokamak devices. It should be noted here that when describing the magnetic field in magnetic confinement fusion devices, it turns out to be convenient to use two different reference frames, the **dynamical** and the **geometrical** ones [6]. In either cases, one of the coordinates is the same and correspond to the direction orthogonal to the nested flux surfaces, which we shall denote with $\rho$. In the dynamical frame the remaining two coordinates are the parallel-to-B direction $\mathbf{g}_{\parallel} := \mathbf{b}$ and the diamagnetic direction, constructed in such a way that the versor, $\mathbf{g}_{\perp}$, lies on flux surfaces but is at any point always orthogonal to $\mathbf{b}$, that is $\mathbf{g}_{\perp} = \mathbf{g}_{\parallel} \times \mathbf{g}_{\rho}$, where $\mathbf{g}_{\rho}$ denotes the versor in the $\rho$ direction. Instead, in the geometrical frame, one exploits the geometrical properties of toroidal devices, thereby introducing a poloidal versor, $\mathbf{g}_{\theta}$, and a toroidal one, $\mathbf{g}_{\varphi}$. These two frames are graphically illustrated in figure 3.1 The idea is next to exploit both these two frames in order to simplify somewhat the set of conservation equations described in § 2.5.1. In particular, plasma transport is much easily described in the dynamical frame, while symmetry of tokamak is manifest. Thus the set of B2.5 equation will contain the derivatives

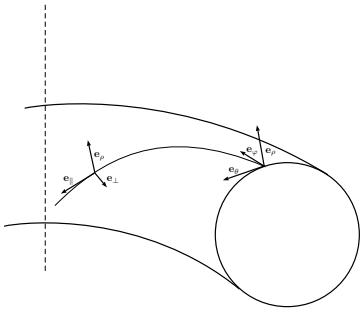

**Figure 3.1:** *Graphical illustration of the two reference frames which can be used to describe transport in a tokamak device. The triad* $\{\mathbf{g}_\parallel, \mathbf{g}_\perp, \mathbf{g}_\rho\}$ *is the dynamical frame, while* $\{\mathbf{g}_\theta, \mathbf{g}_\varphi, \mathbf{g}_\rho\}$ *the geometrical one.*

with respect to the geometrical frame coordinates of quantities which are instead typical of the dynamical frame. The relation between the basis vector of the two frames can be easily obtained using standard tensor analysis techniques [6, 124] and it is given by:

$$\begin{aligned} \mathbf{g}_\parallel &= b_\theta \mathbf{g}_\theta + b_\varphi \mathbf{g}_\varphi \\ \mathbf{g}_\perp &= b_\theta \mathbf{g}_\varphi - b_\varphi \mathbf{g}_\theta \end{aligned} \tag{3.1}$$

Since the geometrical triad is orthogonal, it can be fully described by the Lamé coefficients [6, 124], $h_\theta, h_\rho, h_\varphi$. Thus, one can also write $\sqrt{g} = h_\theta h_\rho h_\varphi$. We can now proceed to derive the set of conservation equations which solved in B2.5, considering for simplicity a pure hydrogen plasma. In what follows we shall use the standard B2.5 convention and setting $x, y, z$ equal to $\theta, \rho, \varphi$.
With these conventions, the ion continuity equation takes the following form:

$$\frac{\partial n}{\partial t} + \frac{1}{\sqrt{g}} \frac{\partial}{\partial x} \left[ \frac{\sqrt{g}}{h_x} n \left( b_x v_{i\parallel} + b_z v_{i\perp} \right) \right] + \frac{1}{\sqrt{g}} \frac{\partial}{\partial y} \left( \frac{\sqrt{g}}{h_y} n v_{iy} \right) = S_n \tag{3.2}$$

where $S_n$ is the ion particle sources, which includes contribution due to recombination, ionisation and charge-exchange reactions. The diamagnetic, $v_{i\perp}$, and radial, $v_{iy}$, ion fluid velocities can be found by taking the cross product of the ion momentum equation with $\mathbf{b}$ and expressing the result in the perpendicular and radial direction [105]. Using the expression for the

ion-electron friction term [12], one can show that [148]

$$\begin{aligned} v_y &= v_y^a + \frac{b_z}{enB}\frac{1}{h_x}\frac{\partial\left(nT_i\right)}{\partial x} + v_y^{\text{in}} + v_y^{\text{vis}} + v_y^s \\ v_\perp &= v_\perp^a - \frac{b_z}{enB}\frac{1}{h_x}\frac{\partial\left(nT_i\right)}{\partial y} + v_\perp^{\text{in}} + v_\perp^{\text{vis}} + v_\perp^s \end{aligned} \tag{3.3}$$

where the $v_y^a, v_\perp^a$ are given by:

$$\begin{aligned} v_y^a &= \frac{b_z}{B}\frac{1}{h_x}\frac{\partial\phi}{\partial x} - D_{\text{an}}^n\frac{1}{h_y n}\frac{\partial n}{\partial y} - D_{\text{an}}^p\frac{1}{h_y n}\frac{\partial\left(nT_i\right)}{\partial y} \\ v_\perp^a &= -\frac{1}{B}\frac{1}{h_y}\frac{\partial\phi}{\partial y} - D_{\text{an}}^n\frac{1}{h_x n}\frac{\partial n}{\partial x} - D_{\text{an}}^p\frac{1}{h_x n}\frac{\partial\left(nT_i\right)}{\partial x} \end{aligned} \tag{3.4}$$

$D_{\text{an}}^p$ and $D_{\text{an}}^n$ anomalous radial transport coefficients, $\Omega_e$ the electron Larmor frequency, $\phi$ is the electrostatic potential and $B := |\mathbf{B}|$. Moreover, in (3.3), the second term correspond to the diamagnetic flow of ions (that is, the quantity proportional to $\mathbf{b}\times\nabla p$), the third to inertia, the fourth to viscosity and the fifth to ion-neutrals interactions. In vector form, the diamagnetic velocity can be written as:

$$\mathbf{v}_{\text{dia}} = \frac{1}{ZeB}\mathbf{b}\times\nabla p \tag{3.5}$$

Moreover, it is not difficult to show that

$$\nabla\cdot\mathbf{v}_{\text{dia}} = \frac{1}{Ze}\nabla p\cdot\nabla\times\left(\frac{\mathbf{b}}{B}\right) \tag{3.6}$$

One can therefore define an effective diamagnetic velocity, $\tilde{\mathbf{v}}_{\text{dia}}$, as

$$\tilde{\mathbf{v}}_{\text{dia}} = \frac{p}{eZ}\nabla\times\left(\frac{\mathbf{b}}{B}\right) \tag{3.7}$$

which gives the same contribution to the particle balance equation as the true $\mathbf{v}_{\text{dia}}$ does (that is $\nabla\cdot\mathbf{v}_{\text{dia}} = \nabla\cdot\tilde{\mathbf{v}}_{\text{dia}}$). In the poloidal-toroidal-radial coordinates system, the effective diamagnetic velocity can be written as

$$\begin{aligned} \tilde{v}_\perp^{\text{dia}} &= \frac{T_i B_z}{eZ}\frac{1}{h_y}\frac{\partial}{\partial y}\left(\frac{1}{B^2}\right) \\ \tilde{v}_y^{\text{dia}} &= -\frac{T_i B_z}{eZ}\frac{1}{h_x}\frac{\partial}{\partial x}\left(\frac{1}{B^2}\right) \end{aligned} \tag{3.8}$$

We can therefore rewrite (3.3) as

$$\frac{\partial n}{\partial t} + \frac{1}{\sqrt{g}}\frac{\partial}{\partial x}\left[\frac{\sqrt{g}}{h_x}n\left(b_x v_{i\parallel} + b_z\tilde{v}_{i\perp}\right)\right] + \frac{1}{\sqrt{g}}\frac{\partial}{\partial y}\left(\frac{\sqrt{g}}{h_y}n\tilde{v}_{iy}\right) = S_n \tag{3.9}$$

where $\tilde{v}_{i\perp}, \tilde{v}_{iy}$ are given by (3.3), with diamagnetic part is now given by (3.8). Note that (3.8) correspond physically to the $\nabla B$ guiding centre drift velocity caused by the ions. This expression is further elaborated in [105] in order to better describe transport in H-mode regimes.
The inertial, viscosity and ion-neutral friction velocity components in (3.3) are expressed in terms of currents [105] as follows:

$$\mathbf{v}_{\text{in}} = \frac{1}{eZn}\mathbf{j}_{\text{in}}, \quad \mathbf{v}_{\text{vis}} = \frac{1}{eZn}\mathbf{j}_{\text{vis}}, \quad \mathbf{v}_{\text{n}} = \frac{1}{eZn}\mathbf{j}_{n} \tag{3.10}$$

The evolution of the parallel ion velocity, $v_{i\parallel}$, is obtained by considering the parallel component of the ion momentum balance. Combining the parallel inertial terms and gyroviscosity [8, 47, 121] in this expression, one finds:

$$\begin{aligned}
&m_i\left[\frac{\partial\left(nv_{i\parallel}\right)}{\partial t} + \frac{1}{h_z\sqrt{g}}\frac{\partial}{\partial x}\left(\frac{h_z\sqrt{g}}{h_x}n\left(\tilde{v}_{i\perp}b_z + b_x v_{i\parallel}\right)v_{i\parallel}\right) + \right.\\
&\left. + \frac{1}{h_z\sqrt{g}}\frac{\partial}{\partial y}\left(\frac{h_z\sqrt{g}}{h_y}n\tilde{v}_{iy}v_{\parallel}\right)\right] = -\frac{b_x}{h_x}\frac{\partial\left(nT_i\right)}{\partial x} - b_x\frac{en}{h_x}\frac{\partial\phi}{\partial x} + F_k + \\
&+ \frac{4}{3}b_x B^{3/2}\frac{1}{h_x}\frac{\partial}{\partial x}\left[\frac{\eta_0 b_x}{B^2}\frac{\partial\left(\sqrt{B}\left(v_{\parallel} + b_x v_{\perp}^{\text{dia}} + b_x v_{\perp}^{E}\right)\right)}{h_x\partial x}\right] + \\
&+ B^{3/2}b_x\frac{1}{h_x}\frac{\partial}{\partial x}\left[\frac{b_x}{\nu_{ii}B^2}\frac{\partial\left[\sqrt{B}\left(q_{i\parallel} + b_x q_{ix}^{\text{dia}}\right)\right]}{h_x\partial x}\right] + \\
&+ \frac{1}{h_z\sqrt{g}}\frac{\partial}{\partial y}\left(\frac{h_z\sqrt{g}}{h_y^2}\eta_{iy}\frac{\partial v_{\parallel}}{\partial y}\right) + \\
&+ \frac{1}{h_z\sqrt{g}}\frac{\partial}{\partial x}\left(\frac{h_z\sqrt{g}}{h_x^2}\eta_{ix}\frac{\partial v_{\parallel}}{\partial x}\right) + S_{n,i}^{m} + S_{\text{fr}_{ie}}^{m} + S_{\text{term}_{ie}}^{m} + b_x nm v_{i\parallel}^2\frac{\partial\log h_z}{h_x\partial x}
\end{aligned} \tag{3.11}$$

where

$$\begin{aligned}
v_{\perp}^{\text{dia}} &= -\frac{1}{enB}\frac{1}{h_y}\frac{\partial\left(nT_i\right)}{\partial y} \\
v_{\perp}^{\text{E}} &= -\frac{1}{B}\frac{1}{h_y}\frac{\partial\phi}{\partial y}
\end{aligned} \tag{3.12}$$

denote the ions diamagnetic and $\mathbf{E}\times\mathbf{B}$ velocity respectively. Before moving on, let us pause to analyse the different terms in equation (3.11). First of all, the diamagnetic terms appearing on the left-hand side of (3.11) are

almost cancelled [105] and therefore velocities normal to the magnetic field in the second and in the third term of (3.11) are determined by (3.3) with the diamagnetic terms substituted by (3.8). The term $F_k$, the Coriolis force, is the result of the combination of the divergence of the parallel momentum flux with the gyroviscosity term, and it is given by [105]

$$F_k = -m_i \left[ \frac{1}{h_z\sqrt{g}} \frac{\partial}{\partial x} \left( \frac{h_z\sqrt{g}}{h_x} n v_\parallel \tilde{v}_\perp^{\mathrm{dia}} b_z \right) + \frac{1}{h_z\sqrt{g}} \frac{\partial}{\partial y} \left( \frac{h_z\sqrt{g}}{h_y} n v_\parallel \tilde{v}_y^{\mathrm{dia}} \right) \right] \tag{3.13}$$

The fifth term on the right-hand side of (3.11) is peculiar and needs further clarification. It, in fact, a contribution to parallel viscosity related to ion heat fluxes and hence temperature gradients. In this contribution, $q_\parallel$ and $q_{ix}^{\mathrm{dia}}$ are given by [105]:

$$q_{i\parallel} = -\kappa_{i\parallel} b_x \frac{1}{h_x} \frac{\partial T_i}{\partial x}, \quad q_{ix}^{\mathrm{dia}} = -\frac{5}{2} \frac{n T_i b_z}{eB} \frac{1}{h_y} \frac{\partial T_i}{\partial y} \tag{3.14}$$

The coefficients $\eta_{ix}$ and $\eta_{iy}$ are related to the classical parallel and perpendicular viscosity coefficients [8, 12, 160]. The latter is replaced by an anomalous value $\eta_2 = n m_i D_{\mathrm{t}}^n$. The remaining terms in (3.11) are more straightforward: $S_{i,n}^m$ is the momentum source due to ion-neutral friction, while $S_{\mathrm{fr}_{ie}}^m$ and $S_{\mathrm{term}_{ie}}^m$ are the two components of th ion-electron friction term. In particular, the first term is the friction related to the fact that ion and electron can have different velocities, while the second is the thermal-related friction force. Their expressions can be found in [43, 160].
The electron parallel momentum equation is much easier to be dealt with. In fact, one can show that it can be reduced to:

$$j_\parallel = \sigma_\parallel \left[ \frac{b_x}{e} \frac{1}{n} \frac{1}{h_x} \frac{\partial \left( n T_e \right)}{\partial x} - \frac{b_x}{h_x} \frac{\partial \phi}{\partial x} \right] - \alpha_{ex} \frac{1}{h_x} \frac{\partial T_e}{\partial x} \tag{3.15}$$

where the coefficient $\alpha_{ex}$ can be found in [160]. The charge conservation equation can be written as:

$$\frac{1}{\sqrt{g}} \frac{\partial}{\partial x} \left( \frac{\sqrt{g}}{h_x} j_x \right) + \frac{1}{\sqrt{g}} \frac{\partial}{\partial y} \left( \frac{\sqrt{g}}{h_y} j_y \right) = 0 \tag{3.16}$$

where the poloidal component of the current is given by

$$j_x = b_z j_\perp + b_x j_\parallel \tag{3.17}$$

The perpendicular and radial components of the current density are obtained by taking the cross product with $\mathbf{b}$ of the total momentum equation

(that is, the sum of the ion and electron momentum equations) and expressing the result in the perpendicular, $\perp$, and radial, $y$, directions. Similar to the case of the particle continuity equation, one can introduce an effective current, denoted with $\tilde{\mathbf{j}}$, which gives the same contribution to $\nabla \cdot \mathbf{j} = 0$ as the ordinary current [105]. The diamagnetic component of the ion current can therefore be replaced by:

$$\begin{aligned} \tilde{j}_{\perp}^{\mathrm{dia}} &= \frac{1}{b_z} \frac{n\left(T_e + T_i\right) B_z}{h_y} \frac{\partial}{\partial y}\left(\frac{1}{B^2}\right) \\ \tilde{j}_{y}^{\mathrm{dia}} &= -\frac{n\left(T_e + T_i\right) B_z}{h_x} \frac{\partial}{\partial x}\left(\frac{1}{B^2}\right) \end{aligned} \tag{3.18}$$

and represents simply the current due to the $\nabla B$ drift [105]. The overall effective current can therefore be expressed as:

$$\tilde{\mathbf{j}} = \tilde{\mathbf{j}}^{\mathrm{dia}} + \mathbf{j}^{\mathrm{in}} + \mathbf{j}^{\mathrm{vis}} + \mathbf{j}^{\mathrm{s}} + \mathbf{j}_{\parallel} \tag{3.19}$$

The second part of the current, $\mathbf{j}^{\mathrm{in}}$, contains contribution from both inertia and gyroviscosity forces. The expressions for the diamagnetic and radial direction of these currents accounts, however, only for the centrifugal forces [105]:

$$\begin{aligned} j_{\perp}^{\mathrm{in}} &= \frac{m_i}{B} n v_{i\parallel}^2 \frac{1}{h_y} \frac{\partial \log h_z}{\partial y} \\ j_{y}^{\mathrm{in}} &= -\frac{m_i}{B} n v_{i\parallel}^2 \frac{1}{h_y} \frac{\partial \log h_z}{\partial y} \end{aligned} \tag{3.20}$$

The overall currents related to the viscosity are given by:

$$\mathbf{j}^{\mathrm{vis}} = \mathbf{j}^{\mathrm{vis}\parallel} + \mathbf{j}^{\mathrm{vis}\perp} + \mathbf{j}^{\mathrm{vis}q} \tag{3.21}$$

The currents components in the diamagnetic and radial directions related to the parallel viscosity (that is, proportional to $\nabla \cdot \pi$) are:

$$\begin{aligned} \tilde{j}_{\perp}^{\mathrm{vis}\parallel} &= -\frac{B_x \eta_0}{3\sqrt{B}} \frac{\partial\left[\sqrt{B}\left(v_{i\parallel} + b_x\left(v_{\perp}^{\mathrm{dia}} + v_{\perp}^{E}\right)\right)\right]}{h_x \partial x} \frac{1}{h_y} \frac{\partial}{\partial y}\left(\frac{1}{B^2}\right) \\ \tilde{j}_{y}^{\mathrm{vis}\parallel} &= b_z \frac{B_x \eta_0}{3\sqrt{B}} \frac{\partial\left[\sqrt{B}\left(v_{i\parallel} + b_x\left(v_{\perp}^{\mathrm{dia}} + v_{\perp}^{E}\right)\right)\right]}{h_x \partial x} \frac{1}{h_x} \frac{\partial}{\partial x}\left(\frac{1}{B^2}\right) \end{aligned} \tag{3.22}$$

The current produced by components of the viscosity tensor connected with the heat fluxes can be written in the same form:

$$\begin{aligned}\tilde{j}_{\perp}^{\text{vis}\parallel} &= -\frac{0.24B_x}{\sqrt{B}\nu_{ii}}\frac{\partial\left[\sqrt{B}\left(q_{i\parallel}+b_x q_{ix}^{\text{dia}}\right)\right]}{\partial x}\frac{1}{h_y}\frac{\partial}{\partial y}\left(\frac{1}{B^2}\right)\\ \tilde{j}_{y}^{\text{vis}\parallel} &= b_z\frac{0.24B_x}{\sqrt{B}\nu_{ii}}\frac{\partial\left[\sqrt{B}\left(q_{i\parallel}+b_x q_{ix}^{\text{dia}}\right)\right]}{\partial x}\frac{1}{h_x}\frac{\partial}{\partial x}\left(\frac{1}{B^2}\right)\end{aligned} \tag{3.23}$$

The contribution from perpendicular viscosity is taken into account only for the radial current:

$$j_y^{\text{vis}\perp} = -\frac{1}{\sqrt{g}}\frac{\partial}{\partial y}\left(\frac{\sqrt{g}}{h_y^2}\frac{\eta_{iy}}{4B}\frac{\partial\left(v_{\perp}^{E}+v_{\perp}^{\text{dia}}\right)}{\partial y}\right) \tag{3.24}$$

The contribution to the current due to ion-neutral friction can be written as:

$$\begin{aligned}j_x^s &= -\sigma_{iN}b_z^2\frac{\partial\phi}{h_x\partial x} - \sigma_{iN}b_z^2\frac{1}{en}\frac{\partial nT_i}{h_x\partial x} + \sigma_{iN}B_x v_{yN}\\ j_y^s &= -\sigma_{iN}\frac{\partial\phi}{h_y\partial y} - \sigma_{iN}\frac{\partial nT_i}{h_y\partial y} - \sigma_{iN}Bv_{\perp N}\end{aligned} \tag{3.25}$$

where $\mathbf{v}_N$ denotes the velocity of the neutrals and $\sigma_{iN}$ is the ion-neutral perpendicular conductivity [105].
The electron energy equation can be rewritten as:

$$\begin{aligned}&\frac{3}{2}\frac{\partial\left(nT_e\right)}{\partial t} + \frac{1}{\sqrt{g}}\frac{\partial}{\partial x}\left(\frac{\sqrt{g}}{h_x}\tilde{q}_{ex}\right) + \frac{1}{\sqrt{g}}\frac{\partial}{\partial y}\left(\frac{\sqrt{g}}{h_y}\tilde{q}_{ey}\right) +\\ &\quad + \frac{nT_e}{\sqrt{g}}\frac{\partial}{\partial x}\left[\frac{\sqrt{g}b_x}{h_x}\left(v_{\parallel}-\frac{j_{\parallel}}{en}\right)\right] =\\ &\quad = Q_e + nT_eB\frac{1}{h_xh_y}\left[\frac{\partial\phi}{\partial y}\frac{\partial}{\partial x}\left(\frac{1}{B^2}\right) - \frac{\partial\phi}{\partial x}\frac{\partial}{\partial y}\left(\frac{1}{B^2}\right)\right]\end{aligned} \tag{3.26}$$

where

$$\begin{aligned}\tilde{q}_{ex} = &\frac{3}{2}nT_e\left[-\frac{b_z}{h_y}\frac{\partial\phi}{\partial y} + b_x\left(v_\parallel - \frac{j_\parallel}{en}\right)\right] - \frac{5}{2}T_e b_z D_{\text{an}}\frac{1}{h_x}\frac{\partial n}{\partial x}\\ &- \kappa_{e\parallel}\frac{b_x^2}{h_x}\frac{\partial T_e}{\partial x} - \kappa_{e\perp}b_z^2\frac{1}{h_x}\frac{\partial T_e}{\partial x} - \frac{5}{2}nT_e^2\frac{B_z}{2}\frac{1}{h_y}\frac{\partial}{\partial y}\left(\frac{1}{B^2}\right)\\ \tilde{q}_{ey} = &\frac{3}{2}nT_e\frac{b_z}{B}\frac{1}{h_x}\frac{\partial\phi}{\partial x} - \frac{5}{2}T_e D_{\text{an}}\frac{1}{h_y}\frac{\partial n}{\partial y} - \kappa_{e\perp}\frac{1}{h_y}\frac{\partial T_e}{\partial y} +\\ &+\frac{5}{2}nT_e^2\frac{B_z}{e}\frac{1}{h_x}\frac{\partial}{\partial x}\left(\frac{1}{B^2}\right)\end{aligned} \tag{3.27}$$

In this expression, $\kappa_{e\parallel}$ is the parallel electron heat conductivity. Its expression has been first derived by Braginskii in [12]. In the latest release of the code it has, however, been substituted with that proposed by Zhdanov in [160]. The heat sources which appears in equation (3.27) are the sum of

- the electron-ion equipartition, $Q_\Delta = \nu_{ei}\left(T_e - T_i\right)$ where $\nu_{ei}$ denotes the electron-ion collision frequency.
- the heat source from electron-ion friction and thermal forces, which is proportional to the electron velocity:

$$Q_{\text{fr,therm}} = \left(S^m_{\text{fr}_{ie}} + S^m_{\text{therm}_{ie}}\right)\left(\frac{j_\parallel}{enZ} - v_\parallel\right) \tag{3.28}$$

- the heat sources $Q_{n,e}$ and $Q_R$ which account for electron-neutral interaction and all processes which results in a radiative recombination of the ions, respectively.

The ion energy balance equation is, analogously, given by:

$$\begin{aligned}&\frac{3}{2}\frac{\partial\left(nT_i\right)}{\partial t} + \frac{1}{\sqrt{g}}\frac{\partial}{\partial x}\left(\frac{\sqrt{g}}{h_x}\tilde{q}_{ix}\right) + \frac{1}{\sqrt{g}}\frac{\partial}{\partial y}\left(\frac{\sqrt{g}}{h_y}\tilde{q}_{iy}\right) + \frac{nT_i}{\sqrt{g}}\frac{\partial}{\partial x}\left(\frac{\sqrt{g}}{h_x}v_\parallel b_x\right) =\\ &\quad= Q_\Delta + Q_{n,i} + \eta_{ix}\left(\frac{1}{h_x}\frac{\partial v_\parallel}{\partial x}\right)^2 + \eta_{iy}\left(\frac{1}{h_y}\frac{\partial v_\parallel}{\partial y}\right)^2\\ &\quad+ nT_i B\frac{1}{h_x h_y}\left[\frac{\partial\phi}{\partial y}\frac{\partial}{\partial x}\left(\frac{1}{B^2}\right) - \frac{\partial\phi}{\partial x}\frac{\partial}{\partial y}\left(\frac{1}{B^2}\right)\right],\end{aligned} \tag{3.29}$$

with $\tilde{q}_{ix}$ and $\tilde{q}_{iy}$ are given by analogous expressions to (3.27) and can be found in [105].

### 3.2.2 Eirene

This section aims to give a brief presentation of the general ideas behind the Monte Carlo code Eirene. The latter, has mentioned in § 2.5.1 is used for the solution of the kinetic equation for neutral particles (atoms and molecules) in the plasma edge.
It is well-known that the advantages of the Monte Carlo methods are mainly related to their capabilities to handle complicated geometries as well as dealing with the multitude of the processes such as those characteristic of atomic physics. On the other hand, the Monte Carlo methods are computationally cumbersome particular when one is interested in having a sufficiently high statistics, which in turn require a sufficiently large amount of Monte Carlo histories.
The evolution of the one particle distribution function describing the $j$-th population of neutrals is described by the Boltzmann equation:

$$\frac{\partial f_j}{\partial t} + \xi \cdot \nabla_{\mathbf{x}} f_j = \sum_{i=1}^{n} \frac{1}{m_i} \int \left( f_j' f_{i*}' - f_j f_{i*} \right) B_{ij} \left( \theta, V \right) \mathrm{d}\theta \mathrm{d}\varepsilon \mathrm{d}\xi_* \quad (3.30)$$

In this equation, $B_{ij}\left(\theta, V\right)$ is defined as

$$B\left(\theta, V\right) := Vb \frac{\partial b}{\partial \theta} \quad (3.31)$$

where $V$ is the relative velocity among the two colliding particles, $\theta$ the scattering angle and $b = b\left(\theta, V\right)$ the impact parameter, calculated from the interaction law of the $i$-th particle with the $j$-th one; $\xi', \xi_*'$ in $f_j'$ and $f_{i*}'$ in the $i$-th term are computed in terms of $\xi, \xi^*, \theta, \varepsilon$ according to the law of conservation of energy and momentum [14]. Notice that (3.30) is written assuming that no external force field is acting on particles; that is, particle motion between collision events is a straight line. In linear transport problem [14, 128], one assumes that the collisions of the particle under consideration (say, the $i$-th one) are with a background, denoted by $b$; then the non-linearities contained in the scattering kernel are no more present. Under this condition, we can write the Boltzmann collision operator, for the interaction of the $i$-th particle with the background $b$, as

$$Q_b\left(f, f_b\right) = \frac{1}{m_b} \int \left( f_b' f_*' - f_b f_* \right) B_b \left( \theta, V \right) \mathrm{d}\theta \mathrm{d}\varepsilon \mathrm{d}\xi_* \quad (3.32)$$

where the species index $i$ as been omitted. Under these conditions, one can show [14, 128] that the Boltzmann equation (3.30) can be written as:

$$\frac{\partial f}{\partial t} + \xi \cdot \nabla_{\mathbf{x}} f + \xi \Sigma \left( \xi, \mathbf{x} \right) f = \int_{\mathbb{R}^3} K\left(\xi', \xi\right) f\left(\xi'\right) \mathrm{d}\xi' + Q\left(\mathbf{x}, \xi, t\right) \quad (3.33)$$

where $K$ in this expression is to be intended as a sum over all background particles with which the $i$-th particle can collide and, similarly, for the definition of the macroscopic cross-section $\Sigma$. Their precise definition can be found in [14, 128].
The discussion made so far applies to any linear transport problem. However, for the case under consideration, the plasma edge, the background particles are simply the plasma species with which neutrals can interact. Self-collisions have been recently included [104] and are implemented in the code via the BGK approximation [14, 128, 128] of the full Boltzmann collision operator. Several types of sources of the test particles are available. The most important for divertor applications are the surfaces sources and the volume sources. The former is used for describing the recycling sources of neutrals (ions neutralised on the solid surfaces) and the latter is used for describing the volume recombination. In both cases the primary sampled particle is an ion. One can also specify surface sources of neutrals to model gas puffing. The recycling sources are specified on the boundary of the B2 grid. It does not always reflect correctly physical location of the wall but the ion fluxes are available only on those surfaces. The velocity distribution function of the background particles (ions) is taken to be a shifted Maxwellian [128], while the velocity of ions incident on a surface is taken to be a truncated shifted Maxwellian distribution,

$$f(\xi) = C(\xi \cdot \mathbf{n}) \exp\left[-\frac{m}{2T}(\xi - \mathbf{v}_d)^2\right], \tag{3.34}$$

In this expression, $\xi$ denote the kinetic velocity of the ions, $\mathbf{n}$ is the surface normal, $\mathbf{v}_d$ and $T$ denote the mass velocity and temperature of the ions in front of the surface. Finally $C$ is a normalising constant. For target surfaces, the sheath acceleration (see Appendix § B) is added. After sampling of velocity, a surface interaction model is applied to the incident ion. The same surface model is used in the case in which the neutral particle is an ion. Eirene considers three kind of surface processes: reflection of fast particles, thermal desorption and sputtering. Several options are available for fast particle reflection [128]. The best option at the moment is to sample the probability of reflection, velocity and the scattering angle of the reflected angle using the pre-computed tables obtained by the TRIM code. The data for different pairs of target-projectile can be found on `www.eirene.de`. If Eirene cannot find the data for the specific pair it takes the available data with the closest reduced atomic mass of the target and the projectile.
Particles which are not reflected as fast particles thermally desorb with a Maxwellian distribution at the wall temperature. The latter is usually set to $0.1\,\mathrm{eV}$ for target surfaces and to $0.04 \div 0.07\,\mathrm{eV}$ for other surfaces. For par-

ticles with incident energy lower than a certain prescribed cut-off (usually $1\,\mathrm{eV}$) the thermal desorption is considered as well. Hydrogen atoms desorb as molecules. Only desorption (no fast reflection) is applied for molecules. A particle absorption coefficient (albedo) can be set for some surfaces to model pumping. Two kinds of sputtering processes are considered: physical sputtering and chemical sputtering. The physical sputtering is described by the modified Roth-Bohdansky formula for the sputtering yield, Thompson energy distribution and cosine angular distribution for emitted particles. The volume processes can be divided into two groups: electron impact collisions and heavy particles collisions. The first group includes ionisation, dissociation and recombination. The collision rates of the electron-impact processes are assumed to be independent of the test particle velocity, due to the high velocity of the electrons. Their rates depend on the electron temperature and, in some cases, also on the electron density [104].
The collisions of heavy particles are the elastic collisions and the charge-exchange collisions. The collision rates for those processes depend on the plasma ion temperature and the velocity of the test particles. Elastic collision may include the neutral-neutral collisions. The reaction rates are tabulated in the datafiles HYDHEL, AMJUEL and METHANE, which are available in the SOLPS code package.

### 3.2.3 SOLPS-ITER code structure

The SOLPS-ITER code can be used in two modalities **standalone** or **coupled**:

- **B2.5 standalone run**: in this case, only the multifluid code B2.5 is used. Neutral species are treated just as the other plasma species (i.e. as a fluid), with their own particle and momentum transport equations in the parallel direction, equivalent to (3.9) and (3.11). The neutrals are assumed to have the same common temperature as all the other ion species, therefore the neutral energy balance becomes simply a component of (3.29). Clearly, terms due to charged particle motions or currents do not appear for neutral species. The volume sources of neutrals are given by plasma recombination rates computed using the ADAS database for atomic processes.
- **B2.5-Eirene coupled run**: in this case, the code is run with an iterative coupling between the multifluid B2.5 code and the Monte Carlo Eirene code for the neutrals. This iterative coupling is consists in the following steps: $i)$ preparation of a the numerical grids for the two codes, $ii)$ the computation of the sources and sinks terms into the fluid

balance equations for each of the plasma species. This procedure is performed by Eirene assuming that the plasma background species are described by a drifting Maxwellian distribution function with local parameters (e.g. temperature) equal to that computed by B2.5 and computing the relevant atomic (or molecular) processes using the Monte Carlo approach. Once each of the Monte Carlo histories is completed, the sources and sinks are computed and, in step $iii$), the B2.5 equation are solved. This whole procedure is repeated until convergence is obtained [128].

- **Eirene standalone run**: in this mode, only the transport neutral species is simulated by performing a single Monte Carlo iteration on a fixed plasma background.

Having described the main modalities in which SOLPS-ITER can be used, we shall now consider briefly its basic structure as well as describing the main inputs. The SOLPS-ITER directory has the following global structure:

```
SOLPSTOP
+---doc
| +---SOLPS_2002_Course
| +---solps
+---scripts
| +---Balance
| +---commands
| +---matlab
| +---MatlabPostProcessing
| +---Matlab_SPb
| +---nc2text_simple
| +---palettes
| +---ITER.ifort64
+---scripts.local
+---modules
| +---Sonnet-light
| +---fxdr
| +---Triang
| +---Uinp
| +---Carre
| +---amds
| +---adas
| +---B2.5
```

```
| +---solps4-5
| +---DivGeo
| +---Eirene
+---lib
| +---ITER.ifort64
+---runs
+---SETUP
```

The main packages are contained in the /modules folder of the SOLPS directory:

- **DivGeo**, is a graphical user interface used for the preparation of the main code inputs. This package require the upload of the equilibrium magnetic field, containing information on the flux surface structure of a given plasma discharge at a fixed instant of time. The current requirement in B2.5 is that the equilibrium magnetic flux surfaces intersect the solid walls only at the divertor target. Additionally, one also needs the information of the structure of the two-dimensional cross-section of the tokamak first wall.
- **Carre** is the main mesh-generating program currently employed in SOLPS-ITER. The code structure is described in details in [132]. It uses the output files created by DivGeo to generate a field-aligned curvilinear grid, in order to avoid numerical diffusion. This means that two of the sides of the quadrilaterals which make up the have their sides lying on a flux surface. An example of such a grid is displayed in figure 3.2. This grid called the **physical grid**. Numerical calculations are instead performed on a logically rectangular grid, called the **computational grid**. To move from the physical mesh to the computational one, a cutting procedure need to be performed. The idea is to cut the physical grid in the proximity of the X point, as illustrated in figure 3.3. A cut (dashed line) is performed along the X-point. The domain is then opened-up and arranged in a rectangle, with the corresponding regions arranged as showed in the figure. At the four sides of the rectangle, called North, West, East and South, suitable boundary conditions are imposed.
- **Triang** is the program which is used to build the triangular mesh for Eirene, using input coming from DivGeo and Carre. Contrary to the computational grid used by B2.5, the Eirene grid extends all across the tokamak poloidal cross section, thereby reaching also remote area of the FW. An example of such a grid is illustrated in figure 3.4.

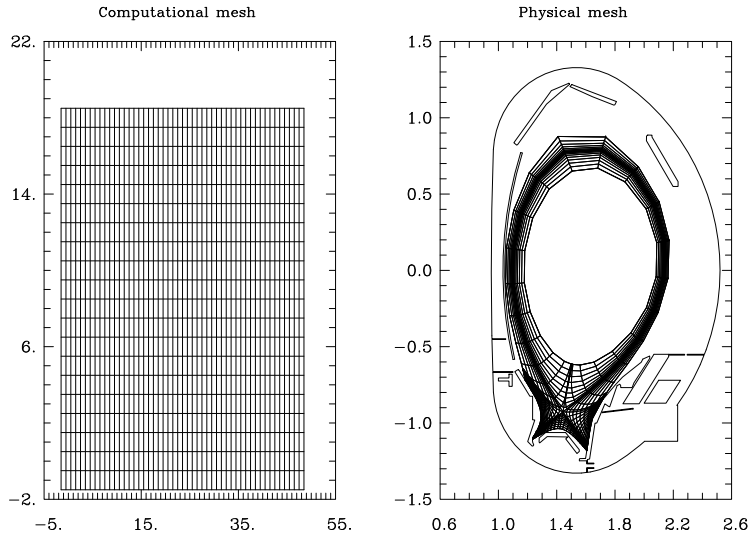


**Figure 3.2:** *Example of a 2D computational grid for the AUG tokamak referred to the plasma discharge* #35617 *at* 2.5 s*. The physical mesh is illustrated on the right, while the computation one on the left.*

- **B2.5** is one of the main fundamental packages of the code, together with Eirene. A detailed description of the main code physics have been described in § 3.2.1. The B2.5 code is completely written in FORTRAN 90 and it is based on a finite volume discretisation of the equations § 3.2.1. At each iteration, corresponding to a single time step, volumetric and surface source terms are computed, solving for momentum conservation, continuity, energy conservation and finally, again, for the continuity equation. The procedure outlined above is repeated for a number of internal iterations to relax the equation solutions before proceeding to the next time step. The process is repeated until convergence is reached. The latter is monitored by analysing the residuals of each equation.
  In either cases, the main program is `b2mn.exe`, which needs input files written by `b2ag.exe`, `b2ah.exe`, `b2ar.exe`, `b2ai.exe`, that we shall now briefly discuss:

  – b2ag prepares the geometry file, `b2fgmtry`, reading the input file `b2ag. dat`, which contains information on the mesh di-

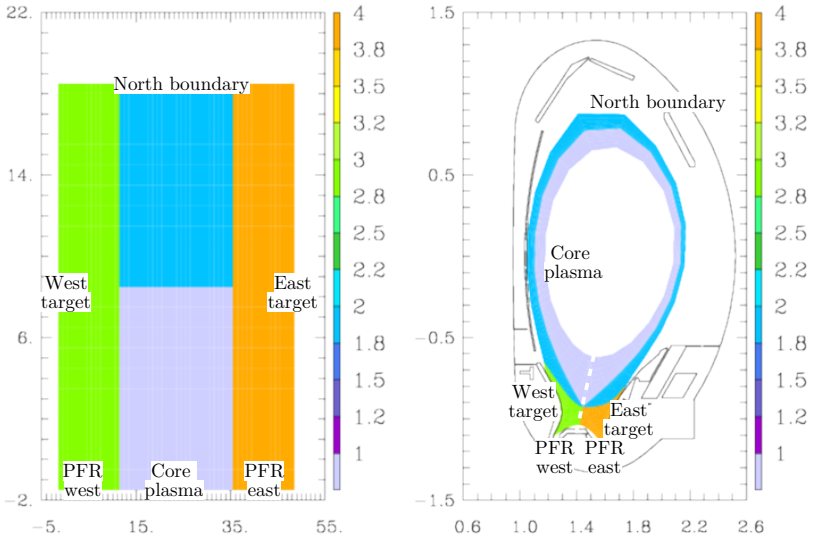


**Figure 3.3:** *Illustration of the cutting procedure performed to move from the physical (right) to the computational domain (left). A cut (dashed line) is performed along the X-point. The domain is then opened-up and arranged in a rectangle, with the corresponding regions arranged as showed in the figure. At the four sides of the rectangle, called North, West, East and South, suitable boundary conditions are imposed.*

mensions which must be provided as an input to `b2ag`.

- `b2ah` prepares the default physics file, `b2fpardf`, reading the input file `b2ah.dat`, which contains information of the different species that are to be simulated by the code. This may include, for example, deuterium and different impurities, such as tungsten, which can be present in the plasma edge due to sputtering.
- `b2ar` prepares the default atomic physics rates file, `b2frates`, reading the input file `b2ar.dat`. The latter specifies the ranges of densities and temperatures for atomic physics tables, taken from different atomic physics packages. The default option is the use of ADAS (Atomic Data and Analysis Structure) [153].
- finally, `b2ai` prepares the default initial plasma state file, `b2fstati`, reading the input file `b2ai.dat`.

Additional input files can be read in from the code. These usually include the `b2.boundary.parameters` for the boundary condi-

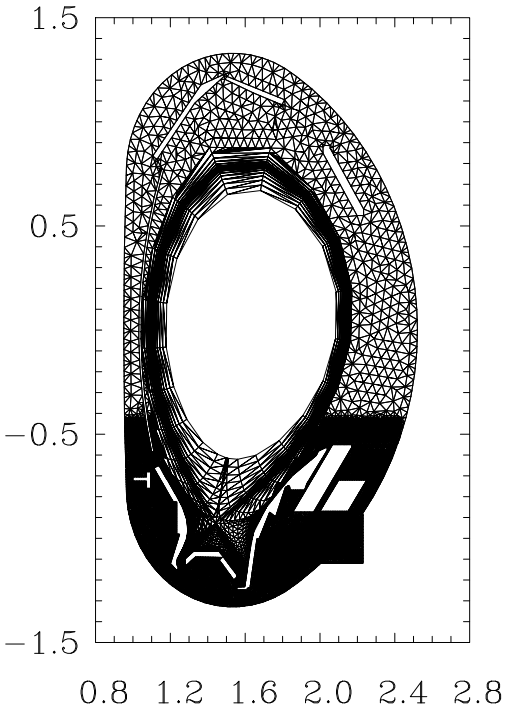


**Figure 3.4:** *Example the triangular mesh used by Eirene. The mesh is unstructured and extends all across the poloidal cross-section of the tokamak (AUG, for the case here reported).*

tions to the plasma fluid equations for each fluid species specified in `b2ah.dat`, the `b2.transport.parameters` for the (anomalous) transport coefficients, the `b2.sources.profile` for the external sources (particle, momentum, electron and ion heat) and the `b2.neutrals.parameters` for the neutral particles information.

- **Eirene** is the Monte Carlo code devoted for studying neutral particles transport in the tokamak edge. It is entirely written in `FORTRAN 90`, as for B2.5. Even though, in principle, Eirene is a three-dimensional code, when coupled with 2D codes (such as B2.5 or SOLEDGE), the toroidal coordinate is neglected and the volume of each cell of the mesh is computed by taking a fixed length in this direction. The main input required by Eirene is a formatted text file called `input.dat`. The latter is produced as an output by DivGeo, using the geometry outputs from both `Carre` and `Triang`. The structure of this for-

matted text file consists of fifteen blocks:

```
***1. Input data for operating mode
***2. Input data for standard mesh
***3A. Input data for "Non-default Standard Surfaces"
***3B. Input data for "Additional Surfaces"
***4. Input data for species specification and atomic physics module
***5. Input data for plasma background
***6. Input data for surface interaction models
***7. Input data for initial distribution of test particles
***8. Additional data for some specific mesh zones
***9. Data for statistics and non-analog methods
***10. Data for additional volumetric and surface averaged tallies
***11. Data for numerical and graphical output
***12. Data for plasma diagnostic module DIAGNO
***13. Data for nonlinear and time-dependent mode
***14. Data for interfacing with routine INFUSR
***15. Data for interfacing with routine GEOUSR
```

The last two blocks of the input file are those regulating the coupling with fluid edge plasma codes, B2.5 in the case of SOLPS. Additional details of the meaning of the remaining blocks can be found in [128].

## 3.3 The erosion and transport code ERO

This section aims to give a brief overview of the Monte Carlo code ERO and its subsequent development, ERO2.0. In particular, we start in § 3.3.1 by giving a brief overview of the basic concepts of the ERO code, as well as presenting its general structure. We consider next the recent code improvements which have been implemented in ERO2.0. In § 3.3.2 we focus in particular on the code capabilities to simulate the evolution of complex morphology due to plasma irradiation. We conclude the section by giving in § 3.3.3 a brief overview of the main code inputs necessary to perform a simulations.

### 3.3.1 ERO code - basic concepts

The 3D Monte Carlo code ERO consists of two main, coupled, parts: the PMI and the impurity particle transport in the plasma. A schematic representation of these two blocks is shown in figure 3.5. The PMI block of the code deals with the interaction between the plasma and the materials. In particular, in this block the amount of sputtered and deposited materials is calculated for each of the surface cells defining the PFC. The following processes are considered in the PMI part of the ERO code:

- physical sputtering,

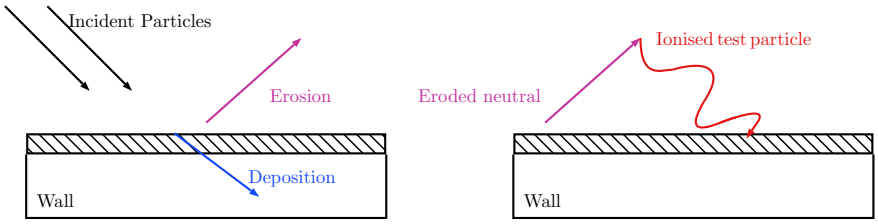


**Figure 3.5:** *Schematic picture showing the ERO code workflow, as well as some of the simulated processes. The two main components of the code are coupled by an iterative scheme.*

- chemical and chemically-assisted sputtering,
- deposition,
- reflection
- surface morphology evolution under plasma irradiation (at least, in the newest ERO2.0 version)

It should be noted that all these processes depend on the combination of the impacting plasma species and surface material as well as on the irradiation parameter (incidence angle and impact energy). Therefore, in principle, one should need to have separate modules for treating contributions coming from different sources of the processes listed above. For example, the overall physical sputtering of the PFCs receive contributions from: $i$) the plasma background species, $ii$) the impurity particles traced by ERO and $iii$) by charge-exchange neutrals. For all these three contributions, the corresponding value of the sputtering yield can be taken from database of precomputed values thanks to the coupling of ERO with SDTRIMSP [19] or directly computed using fitting formulae proposed by Eckstein [18], which can be written as:

$$Y(x) = Y_0 x^{-f} \exp\left[f\left(1 - \frac{1}{x}\right)\cos\theta_{\text{opt}}\right] \tag{3.35}$$

where $Y_0$ denotes the sputtering yield at orthogonal incidence, $f$, $\theta_{\text{opt}}$ are fitting parameters and $x = \cos\varphi$, where $\varphi$ denote the incidence angle. Note that these parameters are function of the incident ion energy.
Physical sputtering by plasma particles require some additional considerations. Indeed, in this case no information is known of the precise energy and angular distribution with which plasma particles reaches the solid materials. This means that one cannot compute the corresponding value of the sputtering yield using equation (3.35) or the database of precomputed

values. In this case, ERO either assumes a reasonable (e.g. mean) constant impact energy (given by $E = 2T_i + 3T_e$, where $T_i$ and $T_e$ denote the ion and electron temperature respectively) and angle and utilizes analytical or numerically pre-calculated distributions in order to compute the plasma sputtering yield [19, 142]. An alternative approach have been recently implemented in the ERO2.0 code, which goes under the name of **sheath tracing**. It consists in a ERO simulations which takes as an input only a limited amount of information of the background plasma, such as the electron temperature, the electron density, the magnetic field intensity and inclination, and the applied bias voltage, and resolve the trajectory of the plasma particles, sampled by a shifted Maxwellian distribution [19]. The incidence angle and energy with which these particles impinge on the surface are then used in the Eckstein fit (cfr. equation (3.35)) to compute the effective sputtring yields.
Once computed the sputtering yields, the code calculates erosion, deposition and other PMI processes once over a short time interval, normally of the order of $0.1\,\mathrm{s}$. The latter is given as an input parameter set by the user and can vary significantly depending on the plasma parameters, interaction layer and the particular task considered.
The next block (cfr. figure 3.5) deals with the transport of these eroded impurities in the plasma using a Monte Carlo approach. That is, the total amount of sputtered material is distributed between test particles, each one representing a large number of real atoms. As is known from Monte Carlo theory, is the total amount of these test particles which ultimately determine the statistics of the simulations. Sputtered particles are usually neutrals, which thus move on straight lines in between collisions. The latter can occur either with background neutrals or with the plasma ions. The code is capable of accounting for several of these interaction, such as ionisation, recombination, plasma-neutral friction, light emission and so on. The atomic processes are dealt with by coupling with the atomic database ADAS [153]. Once ionisation of the sputtered neutrals occur, the ions are now subjected to electric as well as magnetic forces. Ions transport is calculated using the Boris method, resolving also their gyromotion across magnetic field lines. The interaction between the traced ions and the plasma background is computed by solving the Boltzmann equation for the plasma (that is, the Boltzmann equation with the Landau collision integral). Additional details on the PMI and transport capabilities in ERO can be found in [19, 142].

### 3.3.2 ERO2.0 - surface morphology evolution

The ERO code has been recently developed to the 2.0 version [142]. The code utilizes advanced parallelisation scheme and allows for the simulation of complex geometries. This upgrade allowed not only to model the full vessel of a tokamak [142], but also to apply the code to define fine surface structures on the $\mu$m scale and being able to consider the surface morphology influence on the erosion process. The latter aspect is of particular relevance for the present Thesis work and thus in the remaining of this section we shall examine it in more details.
A non-trivial surface morphology can have important impact on the sputtering yield as well as the angular distribution of sputtered particles. This surface morphology feedback on the PMI can be investigated when the increased computational capabilities brought in by ERO2.0 are applied on micro/nanoscale to resolve in some details the fine surface structure and simulate the transport of the sputtered or deposited particles in its vicinity. A non-trivial surface is represented in ERO2.0 as a polygon mesh of surface cells. The rough surfaces in ERO can be either defined numerically (e.g. [19]) or either obtained from dedicated Atomic Force Microscopy (AFM) measurements. Each of the cells defining the surface is, in turn, assumed to be smooth. This means that the sputtering yield as well as the angular distribution of sputtered particles can be computed simply using the ion impact energy and the local incidence angle, $\varphi$, defined as $\cos\varphi = \mathbf{n}\cdot\hat{\boldsymbol{\phi}}$, where $\mathbf{n}$ and $\hat{\boldsymbol{\phi}}$ denotes the local cell surface normal and a versor in the direction of the incident flux, respectively. Furthermore, since one is interested in the simulations of surfaces with characteristic areas of $\simeq \mu\mathrm{m}^2$s, then one can consider the ion flux (as well as other plasma quantities) to be uniform. For each of the surface cells defining the given rough surface, ERO compute the amount of erosion and generate correspondingly an ensamble of test particles. These are further traced by ERO until the leave the simulation volume or collide with neighboring surface structures. Periodic boundaries are implemented in the directions parallel to the surface, in order to avoid particle loss through the side and eliminate uncertainties related to the finite size of the simulation box.
Both sputtering and redeposition influence the surface topography evolution during the plasma irradiation. In order to simulate this evolution, a suitable algorithm has been implemented in ERO2.0. The idea behind it consists in converting the amount of atom loss/gain in a change of thickness (height) of each of the surface cells. This process is schematically illustrated in figure 3.6 in the case of atom loss from a single surface cell.

Each of the surface is the shifted down in the direction of the local surface

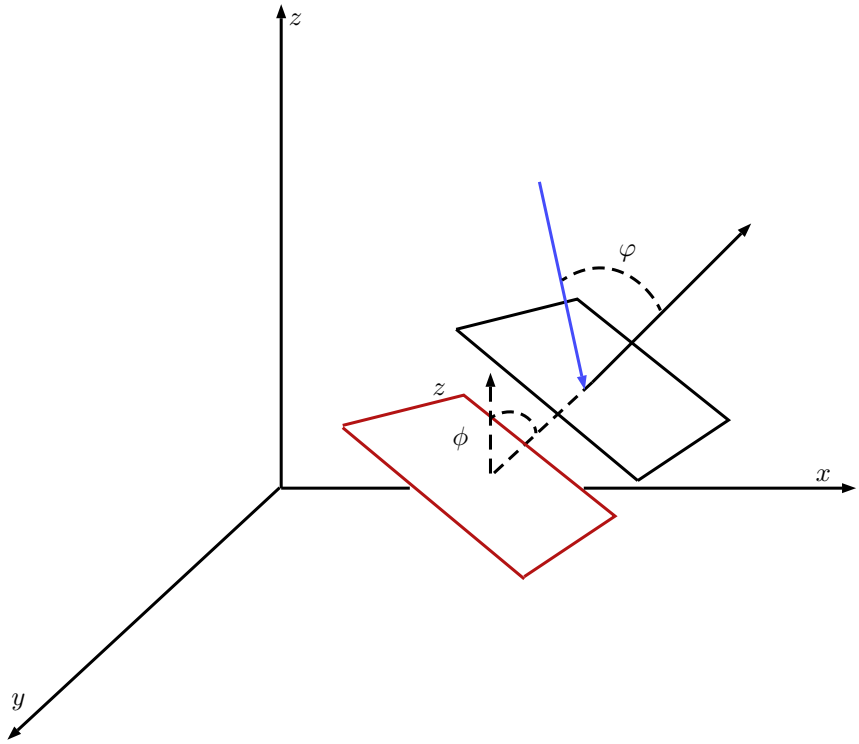


**Figure 3.6:** *Schematic representation of the surface evolution module currently implemented in ERO2.0. A quadrilateral (solid black line) is characterised by its surface normal (solid black arrow). The latter forms an angle $\varphi$ with the impinging ion (solid blue arrow). As a result of the material removal, the quadrilateral is shifted (solid bordeaux line) in the direction of the surface normal, denoted here with a dashed black line, which forms an angle $\phi$ with the vertical $z$ direction.*

normal, $\mathbf{n}$, by an amount proportional to the sputtered thickness

$$\Delta z = \frac{Y \Gamma \Delta t}{n_{\mathrm{at}}} \tag{3.36}$$

where $Y$ is the sputtering yield, $\Gamma$ the local incident ion flux, $n_{\mathrm{at}}$ the number density of the target material and $\Delta t$ the time step. This process is repeated for every cell defining the surfaces and, at the end of the time step, the new surface mesh is recomputed. Smoothing is added at the end of each time step, simply as an average over the vertices of the newly-computed surface mesh.

### 3.3.3 ERO2.0 - main inputs

Having described the main physical processes accounted for in ERO, we shall now turn very briefly to the discussion of the main input necessary for performing a simulations. The latter are of great importance, since the intimately influence the result of the ERO simulation. Recalling the two main blocks into which ERO can be subdivided, the following input data are needed:

- **PMI data**:
  - Sputtering yields, as well as the angular and energy distribution of the sputtered particles
  - Reflection coefficients
- **Atomic Data**:
  - Ionisation, recombination and dissociation rates
  - Photon Emission Coefficients (PEC)
  - Metastable cross-coupling coefficients
  - Elastic collision cross-sections

## 3.4 Experimental methods

### 3.4.1 The Pulsed Laser Deposition

As stated in § 2.6.2, the PLD was chosen as the main deposition technique in the present Ph.D. Thesis work due to its very high versatility and its ability to finely tailor the morphology, structure and composition of the coatings by a careful choice of its main operation parameters.
Here, we shall give some details on the PLD setup available at NanoLab, a schematic representation of which is illustrated in figure 3.7. The laser system is a Q-switched $\mathrm{Nd:YAG}$ laser Continuum Powerlite II 8010, with a pulse duration (FWHM) of $7\,\mathrm{ns}$, maximum repetition rate of $10\,\mathrm{Hz}$ and a maximum energy per pulse of $1.8\,\mathrm{J}$ at its fundamental harmonic (i.e. $\lambda = 1064\,\mathrm{nm}$). The laser pulse enter the vacuum chamber and strikes the target at $45°$. The deposition process can be performed either in vacuum, i.e. $10^{-4}\,\mathrm{Pa}$ guaranteed by a pumping system made by a primary scroll and a turbomolecular pumps, or in presence of a background gas, whose pressure is tuned by a PID controller that regulates the gas mass flow. The background gas can be chemically inert, such as $\mathrm{He}$ or $\mathrm{Ar}$, or reactive, like

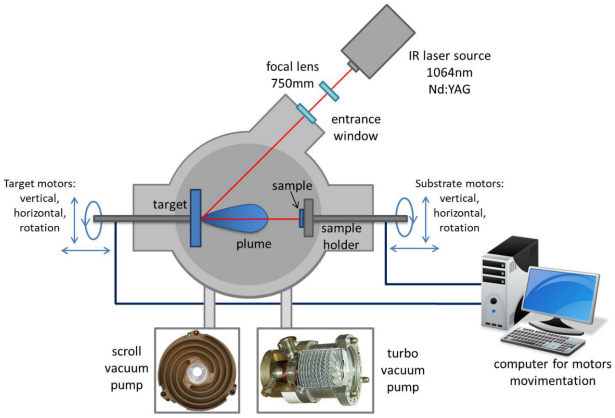


**Figure 3.7:** *Schematic representation of a typical PLD setup. A focalised pulsed laser impinges on a target material with sufficiently high energy density to bring it to a vapour phase. The ablated species can expand in vacuum or in a suitable background atmosphere, finally depositing on top of the substrate.*

$H_2$, $N_2$ and $O_2$. Both the target and the substrate holder are remotely controlled by ad-hoc dedicated software and, combining the holder shift and rotation, it is possible to guarantee the deposits planarity over an area of $\simeq \mathrm{cm}^2$.

### 3.4.2 Coatings characterisation

The coatings which have been synthesised in the present Thesis work have been characterised from the morphological, compositional and topographical point of view by exploiting different techniques, which are briefly described below.

#### 3.4.2.1 Scanning Electron Microscopy (SEM)

In a Scanning Electron Microscope (SEM), a high-energy ($0.2 \div 30\,\mathrm{keV}$) electron beam is focused onto a fine probe that scans the surface of the sample to be analysed. In particular, the interaction of the electron beam (primary electrons) with the specimen results in the generation of backscattered electrons (BSE), secondary electrons (SE) and X-rays. This interaction process is schematised in figure 3.8. BSE are produced by elastic scattering events between primary electrons and atomic nuclei. Since the mass difference between the electrons and the nuclei is very high, the former looses little energy in this interaction. In addition, the backscattering cross-section scales proportionally to the square of the atomic number.

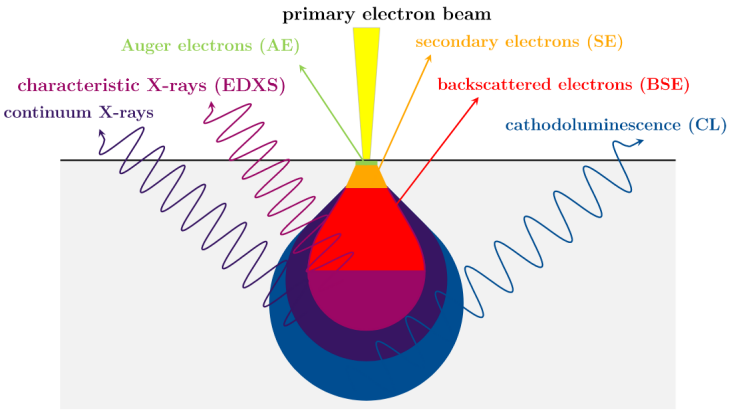


**Figure 3.8:** *Schematic representation showing the interaction of the focused electron beam (primary electron beam) with the specimen surface. This interaction results in the production of back-scattered electrons, secondary electrons and X-rays.*

Thus, the higher is Z the higher will be the number of BSE. Therefore, detecting BSE allows to have a qualitative understanding of the sample compositions. The primary electrons can also interact inelastically within the materials and, more specifically, with the electrons in the atomic nuclei of the sample materials. In this process, if the energy transfer is sufficiently high, then generation of SE can occur. The latter have a kinetic energy lower then $\simeq 50\,\mathrm{eV}$ and can escape from the materials only if the latter is greater than the work function of the material under investigation. This means that SE are quite sensitive of the samples surface. In the inelastic interaction between the primary electron and the electron bounded in the atomic nuclei also X-rays can be produced. The latter results from the electronic transition within the energy level of the sample atoms and, thus, they are characteristic of the sample materials (so-called **characteristic X-rays**). Detecting these characteristic X-rays can therefore allow to retrieve the elemental composition of the sample without, however, giving any information on the eventual presence of bonds between elements. This particular technique of elemental composition analysis goes under the name of **Energy Dispersive X-Ray Spectroscopy** (EDXS). Other signals are produced in principle from the interaction of the sample surface with the primary electron beam, such as Auger electrons, catholuminescence, and so on. These, however, were not considered in this work.
The SEM employed during the Ph.D. activity is a high-resolution Field Emission-SEM Zeiss Supra 40 based on the Gemini column, equipped with

an Oxford EDXS spectrometre, The accelerating voltage ranges from $1\,\mathrm{kV}$ to $30\,\mathrm{kV}$. For the analysis performed in this work, however, a maximum of $15\,\mathrm{kV}$ were employed. The samples holder is connected to five software-controlled motors. The EDXS detector is a solid-state lithium-drifted Silicon detector protected by a Beryllium window with an energy resolution of $10\,\mathrm{eV}$.

#### 3.4.2.2 X-Ray Diffraction

X-Ray Diffraction (XRD) is a powerful non-destructive technique that allows for the identification of the different phases present in the analysed samples, as well as its structural properties, such as crystallite size, preferential growth orientation, and so on. An incident X-Ray beam impinge on the sample surface and it is diffracted by its crystalline planes, as illustrated in figure 3.9. Constructive interference occurs when the path length differ-

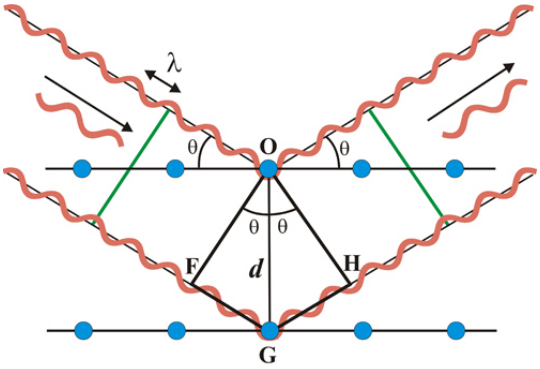


**Figure 3.9:** *Schematic representation of the XRD working principle (Bragg's law).*

ence between the two X-Rays beams scattered from successive crystalline planes is a multiple integer of the incident radiation wavelength, $\lambda$. This is known as the **Bragg's law** and it can be written as follows:

$$n\lambda = 2d_{hkl}\sin\theta_{hkl} \tag{3.37}$$

where $d_{hkl}$ denotes the distance between the crystalline planes with Miller indices $(hkl)$ and $\theta_{hkl}$ is the angle between these planes and the incident X-Ray beam.
In the present Ph.D. work the XRD spectra have been acquired by C. Conti using a Panalytical X'Pert PRO X-Ray diffractometer in the $\theta/2\theta$ configuration, with a Ge-monochromated Cu K$\alpha$1 radiation ($\lambda = 1.5406$). The diffraction pattern were collected at room temperature. The crystallite size

were estimated using the Scherrer equation:

$$\tau = \frac{K\lambda}{\beta \cos\theta} \tag{3.38}$$

where $\tau$ is the mean size of the crystal domain, $K$ is a dimensionless shape factor ($K = 0.9$), $\lambda$ is the incident X-Ray wavelength, $\beta$ is the $\mathrm{FWHM}$ and $\theta$ is the Bragg angle.

#### 3.4.2.3 Annealing treatments

Annealing treatments are widely employed in material science in order to change the physical (and, sometimes, also chemical) properties of a material. For the experimental activity of the present Ph.D., annealing treatment were performed with the main aim to simulate thermal effects which have occurred during plasma exposures in the LPD GyM. These annealings were performed both in vacuum, as well as in a reactive $\mathrm{Ar} - \mathrm{H_2}$ atmosphere. The latter was employed aiming to replicate the typical reducing atmosphere characteristic of $\mathrm{D}$ plasmas.
Thermal treatments were performed in a home-made furnace which consists in a high-vacuum chamber, a heater stage connected to a PID controller and a pumping system, consisting in a primary rotary pump and a turbomolecular pump. The latter allows to reach a nominal background pressure of $\simeq 10^{-6}\,\mathrm{Pa}$. The pressure is measured using a capacitance gauge (BOC Edwards Barocel Pressure Sensor, operational range $100 \div 10^{5}\,\mathrm{Pa}$) and by a Varian Bayard-Alpert gauge (operational range $10^{-8} \div 10^{-2}\,\mathrm{Pa}$). The gas inlet ensure the possibility to introduce gas flow within the vacuum chamber during the annealings. This allows to finely tune the desired atmosphere as well as speeding up (whenever necessary) the cooling process after the annealings. The heater stage, its power supply and controller are provided by TecTra. The heating element is made of pyrolitic Boron Nitride and pyrolitic Graphite. Current flowing into the latter leads to heating through the Joule effect. The temperature is measured by means of a thermocouple which is used as a feedback signal for the PID controller. A Molybdenum shield covering the heating element can be installed in order to reduce the irradiated power, keeping therefore the remaining components safe. This is particularly important for the front viewport, which would otherwise reach excessive temperatures. This system allows to reach operating temperature up to $1200^{\circ}\,\mathrm{C}$ with heating ramps of up to $100^{\circ}\,\mathrm{C/s}$. In additional, an optical pyrometer (Impac IGA 140) is also employed in order to check the actual temperature on the surface of the heating stage.

#### 3.4.2.4 Atomic Force Microscopy

The topographical investigations of the samples analysed in this Ph.D. work were performed by means of an Atomic Force Microscope (AFM), a schematic representation of which is displayed in figure 5.6. s The working principle

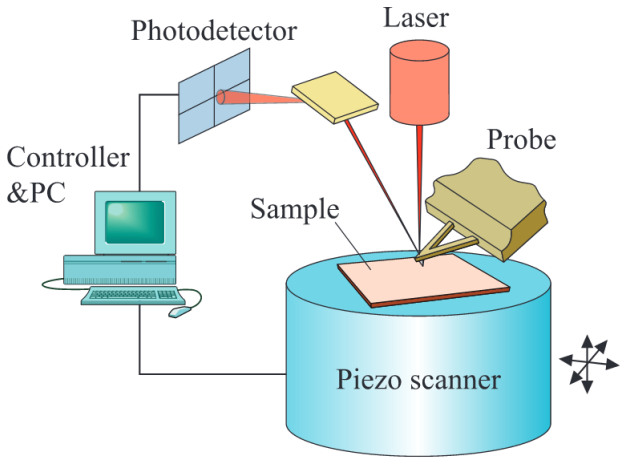


**Figure 3.10:** *Schematic representation of the AFM. From [123].*

of this type of microscope is based on a spring-like cantilever carried by a support, with a sharp tip at its free end. The latter acts as a probe, by scanning the sample surface. A detector, usually a laser focused on top of the cantilever, records its up-down motion and sends the signal to a photodetector and software for subsequent post-processing. There are three different working modalities of the AFM:

- **contact mode** in which, as the name suggests, the tip is in direct contact with the sample surface as it scans through. Measuring the deflection of the cantilever or, equivalently, the force needed to maintain it in contact with the surface allows to retrieve the surface topography.
- **non-contact mode** in which the cantilever oscillates at a given distance from the sample surface, without touching it around its resonant frequency. Depending on the surface roughness of the investigated sample, as the probe scans through it, the resonant frequency changes due to tip-sample Van der Waals forces. By a feedback system, these changes in the resonant frequency can be converted to topographical signals. Non-contact AFM has generally a lower resolution with respect to the contact one and the image can be affected by the presence of small impurities on the surface. Nevertheless, it does not involve

any contact between the probe and the sample, does any damage can be avoided.

- **tapping mode** in which the cantilever oscillates up and down near its resonant frequency, similarly to non-contact mode. However, in this case the probe tip is allowed to touch the sample surface intermittently. The topographical signal is generated by measuring changes in the oscillation amplitude, the latter driven by Van der Waals forces between the tip and the sample. This technique is particularly useful with biological or soft and fragile samples also in liquid, since it does not suffer from friction, adhesion and sample damaging.

The true great advantage of the AFM is its capability of achieving extremely high vertical resolution (of the order of $\simeq \mathrm{nm}$)), depending on the mode used and the samples properties.
During the Ph.D. activities, a ThermoMicroscope Autoprobe CP-Resarch AFM has been used to acquire topography images operated in tapping mode.

### 3.4.3 The Linear Plasma Device GyM

The LPD GyM of ISTP-CNR represents one of the most important apparatus which has been employed in this Ph.D. work. The latter was indeed employed for numerical studies, as well as for experimental exposures of W-based coatings to fusion-relevant plasmas. Due to its importance, in what follows we should describe in some details its main features of relevance for both the numerical as well as the experimental activities of this Thesis.
GyM structure is shown in figure 3.11. The main chamber consists of a cylindrical stainless steel vacuum vessel of 0.25 m diameter and 2.11 m length surrounded by 10 magnetic coils. From figure 3.11, we can see the location of the two radiofrequency (RF) sources delivering up to $3.0\,\mathrm{kW}$ and $1.5\,\mathrm{kW}$, the Langmuir Probe (LP), the gas injection nozzle, the two turbomolecular pumps and the pressure gauge. The main plasma parameters that can be obtained in GyM are reported in table 3.1. From this table, one can see that the plasma density and, correspondingly, the particle flux is rather low if compared to other LPDs reported in table 2.1. Thus GyM is not suited for studying the behaviour of fusion-relevant W coatings in divertor-like plasma regimes. However, the typical particle fluxes and ion energies are similar to that of charge-exchange neutral fluxes at the main chamber of both present-day tokamaks [79, 109] and ITER [88, 110].
The standard magnetic configuration in GyM is obtained connecting all the

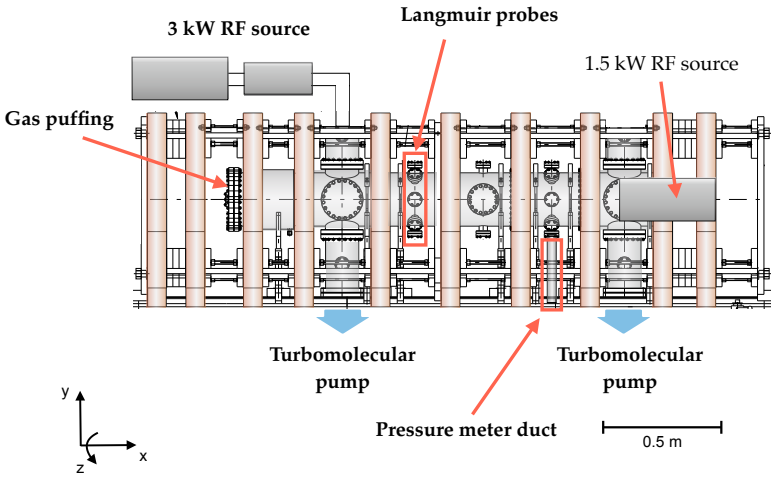


**Figure 3.11:** *Schematic drawing of GyM linear machine with the magnetic field coils and the vacuum chamber. The Langmuir Probe (LP) location, the RF sources at* $2.45\,\mathrm{GHz}$ *capable of delivering up to* $4.5\,\mathrm{kW}$ *and the gas nozzle located at one end of the cylindrical vacuum vessel are shown. The* $1.5\,\mathrm{kW}$ *RF source is reported in figure, but it will not be considered in the following.*

| Main GyM parameters | |
|---|---|
| Neutral pressure | $10^{-5} \div 10^{-4}\,\mathrm{mbar}$ |
| Plasma density | $10^{16} \div 10^{17}\,\mathrm{m}^{-3}$ |
| Electron temperature | $5 \div 10\,\mathrm{eV}$ |
| Particle flux | up to $10^{21}\,\mathrm{m}^{-2}\mathrm{s}^{-1}$ |
| Particle fluence | up to $10^{25}\,\mathrm{m}^{-2}$ |
| Ion energies | $0.1 \div 400\,\mathrm{eV}$ (with bias) |

**Table 3.1:** *Typical plasma parameters measured by Langmuir Probes in GyM.*

10 coils in series, so that the same current flows in each of them. The flux lines of the magnetic field are shown in figure 3.12. From this figure, it is seen that $\mathbf{B}$ is almost axial. Its intensity is modulated by changing the axial coil distance as well as the currents flowing into the coils. The peak magnetic field can reach the value of about $0.13\,\mathrm{T}$.
The plasma in GyM is generated and sustained exploiting the electron cyclotron resonance (ECR) heating mechanism at $2.45\,\mathrm{GHz}$, which directly heats only the electron population. As shown in figure 3.11, the EC system is connected to the vessel through a waveguide, injecting EM waves in O-mode polarisation. In figure 3.13, we show the location on the $(Z, R)$

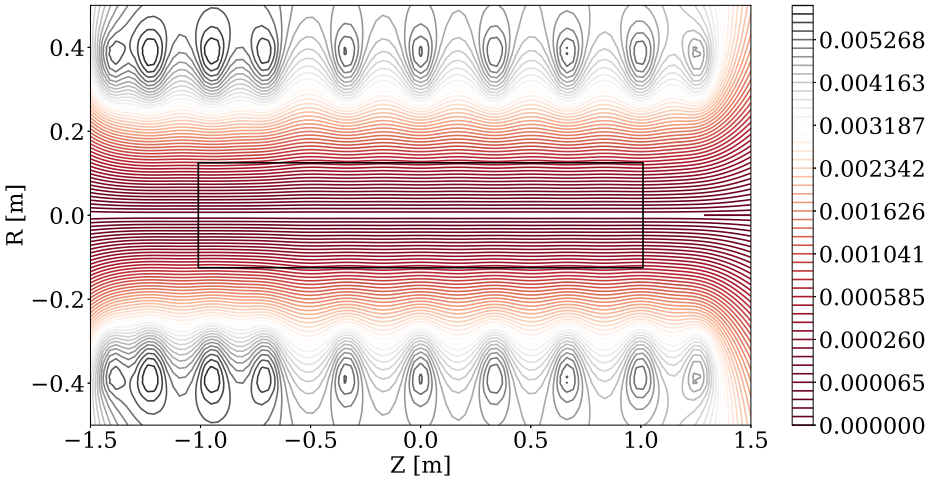


**Figure 3.12:** *Contour lines of the stream-function $\psi$ in $\left[\mathrm{T\,m^2}\right]$ for GyM standard coil configuration at* $600\,\mathrm{A}$. *The solid black lines mark the GyM vacuum vessel.*

plane of the ECR region in GyM for different values of the coil current or, equivalently, for different values of $B$. For the numerical and experimental activities reported in this Ph.D. Thesis, we will consider the magnetic field configuration corresponding to $600\,\mathrm{A}$, for which the ECR is located around a very narrow axial region. Additional resonances might be present in the machine, related to the upper-hybrid branch of the dispersion relation. Their location in the machine is, however, difficult to predict, since they depend on the local plasma density, which is not known a priori. For this reason, in this first work we neglect the presence of such additional resonances. Furthermore, direct measurements of the EC absorbed power are not available at present for the plasma of GyM. The experimental plasma parameters ($n$, $T_e$ and $\phi$) were obtained by means of a Langmuir probe (LP), located $\sim 30\,\mathrm{cm}$ in front of the $3.0\,\mathrm{kW}$ RF source, as shown in figure 3.11. The stainless steel probe tip is cylindrical ($1\mathrm{cm}$ length and $1.5\mathrm{mm}$ diameter) and it is mounted on a movable shaft so that its radial position can be varied to record the radial profile of plasma parameters. In addition to LPs, a high-resolution ($0.06\,\mathrm{nm}$) spectrometre (Horiba Jobin Yvon) for Optical Emission Spectroscopy (OES) is present in GyM for measuring the plasma radiation emitted in the $300 \div 900\,\mathrm{nm}$ wavelength range. The spectrometre consist of a Czerny-Turner monochromator (iH550) coupled to a CCD camera (Synapse) thermoelectrically cooled to $-70^\circ\,\mathrm{C}$. The entrance op-

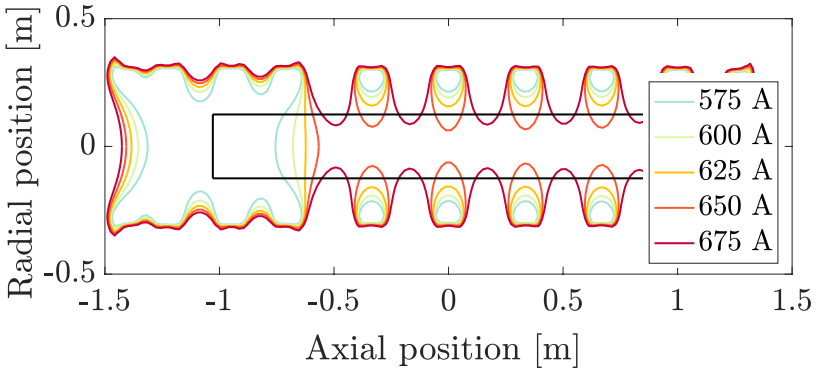


**Figure 3.13:** *ECR location for different values of B or, equivalently, current in the coils.*

tics consists of a focusing lens ($f = 7.5\,\mathrm{cm}$) and an optical fibre ($600\,\mu\mathrm{m}$ core diametre), The line of sight (LOS) intercepts the samples and it is perpendicular to the machine axis.

CHAPTER 4

# SOLPS-ITER simulations of fusion-relevant GyM Ar plasmas

THE aim of this Chapter is to illustrate the main modelling activities which have been performed with the edge plasma code SOLPS-ITER of the LPD GyM. In particular, in § 4.1 we discuss in great details the modelling of LPDs with the SOLPS code package. We first try to answer in § 4.1.1 to the question of how LPDs are seen by edge plasma codes. Next, in § 4.1.2 we deal with the important aspect of how the B2.5 equations (cfr. § 3.2.1) transform when account is make for the simplified structure of the magnetic field in LPDs. We present then in § 4.2 the modelling of Ar plasmas in the GyM LPD. The aim of the simulations are conveniently summarised in § 4.2.2. We next present in § 4.2.3 the main input that have been used for the simulations and illustrate in § 4.3 the corresponding results. It should be noted that, as already mentioned in the Introduction, the part of the results reported in this Chapter have been recently published in a peer-reviewed article [74].

## 4.1 Modelling Linear Plasma Devices with SOLPS

This introductory section aims to presents the (mostly) technical details which are necessary in order to perform LPDs plasmas simulations employing edge plasma codes. The latter, as clearly discussed in § 2.5.1, have been specifically developed in order to model edge plasmas in toroidally symmetric devices but have been nevertheless applied also for LPDs, as briefly discussed in § 2.6.1. In particular, Kastelewicz et al. [127] are the first that applied SOLPS4.0 to a linear geometry and they first showed the computational mesh for LPDs modelling. The same SOLPS version was used in [66] for predicting the main plasma parameters in MAGNUM-PSI. More recent works used SOLPS5.0 to simulate plasma transport in MAGPIE [63] and PROTO-MPEX [64, 78]. In particular, Rapp et al. [54] were the first to describe how to model radio-frequency heated LPDs with SOLPS. The SOLEDGE2D-EIRENE code was applied to PILOT-PSI to understand the effects of different atomic physics models [57]. Effects of pumping efficiency and radial transport coefficients were studied [58] and a quantitative analysis of the importance of transport and atomic processes, based on the two-point model [151], was performed.
Since the cylindrical geometry of LPDs is evidently different than that of tokamaks, the first questions that comes to mind is how are LPDs seen by edge codes. We believe that this discussion has not been addressed in satisfactory details. In addition to this, one also needs to understand how the geometrical simplifications of a linear geometry impact the B2.5 physical model (cfr. § 3.2.1), which again is an aspect not addressed in literature. We believe that this section will provide suitable help for future modeller in order to better understand how to perform LPDs modelling with edge codes.

### 4.1.1 How is a LPD seen by edge plasma codes?

The B2.5 equations are specifically tailored for tokamaks simulations and written in a curvilinear orthogonal coordinate system, as described in details in § 3.2.1. We recall, in particular, that one can use two different reference frames, the dynamical and the geometrical one, in order to properly describe plasma transport. The geometrical reference frame is particularly suited for two-dimensional edge modelling since, in this case, the rotational symmetry of tokamaks is manifest.
The application of SOLPS to LPDs is not straightforward due to the coordinate system implemented in the code. However, LPDs can be seen as zero-aspect ratio, infinite field pitch devices, that is devices in which the

ration $R/a \to 0$ and $B_x/B_z \to \infty$. If these conditions are met, then the one can interpret the geometrical frames coordinates as follows. The $\mathbf{g}_z$ basis vector in linear geometry is along the polar direction, which is the symmetry coordinate in LPDs. Thus, even for these devices the geometrical frame allows to reduce the systems of equations by one, exploiting the symmetry condition. The bi-dimensional problem is solved on the plane parallel to the cylinder axis. Specifically, the $x$-coordinate corresponds to the axial direction and the $y$-coordinate is in the radial direction. This coordinates interpretation just outlined is represented graphically in figure 4.1. The general transformation rules of a vector $\mathbf{v}$ from the dynamical frame to

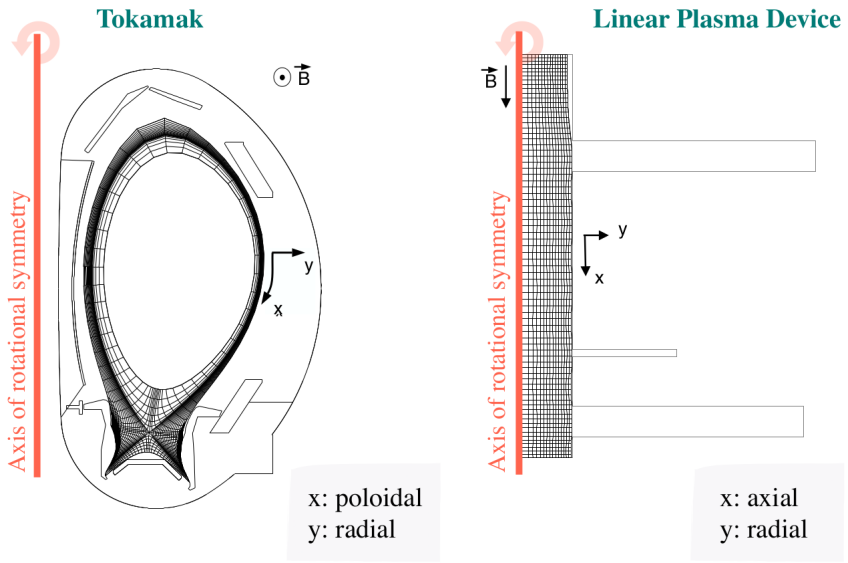


**Figure 4.1:** *Interpretation of the geometrical reference frame moving from a tokamak device to a LPD. In both case the $z$ coordinate is in the symmetry direction (toroidal for tokamaks and azimuthal for LPD) and can thus be ignored.*

the geometrical one (cfr. § 3.2.1) for a linear plasma device reduce to:

$$v_x = b_x v_{\parallel} \qquad v_z = -b_x v_{\perp} \tag{4.1}$$

where $b_x = B_x/B$, and we used the fact that the polar component of the magnetic field, $b_z = B_z/B$, vanishes in a LPD. As we shall see in the forthcoming Section, this eliminates several terms in SOLPS-ITER equations, mainly related to the possibility to investigate drifts.

### 4.1.2 B2.5 equations for Ar plasmas in linear geometries

The simplified geometry and structure of the magnetic field typical of a LPD leads to important simplification to the equations implemented in B2.5 and reviewed in § 3.2.1, which we shall now consider in details. As stated in, we are interested in the modelling of non-hydrogenic plasmas. The B2.5 equations have been, however, derived aiming to simulate hydrogen-dominated plasmas, in which heavier species such as Ar are treated as impurities, so that in principle the application of the B2.5 equations for our simulations is not straightforward. However, the latest version of SOLPS-ITER physics model uses the Zhdanov formulation [160] for the transport coefficients. The resulting equations can be used also in the case of non hydrogen-dominated plasmas, provided that only a single ion charge state is considered. Thus, in the remaining of this section, we shall derive the B2.5 equation in linear geometry and assuming that the plasma is composed by the electron population, a single-charged ion population $\mathrm{Ar}^+$ and the Ar neutral population. In this case, starting from the ion continuity equation and setting $b_z = 0$ one obtains

$$\partial_t n + \frac{1}{\sqrt{g}}\partial_x\left(\frac{\sqrt{g}}{h_x} n b_x v_\parallel\right) + \frac{1}{\sqrt{g}}\partial_y\left(\frac{\sqrt{g}}{h_y} n v_y\right) = S^n_{n,i} \tag{4.2}$$

where the source term $S^n_{n,i}$ is due to ionisation, recombination and charge exchange reactions with neutral atoms or molecules, tracked by Eirene in the SOLPS coupled mode. The radial component of the velocity $v_y$ reduces to:

$$v_y = -D^{\mathrm{an}}_n \frac{1}{h_y n}\partial_y n - D^{\mathrm{an}}_p \frac{1}{n h_y}\partial_y p_i \tag{4.3}$$

In principle, in equation (4.3) one should also consider the presence of viscosity and ion-neutral driven currents, since the latter do not vanish for linear geometries. However, when simulating non-hydrogenic plasmas a choice is made in SOLPS to complete assign currents to the electron population. Their corresponding velocities in the parallel and radial direction can be computes as $v_\parallel = j_\parallel / (en)\,, v_y = j_y / (en)$, respectively. See below, equations (4.14) and (4.15), for the definition of the current components. The electron density is obtained from quasi-neutrality, i.e. in our case is equal to the $\mathrm{Ar}^+$ density everywhere.
The parallel ion velocity, $v_\parallel$, is obtained by solving the parallel ion momentum equation. For the simulations performed in this work, it is given

by:

$$
\begin{aligned}
&m_i\left[\partial_t\left(nv_\parallel\right)+\frac{1}{h_z\sqrt{g}}\partial_x\left(\frac{\sqrt{g}h_z}{h_x}nb_xv_\parallel^2\right)+\frac{1}{h_z\sqrt{g}}\partial_y\left(\frac{\sqrt{g}h_z}{h_y}nv_\parallel v_y\right)\right]=\\
&=-\frac{b_x}{h_x}en\partial_x\phi-\frac{b_x}{h_x}\partial_x\left(nT_i\right)+\frac{1}{h_z\sqrt{g}}\partial_x\left(\frac{\sqrt{g}h_z}{h_x^2}\eta_{ix}\partial_xv_\parallel\right)+\\
&+\frac{1}{h_z\sqrt{g}}\partial_y\left(\frac{\sqrt{g}h_z}{h_y^2}\eta_{iy}\partial_yv_\parallel\right)+S^m_{n,i}+S^m_{\mathrm{fr}_{ie}}+S^m_{\mathrm{therm}_{ie}}
\end{aligned}
\tag{4.4}
$$

where $\eta_{ix}$ and $\eta_{iy}$ are the axial and radial ion viscosity coefficients, respectively. Here, $\eta_{ix}=\eta^{an}+\eta^{cl}$ and $\eta_{iy}=\eta^{an}$, where $\eta^{cl}$ is the Zhdanov classical viscosity coefficient [160] while the anomalous contribution is related to the anomalous diffusion coefficient $D_n^{\mathrm{an}}$ according to $\eta^{an}=m_inD_n^{\mathrm{an}}$ . $S^m_{n,i}$ represents the momentum source due to ion-neutral friction computed by EIRENE, $S^m_{\mathrm{fr}_{ie}}$ is the electron-ion friction force and $S^m_{\mathrm{therm}_{ie}}$ is the electron-ion thermal force, whose expressions are reported in [43].
The energy balance equation for the electron is:

$$
\begin{aligned}
&\frac{3}{2}\partial_t\left(nT_e\right)+\frac{1}{\sqrt{g}}\partial_x\left(\frac{\sqrt{g}}{h_x}\tilde{q}_{ex}\right)+\frac{1}{\sqrt{g}}\partial_y\left(\frac{\sqrt{g}}{h_y}\tilde{q}_{ey}\right)+\\
&+\frac{nT_e}{\sqrt{g}}\partial_x\left(\frac{\sqrt{g}}{h_x}b_x\left(v_\parallel-\frac{j_\parallel}{en}\right)\right)=\\
&=Q_\Delta+Q_{\mathrm{fr,therm}}+Q_{n,e}+Q_R
\end{aligned}
\tag{4.5}
$$

where

$$
\tilde{q}_{ex}=\frac{3}{2}nT_eb_x\left(v_\parallel-\frac{j_\parallel}{en}\right)-\kappa_{e\parallel}\frac{b_x^2}{h_x}\partial_xT_e \tag{4.6}
$$

and

$$
\tilde{q}_{ey}=\frac{5}{2}nT_e\left(-D_n^{\mathrm{an}}\frac{1}{nh_y}\partial_yn-D_p^{\mathrm{an}}\frac{1}{nh_y}\partial_yp_i\right)-\kappa_{e\perp}\frac{1}{h_y}\partial_yT_e \tag{4.7}
$$

Here $\kappa_{e\parallel}$ and $\kappa_{e\perp}=\chi_e^{\mathrm{an}}n$ are respectively the Zhdanov thermal conductivity [160] and the anomalous one for electrons. The electron energy sources on RHS of equation (4.5) are:

- the electron-ion energy equipartition, $Q_\Delta$:

$$
Q_\Delta=\nu_{ei}\left(T_e-T_i\right) \tag{4.8}
$$

  where $\nu_{ei}$ is the electron-ion collision frequency.

- the heat source from electron-ion friction and thermal forces, which is proportional to the electron velocity:

$$Q_{\mathrm{fr,therm}} = \left(S^m_{\mathrm{fr}_{ie}} + S^m_{\mathrm{therm}_{ie}}\right)\left(\frac{j_\parallel}{en} - v_\parallel\right) \tag{4.9}$$

- $Q_{n,e}$ and $Q_R$ are the electron energy sources due to interactions of electrons with neutral Ar atoms and $\mathrm{Ar}^+$ ions, respectively.

Analogously, the ion energy equation can be written as:

$$\begin{aligned}\frac{3}{2}\partial_t\left(nT_i\right) + \frac{1}{\sqrt{g}}\partial_x\left(\frac{\sqrt{g}}{h_x}\tilde{q}_{ix}\right) + \frac{1}{\sqrt{g}}\partial_y\left(\frac{\sqrt{g}}{h_y}\tilde{q}_{iy}\right) + \\ + \frac{nT_i}{\sqrt{g}}\partial_x\left(\frac{\sqrt{g}}{h_x}b_x v_\parallel\right) = Q_\Delta + Q_{n,i} \\ + \eta_{ix}\left(\frac{\partial_x v_\parallel}{h_x}\right)^2 + \eta_{iy}\left(\frac{\partial_y v_\parallel}{h_y}\right)^2\end{aligned} \tag{4.10}$$

The ion energy fluxes, $\tilde{q}_{ix}$ and $\tilde{q}_{iy}$, are given by:

$$\tilde{q}_{ix} = \frac{3}{2}nT_i b_x v_\parallel - \kappa_{i\parallel}\frac{b_x^2}{h_x}\partial_x T_i \tag{4.11}$$

and

$$\tilde{q}_{iy} = \frac{5}{2}nT_i\left(-D_n^{\mathrm{an}}\frac{1}{nh_y}\partial_y n - D_p^{\mathrm{an}}\frac{1}{nh_y}\partial_y p_i\right) - \kappa_{i\perp}\frac{1}{h_y}\partial_y T_i \tag{4.12}$$

where $\kappa_{i\parallel}$ and $\kappa_{i\perp} = \chi_i^{\mathrm{an}} n$ are respectively the classical thermal conductivity and the anomalous one for $Ar^+$ ions. The electrostatic potential $\phi$ can be derived from the current continuity equation. In the $(x, y, z)$ coordinate system it is given by:

$$\frac{1}{\sqrt{g}}\partial_x\left(\frac{\sqrt{g}}{h_x}b_x j_\parallel\right) + \frac{1}{\sqrt{g}}\partial_y\left(\frac{\sqrt{g}}{h_y}j_y\right) = 0 \tag{4.13}$$

The parallel component of the current density, $j_\parallel$, can be obtained from the electron momentum equation (generalised Ohm's law) and it is given by:

$$j_\parallel = \sigma_\parallel\left[\frac{b_x}{e}\frac{1}{n}\frac{1}{h_x}\partial_x\left(nT_e\right) - \frac{b_x}{h_x}\partial_x\phi\right] - \alpha_{ex}\frac{1}{h_x}\partial_x T_e \tag{4.14}$$

where the parallel electrical conductivity $\sigma_\parallel$ and the classical thermo-electric coefficient $\alpha_{ex}$ are expressed according to Zhdanov formulation [160].

The radial component of the current density, $j_y$, accounts only for the anomalous current, $j_y^{\mathrm{an}}$, which reads

$$j_y = j_y^{\mathrm{an}} = -\sigma^{\mathrm{an}} \frac{1}{h_y} \partial_y \phi \tag{4.15}$$

and $\sigma_{\mathrm{an}} = k_{\mathrm{an}} e n$ is the anomalous conductivity. Non vanishing $\sigma_{\mathrm{an}}$ is needed to provide convergence of the numerical scheme, as reported in [102]. For the simulations reported here, $k_{\mathrm{an}}$ was set to $1 \times 10^{-6}$.

## 4.2 Simulation of Ar plasmas in GyM

In this Section, we outline the main objectives related to the SOLPS-ITER simulations of Ar plasmas in GyM. Before doing so, we first start in § 4.2.1 by addressing the applicability of the B2.5 fluid equations for modelling plasmas with parameters typical of the GyM device. Next, in § 4.2.2 by outlining the main simulations parameters that were chosen in order to perform sensitivity scans on code free parameters. The following section (§ 4.2.3) aims to describe the main input parameters that have been used for all the simulations presented in this Chapter.

### 4.2.1 Applicability of the B2.5 equations for modelling GyM plasmas

Before starting with the presentation of the main objectives of the SOLPS-ITER numerical simulations of the GyM device, we discuss here in some details the applicability limits associated to the fluid modelling of plasmas with parameters akin to those produced in the GyM device. Indeed, as we reported in § 3.4.3, typical GyM plasmas are characterised by relatively low densities, typically in the range of $10^{16 \div 17}\,\mathrm{m}^{-3}$. Recalling the discussion that we reported in § 2.5.1 (see also Appendix A), modelling of plasmas by means of fluid equations usually require the mean0free paths for Coulomb collisions to be much smaller than a characteristic *parallel* dimension, as reported in details in Appendix A. This parallel dimension can convincingly be taken as the overall length of the device. Thus, for the modelling of GyM plasmas via fluid equations we need to check that:

$$\lambda \ll L_{\parallel} \tag{4.16}$$

This inequality condition should be further elaborated, since we need to distinguish between the electron and ion populations. Thus, instead of (4.16), we need to verify that:

$$\lambda_{ee}, \lambda_{ii} \ll L_{\parallel} \tag{4.17}$$

where $\lambda_{ee}, \lambda_{ii}$ denote the electron-electron and ion-ion collisional mean-free paths, whose expression can be found e.g. [121]. Thus, using the typical plasma parameters value that we reported in table 3.1, it is not difficult to show that: $\lambda_{ee} \simeq 7\,\mathrm{m}$, $\lambda_{ii} \simeq 1 \times 10^{-3}\,\mathrm{m}$. From this expression, one sees that plasma modelling by means of fluid equations is, in principle, not valid for GyM typical plasmas, since fluid models are derived assuming high-collisionality. One should note that the same can be true also in tokamaks: the collisionality in the SOL is often not high enough to justify a fluid approach (see Appendix A). In general, the problem of the limit of applicability of the fluid model is of great interest, also considering that the alternative complete kinetic approach is in most cases not applicable to describe typical boundary plasmas, due to extreme computational cost. In addition, in his fundamental work [151] showed that the fluid results often remain close to the kinetically retrieved results for the important lower order moments. In SOLPS-ITER, kinetic corrections to the fluid approximation are taken into account by applying the so-called "flux limits" to the parallel fluxes, as reported in A. In all the simulations presented in this chapter, the numerical factors that appear in the flux-limited transport coefficients (see e.g. (A.4) and (A.6)) were set to quite standard values: ion and electron flux limits $\alpha_{e,i}$= 0.15, viscosity, thermo-electric coefficient and friction force flux limit $\alpha = 0.5$.

### 4.2.2 Sensitivity scans

SOLPS contains several free parameters that accounts for physical phenomena that cannot be, at present, simulated self-consistently by the code. Among these, undoubtedly the most important ones are the radial diffusion coefficients, which are introduced in SOLPS (as well as other mean field fluid plasma code) to account for anomalous transport in a simplified (diffusive) manner (cfr. the discussion). The value for these quantities are usually set in order to fit experimental data at a given location in the 2D cross-section of the simulated device. For example, in tokamak this location is take to be the outer midplane. It is of interest to understand what is the impact of these free parameters on the simulation outputs, by performing suitable sensitivity scans. In the case of the GyM LPD, also the overall absorbed electron power delivered by the RF source (cfr. § 3.4.3) is not known a priori. In addition to this, we analysed the impact of changing the pumping efficiency in the numerical simulations. Pumping of neutral particles is accounted for by prescribing in Eirene an absorption probability for neutrals on given pumping surfaces. The latter $p_a$, or *albedo* of

the surface, is related to the particle recycling coefficient RECYCT by $p_a = (1 - \mathrm{RECYCT})$ [128].
In the first sensitivity scan reported in this Ph.D. manuscript, we considered variations in the radial diffusion coefficients, overall absorbed electron heat power and pumping efficiency, as reported in table 4.1. The main aim

| Case | $D_n, D_p$ $[\mathrm{m^{-2}s^{-1}}]$ | $\chi_e, \chi_i$ $[\mathrm{m^{-2}s^{-1}}]$ | $P^{\mathrm{ext}}$ [W] | RECYCT |
|---|---|---|---|---|
| $(a)$ | 1.5 | 1.5 | 800 | 0.985 |
| $(b)$ | 1.5 | 1.5 | 800 | 0.970 |
| $(c)$ | 1.5 | 1.5 | 800 | 0.990 |
| $(d)$ | 0.5 | 1.5 | 800 | 0.985 |
| $(e)$ | 2.5 | 1.5 | 800 | 0.985 |
| $(f)$ | 1.5 | 1.5 | 2400 | 0.985 |

**Table 4.1:** *Radial transport coefficients, overall absorbed electron power and absorption probability considered in the first sensitivity scan.*

of this sensitivity scan consisted in getting a general understanding of the SOLPS-ITER code behaviour when modelling of Ar plasmas is performed. Indeed, it is worth recalling that this code versione has never been applied before for the modelling of non-hydrogenic plasmas.
Starting from the sensitivity scan reported in table 4.1, we next expanded the simulation database by focusing on the variation of the radial particle diffusion coefficients (i.e. $D_{n,p}$) and the absorbed power (i.e. $P^{\mathrm{ext}}$), by keeping fixed the absorption probability. For each of these two quantities, we considered 5 and 6 different values, obtaining a total of 30 different SOLPS simulations. The main input parameters are listed in table 4.2. These additional simulations were performed with the main aim to

| $P^{\mathrm{ext}}$ | 20% | 40% | 60% | 80% | 100% | |
|---|---|---|---|---|---|---|
| $D_{n,p}$ $[\mathrm{m^2s^{-1}}]$ | 0.25 | 0.5 | 1.0 | 1.5 | 2.0 | 2.5 |

**Table 4.2:** *Radial transport coefficients and overall absorbed electron power considered in this second sensitivity scan. The absorbed electron heat power has been normalized to the overall power deliverable by the RF source in GyM, that is* 3 kW.

construct a small database starting from which a Neural Network can be trained. Indeed, the large amount of free parameters in edge plasma code would require to perform a separate simulation to understand the impact related to the variation of each one of them. It is, however, also clear that this

would require a lot of computational power, particularly in B2.5+Eirene coupled simulations, where the Monte Carlo tracking of neutrals histories can be computationally demanding.

### 4.2.3 Main inputs

The most basic inputs of SOLPS-ITER are the two computational grids, one for B2.5 and one for Eirene. From the discussion made in § 3.2.3, we recall that the B2.5 works with a structured curvilinear quasi-orthogonal mesh. This is made of quadrilateral cells with two sides parallel to the magnetic flux surfaces and two in the radial direction. Instead, Eirene uses an unstructured grid made of triangles which covers the whole cross-section of the machine, including secondary ducts outside the cylindrical chamber.
In tokamaks simulations, the Carre code (cfr. § 3.2.3) is used for the construction of the field-aligned B2.5 grid. However, this code cannot be applied in a straightforward manner for LPDs and, for this reason, a dedicated Python code have been development. The details are reported in Appendix C. Here, we shall limit ourselves to brief considerations. The basic idea consists in solving the Grad-Shafranov equation [121] for the stream function $\psi$ considering only currents flowing in external coils, since currents coming from the plasma itself can be neglected in LPD. Once $\psi$ is known, one can then use its contour lines to build a field aligned grid. The so-obtained mesh is shown in orange lines in figure 4.2. As mentioned

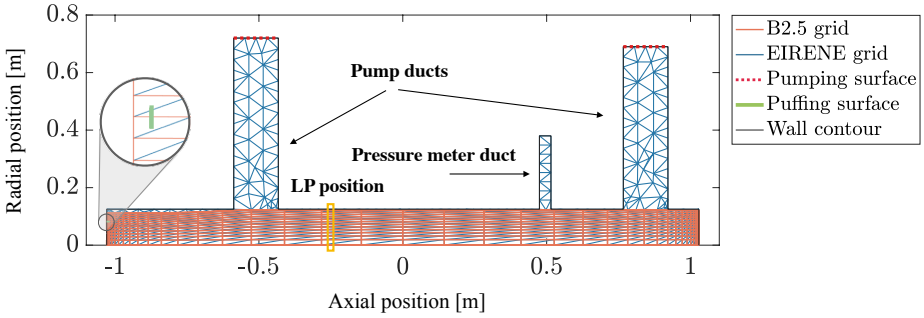


**Figure 4.2:** *GyM computational grids for B2.5-EIRENE simulations. The EIRENE grid covers also the whole 2D cross-section of the device, including the pumps and the pressure meter ducts. The pumping surfaces are shown in dotted red and the puffing surface in green, in correspondence of the west target.*

in 3.2.3, the B2.5 grid is radially limited to a certain outermost surface of constant magnetic flux and cannot intersect the vessel walls at any locations

other then the two basis of the cylinder. It is common to refer to this outer radial boundary as the north boundary of the mesh.
For the construction of the Eirene grid, instead, the code Triang can be used straightforwardly also for LPDs. One has only to define the structure of the vacuum vessel. For the simulations reported here, the latter includes a simplified cross-section of the GyM machine (cfr. § 3.4.3) the pump and the pressure meter ducts, as shown by blue lines in figure 4.2. In principle, in Eirene is possible to implement a full 3D mesh to take into account geometry asymmetries, however here for simplicity we assume azimuthal symmetry around the $x$-coordinate. In this way, the volume of the ducts departing from the main cylindrical chamber is bigger than the real physical volume. In figure 4.2, we also show the pumping and puffing surfaces.
Finally, the puffing surface, which in the experimental setup is on one of the two targets (cylinder basis), is inside the west boundary of the plasma grid and required some care to be implemented in the code. A dedicated transparent surface was included in Eirene grid (shown in green in the inset in figure 4.2), from which we prescribed the puffing strength.
Radial transport is largely dominated by turbulence, which cannot be modelled self-consistently in SOLPS (cfr. § 2.5.1). For this reason, a diffusive ansatz for the turbulent flux is usually adopted, where the values of the diffusion coefficients are treated as free parameters and are adjusted to match experimentally measured plasma profiles.
The power delivered by the RF source was modelled as an additional, user-prescribed, term in the electron energy equation. A precise description of the overall power delivered to the plasma as well as the knowledge of the spatial distribution of the power density require a dedicated study, and it is beyond the scope of the present article. In this contribution, we assume that the power density is constant in the radial direction and Gaussian distributed in the axial direction, that is:

$$S_e^{\text{ext}} = P^{\text{ext}} \exp\left[-\frac{(z - z_{\text{res}})^2}{\sigma^2}\right] \tag{4.18}$$

The mean value, $z_{\text{res}}$, of the Gaussian is fixed at the theoretical resonance location and the variance, $\sigma^2$, is fixed to $0.1\,\text{m}$. The overall power delivered by the source and actually absorbed by the electron population, $P^{\text{ext}}$, is treated as a free parameter, since it is not currently experimentally measured.
As regards the boundary conditions, at the two targets location, standard Bohm sheath conditions were set. On the axis of symmetry (i.e. the machine axis), we assumed vanishing fluxes of all the plasma parameters. Fi-

nally, at the north boundary of the B2.5 simulation domain we imposed a prescribed value for the decay lengths of the plasma parameters: $\lambda_{n_e} = 0.05\,\mathrm{m}, \lambda_{T_e} = 0.05\,\mathrm{m}, \lambda_{\phi} = 0.1\,\mathrm{m}$ and $\lambda_{T_i} = 0.1\,\mathrm{m}$ for the electron density, electron temperature, plasma potential and ion temperature. For the momentum equation, we assumed instead a vanishing value for the parallel momentum flux.
For all the simulations that we performed, the following set of Ar reactions were included:

$$e^- + \mathrm{Ar} \rightarrow \mathrm{Ar}^+ + 2e^-$$
$$e^- + \mathrm{Ar}^+ \rightarrow \mathrm{Ar}$$

Elastic scattering between Ar and $\mathrm{Ar}^+$ was not considered in this work, since the corresponding reaction rates are not included in the available EIRENE databases. All the remaining charge states, from $\mathrm{Ar}^{2+}$ to $\mathrm{Ar}^{18+}$, were also neglected. Indeed, the electron temperature in GyM is rather low (below $8\,\mathrm{eV}$). This, in combination with the low electron density (below $10^{17}\,\mathrm{m}^{-3}$), leads to a low probability for the ionisation of the higher Ar charge states. The validity of this assumption was also checked with a dedicated simulation where the $\mathrm{Ar}^{2+}$ was included, using the same input as for case $a)$ of table 4.1, observing that the ratio $n_{\mathrm{Ar}^{2+}}/n_{\mathrm{Ar}^{+}} \sim 0.1$.

## 4.3 Results and discussion

In this Section, the main results of the SOLPS-ITER simulations will be presented. We start in § 4.3.1 by outlining the results of the sensitivity scan, whose main input parameters are summarised in table 4.1. On the basis of the main qualitative features here reported, we consider next (cfr. § 4.3.2) the quantitative interpretation of the sensitivity scan, by outlining the most relevant contribution in the conservation equations solved by SOLPS-ITER. A first comparison with experimentally available results is then performed in § 4.3.3, showing a good agreement with simulations results. We close this Chapter (cfr. § 4.3.5) by illustrating the preliminary activity related to the construction of a Neural Network for the prection of radial profiles of plasma quantities, such as the electron density and temperature.

### 4.3.1 B2.5-Eirene coupled simulations - sensitivity scan

An analysis of the effects of the absorbed electron power, transport coefficients and pumping efficiency was performed using the B2.5-EIRENE

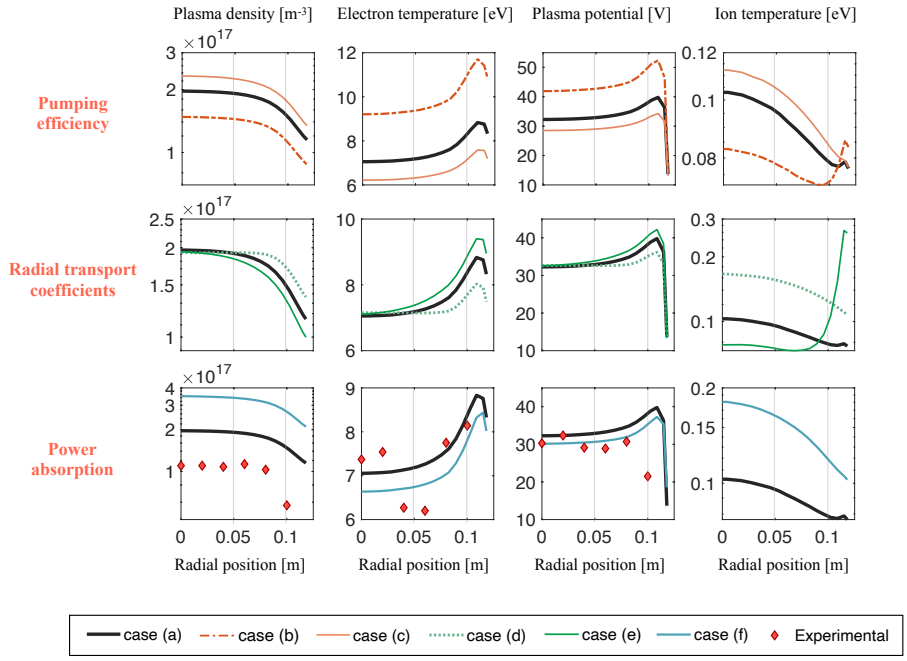


**Figure 4.3:** *Effects of the neutral pumping efficiency (top), radial transport coefficients (middle) and absorbed power (bottom) on the simulated radial profiles of the electron density, electron and ion temperature, and plasma potential. Different colors and line styles correspond to the the different cases in 4.1. The profiles extend from the machine axis ($y = 0$) to the lateral side of the cylinder ($y = 0,125\,\mathrm{m}$). The axial position at which radial profiles are taken correspond to that of the LP (see figure 4.2).*

coupled version of the code. Simulated radial profiles of $n$, $T_e$, $\phi$ and $T_i$ at the axial position of the Langmuir Probe are shown in figure 4.3. The details of the simulations are reported in table 4.1. Case $a$) is the reference one. $b$) and $c$)(orange curves in figure 4.3) show the effect of a lower and higher RECYCT, respectively. Cases $d$) and $e$) (green curves in figure 4.3) do the same for the particle diffusion coefficients, $D_n^{\mathrm{an}}$ and $D_p^{\mathrm{an}}$.
First of all, it can be noted that for all our simulations radial profiles show a rather similar behaviour. The electron density is a monotonic function of the radial position, peaked at the machine axis and slowly decreasing towards the vessel chamber. Electron temperature and plasma potential share a similar profile: they peak near the vessel boundary, where the $n$ is lower. The $T_e$ profile resulting from the simulations is seen to be strictly influenced by the electron power distribution given as input [63]. In our case,

the source is a RF magnetron and the heating mechanism is by electron cyclotron resonance. We guessed a power density, which is radially constant with a Gaussian profile along the axis. This allows to obtain the SOLPS radial $T_e$ profiles of figure 4.3 which increase along $R$. To demonstrate that the power density given as input to the code primarily determines the $T_e$ profile, simulations with a different modelling of the source were carried out. We found that, for a radially Gaussian peaked at the cylinder axis, the $T_e$ profile monotonically decreases with $R$. The similarity between $T_e$ and $\phi$ profiles can be understood by considering that, under radial ambipolarity conditions, $j_y = 0$, the following expression can be obtained for Ar plasmas $\phi(r) = 4.6\, k_b T_e(r)/e$ [151]. This relationship has indeed be checked for the simulated profiles, showing that the $\sigma_{an}$ is low enough not to influence the final simulation result.

Cases $a), b)$ and $c)$ were performed changing only the value of the recycling coefficients of the pumping surfaces. It can be noted that this parameter has a great impact on the simulated radial profiles. For the lowest value, case $b)$, of the recycling coefficient (that is, when the neutrals absorption probability is the highest) $n$ reduces significantly, while $T_e$ and $\phi$ increase, with respect to case $a)$. This can be reasonably understood as due to the fact that the amount of power delivered is equal for all the three cases, but the neutrals in the system is lower in case $b)$ and highest in case $c)$. For case $c)$, thus, the energy absorbed by the electrons due to the external RF source is quickly lost by ionisation of neutrals, whose density is higher for case $c)$. As a consequence of the increased electron density, one can notice that the ion temperature also slightly increases for case $c)$. Since ions are not directly heated by the RF source, their only relevant energy source comes from electron-ion collisions (energy equipartition), whose frequency scales proportionally to the plasma density.

In cases $a), d)$ and $e)$ only the radial diffusion coefficients where varied. $D_n^{\mathrm{an}}$ and $D_p^{\mathrm{an}}$ were varied simultaneously, so that the overall effect of radial particle diffusion is taken into account. Comparing the black and green lines in figure 4.3, one can notice that the greatest impact of this parameter is on the shape of the simulated radial profiles, while the values of electron density, temperature and plasma potential at the axis are left unchanged. In particular, $n$ is almost flat up to larger radial positions when the radial transport coefficients are lower - case $d)$, and $T_e$ and $\phi$ maxima reach lower values. For higher diffusion coefficients - case $e)$, the opposite trend is obtained, consistently with the fact that a larger number of particles is removed radially.

Cases $a)$ and $f)$ show the effect on the plasma solutions of an increased

power absorbed by the electron population. One can notice that, as a consequence of external power variations, the strongest impact is on the electron density, while the electron temperature and plasma potential are almost unchanged. A rise in the plasma density as a consequence of an increased ECR heating power can be understood as due to the fact that, with a fixed amount of neutrals in the system, the excess in the electron energy is efficiently dissipated in collisions with $\mathrm{Ar}$ atoms leading to their ionisation. This is consistent since the overall degree of ionisation in the GyM plasma is rather low.

### 4.3.2 B2.5-Eirene coupled simulations - two-point analysis

To provide additional physical insight to the sensitivity scan reported in the previous section, here we present a two-point analysis based on the SOLPS-ITER equations [58, 151]. Here, we integrate the steady state density and electron temperature conservation equations along the axial direction for each flux tube, that is the volume between to adjacent flux surfaces. In this way, we obtain an equality between the difference of upstream (west target, $u$) and downstream (east target, $d$) fluxes and all the remaining terms, which are treated as sources. Applying these ideas to equation (4.2) we obtain:

$$\begin{aligned} \mathrm{d}A_{\perp}\Gamma_x|_u^d = &- \int_u^d \frac{1}{\sqrt{g}}\partial_y\left(\frac{\sqrt{g}}{h_y}nv_y\right)\sqrt{g}\mathrm{d}x\mathrm{d}y + \\ &+ \int_u^d S^n_{n,i}\sqrt{g}\mathrm{d}x\mathrm{d}y \end{aligned} \tag{4.19}$$

where $\mathrm{d}A_{\perp} = h_y h_z \mathrm{d}y$ is the perpendicular cross-sectional area of the flux tube, and $\Gamma_x = b_x n v_x$. This procedure is performed for each flux tube and the resulting contribution are summed over, to obtain the total particle balance. The same is done also for the electron energy.
The graph on top of figure 4.4 shows with different colors each contribution on the right-hand side of equation (4.19), while the bottom graph represents the corresponding analysis for the electron energy balance, starting from equation (4.5).
From the density analysis, it can be noted that the strongest (positive) source term in the continuity equation is represented by the electron ionisation of neutral $\mathrm{Ar}$ atoms in $\mathrm{Ar}^+$. Moreover, we can see that ionisation is stronly influenced by the external power absorbed by electrons: this source term (shown in light blue in the top part of figure 4.4) is almost constant for cases $a) - e)$, where the external ECR power is fixed at $800\,\mathrm{W}$, and it increases significantly for case $f)$, where the external power is increased

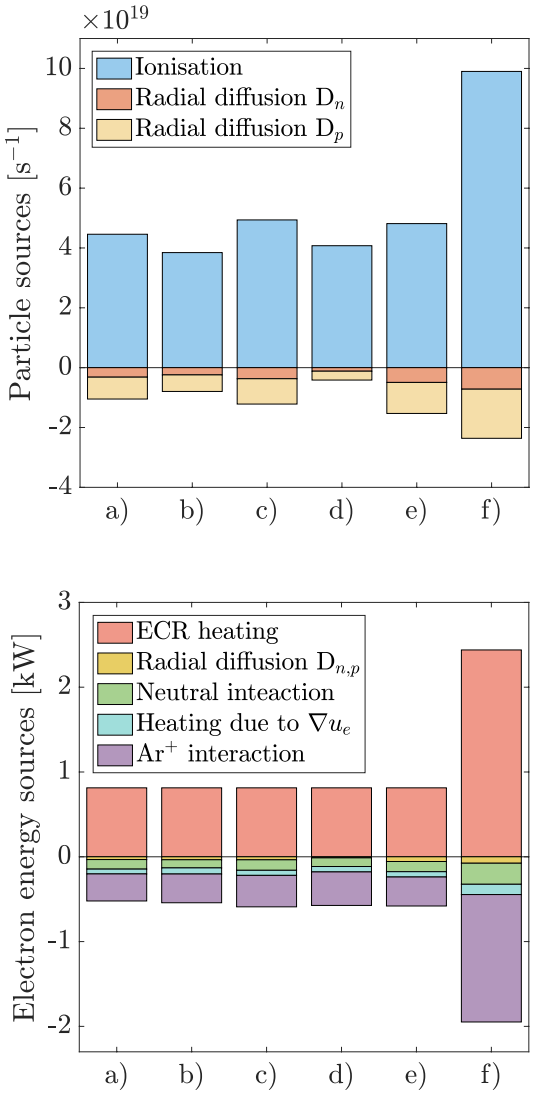


**Figure 4.4:** *Particle (top) and electron energy (bottom) source terms for the cases reported in table 4.1. The* $\mathrm{Ar}^+$ *interaction term in the graph at the bottom is an effective ion recombination rate.*

to $2400\,\mathrm{W}$. Density and pressure-driven diffusions act instead as negative source terms. Recombination has not been reported since negligible in all simulations. Cases $a)$ - $e)$ show almost the same overall balance between

ionisation and radial transport. Other slight differences that can be noted in the trends of figure 4.4 may be explained with reference to table 4.1. For example, lower and higher radial transport contribution shown in case $d)$ and $e)$ respectively, is consistent with the imposed values of $D_n^{\mathrm{an}}$ and $D_p^{\mathrm{an}}$, also if compared to the reference case $a)$. On the other hand, case $c)$ shows higher ionisation, since more neutral atoms are present in the system to be ionised, due to lower pumping efficiency.
Similar considerations apply also for the electron energy balance, shown in figure 4.4 at the bottom. The strongest interactions for cases $a) - c)$ occurs with the neutral $\mathrm{Ar}$ atoms, while the remaining contributions play only a minor role. Specifically, cases $a) - e)$ show a rather similar energy balance. Case $f)$, where only the absorbed electron power was increased, is characterised by a strong boost in the the $\mathrm{Ar}^+$ interaction term. This quantity includes all the electronic excitation of $\mathrm{Ar}^+$ which ultimately leads to radiative losses and the ionisation of $\mathrm{Ar}^+$ atoms to higher ionisation states, which was not included in the model.

### 4.3.3 B2.5-Eirene coupled simulations - comparison with experimental results

A first comparison with experimentally available measured radial profiles of the electron density, temperature and plasma potential was performed, in order to test the capability of the code to reproduce both qualitatively and quantitatively the experimental data. The experimental data were taken with the following GyM configuration: $i)$ coil currents fixed to $600\,\mathrm{A}$; $ii)$ gas puff intensity of $1\,\mathrm{sccm}$ of $\mathrm{Ar}$; $iii)$ RF power $1800\,\mathrm{W}$. For all the considered cases, $n$, $T_e$ and $\phi$ are in the range of the experimental parameters of table 3.1. In all the simulations presented, the ion temperature is always below $0.2\,\mathrm{eV}$, which is consistent with the fact that only the electrons are heated by the external power source and the low $n$, does not allow for an efficient energy equipartition. The comparison of the experimental points to the simulated radial profiles is shown in the bottom graph of figure 4.3. One can notice a good qualitative agreement between measurements and simulations. Firstly, the monotonic decreasing shape of the density profile is well captured. The simulated plasma potential slightly overestimates the increasing behaviour near the radial boundary with respect to the experimental profile. Finally, the behaviour of the experimental electron temperature is well captured by the simulations at the center and at the border of the machine, while the experimental dip around $r \simeq 0.05\,\mathrm{m}$ is not properly reproduced. A possible explanation for this is related to the lack of a

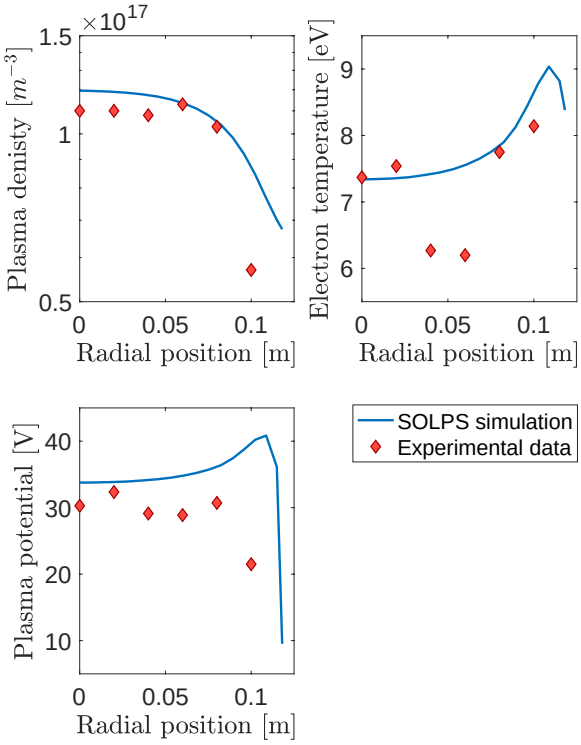


**Figure 4.5:** *Radial profiles of the electron density, temperature and plasma potential, using the same input of case a) but with the absorbed power reduced to* 400 W.

detailed modelling for the ECR source, which leads to the assumption of a radially constant absorption profile. A more detailed experimental campaign is planned, using a smaller spherical LP (2.5 mm radius) to enlarge the set of available experimental data both radially and axially. Moreover, a better investigation of the experimental uncertainty is needed, but from a first estimate values $\sim 1\,\mathrm{eV}$ are consistent with the experimental technique used. Finally, dedicated studies on the RF wave propagation and absorption into the plasma should be considered.

Considering the bottom-left graph in figure 4.3, quantitative discrepancy is seen in the electron density up to a factor of 2, while the values of electron temperature and plasma potential are quite well captured. To better reproduce the density value at the axis, according to the results of the analysis reported in the previous section, we performed an additional simulation with the same parameters as for case $a$) of table 4.1, but we reduced the absorbed electron power to 400 W. Radial profiles of the electron density,

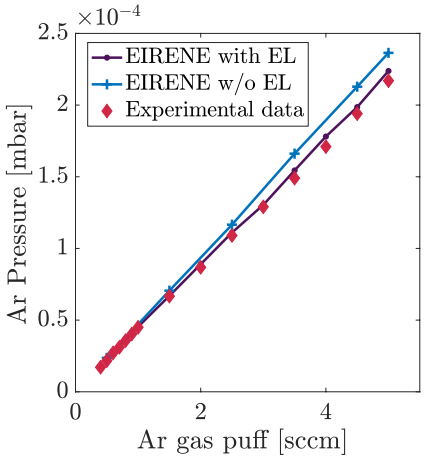


**Figure 4.6:** *Neutral pressure at the gauge location for different values of the* Ar *puffing strength.*

temperature and plasma potential are shown in figure 4.5 and compared with experimental data. Here a satisfactory quantitative agreement between all simulated plasma quantities is clear. However, these good results concerning plasma quantities are obtained at the expenses of a factor $\sim 20$ discrepancy on the neutral pressure. Indeed, from the code we obtained a neutral pressure of $p_n = 2.78 \times 10^{-6}\,\mathrm{mbar}$, which strongly underestimates the experimental value of $p_{exp} = 54.6 \times 10^{-6}\,\mathrm{mbar}$. We address this issue in the following section.

### 4.3.4 EIRENE standalone simulations

In order to better investigate the discrepancy in the neutral pressure, we fixed the RECYCT coefficient with dedicated simulations. We used EIRENE in standalone mode to simulate the pre-plasma condition, providing to the code a background of Ar gas, with a negligible degree of ionization. In this way, the only code free parameter is the pumping surfaces albedo. To match the experimentally measured neutral pressure for a puffing strength of $1\,\mathrm{sccm}$, the recycling coefficient of the pumping surfaces was set to $\mathrm{RECYCT} = 0.99682$. Having fixed RECYCT to this value, the gas puff was then varied in the range $0.5 - 5\,\mathrm{sccm}$ and the simulated neutral pressure at the gauge location shown in figure 4.2 compared with experimental data. Results are shown in figure 4.6. As can be seen, a good qualitative and quantitative agreement was obtained. For low gas-puff values (below $2.5\,\mathrm{sccm}$), the simulated pressure (light blue line) shows a linear trend, in

agreement with the experimental data (red diamonds). For higher values of the puffing strength, the experimental pressure is slightly below the simulated linear trend. This is due to the fact that our EIRENE model does not include neutral-neutral collisions. Additional simulations were thus performed including $\mathrm{Ar} - \mathrm{Ar}$ elastic collisions in the basic set of atomic reactions considered by EIRENE and treated with the BGK approximation [128]. As can be seen from the violet line figure 4.6 the inclusion of elastic $\mathrm{Ar} - \mathrm{Ar}$ allows to slightly decrease the simulated pressure, better recovering the experimental points. However, it should also be noted that no significant deviation occurs for $1\,\mathrm{sccm}$ of Ar, that is for the reference case that we considered in this work.

### 4.3.5 Neural Network construction for radial profile prediction - preliminary investigation

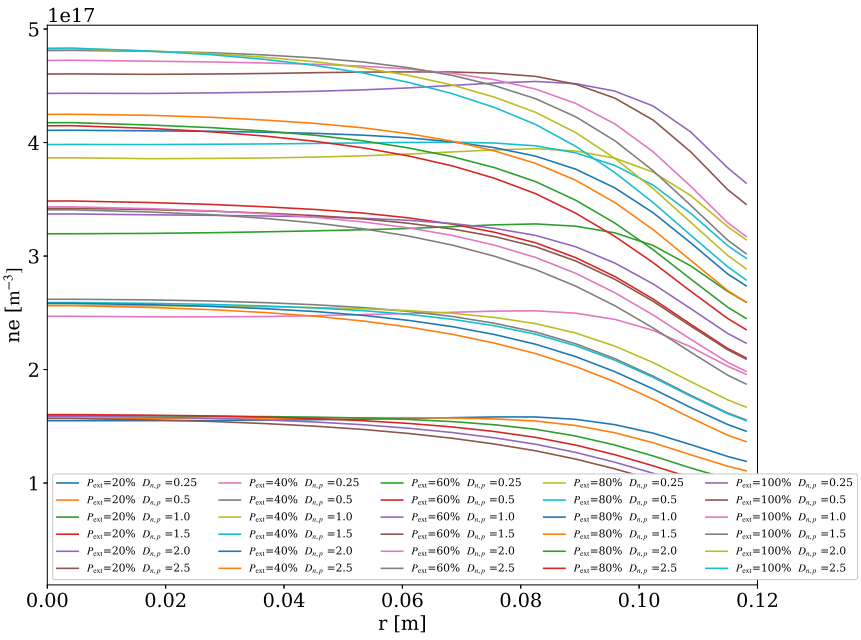


**Figure 4.7:** *Electron density radial profile for the* 30 *different cases corresponding to the variation of the radial diffusion coefficients and absorbed electron heat power.*

As mentioned in § 4.2.2, the sensitivity scan reported in table 4.1 has been further expanded, aiming to construct a SOLPS-ITER simulations database

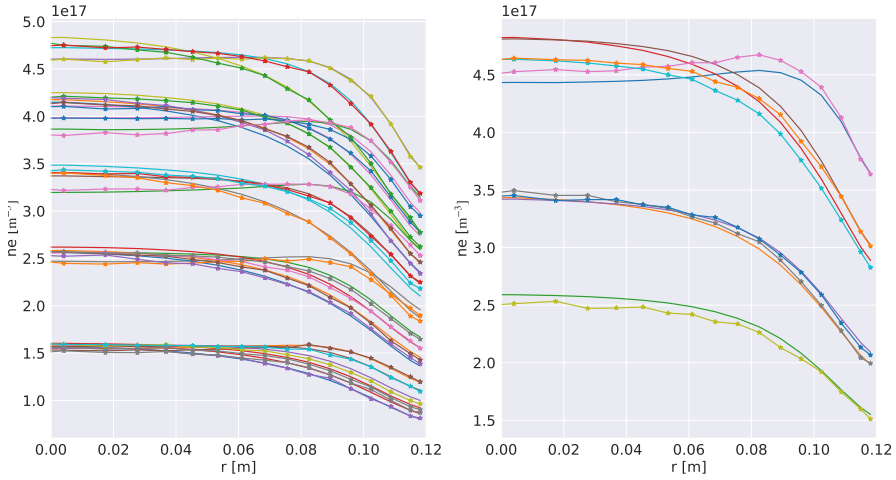


**Figure 4.8:** *Comparison between the input electron density radial profiles and the ones obtained from the NN, for the training set (left) and the test set (right). Diamonds are used as a marker to denote the NN results for both the train and the test set.*

from which a Neural Network (NN) can be trained. The underlying idea is to let the NN be able to reproduce and predict the SOLPS radial profiles of the main plasma parameters, such as the electron density, electron temperature and plasma potential. However, for this preliminary investigation, only the electron density radial profiles have been used as the training input and output of the NN. In the remaining of this section, we shall describe the main preliminary results that have been obtained. First, we start by reporting in figure 4.7 the radial profiles of the electron density for the 30 different cases that we considered here. Here and in the rest of this section, $P^{\text{ext}}$ is expressed in percentage of the overall power delivered by the RF source in GyM, which amounts to $3\,\text{kW}$, as described in § 3.4.3. This figure shows that the electron density nicely scales with the absorbed electron heat power, while the radial diffusion coefficients simple affect their shape, thus confirming the results reported in the previous section. Differently, the electron temperature (not shown here) does not cluster in a similar manner with increasing $P^{\text{ext}}$, as already been noted previously. The NN here considered is a simple multi-layer (six) Perceptron, which was built using the `keras` API in `Python`, building on top of the well-known `TensorFlow` library. The first layer of the NN (Input) takes as inputs the radial profiles of the electron density for all the free parameters combination (radial dif-

fusion coefficients and absorbed electron power, in this case) considered, 30 in our case. The output layer returns the radial profile of the electron density and consists of a total of 17 nodes, which correspond to the points making up the radial profiles given as an input to the NN. An hyperbolic activation functions is used for all the layer of the NN, with the exception of output layers, where a linear activation function has been used.
The NN has been trained by randomly splitting the database into train and test input, as is common practice. In particular, the test set is $1/5$ of the database dimensions, so that a total of 6 profiles are used for testing, while the remaining 24 for training. This splitting procedure is repeated for 3 times, in which the NN is trained for 4000 epochs. The performance of the NN was checked by monitoring the behaviour of the metric (mean-squared error) for both the training and the testing set of simulations. Training is stopped whenever the mean-squared error stop is decreasing.
In figure 4.8 shows a comparison between the input electron density radial

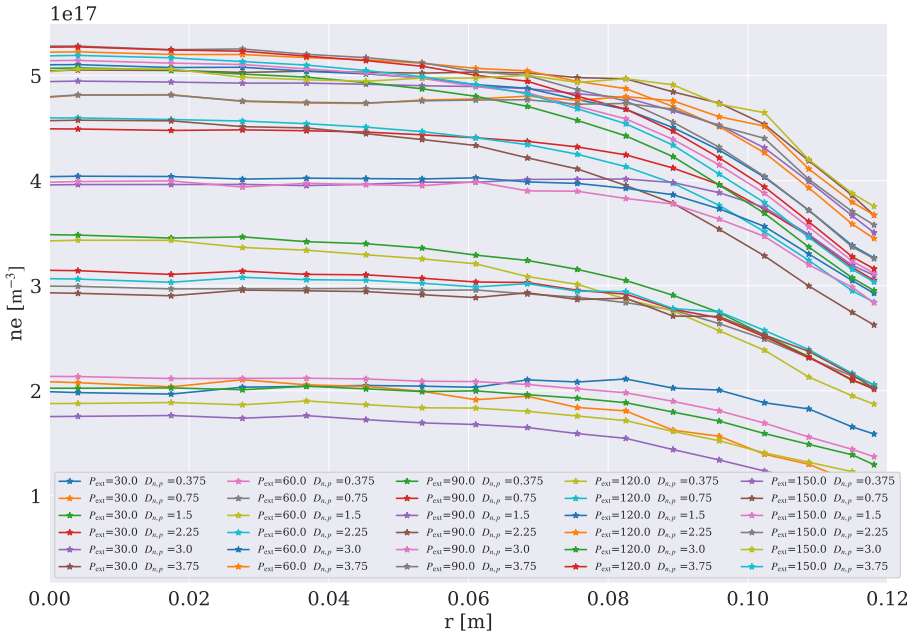


**Figure 4.9:** *Electron density radial profiles obtained by the NN by multiplying the inputs reported in table 4.2 by 1.5.*

profiles and the ones obtained from the NN, for the training set (leftmost

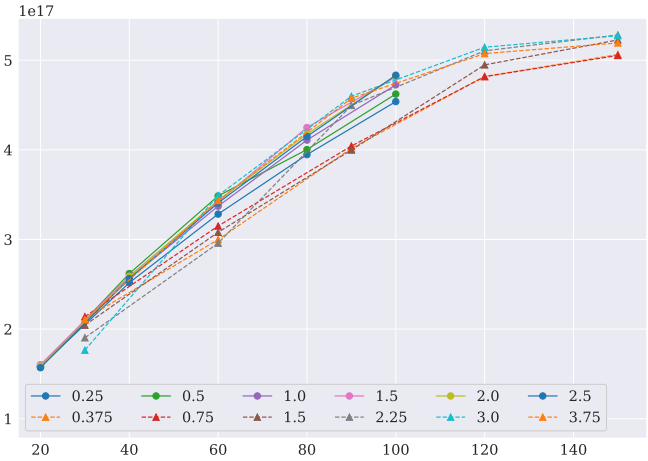


**Figure 4.10:** *Maximum value of the electron density as a function of the electron heat power, for each value of $D_{n,p}$. The dashed lines correspond to the results obtained for the NN in which the main input reported in table 4.2 have been multiplied by a factor of 1.5.*

figure) and the test set (rightmost figure). It can be seen that the NN is able to capture the radial profiles of the electron density in the test set.
Once trained the NN can be used to predict the same radial profiles for new input radial diffusion coefficients ($D_{n,p}$) and electron heat power ($P^{\text{ext}}$). In principle, in order to check the generalisation capabilities of the NN, one should also perform SOLPS-ITER simulations with these new input parameters and check the veridicity of the prediction. However, this validation step was not performed in this work. Figure 4.9 shows the radial profiles of the electron density obtained by the NN by multiplying the input reported in table 4.2 by a factor of $1.5$. One sees that the NN is able to generalise quite well, producing radial profiles that are consistent with the given input. Indeed, one can see from figure 4.9 that for input powers above $100\%$, the NN seems to predict a saturation effect of the electron density to values around $\simeq 5 \times 10^{17}\,\mathrm{m}^{-3}$.
To better highlight this aspect, we computed for both the NN prediction as well as for the overall set of SOLPS-ITER simulations the maximum value of the electron density and plot the results as a function of the electron heat power, for each $D_{n,p}$ value. Results are shown in figure 4.10. One sees that in the input database the trend in the maximum electron density seems to show a saturation at input electron heat power approaching $100\%$. The

same trend is quite well captured by the NN, at least in the same power range. However, for $P^{\mathrm{ext}}$ exceeding $100\%$, the NN predict a much sharper saturation of the electron density.

CHAPTER 5

# ERO2.0 modelling of nanoscale morphology evolution

THIS Chapter aims to presents the modelling surface morphology evolution at the nanoscale using the ERO2.0 code. We start first (cfr. § 5.1.1) by giving a general overview of the literature models that have been proposed in order to describe the evolution of the surface morphology under ion irradiation. Next, we focus in § 5.1.2 on particular model that have been proposed by Škereň et al. [101], which accounts also for the effect of the sputtering yield dependence on the crystalline orientation. By analysing this model, we find great similarities with what is currently implemented in the ERO2.0 code, which prompts us to push this comparison forward. In particular, we first implement the Škereň's model (SM) in the FreeFem++ framework and verify (cfr. § 5.2.2) that the so-obtained FreeFem model (FM) is able to reproduce the main results reported in [101]. Next, in § 5.2.3, we perform a first comparison of the ERO2.0 code and the FM on a simple analytically-defined W surface. Hav-

ing highlighted the conditions under which the two codes produce similar results, we consider in § 5.2.4 the surface morphology evolution of a realistic W surface with the ERO2.0 code after irradiation with Ar plasma. This surface was produced in the framework of the experimental activities of my Ph.D. The following section, cfr. § 5.2.5, illustrates the ERO2.0 modelling activities of the same W morphology exposed to a He plasma and compare it experimentally-available data, obtained in the framework of this Ph.D.

## 5.1 Theory of morphology evolution under ion irradiation

This section aims to give a brief overview of the models that have been put forward in literature in order to describe how a surface evolves when irradiated with energetic ions. It should be noted that this literature lies outside the world of magnetic nuclear fusion and, in particular, of PMI studies.

### 5.1.1 Review of literature models

Models describing surface evolution under ion irradiation are particularly interesting in the field of thin films and semiconductor fabrication, where the sputter erosion is employed as a tool for etching important patterns for the production of integrated circuits. In this field, it is rather well known that under certain conditions a periodic ripple pattern develops on the surface of both semiconductors and metals [67, 144]. This was first observed in 1956 by Navez et al. [131], by bombarding a glass surface with an ion beam of air. They observed the formation of a new surface morphology (cfr. figure 5.1), which was found to be strongly correlated with the incidence angle, $\theta$, of the ion beam. Figure 5.1 show the results of the experiments reported by Navez et al. A clean glass surface was exposed for 6 h to an air ion beam, varying the angle of incidence, $\theta$. The surface was found to be covered by a ripple, wave-like, pattern with orientation and characteristic wavelengths dependent on $\theta$.
The first theoretical description of the experiments reported in figure 5.1 was provided by Bradley and Harper (BH) [11], based on the theory of sputtering proposed by Sigmund [147]. We recall from the discussion made in § 2.1.1 that energetic ions can penetrate the first layers of the material, progressively losing their energy through collisions. In this process, if surface atoms acquire enough energy they can escape from the material. However, Bradley and Harper noted that process of energy deposition was dependent also on the local curvature of the surface. From this, the authors derived a model, known as the BH model, that describe the evolution of the surface

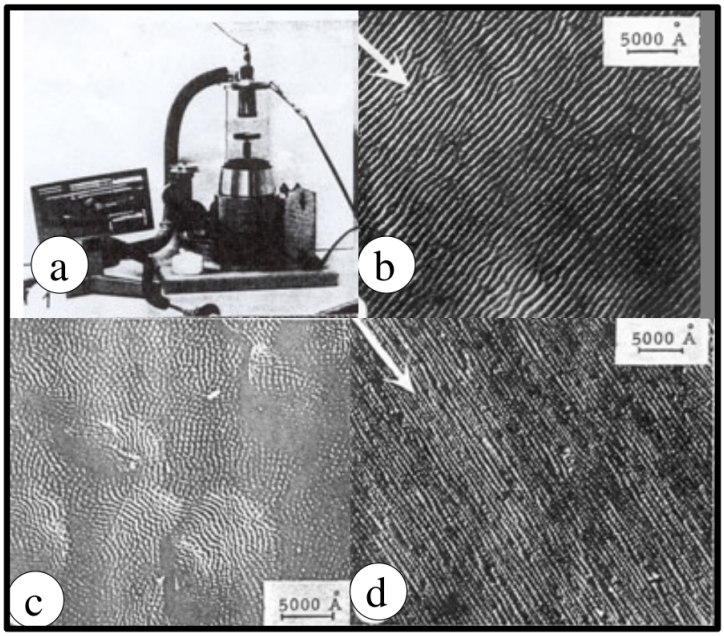


**Figure 5.1:** *Experiment performed by Navez et al on glass. Figure a) show the ion gun used to irradiate the glass samples. Figure b) shows the glass surface after 6h of bombardment at $\theta = 30°$. The arrows indicate the projection of the ion beam on the surface. It can be cleary seen that the developed rippled pattern is aligned with the ion beam direction. Figure c) and d) show the same glass surfaces, this time irradiated at $\theta = 0$ and $\theta = 80°$. It is seen that, at $\theta = 80°$, the ripples align perpendicularly to the ion beam. From Valbusa.*

height, $h$, under ion irradiation as:

$$\frac{\partial h}{\partial t} = -Y_0(\theta) - \frac{\mathrm{d}Y_0}{\mathrm{d}\theta}\frac{\partial h}{\partial x} + \nu_{\parallel}(\theta)\frac{\partial^2 h}{\partial x^2} + \nu_{\perp}\frac{\partial^2 h}{\partial y^2} \tag{5.1}$$

where $Y_0(\theta)$ denotes the sputtering yield of a flat surface. The second term on the RHS describes the drift of surface features along the $x$-axis, while the remaining two describe the dependence of the sputtering yield on the local surface curvature. By Fourier analysis of this equation, BH found that under certain irradiation conditions the surface is unstable under periodic perturbation.

The BH theory just outlined above represents the first serious attempt towards the explanation of pattern formation on amorphous materials when irradiated with energetic ions. Several additional models have been put forward in order to improve the original work of Bradley and Harper. A comprehensive review is provided [130, 144].

In general, as stated in [117], the basis of the continuum theory is the description of the surface morphology in terms of the height function, $h$, which gives the surface position $z = h(\mathbf{x}, t)$ above a point $\mathbf{x}$ in the substrate plane at time $t$. The height function satisfies an evolution equation of the general form:

$$\partial_t h = \mathcal{F}[\nabla h, \Delta h, \dots] \tag{5.2}$$

where $\mathcal{F}$ is a functional that must be chosen appropriately in order to encode the relevant physical processes which contribute to the evolution of the surface morphology. Notice that $\mathcal{F}$ depends on the derivatives of $h$, but it is generally independent on $h$ itself, because as can be expected the evolution does not depend on constant shifts of the reference plane, that is invariant under the translation $h \to h + C$. Moreover, usually the functional $\mathcal{F}$ is constructed in such a way that the evolution equation admits a solution corresponding to a flat and featureless surface. The latter can be, in general, either parallel to the reference plane or inclined relative to it with a tilt vector $\mathbf{m}$. In growth and erosion processes the mean height of the flat surface grows or recedes with some velocity $v$. The general flat solution of equation (5.2) can thus be written as:

$$h_0(\mathbf{x}, t) = \mathbf{m} \cdot \mathbf{x} + vt \tag{5.3}$$

The emergence of pattern formation on the surface is determined by the instability (either linear or non-linear) of this flat solution.

### 5.1.2 The Škereň's model

A particularly interesting model that has been recently proposed is the one by Škereň et al [101]. The latter was developed in order to interpret the mechanism of pattern formation on polycrystalline materials, such as metals. Under inclined incidence angle, the latter show indeed a patterning phenomena akin to that commonly observed for amorphous materials. In their work, the authors describe the formation of periodic ripples on polycrystalline materials by implementing a model which accounts for the dependence of the sputtering yield on: $i$) the local ion incidence angle and $ii$) the crystalline orientation of the grains. These assumptions lead to the following choice of the $\mathcal{F}$ functional just described in the previous section:

$$\frac{\partial h}{\partial t} = -\Omega\Gamma\frac{\cos\varphi}{\cos\phi}Y(\varphi)\,G(x, y) - B\Omega\Gamma\cos\varphi\Delta^2 h \tag{5.4}$$

In this expression, $\Omega$ denotes the volume occupied by the metal atoms in the lattice, $\Gamma$ is the incident ion flux, $Y(\varphi)$ is the sputtering yield while $\varphi$

and $\phi$ are defined according to the following formulae:

$$\begin{aligned} \cos\varphi &= \frac{\cos\theta + \partial_x h \sin\theta}{\sqrt{1+|\nabla h|^2}} \\ \cos\phi &= \frac{1}{\sqrt{1+|\nabla h|^2}} \end{aligned} \tag{5.5}$$

and denote the local incidence angle and the offset angle. The former accounts for the fact that the ion interact with the surface at an angle different from their nominal incidence value, which we should call $\theta$. Indeed, a given point on the surface can be specified by the vector $\mathbf{x} = (x, y, h(x, y))$. Furthermore, from elementary calculus, it is known that the normal to a cartesian surface can be computed:

$$\mathbf{n} = \frac{\partial_x \mathbf{x} \times \partial_y \mathbf{x}}{|\partial_x \mathbf{x} \times \partial_y \mathbf{x}|} = \frac{(-\partial_x h, -\partial_y h, 1)}{\sqrt{1+|\nabla h|^2}} \tag{5.6}$$

If we further assume that the ions impinge on the surface in the $x - z$ plane, then one easily derives equation 5.5. The offset angle, $\cos\phi$, is instead introduced to account for the fact that under ion irradiation the surface erodes in the direction of the local surface normal rather then vertical downwards [130]. The last term in (5.4) describes surface relaxation by adatoms diffusion and $\Delta^2$ denotes the biharmonic operator [101, 130]. In [101] this contribution is taken to be directly proportional to the local incidence ion flux, in order to describe the increase mobility of adatoms at high values of the ion flux [144]. The function $G(x, y)$ in (5.4) is introduced to account for the sputtering yield dependence on the crystalline orientation. In [101] this quantity is modelled by simulating crystalline grains as voronoi cells, assigning each of them a sputtering yield value drawn from a uniform distribution [101]. The sputtering yield dependence on the local incidence angle, $Y(\varphi)$, in the Škereň's model (cfr. equation (5.4)) is computed using the same fitting formulae as those implemented in the ERO2.0 code (cfr. § 3.3.1).

Equation (5.4) is a highly non-linear partial differential equation that describe the surface evolution under ion irradiation. The non linearities comes from the dependences of the sputtering yield on the local incidence angle, which in turn is a non-linear function of the derivatives of $h$. In addition to this, the $G$ function which describes the crystalline orientation dependence of the sputtering yield introduces interesting effects. Indeed, the $\mathcal{F}$ functional in the Škereň's model does not admit any flat solution, as can

be easily checked. This is intuitively obvious if one considers the fact that, under ion irradiation, each of the crystalline grain erodes at a different rate, which means that the surface tends to roughen at the initial phase of the irradiation.

### 5.1.3 Comparison between ERO2.0 and Škereň's model

The model proposed by Škereň of polycrystalline metal erosion shows great similarities with the current surface evolution module implemented in the ERO2.0 code. The latter has been described in great details in § 3.3.2. Indeed, in both ERO2.0 and the Škereň's model the sputtering yield is computed starting from the local incidence angle, which in turns depend on the local surface normal. In the ERO2.0 case, this operation is performed in a discrete manner, that is for each of the quadrilaterals which defines the surface. This is well represented by equation 3.36. In addition, in ERO2.0 once the erosion of each of the surface quadrilaterals has been computed, each of the surface cells is shifted downwards in the direction of the local surface normal, exactly in the same manner as it occurs in the Škereň's model. We can thus write a "continuous" version of equation (3.36) according to the following formula:

$$\frac{\partial h}{\partial t} = -\Omega\Gamma\frac{\cos\varphi}{\cos\phi}Y\left(\varphi\right) \tag{5.7}$$

where the symbols have the same meaning as those of equations (5.4). This comparison can be push forward, by recalling from the discussion performed in § 3.3.2, that ERO2.0 also performed an additional step of mesh reconstruction once each of the surface quadrilaterals has been evolved according to equation (3.36). This process involves an averaging procedure over the vertices of the neighbouring quadrilaterals. One can say that this averaging procedure actually represents the smoothing due to surface diffusion which appears in the Škereň's model, although greatly simplified with respect to the latter. It should be noted that, in writing equation (5.7), we have implicitly considered only the contribution due to ion erosion. In principle, however, ERO is also able to tracking eroded particles that redeposits onto the surfaces, which is not accounted for in the Škereň's model.

## 5.2 Results

This Section aims to present the main results related to the modelling of nanoscale morphology evolution. In particular, in § 5.2.1 the implementation of the Škereň's model (SM) in the FreeFem++ framework is illus-

trated. Next, in § 5.2.2 we check the correct numerical implementation of our FreeFem++ model (FM) by replicating the main results reported by Škereň [101]. In § 5.2.3 we perform a more quantitative comparison of the FM model with ERO2.0, by modelling the morphology evolution of a simple W sawtooth surface and outline, in particular, the conditions under which ERO2.0 and the FM produce similar results. In § 5.2.4 we apply the ERO2.0 code for the modelling of realistic W surface topography, retrieved directly from dedicated experimental measurements which have been carried on in the framework of this Ph.D. work. We consider first their morphology evolution when irradiated with Ar plasmas. Next, we illustrate in § 5.2.5 the results related to the exposures of the same W morphology to He plasmas. Furthermore, we provide here a comparison between the simulated surface morphology and the one obtained from experiments carried on in the GyM device, which have been performed in the framework of this Ph

### 5.2.1 Implementation of the Škereň model in FreeFem++

In this section, we shall briefly describe the implementation of (5.4) which we used for the simulations performed in this work. We solve the surface morphology equation (5.4) using finite elements in space and finite differences in time, by means of FreeFem++. The latter is a framework written in C++ which allows for the implementation and solution of physical models using finite element method [119].
In order to make a comparison between a theoretical model and ERO2.0, in this work we shall consider a slight simplification of the equation originally proposed by (5.4). In particular, we shall neglect the dependence of the diffusion term, that is the second term on the right-hand-side of equation (5.4), on the local ion flux, given by $\Gamma \cos\varphi$. With this assumption, the smoothing coefficient $B$ can be written using a formula first proposed by Herring and Mullins [122, 134]:

$$B = \frac{D_s \gamma \Omega^2 \nu}{k_B T} \tag{5.8}$$

where $D_s$ is the coefficient of surface diffusion, $\gamma$ the surface free energy per unit area, $\nu$ the number of diffusing atoms per unit area, $k_B$ the Boltzmann constant and $T$ the temperature.
In addition, the $G$ function which describes the dependence of the sputtering yield on the crystalline orientation, is implemented in a simpler way with respect to what described in Škereň [101]. Here, we consider the subdivision of the computational domain in a fixed number of squared regions.

In each of these, $G$ assumes the form of a random number sampled from a uniform distribution between $0.5$ and $1.5$, having $1$ has a mean value. In this way, to each region is assigned a different sputtering yield at orthogonal incidence, $Y_0$, in the range $0.5Y_0 \div 1.5Y_0$ with a mean value equal to $Y_0$. We shall see that, although simplified, this treatment is sufficient in reproducing the main qualitative features reported in [101]. Indeed, in spite of these two simplifications, the model is still capable of generating a ripple morphology at inclined angles of the impinging ion beam.
As regards the numerical implementation, we first discretize (5.4) using finite differences in time, treating the biharmonic operator implicitly and the erosion part of (5.4) explicitly. That is, the height function $h$ describing the surface morphology at $n$-th step is used for the computation of the angle-dependent part of equation (5.4). Therefore, we can write the semi-discretisation in time of equation (5.4) as:

$$\frac{h^{n+1} - h^n}{\Delta t} = -\Omega\Gamma \frac{\cos\varphi^n}{\cos\phi^n} Y\left(\varphi^n\right) G\left(x, y\right) - B\Delta^2 h^{n+1} \tag{5.9}$$

Space discretisation is performed using piecewise $P2$ non conform finite elements implemented in FreeFem++. Equation 5.9 can be solved by imposing periodic boundary conditions. Another possibility consists in imposing a vanishing normal component of the smoothing current, that is $\boldsymbol{n} \cdot \nabla\left(B\Delta h\right) = 0$. Unless, stated otherwise in the results presented in this Chapter, periodic boundary conditions are used. For the sake of simplicity, in the following we shall refer to equation (5.9) as the FreeFem (FM) model.

### 5.2.2 Validation of the Škereň's model

We validate the FM by considering $\mathrm{Ar}^+$ ion beam irradiation on a polycrystalline flat $\mathrm{Ni}$ target. The ion parameters are similar to the ones reported by Škereň et al. [101]. In particular, the incident ion flux is $\Gamma = 1.22 \times 10^1\,\mathrm{ions/nm^2 s^1}$ with a corresponding ion energy of $5\,\mathrm{keV}$. The sputtering yield fitting parameters of equation (3.35) can be found in [101]. According to what reported in [101], we simulate the surface morphology evolution at $300\,\mathrm{K}$ (room temperature). In this condition, the thermally activated smoothing coefficient of $\mathrm{Ni}$ equals $1.04 \times 10^{-11}\,\mathrm{nm^4/s}$. The simulation domain is a square having a surface of $200 \times 200\,\mathrm{nm^2}$. We subdivide this domain into $20 \times 20$ squared regions, assigning each of them a different sputtering yield multiplier, as described previously. We simulate irradiation on $\mathrm{Ni}$ target for an overall fluence of $600\,\mathrm{ions/nm^2}$, varying

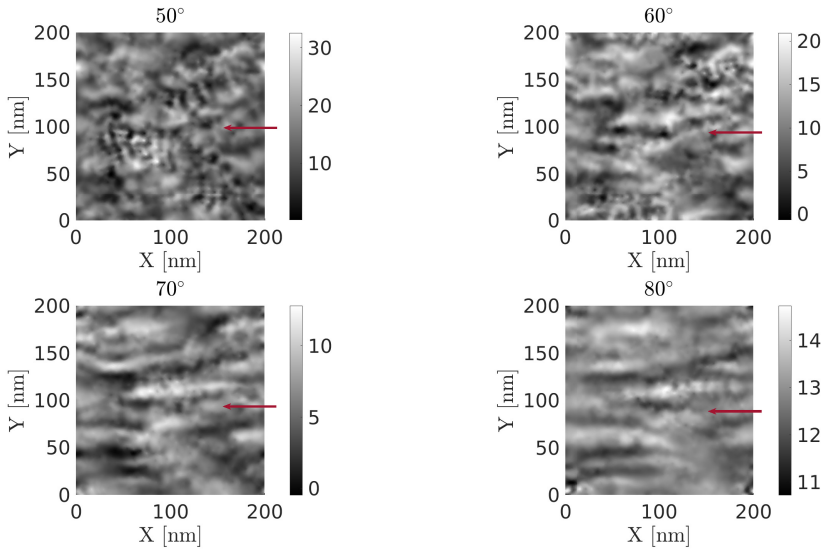


**Figure 5.2:** *Simulated* Ni *surface morphology with the Škereň model equation, varying the angle of incidence in the range* $50°, 60°, 70°, 80°$*, for an overall fluence of* $600\,\mathrm{ions/nm^2}$*. It can be seen that for grazing incidence the surface develops a clear ripple pattern oriented towards the incident ion beam, denoted with a red arrow in figure. The colorbar is in nanometers*

| 50° | 60° | 70° | 80° |
|---|---|---|---|
| 3.71 | 2.87 | 1.71 | 0.42 |

**Table 5.1:** *Estimated post-exposure average roughness retrieved at the end of the simulations, for the four irradiation conditions considered. Values are expressed in nanometers.*

the nominal angle of incidence in the range $50°, 60°, 70°, 80°$. The simulated surface morphology is shown in figure 5.2. The corresponding, post-exposure, roughness are reported in table 5.1. It can be seen that for grazing incidence, that is $\theta \geq 70°$, a ripple pattern develops on the surface. These structures are clearly aligned with the nominal ion incidence angle and no resemblence with the original (flat) morphology can be seen. As the nominal incidence angle decreases, one sees a progressive disappearence of the previously observed aligned surface structures (ripples). Instead, only a roughening of the original (smooth) surface can be observed. It should be noted that the dependence of the sputtering yield on the crystalline orientation is a fundamental ingredient for the development of ripples. Indeed,

if no mechanism which describes different erosion of grains is introduced in the model, then no such features appear on the surface. That is, if one starts from a flat surface, the latter is preserved at the end of the irradiation, as can be expected.

### 5.2.3 Comparison between Škereň and ERO2.0 on numerical surfaces

Having checked that the numerical implementation of equation (5.4) is capable of reproducing the main features reported by Škereň et al., in this section we compare ERO2.0 predictions with respect to the model equation ones (5.9). Due to its paramount importance in PMI research, we consider now a W surface, and we choose a simple sawtooth initial morphology with average surface roughness $R_a$ equal to 62.5 nm. This choice is related to the will of underlying possible differences in smoothing effects, which could be more clear on the sharp edges of this morphology with respect to e.g. a sinusoidal one. The simulated exposures are performed in a pure $Ar^+$ ion flux with ion energy set to $300\,eV$ and considering two different values of the nominal incidence angle, namely $0$ and $20°$. The choice of $Ar^+$ ions is simply related to the need of reducing the computational demand of the simulations, exploiting the high sputtering yield of $Ar^+$ ions on W. In this way, it is possible to obtain important surface modifications even at lower fluences. Since, at present, ERO2.0 cannot account for the crystalline dependence of the sputtering yield, we set in the model equation (5.9) $G = 1$. For both the model equation and the ERO2.0 simulations we employ the sputtering yield fitting proposed by Eckstein (cfr. § 3.35). The ion flux is set to $2.68 \times 10^{20}\,ions/m^2s$. For both the ERO2.0 and the Škereň model, we simulate the irradiation corresponding to an overall fluence on the samples of $5.36 \times 10^{20}\,ions/m^2$. These parameters are typical of $Ar^+$ in the GyM LPD. In the model equation we can set realistic values for the surface smoothing coefficient, $B$. In particular, for W using equation (5.8) and considering a surface temperature of $600\,K$ to be more coherent to fusion applications, one finds $B = 0.17\,nm^4/s$.
We start by considering the post-exposure surface morphology for normal incidence angle as simulated by ERO2.0. To this end, we compute $x$-directed slices across the simulations plot them for four different values of the ion fluence. Results are shown in figure 5.3 (dashed lines). From this, one can see that the surface progressively smooths as the ion fluence increases, moving from an initial average roughness $R_a$ of approximately 63 nm to the final 10 nm at the highest fluence. Each of the two valleys

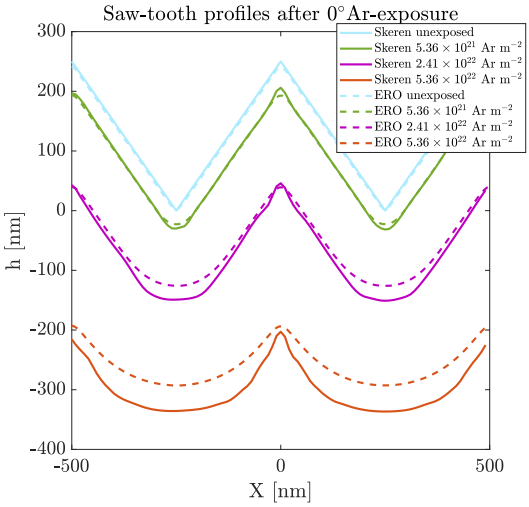


**Figure 5.3:** *Comparison between the 1D cut computed along the $y$ direction for both ERO2.0 (continuous lines) and the model equation (dashed lines) for different values of the ion fluence.*

which make up the original morphology is progressively eroded, resulting in a concave (almost parabolical) shape. This can be easily understood since in the ERO2.0 surface morphology evolution module there is no term which promotes roughening, as opposed to the $G$ function of (5.9).
The same morphology was simulated using the FM (cfr. (5.9)). Results are shown in figure 5.3 (continuous lines). One can see that there is a fairly good qualitative and quantitative agreement between the two sets of 1D profiles. Differences become more marked as the ion fluence increases, due to the different way in which smoothing is treated in the two codes. In particular, at the highest fluence, an average roughness $R_a$ of about 30 nm is obtained, which is quite higher than the ERO2.0 one at the same fluence. This difference cannot be ascribed as due to redeposition phenomena, which are accounted in ERO2.0 but not in FM, since the redeposition flux is almost five order of magnitude less than the erosion one. Indeed, in LPds due to the geometry of the system and to the use of weakly magnetised plasmas, the redeposition of W is much less important than in tokamaks, wwere one often gets more than $90\%$ of prompt redeposition.
As a further comparison, we consider the irradiation of the same W saw-tooth surface exposed to $Ar^+$ ions at a nominal incidence angle of $20°$. Results are shown in figure 5.4, while average roughness is reported in table 5.2. As it occurs for the simulation performed at normal nominal inci-

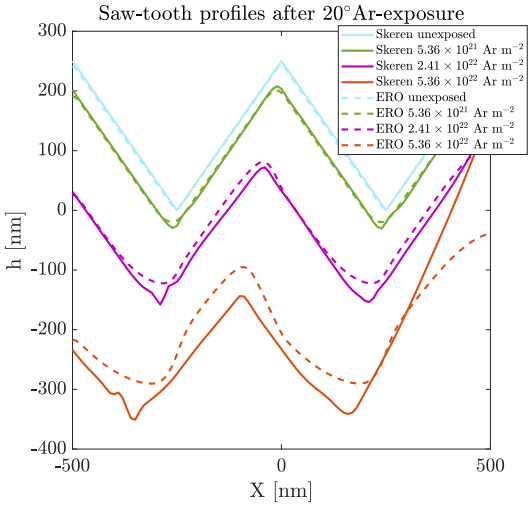


**Figure 5.4:** *Comparison between the 1D cut computed along the $y$ direction for both ERO2.0 (continuous lines) and the model equation (dashed lines) for different values of the ion fluence, for the simulations performed at $20°$ of ions incidence.*

| | Unexposed | $5.36 \times 10^{21}$ | $2.41 \times 10^{22}$ | $5.36 \times 10^{22}$ |
|---|---|---|---|---|
| ERO $0°$ | 62.5 | 60.7 | 23.3 | 10.0 |
| Škereň $0°$ | 62.5 | 62.8 | 55.4 | 31.7 |
| ERO $20°$ | 62.5 | 61.6 | 69.7 | 90.7 |
| Škereň $20°$ | 62.5 | 62.4 | 63.5 | 90.4 |

**Table 5.2:** *Estimated post-exposure average roughness retrieved at the end of the simulations, for both the ERO2.0 code and the Škereň model. Data are presented as a function of fluence for both $0°$ and $20°$ incidence angle. Roughness values are expressed in nanometers, while fluence is expressed in Ar $m^{-2}$*

dence, one can see that there is a good agreement between ERO2.0 and the FM. Again, differences become more marked as fluence increases. In this case, surface roughness increases with fluence, and the final $R_a$ is around 90 nm for both ERO2.0 and Škereň. However, the shape of the profile at the highest fluence is quite different in the two cases, while redeposition remains negligible even at this incidence angle. It is worth stressing that the FF simulations were performed with non periodic boundary conditions, that is by imposing a vanishing normal component of the smoothing current, as discussed in Section 5.2.1. Indeed, currently ERO does not allow for a periodic boundary condition in the surface evolution.
As a final analysis, we include the presence of crystalline grains variation of the sputtering yield in the sawtooth simulations with the Škereň model. We perform a sensitivity analysis of the ratio between average surface roughness $R_a$ and grains dimension D, in order to find for which values it is possible to recover the single crystal (SC) profile, which is the only one that can be currently simulated with ERO2.0. To this end, we carry out a series of simulations by varying the dimension of grains D and maintaining costant the initial roughness $R_a$, considering a final fluence of $2.36 \times 10^4$ ions/nm$^2$. The resulting 1D profiles are shown in figure 5.5. A small ratio, such as in the 0.625 and 1.25 cases, leads to important fluctuations of the profile around the SC case (red), which has a sputtering yield equal to the mean value of the ones associated to the different grains. However, decreasing the dimension of grains, these fluctuations are heavily reduced, and the SC solution can be almost recovered in the 6.25 case.

### 5.2.4 ERO2.0 modelling of realistic surfaces exposed to Ar plasmas

Having identified the conditions into which the surface morphology evolution module implemented in ERO2.0 gives reliable predictions with respect to grains orientation, in this section we consider the modelling of a realistic W surface whose properties are inside this reliability domain. The W sample here considered as been produced within the framework of the present Ph.D. work. Additional details will be thus provided within the forthcoming Chapter. For the time being, it suffices to not that this morphology morphology was chosen since it closely resembles that of AUG W-coated Graphite tiles [32]. The coating topography (cfr. figure 5.6) was retrieved from experimental measurements, using a Thermoscope Atomic force Microscopy (AFM) in tapping mode. The W morphology that we considered here is characterised by a preferential growth, so that all the crystalline grains are aligned along the $\langle 110 \rangle$ orientation. This means that our W sur-

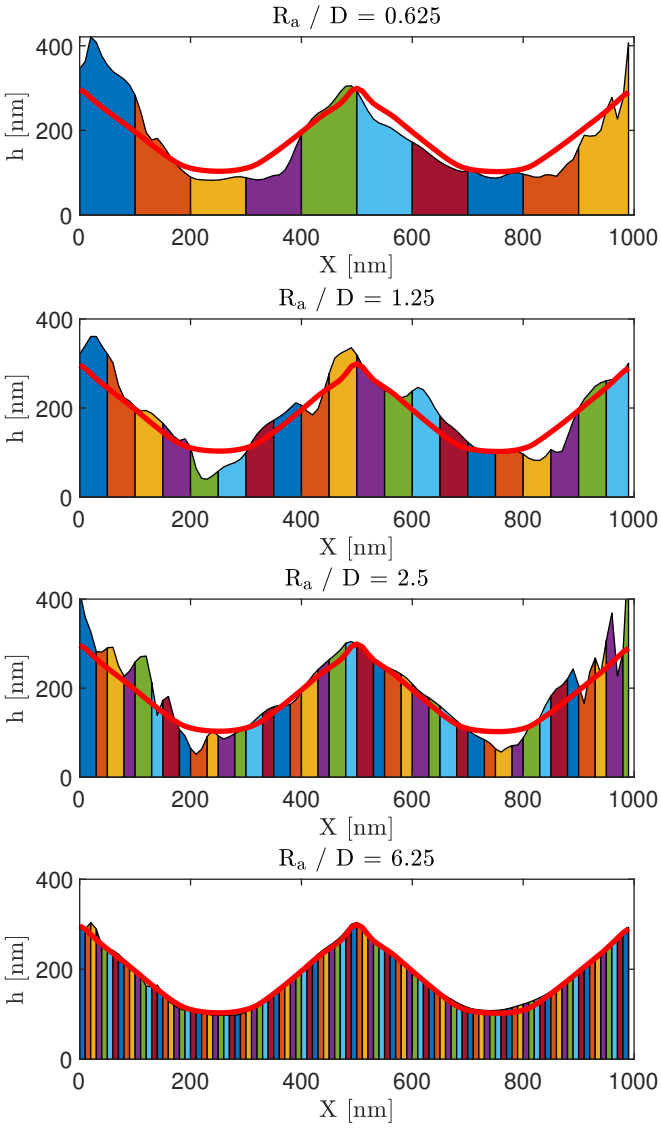


**Figure 5.5:** *Comparison between the 1D cut along the $x$ direction to vary the ratio between initial average roughness $R_a$ and grains mean dimension D, for a fluence of $2.36 \times 10^4$ ions/nm$^2$, computed with the model equation. The SC solution (red) is almost recovered when the ratio is sufficiently high.*

| $E_{ion}$ [eV] | $n_e$ [ions $m^{-3}$] | $T_e$ [eV] | $\phi$ [ions $m^{-2}s-1$] |
|---|---|---|---|
| 150 | $1.0 \times 10^{17}$ | 7.00 | $4.28 \times 10^{20}$ |
| 150 | $5.77 \times 10^{16}$ | 7.85 | $8.72 \times 10^{20}$ |

**Table 5.3:** *Main* Ar *and* He *plasma parameters used for the ERO2.0 simulations of the realistic* W *surfaces.*

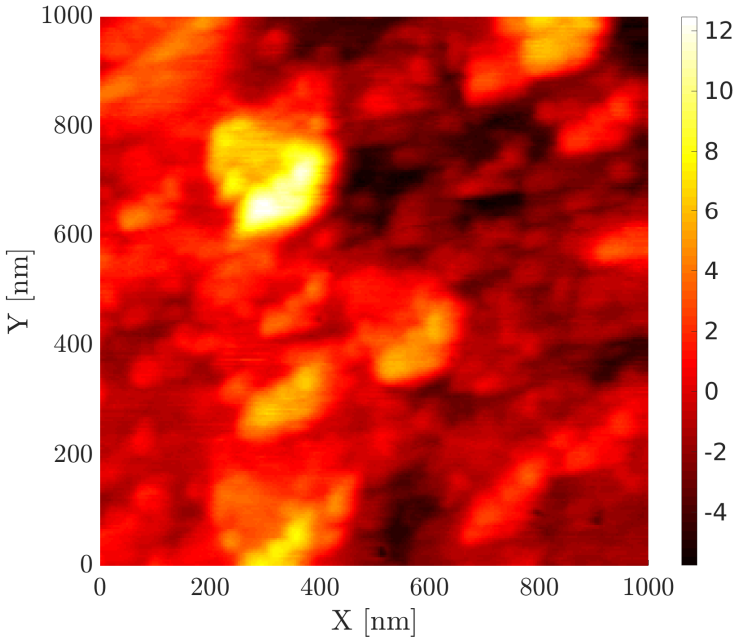


**Figure 5.6:** *AFM image of the as-deposited* W *coating. The colorbar is in nanometers.*

face in spite of being polycrystalline, it has one and only one crystalline orientation, thus allowing to choose $G = 1$ for the whole surface. Starting from the AFM measurements one can construct 3D surfaces which can be read in by the ERO2.0 code. As regards the plasma background, needed for the ERO2.0 simulations, we consider here a uniform plasma of $Ar^+$ ions. The main plasma parameters are reported in table 5.3. The flux is calculated by the code simply as the product of the plasma density and sound velocity, and it settles to a value of $4.28 \times 10^{20}$ ions $m^{-2}$ $s^{-1}$. We simulated the surface evolution due to plasma ion irradiation for an overall fluence of $1.74 \times 10^{24}\,\mathrm{ions/m^2}$. The ion energy is set to $150\,\mathrm{eV}$, well above the sputtering threshold of Ar on W.
In figure 5.7, we show the topography retrieved at the end of the ERO2.0

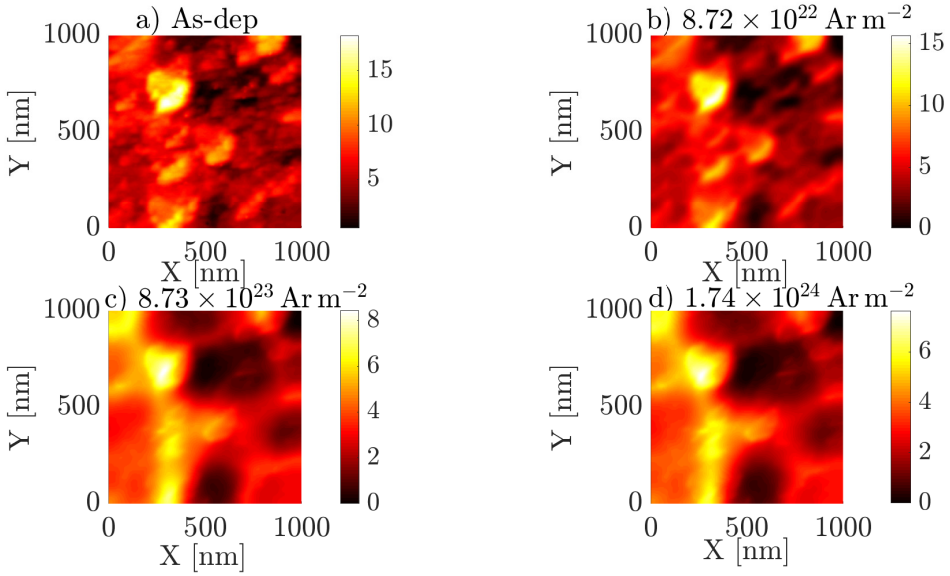


**Figure 5.7:** *Synthetic AFM images obtained from the ERO2.0 simulations as a function of the ion fluence. One can sees that there is a progressive smoothing of the original surface morphology. The colorbar is in nanometers.*

| Fluence [ions/m$^2$] | Ar | He |
|---|---|---|
| As-dep | 2.07 | 2.07 |
| $8.72 \times 10^{22}$ | 1.86 | 2.01 |
| $8.72 \times 10^{23}$ | 1.36 | 1.78 |
| $1.74 \times 10^{24}$ | 1.27 | 1.63 |

**Table 5.4:** *Average surface roughness $R_a$ of the realistic W sample after Ar and He exposure simulations. Values are expressed in nanometers.*

simulations for different values of the ion fluence, while the corresponding average surface roughness is reported in table 5.4. One can see that there is a progressive smoothing of the original surface morphology as the ion fluence increases. This observation is in accordance with the way the code calculates the evolution of the surface. As previously shown, having evaluated the eroded thickness for each quadrilateral, ERO2.0 reconstructs the final morphology by averaging the heights of neighbouring cells, thus resulting in an overall smoothing of the surface.
The morphology of the coating used in this work closely resembles that of AUG W-coated graphite tiles, which are produced by combined magnetron sputtering ion implantation technique. However, due to the different depo-

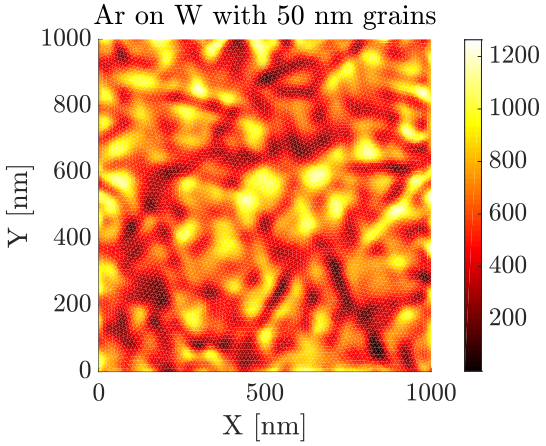


**Figure 5.8:** *Synthetic AFM image obtained with the Škereň model equation after a fluence of* $1.74 \times 10^{23}$ *Ar* $m^{-2}$ *and imposing the presence of 50 nm grains with different orientations, obtaining a ratio* $R_a$ */ D of approximately* $0.04$*. The colorbar is in nanometers.*

sition technique, the crystalline structure of these W-coated tiles is characterised by the presence of grains with different orientation, differently from the highly-oriented W coating obtained via PLD. Therefore, we investigated the effects of the presence of grains on samples having the same c-W morphology. To this end, we have included the possibility of importing synthetic AFM images also in our FF model based on Škereň equation. Since our coating sample presents always the same grain orientation, one should impose $G = 1$. However, we have already shown in the previous section that in this case the Škereň model is in good agreement with the ERO one. Moreover, it should be noted that the coatings used in nowadays tokamaks are often polycrystalline with different grain orientations on their surface. For this reason, we perform a simulation with the Škereň equation, considering the same initial surface but imposing the presence of grains with dimension of the order of 50 nm. Taking into account the initial average roughness in table 5.4, the ratio $R_a$ / D for this case is approximately $0.04$. The results of this simulation can be seen in figure 5.8. In this case, the presence of grains on an initial almost flat surface can induce an important roughening ($R_a \approx 160$ nm), which can not be catched by the ERO simulations. This is in accordance with the results of the previous section, in which the single crystal profile could be recovered only with a ratio $R_a$ /

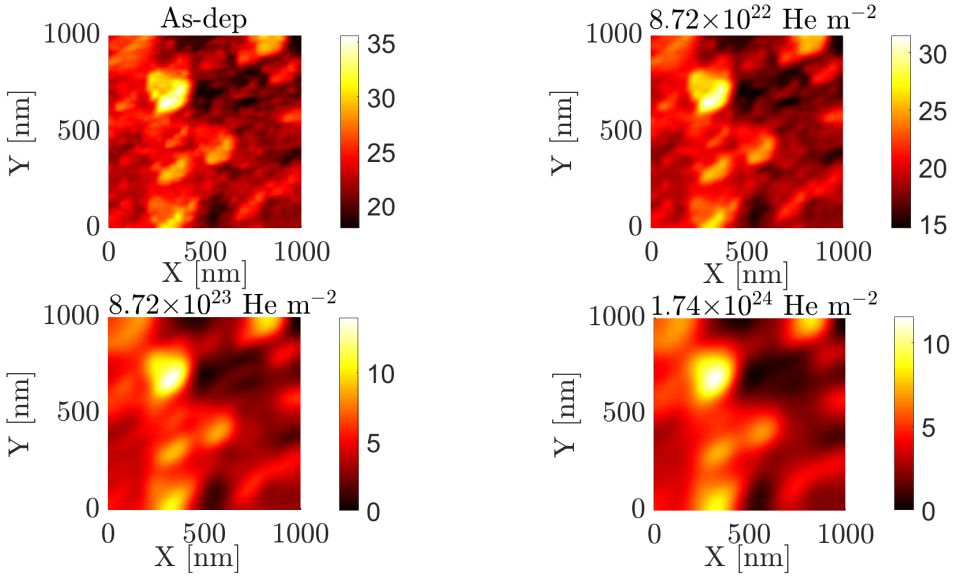


**Figure 5.9:** *Synthetic AFM images obtained from the ERO2.0 simulations as a function of the ion fluence. One can sees that there is a progressive smoothing of the original surface morphology. The colorbar is in nanometers.*

D above 5.

### 5.2.5 Comparison between ERO2.0 simulations and experimental He-plasma exposures

In this section, we further progress the analysis of the ERO2.0 code, by simulating the morphology evolution of the same W sample considered in the previous section exposed to $He^+$ plasma, and making a comparison with experimental results. These experiments were performed in the framework of this Ph.D. by a Ms.C. student which I co-supervised. Additional details will be provided in the forthcoming Chapter. The main plasma parameters considered in the simulations are reported in table 5.3. The incident ion energy was kept equal to that of the $Ar^+$ simulations by properly biasing the samples holder in the simulations. Finally, the overall fluence was kept equal to that of $Ar^+$ simulations.
In figure 5.9, we show the synthetic AFM images at the end of the ERO2.0 simulations for different values of the ion fluence, while the corresponding average surface roughness is reported in table 5.4. One can see that there is a progressive smoothing of the pristine surface morphology as the ion fluence increases. However, this smoothing effect is reduced with $He^+$ ions,

probably due to the lower sputtering yield with respect to $Ar^+$ one.
In addition to the surface morphology, for the He simulations we also numerically evaluated the erosion rate, since the latter was also measured experimentally, as detailed afterwards. In particular, two different values were obtained from simulations, which correspond to the two ways by which the sputtering yield can be evaluated in ERO2.0, namely with or without sheath tracing. In the former case, for a 1 $cm^2$ area, the erosion rate is almost one order of magnitude lower with respect to the latter, moving from $2.29 \times 10^{13}$ atoms/s to $1.02 \times 10^{14}$. We will see in the following that the exploitation of the sheath tracing allows to obtain far more reliable results in terms of erosion rate.
As already mentioned, the plasma exposure of the W morphology considered for the simulations to He plasma was performed in the linear device GyM (cfr. § 6). The main plasma parameters measured during the exposure by a Langmuir probe are similar to those considered for the ERO2.0 simulations, and are reported in table 5.3. As it happens for ERO2.0, the energy of the ion species is set to 150 eV by properly biasing the samples holder during the exposure. The difference with respect to the ERO2.0 modelling is that the experimental fluence is about a factor of 4 higher, reaching a value of $7 \times 10^{24}$ He $m^{-2}$. The reason for this is related to the computational load of the simulations, which has limited the fluence considered here. The experimental flux, $4.82 \times 10^{20}$ ions $m^{-2}$ $s^{-1}$, is slightly lower with respect to the simulations one. Indeed, the plasma ion flux is automatically computed in the ERO2.0, simply as the product of the plasma density and the sound velocity. This quantities are given, in ERO2.0, as an input. However, in the experimental evaluation of the same quantity, the ion flux, from the Langmuir Probe an additional pre-factor of $1/2$ is added to the electron density. Indeed, at the sheath entrance the electron density can be calculated as $n_{SE} \simeq 0.5 n_e$, where $n_e$ is the bulk plasma density [151].
The experimental erosion rate is calculated by means of Scanning Electron Microscopy analysis of the exposed sample cross-section, as discussed in details in Chapter 6. The obtained value, $1.72 \times 10^{13}$ atoms/s for a 1 $cm^2$ area, is in good agreement with the sheath-tracing numerically-evaluated one, $2.29 \times 10^{13}$ atoms/s, while the one calculated without sheath-tracing is almost one order of magnitude higher. This is one of the first demonstrations of the accuracy of this new functionality of the ERO2.0 code.
Finally, the post exposure W surface morphology is reported in figure 5.10, where we show an AFM plain view (top) and a SEM one (bottom). From the AFM view it is possible to glimpse the formation of an intricate pattern of ripples having different orientations, which are more evident on the

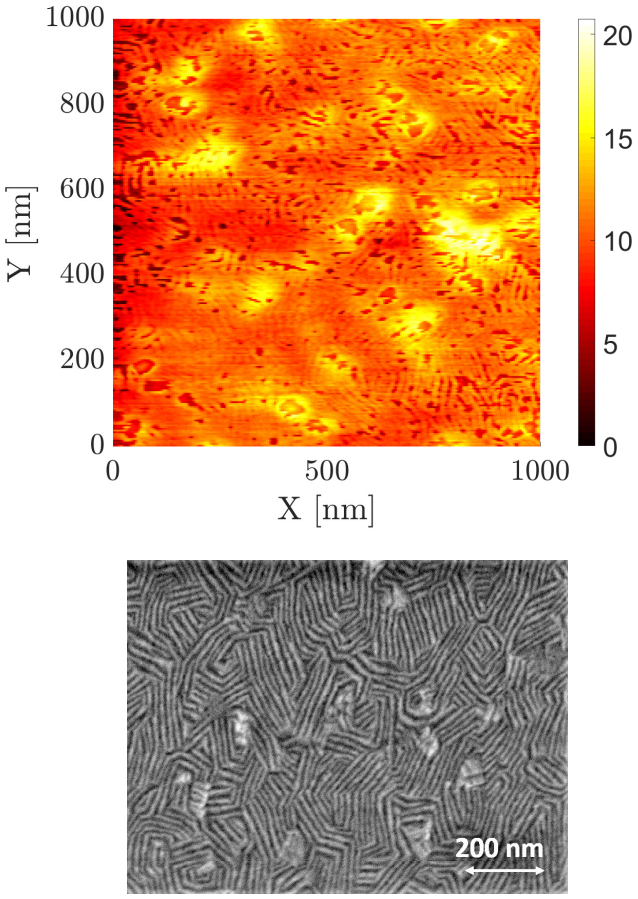


**Figure 5.10:** *Post exposure AFM (top) and SEM (bottom) plain view showing the results of the ion irradiation on the* W *morphology. One can see that an intricate pattern of ripple-like structures develops on the surface. The colorbar in the AFM figure (top) is in nanometres.*

SEM one. Moreover, these ripples seem to be generally confined within the crystalline grains of the W morphology.

## 5.3 Discussion

A detailed investigation of the ERO2.0 code revealed a close resemblance between the model it currently implements for evolving the surface morphology under ion irradiation and that put forward by Škereň et al. [101]. In particular, the recently upgraded ERO2.0 is able to account for all the effects taken into consideration by Škereň, with the sole exception of:

- the dependence of the sputtering yield on the crystalline orientation, i.e. the $G$ function which appears in (5.4) and,
- the surface smoothing term, which is treated in an approximate way in ERO2.0, that is by averaging over the vertices of each surface cell.

Numerical simulations performed on simple numerical surfaces without accounting for the dependence of the sputtering yield on the crystalline orientation, revealed a good agreement between ERO2.0 and the Škereň model, for different ion incidence angles. The only differences observed could be related to the simplified way in which smoothing is treated in the former code. The addition of the $G$ function to the model equation in the simulation of the numerical surfaces, showed that it plays an important role in determining the surface morphology after ion irradiation. However, when grains are sufficiently small with respect to surface roughness, one can obtain the results of the simulations when no account is made for the variation of the sputtering yield among grains. This result allows to rely on ERO2.0 solutions not only in the case of a single grain surface, but also when the ratio between surface roughness and grains dimension is sufficiently high. This observation is in accordance with what was found in previous studies for metallic diagnostic mirrors in tokamaks [26, 71]. Indeed, it was shown that the use of polycrystalline materials could prevent the good operation of this kind of devices, due to the increased surface roughness in erosive plasma conditions. Therefore, two possible solutions were found, namely moving to single crystal mirrors [26] or to nanocrystalline ones [71], which present a similar behaviour with respect to the former.
Simulations performed on realistic W morphology obtained from dedicated AFM measurements showed a progressive smoothing after both Ar and He ion irradiation. This observation is in accordance with the way into which the code calculates the evolution of the surface. Indeed, in absence of a $G$

function there is no mechanism active to promote roughening of the surface. As previously shown, having evaluated the eroded thickness for each quadrilateral, ERO2.0 reconstructs the final morphology by averaging the heights of neighbouring cells, thus resulting in an overall smoothing of the surface. In particular, smoothing is more effective for Ar-plasma simulations, probably due to its higher sputtering yield on W.
This seems to show that the model proposed by Škereň and, as a consequence, that implemented in ERO2.0 is incomplete, and it may be possible that additional terms should be added to the surface morphology equation to explain the discrepancies. Literature studies explain the formation of ripple-like nanostructures on ion exposed materials with the dependence of sputtering yield on surface curvature [11] or as a consequence of adatoms diffusion [144], but both models are unable to predict ripples in the conditions of this work, namely orthogonal incidence and high surface temperature. Other theories try to correlate the wavy structures with the formation of helium bubbles behind the surface [81]. In fact, He, during plasma exposure, can be trapped at defects and push the W lattice as pressure inside bubbles increases. This slipping effect results of course in different surface structures according to the crystallographic orientation of the grains. Since the investigation of the formation of He bubbles would require Transmission Electron Microscopy (TEM) measurements which were not available during this work, these will be subject of future studies. However, as suggested also in previous works [145], the observation of jagged edge nanostructures on W-bulk samples seems to be hardly related to slipping effects. A more detailed discussion on the possible mechanisms responsible for nanostructures formation will be provided in the following Chapter.

CHAPTER 6

# W-based coatings production and exposures in the linear plasma device GyM

THIS Chapter aims to present the main results related to the experimental work carried on in the present Ph.D. project. In particular, we start in § 6.1 by describing the W coatings production using the Pulsed Laser Deposition apparatus available at Nanolab. We describe here also their characterisation in terms of morphology and composition using SEM and EDS analysis. The following section, § 6.2, is dedicated to the illustration of the exposures to D plasmas of a selection of the PLD-produced coatings in the LPD GyM. In particular, we present in § 6.2.2 the main selected exposures parameters and in § 6.2.3 we highlight the main results. An equivalent analysis is performed for the exposures to He plasmas in GyM (cfr. § 6.3). We conclude this Chapter with the discussion of the observed plasma-induced modifications, § 6.3.5.

## 6.1 Production and characterisation of fusion-relevant W coatings via PLD

This Section describes the production and characterisation of fusion-relevant W coatings using the Pulsed Laser Deposition apparatus available at NanoLab. As already mentioned (see § 3.1), the production of W-based coatings during my Ph.D. work exploited previous knowledge in this field obtained here at NanoLab. Thus, the choice of the main deposition parameters (laser energy and fluence, background gas and pressure, etc.) is largely based on these previous results.

### 6.1.1 Metallic W-based coatings

Metallic W-based coatings have been obtained by the ablation of a pure (99.99%) W target either in vacuum or in inert (He and Ar). For all the coatings, we exploited the second harmonic ($\lambda = 532\,\mathrm{nm}$) of our Nd : YAG laser. Unless stated otherwise all the W-based coatings were deposited on flat Si (100) substrates. The following W films have been produced (cfr. table 6.1):

- **columnar-W** (c-W), obtained by PLD in vacuum conditions ($\simeq 10^{-3}\,\mathrm{Pa}$). These c-W films have been chosen since they mimic the morphology of combined magnetron sputtering ion implation W-coated tiles in full-W machines such as AUG [31, 32].
- **amorphous-W** (a-W), obtained by PLD in an inert He atmosphere with a background pressure of $70\,\mathrm{Pa}$. These a-W films have have been chosen since they are similar to W-based redeposits found on the FW with high energies (tens of eV).
- **porous-W** (p-W), obtained by PLD in an inhert Ar atmosphere with a background pressure of $50\,\mathrm{Pa}$. These p-W films have been chosen since they are similar to W-based redeposits found on the FW with low energies ($\simeq 1\,\mathrm{eV}$) [72, 114].
- **fuzzy-like W** obtained by PLD in an inhert Ar atmosphere with a background pressure of $100\,\mathrm{Pa}$. In this case, since previous results were not available at NanoLab, a detailed study of the morphology variation by tuning PLD parameters have been performed, mostly focusing on the laser systems, i.e. changing its energy and fluence, as reported in Table 6.1. These fuzzy-like W films have been produced aiming to mimic the peculiar morphology of the fuzzy-W (see § 2.4.2) [72, 114].

| | Laser Energy [J] | Laser Fluence [J cm$^{-2}$] | Background atmosphere | Background pressure [Pa] | O content [% at] |
|---|---|---|---|---|---|
| c-W | 760 | 11.5 | Vacuum | $\simeq 10^{-3}$ | 0 |
| a-W | 760 | 11.5 | He | 70 | 20 |
| p-W | 760 | 11.5 | Ar | 50 | 50 |
| fuzzy-W | 400, 300, 253, 196 | 3.7, 2.8, 2.3, 1.8 | Ar | 100 | 55 |

**Table 6.1:** *Summary of the metallic* W*-based coatings deposited using the PLD. For the c-*W*, a-*W *and p-*W *the PLD parameters were chosen on the basis of previous results obtained at NanoLab (see e.g. [36]). The* O *content in the* W *coatings here reported was evaluated using EDXS measurements.*

These coatings were thoroughly characterised in their morphology by means of SEM measurements. Figure 6.1 shows the SEM plain views of the as-deposited c-W, a-W and p-W. In addition, the inset in each figure reports

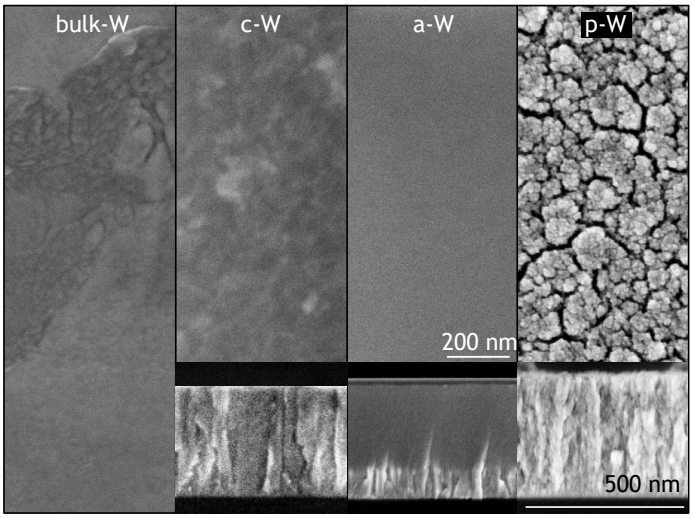


**Figure 6.1:** *SEM plain views of the as-deposited c-*W*, a-*W *and the p-*W*. The leftmost figure shows a SEM plain view of polycrystalline Plansee* W *sample, for comparison with the other morphology. The inset show the corresponding cross-sectional morphology. The latter was obtained by cleavage of the underlying* Si *substrates.*

the results of the SEM cross-sectional analysis of the samples. The latter were obtained by cleavage of the coatings after deposition. The coatings shown in figure 6.1 were deposited on Si substrates. Additionally, the c-W morphology for the D exposures (cfr. § 6.2) was also deposited on mirror-like and rough W and also on mirror-polished Gr, each substrate with a

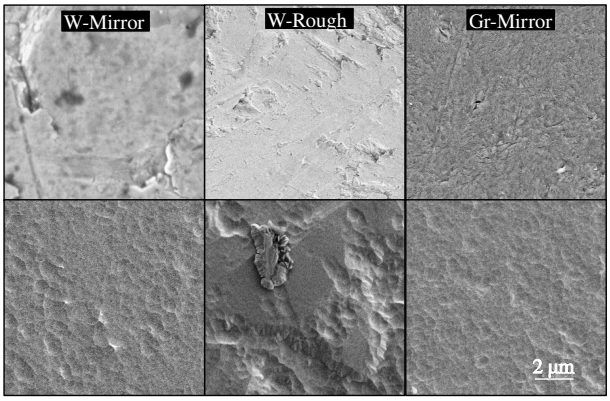


**Figure 6.2:** *SEM plain views of the W and Gr substrates without coating (top row) and with the c-W film (bottom row) deposited on top. The length scale ($2\,\mu$m) is the same for all the images. One can see that the coatings follow quite well the substrate topographies, with a comparable average roughness.*

thickness of about $\sim 1\,$mm. W substrates were given a surface roughness of around $400\,$nm by a mechanical treatment, which was performed using a lapping machine, changing the grit of the sandpaper. SEM plain views of the c-Ws deposited on these substrates is reported in figure 6.2, while their measured roughness is shown in table 6.2. In particular, from the

| Substrate | W mirror | W rough | Gr mirror | Si mirror |
|---|---|---|---|---|
| $R_a$ [nm] | 95 | 500 | 95 | 0.6 |
| c-W coatings | W mirror | W rough | Gr mirror | Si mirror |
| $R_a$ [nm] | 75 | 527 | 69 | 0.6 |

**Table 6.2:** *AFM measurments of the substrates and c-W coatings average roughness ($R_a$), measured by AFM over an area of $70 \times 70\,\mu$m$^2$.*

morphological analysis one sees that:

- the c-W samples are characterised by a compact morphology. Small crystalline domains can be identified on the surface of the sample. Indeed, XRD measurements of these coatings (see [36]) in $\theta \div 2\theta$ configuration show that the c-W has a crystalline structure, with a preferential growth aligned along the $(110)$ crystalline grain orientation of the $\alpha$-phase of W. Exploiting the Scherrer's equation, the crystallite

size is estimated to be $\simeq 18\,\mathrm{nm}$ (see [36, 73]).

- the a-W samples are characterised by a compact morphology. However, differently from the c-W, the presence of a He background atmosphere heavily impact the crystallinity of the samples. This can be seen qualitatively from the SEM measurements reported in 6.1, both from the plain views as well as from the cross-sectional analysis, since the coating appears to be featureless. This assertion founds confirmation from the XRD measurements reported in [36], where no peaks associated to the $\alpha$ phase of W could be detected.
- the p-W samples are characterised by an open (cauliflower) morphology. The Ar background atmosphere effectively slow down the ablated species before they deposit on the substrate. This results in an open morphology, with open columns which develop vertically from the substrate. Structural measurements by XRD analysis of these samples (see [36] showed no peaks, thus confirming that this film is amorphous.

As regards their composition, the O content (cfr. table 6.1) was evaluated by means of dedicated EDXS measurements after the deposition. It can be noted that the more compact morphology, namely the c-W, does not show any O contamination. On the other hand, for the a-W and p-W deposited in He and Ar atmosphere respectively, an O signal is detected.
The peculiar open morphology of the p-W samples was pushed further by increasing the Ar background pressure and, simultaneously, by reducing the laser energy (cfr. table 6.1), so that in plume nanoparticles clusters formation could be promoted. The aim here is to produce a morphology similar to that of the fuzzy-W. SEM plain views of the as-deposited samples is shown in figure 6.3. The SEM analysis reveal that the morphology deeply changes as the laser fluence decreases. In particular, for the two highest fluences (namely 3.7 and $2.8\,\mathrm{J/cm^2}$) the morphology is still characterised by a tree-like structure, akin to that reported before for the p-W, the difference being the more openness of the cauliflowers. However, when the fluence is reduced to $2.3\,\mathrm{J/cm^2}$ the morphology changes, as shown in figure 6.4. In particular, it can be seen that the cross-section now shows a random assembly of nanoparticles trees. Further decreasing the laser fluence to $1.8\,\mathrm{J/cm^2}$ leads to an additional morphology change, resulting in the development of a W foam rather than the typical fuzz structure (see figure 6.5 $c$)).
A comparison of the different W foams with real fuzzy-W has been also performed, aiming to identify the best PLD parameters that allow to better mimic its characteristic morphology. Results are reported in figure 6.5.

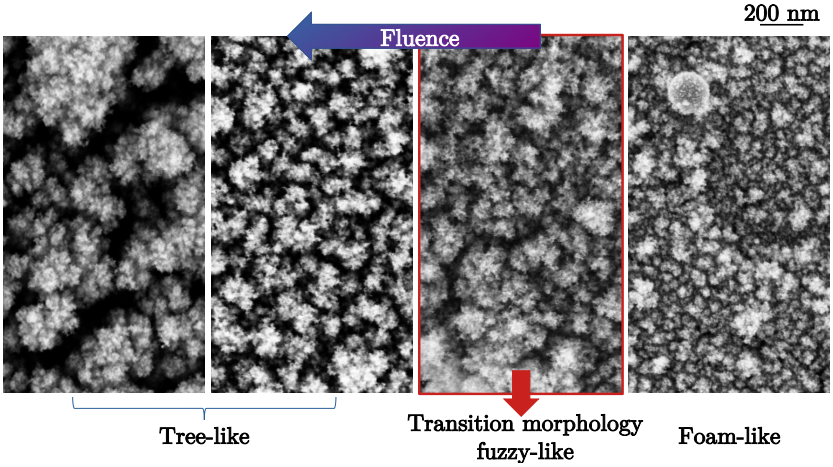


**Figure 6.3:** *SEM plain views of the fuzzy-like* W *morphology, by changing the laser energy and, hence, its fluence. The arrow shows the direction of increasing laser fluence (cfr. table 6.1).*

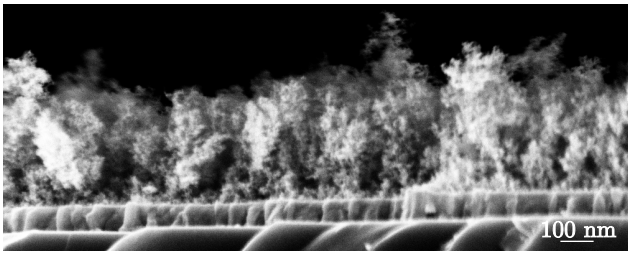


**Figure 6.4:** *SEM cross-section of the fuzzy-like* W *samples deposited at a laser fluence of* $2.3\,\mathrm{J/cm^2}$. *A thin c-*W *interlayer was added prior to the deposition of the fuzzy-like* W *morphology to better mimic the real fuzzy* W *morphology, which develops on top of* W. *A structure characterised by a random assembly of nanoparticles trees can be appreciated.*

Here, we compare the fuzzy-W morphology obtained by Kajita et al. [97] after the exposures of a Magnetron Sputtering-deposited W saample to a He plasma, and the fuzzy-like W ones obtained in this Ph.D. work by PLD with a laser fluence of 2.3 and $1.8\,\mathrm{J/cm^2}$. One can see that, for the coating

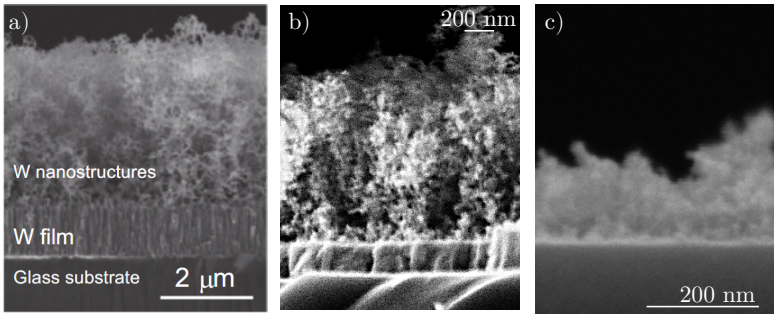


**Figure 6.5:** *Real fuzzy-*W *morphology obtained after the exposures of a Mangetron Sputtering-deposited* W *sample to a* He *plasma (*a*)) [97]. Fuzzy-like* W *obtained by PLD in this Ph.D. work (figures* b*) and* c*)) with a laser fluence of* 2.3 *and* $1.8\,\mathrm{J/cm^2}$.

deposited at $2.3\,\mathrm{J/cm^2}$ (cfr. figure 6.5 *b*)), there is a good morphological agreement with the real fuzzy-W. However, upon a closer look between the two, one notice that there is a factor of 10 in the characteristic dimension, i.e. the fuzzy-like W shows the same features of the real fuzzy-W if the latter is shrinked by one order of magnitude. In addition to this, one should also observe that the PLD-produced fuzzy-like W shows a rather high O content, as reported in table 6.1, of around 55% at. This value is higher with respect to that of real fuzzy-W found after the exposure of W to He plasmas, which is around $\simeq 5\%$ [97].

## 6.2 W and W-based coatings exposures to D plasmas

In this Section, a description of the results related to the exposures of the PLD-produced W coatings to GyM D plasmas is presented. We start in § 6.2.1 by showing the main motivations behind the experimental campaign. This should to better undertsand the choice of plasma exposures parameters that we considered (cfr. § 6.2.2). D plasma induced modifications are finally discussed in § 6.2.3.

### 6.2.1 Motivations

As detailed in Chapter 2, PMI has a deep impact on the overall behaviour of the W, which needs to be studied in a controlled environment. Fusion-

relevant plasma exposures of both bulk (polycrystalline) W and W coatings are usually performed in LPDs, due to their inherent simplicity, being nevertheless capable of producing plasmas with particle fluxes similar to those present in the different regions on the first-wall of both present day tokamaks and ITER (cfr. Chapter 2).
D plasma exposures of W results in important modifications at the micro and nanoscale, as detailed in § 2.4.1. Surface modifications at the nano/micro-scale have been extensively investigated in literature. However, these studies usually focus on W, exposed to plasmas with low energy ($\sim 40\,\mathrm{eV}$) of the ion species and with fluxes which are typical to those present at the divertor of present-day tokamaks ($\sim 10^{22\div24}\,\mathrm{m^{-2}s^{-1}}$). Much less attention has been instead paid to the behaviour of W after the exposures to medium flux ($10^{20}\,\mathrm{m^{-2}s^{-1}}$) and high energy ($> 100\,\mathrm{eV}$) D plasmas. D plasmas with these characteristics mimic charge-exchange neutrals (CXNs) fluxes at the main chamber of both present-day tokamaks [79, 109] and ITER [88, 110]. PMI studies concerning exposures to CXNs-like plasmas are related to ITER main chamber or structural materials such as beryllium and Eurofer, and usually focus on D retention and erosion (e.g. [33,69,90]). On the other hand, modifications at the nano/micro-scale of bulk W and nanostructured W coatings due to CXNs-like fluxes in a full-W DEMO-like scenario have not been addressed. It is thus of interest to study the modifications of W at both the nanoscale (formation of nanostructures) and the mesoscale (formation of blisters) in the peculiar regime of CXN-like plasma fluxes and ion energies and compare them with the above-mentioned literature results.
For these reasons, polycrystalline (bulk) W and W coatings having different morphology, structure, crystallinity and composition produced via the PLD technique were exposed to the medium flux deuterium plasma in GyM (cfr. § 3.4.3), tuning the energy of the impinging ion species in the range of $20 \div 300\,\mathrm{eV}$ by properly biasing the samples holder. Among the various W coatings outlined in the previous sections, we considered here:

- c-W, since it resembles the W-coated tiles in full-W machines such as AUG.
- a-W, since it mimic W which redeposits on the FW with high energy (tens of eV)
- p-W, since it mimic W which redeposits on the FW with low energy ($\simeq 1\,\mathrm{eV}$)

All these W coatings were deposited on flat Si (100) substrates. The rea-

son for this is to allow for an easier post-exposure analysis of the samples cross-sections, which can be performed by cleavage of the substrate, that is by cutting it along crystallographic directions applying a proper pressure. To address the role of the substrate in the plasma-induced modifications, the c-W morphology was also deposited on polycrystalline W and on fine grain graphite. The influence of the substrate materials in the observed plasma-induced modifications is thoroughly discussed in the text. Finally, to separate the combined effects of particle and thermal loads due to the plasma exposures, dedicated annealing experiments were also done on selected nanostructured W morphology.

### 6.2.2 GyM D plasmas parameters

A detailed description of the GyM device has been presented in § 3.4.3. Here, we shall limit ourselves to report the main exposures parameters that were chosen to investigate the D-induced modifications on our W samples. For the exposures performed in this work, the Langmuir Probe was positioned on the axis of the machine $\simeq 0.5\,\mathrm{m}$ in front of the samples holder. Deuterium was used as the working gas. Campaign-averaged electron density ($n_e$), electron temperature ($T_e$), plasma potential ($V_p$) and particle ion flux ($\phi$) are reported in table 6.3. For all the experimental campaign, the

| $n_e$ [$\mathrm{m}^{-3}$] | $T_e$ [eV] | $V_p$ [V] | $\phi$ [$\mathrm{m}^{-2}\mathrm{s}^{-1}$] | $\Phi$ [$\mathrm{m}^{-2}$] |
|---|---|---|---|---|
| $6.2 \times 10^{16}$ | 6.8 | 23.7 | $5.1 \times 10^{20}$ | $6.7 \times 10^{24}$ |

**Table 6.3:** *Campaign-averaged electron density, electron temperature, plasma potential, ion flux and fluence by the LP located at the machine axis in front of the samples holder.*

exposure time was $4\,\mathrm{hours}$. Together with the measured ion flux reported in table 6.3, this led to a fluence ($\Phi$) on the samples of about $6.7 \times 10^{24}\,\mathrm{m}^{-2}$. The samples holder (see figure 6.6) has a stainless steel mask and can accommodate up to four ($10 \times 10\,\mathrm{mm}$) squared specimens. In order to investigate the modifications induced to the W coatings by the plasma of GyM as a function of the ion energy, different (negative) bias voltages were applied to the samples holder. All the W morphology were exposed to the following bias voltages: *i*) no bias, *ii*) -100 V, *iii*) -200 V, *iiii*) -300 V, which correspond to an energy of the impinging ion species on samples in the range $20\,\mathrm{eV}$, $120\,\mathrm{eV}$, $220\,\mathrm{eV}$ and $320\,\mathrm{eV}$, respectively. Instead, the c-W deposited on mirror-like and rough W were exposed with no applied bias voltage. For clarity, only the absolute values of the applied bias voltage will be considered in the following. Erosion measurements were performed

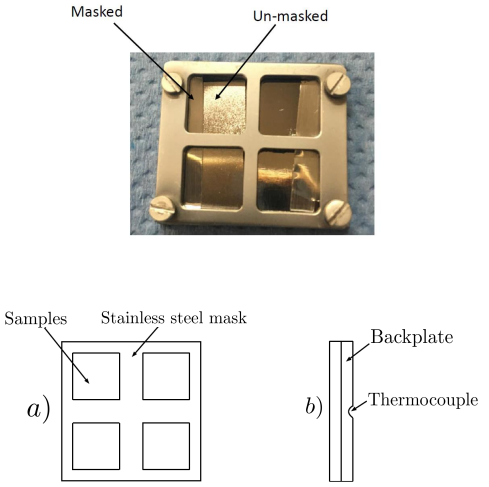


**Figure 6.6:** *Top: picture of the samples holder, showing the details of the samples preparation before exposures. Bottom: schematic view of the samples holder. a) top view; b) side view, showing the location of the thermocouple located at the backplate.*

via SEM analysis of the cross-section, partially masking them with a small molybdnenum sheet (cfr. figure 6.6) to evaluate the eroded step. The values of the bias voltages were chosen because the corresponding energy of the ion species are typical of high-energy charge-exchange neutrals impinging on the main chamber of ITER. Moreover, they are, below, around and above the sputtering threshold of Magnetron Sputtering-deposited W (as reported by Sugiyama et al. in [152]), respectively. The samples-holder is water-cooled ($\sim 13^\circ$ C) and removes the impinging power and after about 30 minutes of the exposures a steady-state temperature is reached. A thermocouple is located behind the back-plate. The temperature readings are $100^\circ, 120^\circ, 190^\circ$ and $260^\circ$ C for the four bias conditions that we considered in our work. A specific characterisation of the temperature difference between the thermocouple at the backplate and the surface of the samples was carried on employing an external heating source. The surface temperature was estimated to be higher than that at the backplate by $\sim 120^\circ$ C.

### 6.2.3 Results - nanostructures

In this Section, the results concerning concerning the modifications of the metallic W morphology at the nanoscale are be presented.
Figure 6.18 shows high-magnification SEM plain-views of the exposed W coatings deposited on Si and the bulk W samples at increasing bias volt-

age. One can notice that no modification at the nanoscale occurs for all the

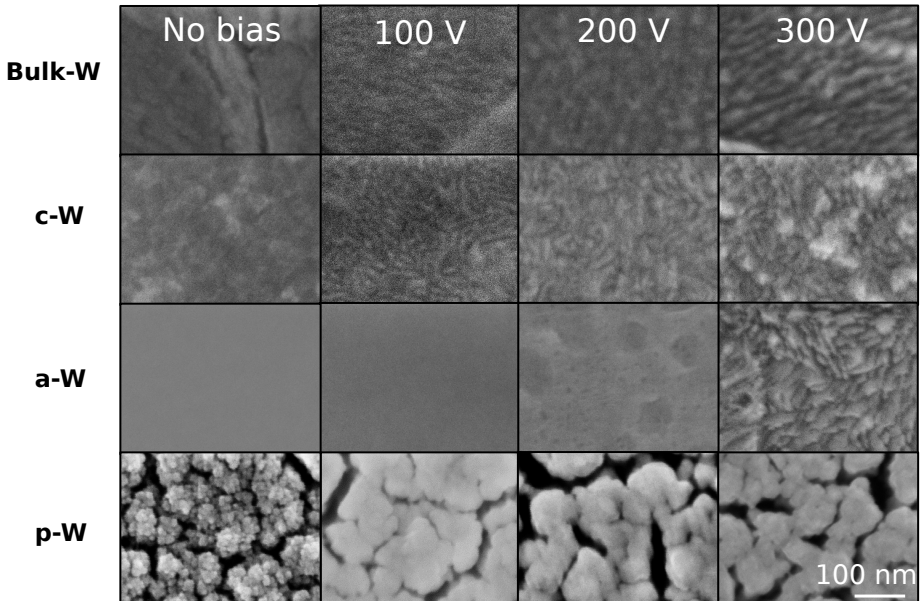


**Figure 6.7:** *SEM plain views showing a summary of the surface morphology evolution due the irradiation at increasing bias voltages, for bulk W and W coatings deposited on flat* Si. *The exposure performed with no applied bias voltage showed no induced modifications at the nanoscale.*

exposed morphology when no bias is applied. For an applied bias voltage of 100 V nanostructures start to develop on the bulk-W. Low-magnification SEM analysis on the bulk-W revealed the formation of three different type of nanostructure (ripple-like, spongy-like and jagged-like), as can be noted from figure 6.8, which are depending with the particular grain considered. The ripple-like nanostructure observed on the bulk-W developed also on the c-W film, while the other two reported in figure 6.8 were not seen in any of our exposures. As it happens for the bulk-W, the ripples are confined within the grains, whose dimension is around 20 nm. Figure 6.9 allows to appreciate that the ripple nanostructure is just few nanometers deep. The a-W films showed, instead, the development of a hole-like nanostructure at 200 V. Furthermore, at 300 V one can observe the formation of a ripple-like structure similar to that developed on the bulk-W and c-W coating. Considering finally the p-W films, SEM analysis at the nanoscale revealed no formation of any feature, but rather a progressive smoothing of the surface after the plasma exposure, with coalescence of the original, cauliflower-like morphology. This smoothing effect, observed for applied bias voltages

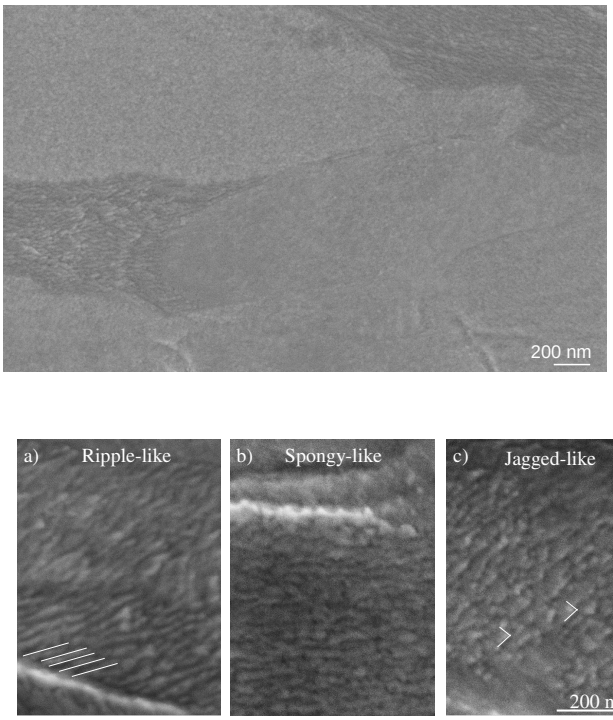


**Figure 6.8:** *Low magnification SEM plain view (top) of the bulk-W exposed at* $300\,\mathrm{V}$*, highlighting the strong dependence of surface nanostructures on the crystalline grains. Ripple-like a), spongy-like b) and jagged-like c) nanostructures (bottom) observed on different crystalline grains on the bulk-W exposed at* $300\,\mathrm{V}$*. White lines are added in figures a) and c) to help appreciate the differences between the ripple and jagged-like nanostructures.*

$\geq 100\,\mathrm{V}$, is related to the progressive erosion of the p-W films, which has been evaluated by SEM cross-sections of the samples. For the exposures performed at $100\,\mathrm{V}, 200\,\mathrm{V}$ and $300\,\mathrm{V}$ we estimated an erosion of about $23.3\,\mathrm{nm}, 56.7\,\mathrm{nm}$ and $69.7\,\mathrm{nm}$ respectively. A summary of the observed nanostructures is shown in table 6.4.

| | no bias | 100 [V] | 200 [V] | 300 [V] | Type |
|---|---|---|---|---|---|
| b-W | none | yes | yes | yes | spongy, jagged and ripple-like |
| c-W | none | yes | yes | yes | ripple-like |
| a-W | none | none | yes | yes | hole (200 V) and ripple-like (300 V) |
| p-W | none | none | none | none | - |

**Table 6.4:** *Summary of the nanostructures observed on the coatings deposited on* Si *and the bulk-W samples exposed to* D *plasmas changing the ion energy.*

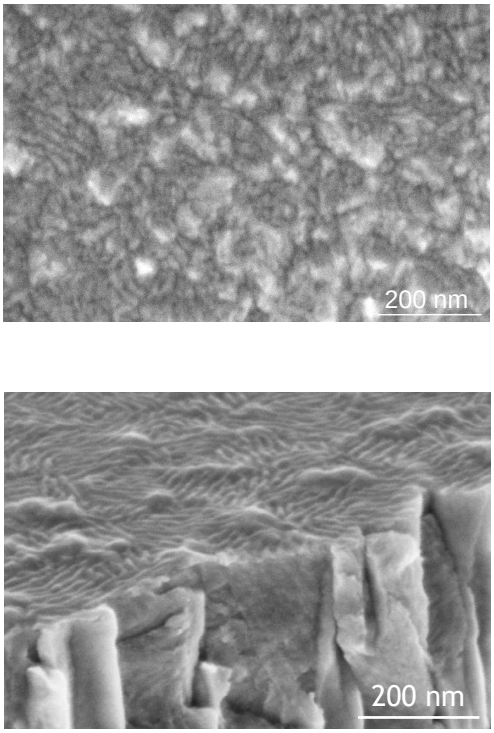


**Figure 6.9:** *SEM plain view (top) of the c-W exposes at* 300 V*, showing that the ripple-like nanostructure is well confined within the crystalline grains. Tilted SEM cross-section (bottom) of the c-W exposed at* 300 V*, showing that the ripple nanostructures are few nanometer deep.*

### 6.2.4 Results - blisters

SEM analysis of the compact a-W and c-W films deposited on flat Si showed the formation of micrometric-sized blisters, while no such features developed on the p-Ws. SEM analysis highlighted a reduction of blisters size by increasing the bias voltage, as can be observed from figure 6.10, particularly if one compares the exposure performed at 300 V to that where no bias is applied. For all the exposures and W morphology, blisters are $\mu$m-sized, the sole exception being the a-W exposed at 300 V, were much smaller blisters (nm-sized) were observed.
Blisters are also seen to strongly depend on the substrates properties. In particular, the c-W films deposited on rough W did not show any blister. The same also occurs for c-W deposited on mirror-polished Gr. However, for

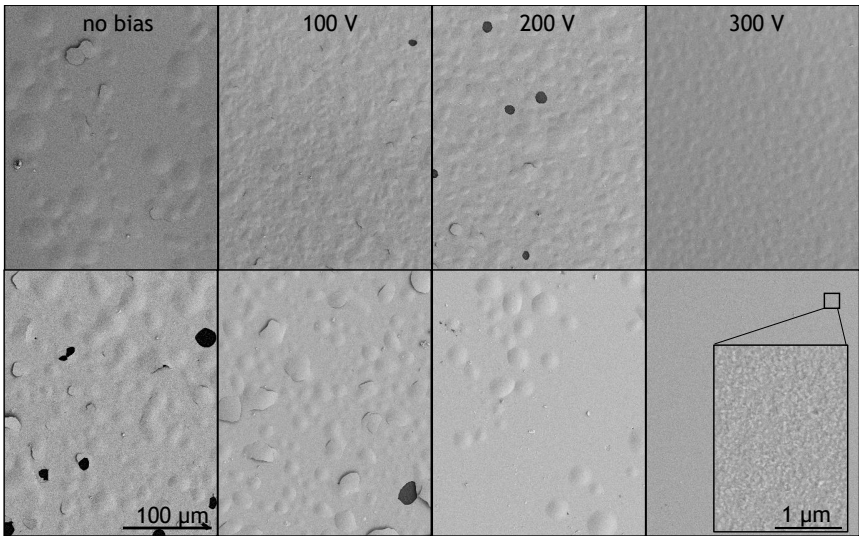


**Figure 6.10:** *SEM plain view showing the evolution of the blisters size, shape and number as a function of the applied bias voltage for the c-W (top row) and a-W (bottom row) coatings deposited on* Si*. The inset for the a-W exposed at* 300V *shows, in this case, blisters are much smaller (nanometric-sized).*

the c-W deposited on mirror-polished W and exposed to floating potential, the development of micrometer-sized blisters on the surface was observed, as shown in figure 6.11. The inset in the figure highlights corresponding AFM topographies on different spot of the sample, which allow to better appreciate the strong zone dependence of the blister size and shape. AFM and SEM measurements allow to appreciate the strong qualitative differences between blisters formed on the c-W deposited on mirror-polished W and flat Si (cfr. figure 6.10). On the one hand, one sees that blisters on flat Si appear to be higher in number and much more uniformly distributed. On the other hand, for the c-W deposited on mirror-polished W, blisters with different shape and height appear on top of the surface, with regions characterised by a strong coalescence of small-sized bubbles. A summary of blisters observed on the samples exposed in this work is reported in table 6.5.

### 6.2.5 Results - recrystallisation dynamics of the a-W samples

The last two sections showed that the plasma exposures result in important modifications at the nano and microscale of the W samples. However, the plasma carries not only particles, but also energy which can have important effects on the W layers. Because of their amorphous-like structure (cfr.

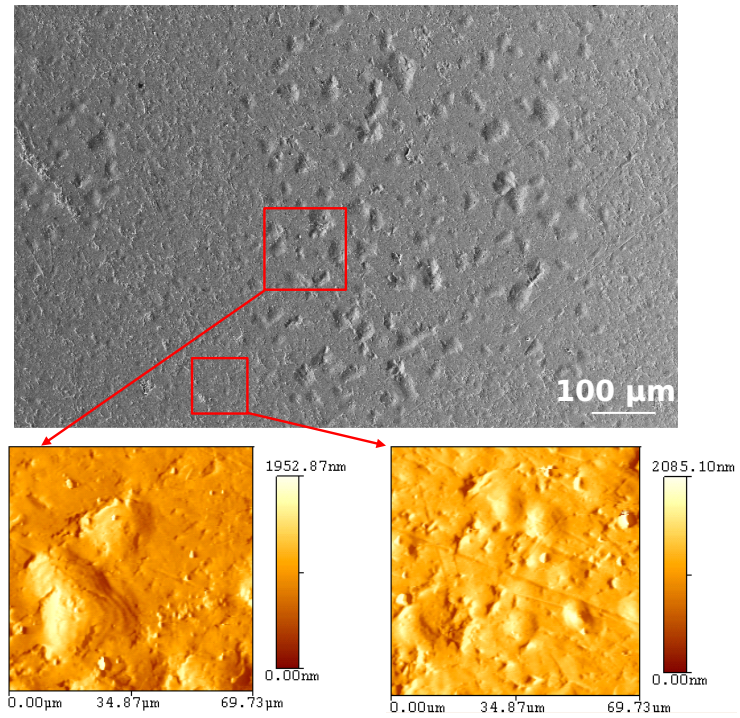


**Figure 6.11:** *SEM image of the blisters development after the plasma exposure on the c-W film deposited on mirror-polished W. The red insets highlight zone where AFM measurements were performed.*

| | | no bias | 100 V | 200 V | 300 V |
|---|---|---|---|---|---|
| | b-W | none | none | none | none |
| c-W | W mirror | yes | - | - | - |
| | W rough | none | - | - | - |
| | flat Si | yes | yes | yes | yes |
| | a-W | yes | yes | yes | yes |
| | p-W | none | none | none | none |

**Table 6.5:** *Summary of the blisters observed on the surface of the samples exposed in this work. A dash denotes the fact that a particular sample was not exposed in the reported experimental condition.*

§ 6.1.1 and also [36]) far from thermodynamic equilibrium, the a-W films are very sensitive with respect to temperature. Indeed, in [37] it has been shown that vacuum annealing at $450 - 500°C$ is enough to induce the crystallization of the a-W morphology [37].
To investigate the impact of the plasma on the crystallinity of the a-W films,

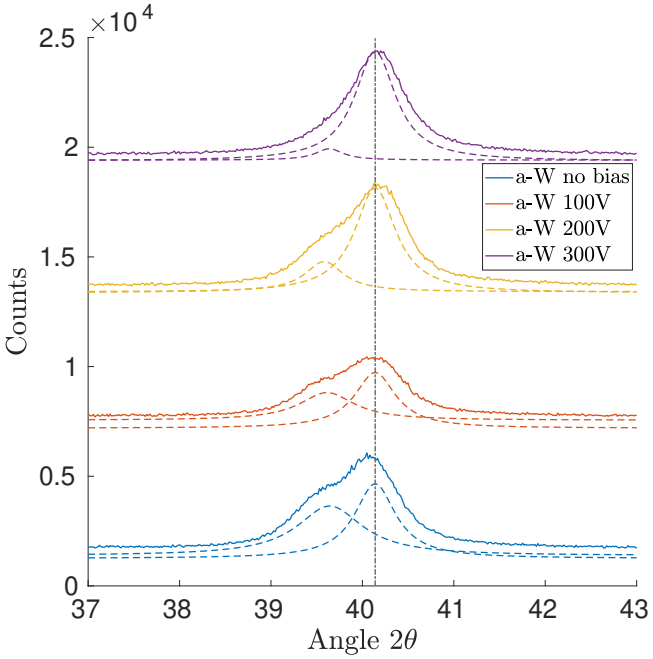


**Figure 6.12:** *XRD diffractograms of the exposed a-W samples. For each diffractoraph, the dashed lines denote the two lorentzian functions used to fit the data. One sees that the intensity of the lorentzian associated with the amorphous character of the a-W morphology progressively reduce. The dashed vertical line denotes the diffraction angle which corresponds to the* $\langle 110 \rangle$ *crystalline orientation of* $\alpha-W$.

XRD measurements were performed on the exposed a-W samples with bias $0 \div 300$ V. The diffractograms are shown in figure 6.12. It can be noted that all the spectra are characterized by a dominant peak located at $2\theta \simeq 40.1°$ and a shoulder. The peak is associated with the $\langle 110 \rangle$ crystalline orientation of $\alpha$-W and it is due to the c-W crystalline adhesion layer [36]. The shoulder located to the left of the main peak, at about $39.6°$ is related to the broad amorphous band typical of the a-W morphology [36]. A fit, reported in figure 6.12, of the acquired spectra was performed using the sum of two Lorentzian functions; to account for the presence of the c-W interlayer, whose properties do not change during plasma exposures, one of the two Lorentzian was given a fixed peak position and FWHM, corresponding to those measured on an as-deposited c-W [36]. It can be noted that increasing the bias voltage, the shoulder progressively disappears and at 300 V only a small contribution remains. This analysis points to the fact that a crystallisation of the a-W has occurred during the exposures performed at the

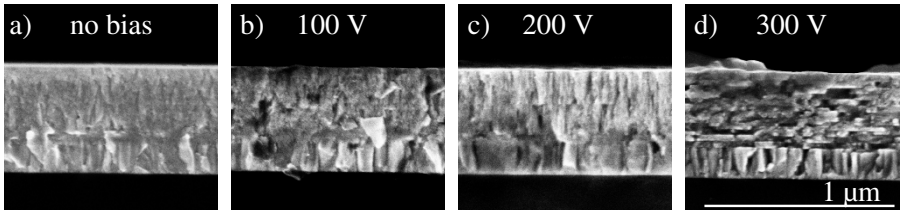


**Figure 6.13:** *SEM cross-sections of the a-W coatings after the exposures at no bias a),* 100 *b),* 200 *c) and* 300 V *d).*

highest energy. Cross sectional SEM analysis of the exposed samples is reported in figure 6.13. It can be noted that increasing bias voltage up to 100 V results in a slight change of the morphology. At 200 V a columnar-like morphology appears. At 300 V the formation of the crystallised nanolayers is evident indicating a crystallisation of the a-W film. Due to the amorphous nature of the coatings the crystallisation is likely to happen at much lower temperatures compared with microcrystalline bulk W and compatible with the exposure temperatures.
To better address this point a dedicated annealing campaign has been performed with the aim of better characterise the crystallisation and recrystallisation dynamics of both a-W and c-W films. The films were deposited on quartz slides. No c-W interlayer was added on these substrates before depositing the a-W films. The annealings were performed in high vacuum ($10^{-6}$ Pa) varying the temperature in the range $100° \div 1250°$ C in $50°$ C increments, the dwell time set was one hour. Figure 6.14 shows the mean crystallite size of a-W and c-W films as a function of the annealing temperature, as computed from XRD measurements using the Scherrer's formula applied to the peak associated with the $\langle 110 \rangle$ crystalline orientation of $\alpha$-W. It is worth to note that peak broadening of the XRD spectra is affected by the effects of the strain as well as the crystallite size [44]. Thus the use of the Scherrer method, that neglects the broadening contribution related to stresses may lead to an underestimation of the crystallite sizes. Crystallite dimension of c-W film does not appreciably change in the range $20 \div 650°$ C, the mean crystalline dimension remains about 15 nm typical of physical vapor deposited films. At $650°$ C a rapid recrystallization of the film occurs, the mean crystallite size from raised from 15 nm to 90 nm (that is the limit dimension appreciable with the Scherrer's formula). This value of recrystallization temperature is lower with respect

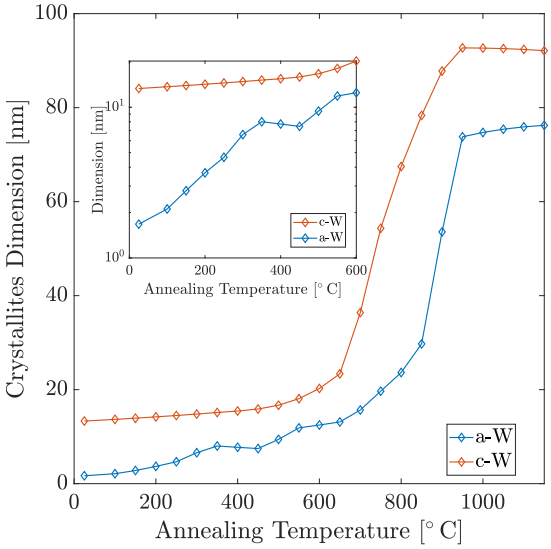


**Figure 6.14:** *Mean crystallite size for the a-W and the c-W as a function of the annealing temperature as computed from XRD measurements using the Scherrer's formula. The inset shows that in the temperature range* $0 \div 600°$ *the mean crystallite size of the c-W is almost constant, while it increases for the a-W already for relatively low annealing temperatures.*

to the one of microcrystalline W (about $1000°$ C), this difference has to be ascribed at the nanocrystalline nature of c-W film. Due to their amorphous structure, the a-W films are even more sensible with respect to temperature than c-W films. The film starts to crystallise already at low temperatures ($200 \div 300°$ C). The growth is linear up to $650°$ C going from $2\,\mathrm{nm}$ to $15\,\mathrm{nm}$ and is related to the grow of the crystalline domains and grain refinement from low energy defects such as dislocations. Above this temperature a sudden increase in crystallinity, from 15 nm up to 80 nm, occurs due to re-crystallisation of the film similarly to what happened in c-W films. For both the a-W and c-W at temperatures above $1000°$ C, the crystallite size rises with a little slope. A second session of annealings at $200°$ C, $450°$ and $600°$ was performed on the a-W films deposited on Si with the same features of the exposed samples (c-W as interlayer) to perform SEM cross-section analysis, see figure 6.15. It can be noted that, coherently with the changes in crystallinity, the cross-sectional morphology changes already at $200°$, if compared to that of the as-deposited a-W reported in figure 6.1. These changes become more evident at $450°$, were a columnar-like growth, akin to that of the c-W morphology, is promoted (cfr. figure 6.1). At $600°$ C, a

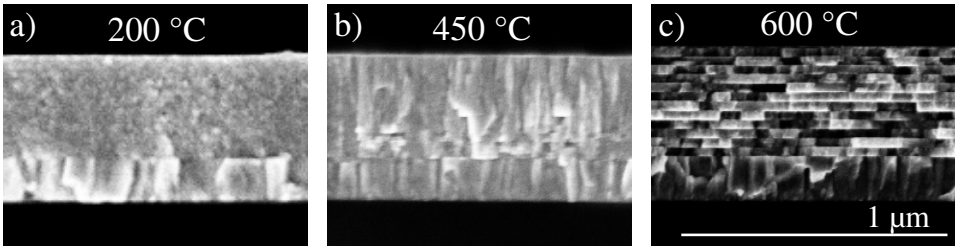


**Figure 6.15:** *Cross-sectional morphology obtained by SEM analysis of the a-W annealed at* 200° *a),* 450° *b) and* 600° C *c).*

peculiar layered structure develops. Each layer has a thickness of $\sim 40\,\mathrm{nm}$, and a morphology similar to the c-W interlayer, looking like a crystallisation layer by layer. The presence of such nanolayers is probably connected with the pulsed regime of the laser as well as with the movement of the ablation target during the deposition process. It is worth noting that due to the Si cleavage technique, the features of the cross section are influenced by the mechanical properties of the film (i.e. its ductility). W, due to its high ductile-to-brittle transition temperature, is quite fragile. Thus, every single W layer gets singularly broken during the cleavage resulting in a "rough" and irregular cross section.

### 6.2.6 Results - Erosion of the W coatings

The W coatings considered in this work are characterised by an unconventional morphology and composition, if compared with those of the bulk W. It is thus of interest to evaluate their sputtering yields. To this end, one should have a very precise characterisation of the plasma composition, which in the low density range of GyM is difficult, due to the very low ionisation fraction (limited to some percent) and the presence of long-lived molecular ions such as $D_2^+$ and $D_3^+$. Moreover, one should also consider the possible influence of impurities in this evaluation. Impurity might come from the sputtering of the stainless-steel mask of the sample holder and it is biased as well as the samples. However, sputtering of W samples due to these impurities might be negligible due to the fact that their ionisation mean-free path in GyM is comparable with the machine size, since the electron density is relatively low. For these reasons, in this work only a preliminary attempt to the evaluation of the erosion was performed. Two morphologies, namely the c-W and p-W deposited on top of flat Si, were selected, since they are the ones most different from each other. Further-

more, the c-W morphology is that characterised by thermophysical properties more similar to that of the pristine W [40]. Results are shown in fig-

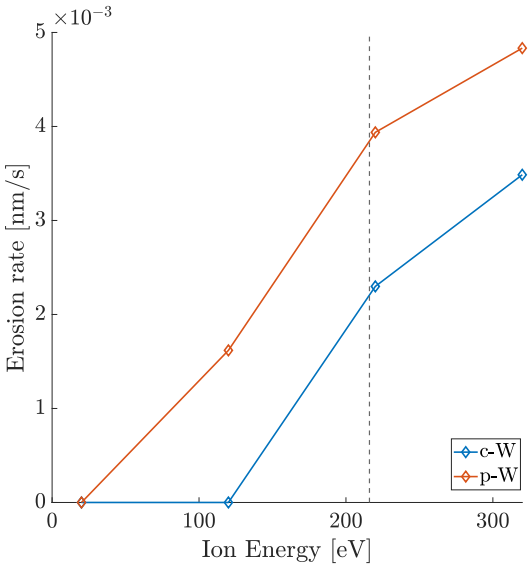


**Figure 6.16:** *Erosion rate (in* nm/s*) of the c-*W *and p-*W *coatings as a function of the ion energies. The dashed vertical line denotes the sputtering threshold of sputtering-deposited* W *as reported in [152].*

ure 6.16, where we report the erosion rate as a function of the applied bias voltage. It can be noted that the p-W coatings show a significant erosion already for an applied bias voltage of 100 V, while no step was measured for the c-W films under the same conditions, which suggest that the sputtering threshold of the p-W morphology is lower than that of the c-W. This can be related to the high O content (up to 60 % at.) in the near surface of the p-W coating. to the intrinsic oxygen content of the p-W coating [36]. A further confirmation of this comes from Energy Dispersive X-Ray Spectroscopy (EDX) measurements, taken on both the masked and the un-masked part of the samples. In this way, one can evaluate whether oxygen is preferentially sputtered. Results are reported in table 6.6. One can see that, in the masked part of the p-W sample, the O content slightly increases at higher applied bias voltages, while on the un-masked part O strongly reduces by almost a factor of two with respect to the initial concentration.
At 200 V of applied bias voltage, the c-W coating is also eroded. This should be expected since, assuming that its behaviour is akin to that of sputtered-deposited W, the sputtering threshold should be in the range of $\simeq$ 220 eV, as reported by [152] and the references quoted therein.

| | no bias | 100 V | 200 V | 300 V |
|---|---|---|---|---|
| Masked | 59.2 % | 59.8 % | 61.3 % | 60.8 % |
| Un-masked | 58.2 % | 49.6 % | 47.1 % | 37.8 % |

**Table 6.6:** O *content in the masked and un-masked part of the p-*W *samples, exposed at increasing bias voltages. The* W *concentration is readily obtained as the complementary of the* O *one. It can be noted that there is a strong reduction in the* O *content in the un-masked part of the samples, while in the masked part* O *slightly increases. This points out to a preferential sputtering of* O.

### 6.2.7 Discussion

#### 6.2.7.1 Nanostructures formation

The nanostructures observed after divertor-like exposure possess precise features. Xu et al. [49] report on the strong correlation between the nanostructure type and the crystalline grain orientation on Plansee W after the exposures to a high-flux ($10^{24}\,\mathrm{m^{-2}s^{-1}}$) D plasma, at an overall fluence of $7\times10^{26}\,\mathrm{m^{-2}}$. The ion energy was fixed to $\sim 38\,\mathrm{eV}$. In that study, three main types of surface nanostructures were identified: ripple, spongy and jagged. These last two were seen to form on those grains with a surface normal orientation directed along the $\langle 100\rangle$ and $\langle 111\rangle$ directions. The ripple nanostructure, instead, develops on those grains with other crystalline orientations. As reported in literature, two different mechanisms can contribute to the formation of surface nanostructures. In [49], their development on polycrystalline W exposed to a low energy ($\simeq 38\,\mathrm{eV}$) high flux deuterium plasma ($> 10^{24}\,\mathrm{m^{-2}s^{-1}}$, for an overall fluence of $10^{26}\,\mathrm{m^{-2}}$) has been correlated with the build-up of the D concentration near the surface, leading to a stress field. The high stress stored in the subsurface induces surface reconstruction. In addition the stress field hinders the diffusion of D toward the bulk, so that the D atoms cluster in nanocavities close to the surface causing the cyclic process of trap-mutation and dislocation loop punching and gliding, finally resulting, especially for the $\langle 111\rangle$ and $\langle 100\rangle$ orientations, in the formation of nanostructures on the top surface. In the exposures here reported, we see a nanostructures development on the surface of both Plansee (bulk) W and compact W films (both c-W and a-W) deposited on Si after the exposures to medium D fluxes ($\simeq 5\times10^{20}\,\mathrm{m^{-2}s^{-1}}$) of GyM for an overall fluence of $\sim 6\times10^{24}\,\mathrm{m^{-2}}$, if the energy of the impinging ion species is sufficiently high ($\gtrsim 100\,\mathrm{eV}$). The nanostructures obtained after the exposures performed in GyM show the same morphologies of the nanostructures obtained in literature under divertor-like conditions (see figure 6.8). In-

deed, considering the Plansee (bulk) W, the formation of the same spongy, jeagged and ripple-like structures is seen to develop. The c-Ws showed the formation of only the ripple-like nanostructure, in agreement with the fact that XRD measurements show that the preferential crystalline orientation is $\langle 110 \rangle$. From these observations we can state that the formation mechanisms are the same for tungsten exposed at divertor-like plasmas or CXN-like ion fluxes. The use of energetic ion induces the development of such nanostructures at much lower fluence values ($10^{24}\,\mathrm{m}^{-2}$ vs $10^{26}\,\mathrm{m}^{-2}$). In the present case the high energy ($100 \div 300\,\mathrm{eV}$) of the impinging species is probably enhancing the stress field present in the films leading to an early development of the nanostructures even at medium fluxes ($\sim 10^{20}\,\mathrm{m}^{-2}\mathrm{s}^{-1}$) and fluences ($6 \times 10^{24}\,\mathrm{m}^{-2}$).
In addition, since in the case of the exposures performed at $300\,\mathrm{V}$ we are over the sputtering threshold, sputtering effects could contribute to the formation and evolution of surface nanostructures. In particular, the ripple-like nanostructures that we observed on the c-W and b-W show some similiarities with the ones reported by Škereň et al. in [101], as we discussed in details in Chapter 5. We recall here that, after irradiation at energies well above the sputtering threshold, the formation of ripples at the nanoscale might be explained as due to the local variation of the sputtering yield which in turn is related to the crystalline orientation of the grains and the local ion incidence angle [101].
Exploiting the peculiarity of our nanostructured films we have the chance to study the role of crystallinity in the formation of surface nanostructures. The extension in plain of the nanostructures is seen to be related to the grain size of W (micrometric domains for bulk-W and nano domains for c-W). The presence of a crystalline grain seems to be a strong requirement for the formation of the nanostructures. In fact, the amorphous a-W films do not show any formation of nanostructures at low energy (below $\sim 200\,\mathrm{eV}$) when the film maintained its original amorphous morphology (cfr. § 6.2.5). This hypothesis is further supported by the fact that the p-W, which do not have a crystalline structure [36], did not developed any nanostructure. The development of nanostructures on a-W film takes place only after a consistent crystallization of the film.
Nanostructures formation on c-Ws and a-Ws films deposited on bulk Plansee W was also studied in [155] after exposures to a flux of $1.4 \times 10^{24}\,\mathrm{m}^{-2}\mathrm{s}^{-1}$, fluence of $2.5 \times 10^{26}\,\mathrm{m}^{-2}$ and an applied bias voltage of $-40\,\mathrm{V}$. In that case for the c-W also jagged-like nanostructures develop on the surface in addition to the already observed ripple structures. This additional morphology could be explained as due to the fact that the c-W film in [155] was

grown on Plansee W and thus might present additional W crystallographic orientation other than the $\langle 110 \rangle$, as detailed in [85]. As discussed before, these additional grain orientations favour the growth of different types of nanostructures. The a-W films of [155] also developed ripple-like surface nanostructures but with a random orientation. This could be ascribed at the effect of the higher flux and fluence respect to the present experiment, in addition a partial recrystallisation migth occur since in [155] the surface temperature was kept to $250°$ C which we showed (cfr. § 6.2.5) to be sufficient to initiate a first stage of recrystallisation.

#### 6.2.7.2 Blister formation

In our exposures, we showed that the morphology of the W coatings play a major role in suppressing blistering. Indeed, the p-W films did not blister under any of the exposures conditions considered here, as already reported in [138]. This might be due to the open morphology of this coating, which lead to a preferential desorption of $D_2$ gas trapped in the bulk of the coating. Furthermore, we showed that blistering on compact (columnar and amorphous) deposited on flat Si occurs in any of the considered exposure conditions. The shape and size of the blisters are, however, influenced by the applied bias voltage. In particular, we showed that smaller blisters are found at higher energies, and vice versa. This behavior is different with respect to bulk W where smaller blisters are favored by low energy [60].
As summarised in table 6.5, the blistering is also influenced by the surface roughness. In particular, in this work we showed that blisters can be strongly suppressed by surface roughness. Blistering is observed to occur for the W coatings deposited on flat Si and mirror-polished W, but are suppressed for rough substrates. This result finds confirmation from literature [27, 137], where however blistering suppression was observed on bulk materials and on powder metallurgy W, as in our case, for coatings.
Combining our results with literature data, we can say that the mechanism for blistering on coatings and on bulk metals are different. Indeed, for blistering on bulk metals under low energy plasma ($< 100\,\mathrm{eV}$) fluxes below $10^{23}\,\mathrm{m^{-2}s^{-1}}$, the mechanisms of crack growth and loop punching are often mentioned and refer to a plastic deformation due to D supersaturation [106]. Considering W, during the implantation of low energy deuterium ions, if the incident flux is higher than the rate of D diffusion out of the implantation range, combined with the low solubility of D in W, then a high D concentration (supersaturation) in the near surface results. This leads to stresses that are relaxed by blistering. For coatings, blistering is due to a different mechanism. In [155], blistering on W films morphologies simi-

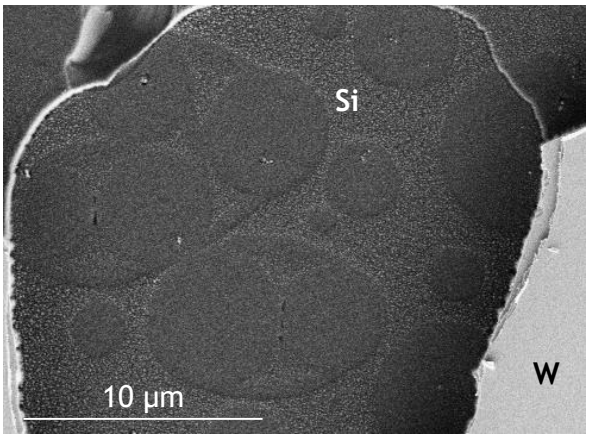


**Figure 6.17:** *SEM plain view showing the details of blister formation due to the accumulation of D at the* $\mathrm{Si}-\mathrm{W}$ *interface.*

lar to those considered in the present work was reported after low energy divertor-like (fluxes $\sim 10^{24}\,\mathrm{m}^{-2}\mathrm{s}^{-1}$ for an overall fluence of $\sim 10^{26}\,\mathrm{m}^{-2}$), plasma exposures. These studies revealed that blistering is likely to be related to the accumulation of the D at the $\mathrm{Si}-\mathrm{W}$ interface. The plausibility of this mechanism is confirmed from our exposures, as can be noted from figure 6.17, where we show a SEM plain view of the a-W coating locally delaminated due to blister-induced stresses. One readily observes the growth of spherical bubbles which can reach the $\sim 1\,\mu\mathrm{m}$ size before coalescence with other, similar, blisters occurs. The process of blister growth and coalescence continues until the pressure inside is sufficiently high to promote delamination of the coating.
In addition to coating's morphology, the roughness of the substrates and the coating's thickness, blistering can be also influenced by the residual stress at the coating-substrate interface. As regard this latter aspect, in [85] D retention in W films deposited by Magnetron Sputtering (MS) on mirror-polished Plansee W and Si is investigated by Nuclear Reaction Analysis, after exposures to a D plasma in PlaQ with fluences in the range of $10^{24}\,\mathrm{m}^{-2}\mathrm{s}^{-1}$ and ion energy of $38\,\mathrm{eV}$. The morphology of the W coatings grown by MS is very similar to that of our c-Ws. Blistering was observed only for the W film grown on Plansee W. This result can be explained by a residual-stress argument. Indeed, it is known (e.g. [56]) that residual stresses at the film-coating interface strongly depend on $i$) the film and substrate materials and $ii$) on the deposition technique: $i$) are due to thermal stresses, while $ii$) strongly depend on the energy of the species deposited

on the substrate. The final state of residual stress depends on which of these two mechanisms dominate over the other. For high energy of the impinging species during the deposition (as it happens for PLD-deposited coatings) the latter usually dominates over the former. It is likely that the process of blister growth is strongly inhibited by tensile stresses, while it is favoured by a compressive stress. Indeed, in our case the growth of a blister induces a compressive stress that adds to the already compressed films. This argument applies, of course, for the compact coatings (c-W and a-W) where the energy of the species deposited on the substrate after the ablation process is high. To relax the pressure-induced stress, the film buckle leading to its detachment from the interface. The opposite happens in the case of a tensile residual stress (as it occurs for films deposited by MS), where the strain induced by the blister is inhibited.

## 6.3 W and W-based coatings exposures to He plasmas

This Section aims to summarise the main results related to the exposures of different W morphology to GyM He plasmas. The results reported here have been obtained in collaboration with a Ms.C. student which I co-supervised. Similarly to what presented in § 6.2, we start by providing the motiviations behind the experimental campaign. This should allow to better undertsand the choice of plasma exposures parameters that we considered (cfr. § 6.3.2). He plasma induced modifications are finally discussed in § 6.3.3. We recall that the He plasma exposures here reported were carried out by a Ms.C. student which I co-supervised.

### 6.3.1 Motivations

As stated in § 2.4.2, He can have important impact on the morphological and structural modifications of W, particularly in the case of fuzzy-W formation. In this respect, depsite the great amount of studies the detailed mechanism for the formation and development of this peculiar morphology is still largely unknown. Furhermore, only very few articles have tried to investigate the effects of He plasma on W in conditions outside the domain routinely recognised as the one in which fuzzy-W develops, and even less have taken into account the possible effects of unconventional morphology and structure, such as those of the W coatings produced via the PLD. We recall from the discussion made in § 2.4.2 that fuzzy-W develops provided that the following conditions are met:

- particle fluence $\geq 10^{24}\,\mathrm{He/m^2}$

- He energy in the range $20 \div 30\,\mathrm{eV}$
- surface temperature $T_{\mathrm{surf}} > 0.25 T_{\mathrm{melt}}$, where $T_{\mathrm{melt}}$ denotes the melting temperature

To investigate the morphology, structure and composition dependence of the He induced modifications, the following W samples were considered:

- c-W
- p-W
- fuzzy-like W

All these coatings were deposited on flat Si $(100)$ substrates in order to facilitate post-exposures analysis. Furthermore, as it occurred for the D exposures, the W films were partially masked prior to the plasma irradiation with small Mo sheets, in order to assess the erosion by SEM analysis (see the discussion reported in § 6.2.2). Unfortunately, only one sample of fuzzy-like W was available for the exposures, so that this last morphology was only exposed to condition $a)$ in table 6.7. In addition to the PLD-produced coatings, a bulk W samples was also loaded, for both exposures $a)$ and $b)$, in order to compare results with literature data.

### 6.3.2 GyM He plasmas parameters

In order to investigate the surface modifications, nanostructure formation and erosion of the different W morphology outside the domain necessary for fuzz formation, we have taken as starting point the work of Sakamoto et al. [92], where exposures of bulk polycrystalline W has been performed. Inspired, by the main plasma parameteres reported by the authors, two different exposure conditions were considered in GyM. A summary of the main plasma parameters is reported in reported in table 6.7. In the last col-

| Exposure | $\phi\ \left[\mathrm{m^{-2}s^{-1}}\right]$ | $\Phi\ \left[\mathrm{m^{-2}s^{-1}}\right]$ | Bias [V[ | $T_{\mathrm{bp}}\ [^{\circ}C]$ |
|---|---|---|---|---|
| a) | $5 \times 10^{20}$ | $7.01 \times 10^{24}$ | -50 | 297 |
| b) | $4.8 \times 10^{20}$ | $6.94 \times 10^{24}$ | -120 | 347 |

**Table 6.7:** *Details of the main* He *plasma parameters achieved in GyM during the* He *exposures.*

umn, we reported the temperature reading by the thermocouple pressed behind the backplate, as it occurred for the exposures performed to D plasmas (see the discussion made in § 6.2.2). In particular, a temperature difference

of around 100 K between the backplate and the W surfaces is expected. It should be noted that, even accounting for this difference, it is possible to ensure with good confidence that the samples surface remained below the fuzz formation threshold.
As already stated, the main He exposures parameters were chosen on the basis of [92]. However, differently from this study, the exposure $b)$ was performed with an applied bias voltage of $-120$ V. In this way, also accounting for the plasma potential, the energy of the impinging ion species was raised to $\simeq 150$ eV. This particular value was chosen since it is above the sputtering threshold of policrystalline W exposed to He which is known to be around $\simeq 105 \div 110$ eV, as reported in [113].

### 6.3.3 Results - nanostructures formation

In this section, we report the modifications of the plasma-induced modifications at the nanoscale.
Figure 6.18 reports a summary of the He induced modifications of the different W samples for the two exposures conditions $a)$ and $b)$ reported in table 6.7. From this figure, one can see that a ripple-like nanostructures develop on the surface for both the c-W and bulk-W, already for energies of 80 eV. These nanostructures become more marked increasing the energy to 150 eV. On the other hand, the p-W and fuzzy-like W does not show the formation of any nanostructures. Rather, on the p-W a progressive smoothing of the surface occurs, while on the fuzzy-like W a coalescence of the arborescent morphology occurs. This effect seems to be strongly connected with the energy of the impinging ion species.
Particularly interesting is the analysis of the nanostructures developed on the b-W. As it occurred for the exposures to D plasmas, a further investigations by SEM revealed a strong dependence of the nanostructures qualitative features on the crystalline grains. This is shown in figure 6.19. In particular, the width of the undulations and their from is a function of the grain orientation, as reported by Sakamoto et al. in [92]. However, one should notice that in our case the exposures conditions were not exactly the same as those reported by the authors of [92]. Indeed, the fluence for the GyM exposures was lower and the energy of the impinging ion species higher than the ones reported by Sakamoto et al.
The nanostructures observed on the c-W samples have some important differences with respect to the ones observed on the bulk-W. Indeed, as seen from figure 6.18, they cover the entire exposed surface and no dif-

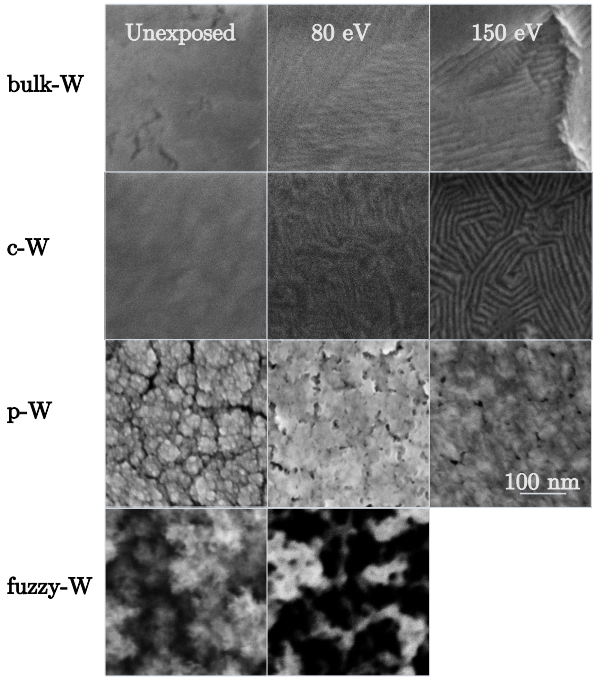


**Figure 6.18:** *SEM plain view showing a summary of the surface morphology evolution at the nanoscale after the exposures in plasma conditions a) and b) of table 6.7. The length scale applies for all the SEM figures.*

ferences can be appreciated moving from one position to another. Said otherwise, some ripples seem to be able to overcome the grain dimension (about $50\,\mathrm{nm}$) and some others close on themselves forming an intricate spiraling pattern. All these features are absent on the bulk-W samples.

### 6.3.4 Results - erosion of the W coatings

Erosion measurements of the W samples was evaluated by performing SEM cross-sections measurements, similarly to what already reported in cfr. § 6.2.2). Thus, for this reason, only the erosion of the W coatings was assessed. For the fuzzy-like W, the erosion measurements were not possible with sufficient confidence due to its non compact nature and its extremely variable height along the cross-section, even before exposure. Table 6.8 shows the erosion rate of the c-W and p-W coatings as a function of the incident ions energy. It should be noted that no step could be measured on the c-W for incident ion energies of $80\,\mathrm{eV}$, consistently with the fact that the threshold for physical sputtering of bulk-W is in the range

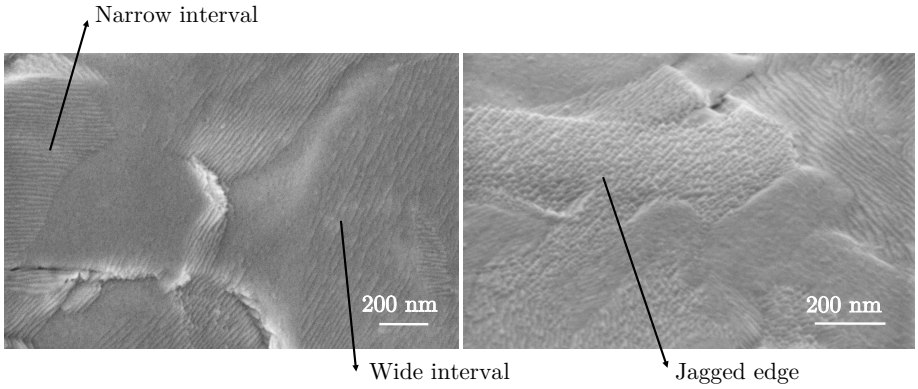


**Figure 6.19:** *Low magnification SEM images showing the dependence of the nanostructures qualitative features on the particular crystalline grain. The chosen nomenclature for the identification of these nanostructures is based on Sakamoto et al. [92] to facilitate comparison with their results.*

| | 80 eV | 150 eV |
|---|---|---|
| c-W | 0 | 2.7E-03 |
| p-W | 3.8E-03 | 7.6E-03 |

**Table 6.8:** *Erosion rate (in* nm/s*) of the* c-W *and* p-W *coatings exposed to* He *plasmas as a function of the incident ions energy.*

$105 \div 110$ eV. At 150 eV, instead, the c-W starts to erode. The p-W shows a significant erosion also below the sputtering threshold of bulk-W, as already noted in § 6.2.6. Again, this points to the fact that the sputtering threshold of the p-W is lower than than of the c-W. At 150 eV the erosion rate of p-W is more than double that of the c-W, which can be explained as due to the fact that the p-W has a much lower density than that of c-W [36].

### 6.3.5 Discussion

After He exposures, the development of surface nanostructures been observed on the c-W coatings and the b-W, in plasma conditions well outside the domain for fuzz formation (cfr. § 6.3.1). On the other hand, no nanostructuring was observed for the porous coatings, namely the p-W and fuzzy-like W samples, that is on the W films which do not show any crystalline structure. Thus, as already observed in § 6.2.7.1, we can conclude that cristallinity plays a pivotal role in the formation of surface nanostruc-

tures also in the case of He plasma exposures.
The relevance of the morphology change after irradiation is a strong function of the incident ion energy, as clearly seen from figure 6.18. In particular, surface modifications at the nanoscale start to appear on the surface for He energies around $\simeq 80\,\mathrm{eV}$ and become more marked at $150\,\mathrm{eV}$. This observation is of relevance. Indeed, we recall that the sputtering threshold for W irradiated with He is around $105 \div 110\,\mathrm{eV}$ according to [113]. This suggests that sputtering phenomena do play a major role in determining the evolution of surface nanostructures at ion energies above the sputtering threshold, that is for the exposures performed at $150\,\mathrm{eV}$, but cannot be claimed to be responsible for their development at $80\,\mathrm{eV}$. This argument apply, however, only if one is sure that no heavy plasma impurities contribute to the sputtering of our samples.
The literature related to sputter-induced morphology change have already been summarised in Chapter 5. Here, we will recap the main literature results, particularly focusing on trying to understand whether these can explain our findings. We recall that, historically, one of the first attempt to describe surface morphology evolution (i.e. ripples formation) after energetic ion irradiation was proposed by Bradley and Harper (cfr. equation (5.1)) on the basis of the Sigmund's theory of sputtering. We recall, further, that this equation was derived having in mind amorphous materials. In addition, the ripples formation is describe in this model as due to instability related to the sputtering yield dependence on the incidence angle, $\theta$. In particular, for low angles of incidence, a ripple pattern perpendicular to the ion beam should develop, while for grazing incidence the ripple pattern should become parallel to the ion beam. For incidence angles almost aligned with the surface normal, the ripple pattern should cease and instead be replaced by pits, as reported in [11]. These observations are in compliance with the observations on the amorphous solids, whereas on metals only ripples parallel to the ion beam can be observed in off-normal incidence [101]. Moreover, it has been observed that ripples formation on crystalline materials should cease at low temperature, while BH instability is not thermally activated. Thus BH is not responsible for pattern formation in our exposures. Neither is, however, the mechanism proposed by Škereň (cfr. § 5.1.2). Indeed, we recall that the letter describe ripples formation as due to: $i$) the crystalline grains orientation dependence of the sputtering yield and $ii$) the dependence of the sputtering yield on the local incidence angle, $\varphi$, provided that the nominal incidence angle, $\theta$, is inclined with respect to the normal. This is clearly in contrast with our exposures, where ripples were observed at normal incidence.

A model that tries to overcome this limitation has been proposed by Valbusa et al. [156], which takes into account the so-called Ehrlich-Schwoebel (ES) barrier. In particular, to this effect, surface adatoms that on the surface can encounter an energy barrier when trying to descend atomic steps, and its efficiency is a function of the crystallographic orientation. With this model, ripples formation is possible even at normal incidence [156]. Furthermore, since the threshold for adatoms formation is well below the one needed for physical sputtering to occur (cfr. [133]), then the ES barrier could explain ripples formation in our exposures. However, according to the authors, ES barrier can be considered responsible for ripples formation only if the temperature is sufficiently low, that is lower than 350 K, since adatoms would have otherwise enough energy to overcome the potential barrier step. Since, in our case the surface temperature is above this value, one cannot ascribe the ES barrier to be responsible for nanostructuring in our exposures.
Other theories try to correlate the undulating structures with the formation of He nanobubbles [80]. Indeed, similarly to what stated in § 6.2.7.1, He can be trapped at defects and push the W lattice as pressure inside the bubbles increases. This slipping effect results in different surface structures according to the crystallographic orientation of the grains [80]. The possible formation of He bubbles could not be investigated in this thesis work, additional studies should be performed to verify this phenomenon. However, as suggested also in previous studies, the observation of jagged edge nanostructures on W-bulk seems to be hardly related to slipping effects [92].

CHAPTER 7

# Conclusions

In this Ph.D. work, investigations in the field of Plasma-Material Interaction (PMI) in Linear Plasma Devices (LPDs) were carried on, adopting an in-depth numerical and experimental approach. In this last Chapter we shall draw the main conclusion of this work, starting first from a brief recap of the main body of the thesis.
Chapter 1 described in details the physical principles of nuclear fusion and, in particular, how to achieve these reactions on Earth in a controlled environment for energy production purposes. Here, the magnetic confinement strategy was outlined and the tokamak concept was introduced, showing the necessity of field line twisting starting from a single particle picture. We concluded the Chapter by presenting the ITER project.
In Chapter 2, we focus on the pivotal aspect of PMI in magnetic confinement research. Here, we detailed the most relevant physical processes that occur when plasmas and solid materials touch each others. We stressed, in particular, the strongly coupled and multi-scale nature of these physical phenomena, thus introducing in a natural manner the necessity to use both a numerical as well as an experimental approach to study and control PMI.

The most relevant numerical codes for the plasma and the materials modelling were introduced. Additionally, the important role of LPDs in PMI research was presented.
In Chapter 3, the main computational and experimental tools that were used in this Ph.D. work were outlined. More importantly, here we discussed the main goal of the present Ph.D. work, which consisted in performing a numerical and experimental study of PMI in LPDs. The focus was mainly on non-hydrogenic plasma species (Ar and He) and W. In particular, in light of the open questions that we posed in 3 and of the main results which have been summarised in Chapters 4, 5 and 6, we can say that, as far as the numerical side of this Ph.D. is concerned:

- *Can edge plasma codes be applied to LPDs with suitable adaptations?* The detailed code analysis (cfr. Chapter 4) that I performed during my Ph.D. work in close collaboration with another Ph.D. candidate allowed me to understand that edge plasma codes such as SOLPS can be applied also to LPDs, by exploiting the code feature that are alrealy implemented. In particular, thanks to the analysis carried on, it was possible to get for the first time a full understanding of how this code works when applied to the simplified geometry of linear machines. Additionally, the modelling of pure Ar plasmas was also performed for the first time with the SOLPS-ITER code.

- *What are the most relevant terms in the SOLPS equations that ultimately the GyM parameters in its current configuration?* Thanks to the dedicated sensitivity scan on SOLPS-ITER free parameters (cfr. Chapter 4), I was able to understand that the main plasma parameters in GyM are mostly influenced by the interaction with neutral atoms, while plasma transport only plays a minor contribution, at least in its current configurations.

- *Can we predict experimentally-measured plasma parameters in GyM?* The results of the sensitivity scan reported in Chapter 4 were compared with experimentally available plasma parameters in the GyM LPD showing that the overall qualitative and quantitative trends are well captured by the simulations. Additionally, expanding further the database of available SOLPS simulations, a NN capable of generalising from its training set was developed.

- *Can we simulate numerically the surface morphology evolution via ERO2.0 and compare the results with experimental measurements?* The detailed analysis of the ERO2.0 code that I performed in this

Ph.D. work (summarised in Chapter 5) allowed me to critically analyse its model for surface morphology evolution. In particular, the literature study that I conducted in collaboration with a Ms.C. student that I co-supervised allowed me to identify a model - the Škereň's model (SM) - which shows a great similarity with the one currently implemented in ERO2.0. A careful comparison of the SM on simple, analytically-defined surfaces, and realistic W surfaces retrieved from experiments (reported in Chapter 6) carried on in the framework of this Ph.D. work showed a satisfactory agreement. However, the comparison of the SM and ERO2.0 with experimentally-available data revealed discrepancies which point to deficiencies in both models.

Similarly, as regards the experimental aims:

- *What is the behaviour of nanostructured W samples when exposed to the GyM plasmas?* The exposures of W samples in GyM D and He plasmas (summarised in Chapter 6) revealed several modifications at the nano and micro-scale. This modifications were also previously reported in literature, but here they were observed in a rather new plasma regime, in terms of ion energy and particle fluxes. The exposures allowed me to further extend literature results regarding possible explanation for their formation.

- *What are the qualitative features of the plasma-induced modifications on these specimen and how do they relate to those of bulk W?* Plasma-induced modifications on the PLD-deposited unconventional W coatings were thoroughly compared with those observed in our exposures on policrystalline W. Interestingly, we observed on both similar modifications, in spite of the fact that their structure, morphology and composition can differ substantially.

A natural continuation of this Ph.D. project involves both numerical and experimental activities. These could deal with:

- For the SOLPS-ITER modelling, additional sensitivity scan could be performed, varying not only the main code free parameters reported in Chapter 4, but also the plasma species (e.g. He or $D_2$). This will allow to build a much larger database of numerical simulations with respect to that considered in the framework of this Ph.D. work (see, in particular, § 4.3.5). The latter can, in turn, be used to further improve the Neural Network build as a preliminary activity during this Ph.D.

- For the ERO2.0 modelling, the implementation of additional physics

can be pursued, adding for example the dependence of the sputtering yield on the crystalline grain orientation. Further benchmark of code results could also be performed, by dedicated exposures of PLD-produced coatings.

- An integrated coupled SOLPS+ERO2.0 modelling of GyM is also of great relevance. This would allow to interpret experiments carried on in GyM related to the measurements of the S/XB spectroscopy parameter.
- The production of other W-based coatings could be pursued via the PLD. One possibility could consists in the precise and simple morphology, such as for example periodic sines and pillars, to be given as an input for ERO2.0 modelling.
- Exposures of the aforementioned coatings to GyM fusion-relevant plasmas aiming to benchmark ERO2.0 results.

# Appendices

APPENDIX $\mathcal{A}$

# The validity of the fluid approximation in edge modelling

Fluid edge plasma models are largely based on the equations originally proposed by Braginskii in [12]. However, the validity of a simplified fluid description of the plasma should not be taken for granted, even for common neutral fluids described by the Navier-Stokes equations. Indeed, it is known from kinetic theory that such a description ceases to be valid when the characteristic length scale of the system, $L$, become comparable with the particles **mean-free path** $\lambda$, that is the path travelled by fluid particles in between collisions. Thus for a neutral fluid to be described by fluid equations the following condition should be satisfied:

$$L \gg \lambda \tag{A.1}$$

If this condition is not satisfied, then one needs to describe the fluid kinetically.
In the case of a plasma, condition (A.1) needs to be somewhat rephrased. Indeed, as already mentioned, transport in a magnetised plasma is strongly

anisotropic, occurring much faster in the parallel direction than the perpendicular one. Plasma transport in the former direction is called **classical**. It is indeed rather well understood and a complete theory for it exist based on perturbative solution of the Boltzmann equation for the plasma [8, 12, 160]. Due to this anisotropy of the plasma transport, the condition (A.1) can be somewhat relaxed [12, 121]. Indeed, since the motion of a charged particle is bounded in the direction orthogonal to the magnetic field, then one needs to distinguish two different macroscopic length scales $L_\parallel$ and $L_\perp$, and write the conditions for the applicability of the fluid modelling as

$$L_\parallel \ll \lambda, \quad L_\perp \gg \rho \tag{A.2}$$

where $L_\parallel, L_\perp$ denote respectively the characteristic parallel and perpendicular scale of variation of the macroscopic quantities, while $\lambda, \rho$ correspond to the mean-free path and the Larmor radius. We need then to identify suitable parallel scale lengths in order to verify the inequality (A.2). The macroscopic scale length of variation of the scrape-off layer can be taken to be [151]

$$L_\parallel = \frac{\pi a}{B_\theta} B_\varphi \tag{A.3}$$

at least in the case of poloidal divertor or toroidal limiter. In this expression, $a$ denotes the minor radius, while $B_\theta, B_\varphi$ denote respectively the poloidal and toroidal component of the magnetic field.
In table A.1 two examples are given comparing the comparing the mean

| | JET | CMOD |
|---|---|---|
| $T_e$ [eV] | 50 | 10 |
| $n_e$ [$\mathrm{m}^{-3}$] | $10^{19}$ | $10^{20}$ |
| $L_\parallel$ [m] | 40 | 8 |
| $\nu_e$ | 25 | 1000 |
| $\lambda_{ee}, \lambda_{ii}$ [m] | 2.5 | 0.01 |
| $\tau_{\mathrm{SOL}} = L/c_s$ [m] | 0.6 | 0.3 |

**Table A.1:** *Representative SOL conditions. $\nu_e$ denotes here the ratio of the electron collision frequency to the electron bounce frequency. The bounce frequency is that at which electrons trapped in banana orbits oscillate back and forth between the turning points. If $\nu_e \gg 1$, then the collisionality is too strong to permit the electrons to behave neo-classically. From [151].*

free path, $\lambda$, and the characteristic parallel macroscopic dimension, $L_\parallel$, for JET and the Alcator CMOD tokamak. This table shows that the SOL is usually sufficiently collisional to ensure that a fluid description in the parallel

direction can be applied. However, in some circumstances the situation can be sometimes marginal. In addition, when a plasma interact with solid surfaces, the formation of the sheath occurs [151].This region presents a characteristic scale of variation approximately equal to the Debye length which can be extremely small and thus comparable with respect to the collisional mean-free path. In fluid codes, it is therefore customary to take the sheath entrance as the boundary of the computational domain and to impose appropriate boundary condition [151].
To make sure that the steep gradients expected near the sheath entrance do not lead to unphysical results, special measure such as heat flux limiters (e.g. [21]) need to be taken. For example, consider heat transport for the sake of simplicity, if the heat gradients in the plasma are large the diffusive approximation breaks down. This failure occurs when the mean free path of the electrons approaches the spatial scale of the temperature gradient. In this regime the heat transport is dominated by hot electrons free streaming from the hot portions of the plasma to the cooler regions. These hotter electrons are characterised by a much lower value of the mean-free path and, therefore, they can be much less collisional that the average electrons. In such conditions, using the fluid approximations for the parallel heat fluxes and viscosity lead to a non-physical result in case of steep gradient [151]. To take this into account, still remaining within the fluid approximation, corrections to the classical fluid transport coefficients are introduced. In B2.5 the following expression with so-called **flux limits** are available

$$\kappa_{\parallel} = \frac{\kappa_{\mathrm{SH}}}{1 + |q_{\mathrm{SH}}/q_{fl}|} \tag{A.4}$$

with the classical Spitzer-Härm heat flux:

$$q_{\mathrm{SH}} = -\kappa_{\parallel,\mathrm{SH}} \nabla_{\parallel} T_e \tag{A.5}$$

and the flux limit:

$$q_{fl} = \alpha n_e T_e^{3/2} \sqrt{m_e} \tag{A.6}$$

From kinetic simulations for electrons the coefficient $\alpha$ in this expression is about $\simeq 0.2$; however, the situation for ions is much less clear. A similar discussion applies also to the momentum heat flux.

APPENDIX B

# The Plasma Sheath

In all plasma applications, it occurs that the plasma touches the solid walls of the vessel used to contain it. For example, it the relevant case of MCF, this can occur due to plasma leaking from the confinement region. One thus need to address the important question of what does it happen when the plasma touches the wall. We shall consider here the simple case of a plasma confined in a 1D region of space and, furthermore, limit ourselves to the consideration in which the magnetic field is directed parallel to the solid walls.

We start first by giving some qualitative understanding of the relevant processes. When ions and electrons touches the wall they recombine and are therefore lost. However, since the electrons have much higher thermal velocities (due to their smaller mass) than the ions, they are lost faster and leave the plasma with a net positive charge. The plasma must therefore have a positive potential with respect to the wall. This potential cannot be distributed across the entire plasma, due to the Debye shielding phenomenon, discussed in § 1.2, which confine the potential variation in a thin region of space, of the order of several Debye lengths in thickness. This

layer, which develops everytime a plasma touches a solid surface, is called the **sheath**. The sheath forms a potential barrier so that the lighter species (usually electrons) are confined electrostatically. The height of this potential barrier adjust itself in such a way to maintain ambipolarity, i.e. an equal flux of electrons and ions reaching the walls.
To describe the potential distribution in the sheath, we shall consider again the discussion made in § 1.2, this time also considering the motion of the ions. We let $x = 0$ be the location were the ion enters the sheath main plasma and assume that they have a drift velocity of $v_0$. The latter is required in order to account for the ions that are lost to the wall. In principle, ions that enters this region are described by a suitable distribution function. For simplicity, however, we shall consider the case in which $T_i \to 0$ so that all ions have the same velocity. Furthermore, since the characteristic dimension of the sheath is of the order of some Debye lengths, we may further assume that it is collisionless. Under this circumstances, the ion velocity distribution in the sheath can be easily computed using the conservation of energy, obtaining:

$$v\left(x\right) = \left(v_0^2 - \frac{2e\phi}{m}\right)^{1/2} \tag{B.1}$$

Using the ion continuity equation, one can then obtain the ion density distribution in the sheath:

$$n_i\left(x\right) = n_0 \left(1 - \frac{2e\phi}{mv_0^2}\right)^{-1/2} \tag{B.2}$$

The electron population is instead described by the Boltzmann factor relation:

$$n_e\left(x\right) = n_0 \exp\left(\frac{e\phi}{kT_e}\right) \tag{B.3}$$

Substituting this expression in the Poisson equation, one obtains:

$$\epsilon_0 \frac{\mathrm{d}\phi^2}{\mathrm{d}x^2} = en_0 \left[\exp\left(\frac{e\phi}{kT_e}\right) - \left(1 - \frac{2e\phi}{mv_0^2}\right)^{-1/2}\right] \tag{B.4}$$

In particular, setting:

$$\chi = \frac{e\phi}{kT_e}, \quad \xi = \frac{x}{\lambda_D} = x\left(\frac{n_0 e^2}{\epsilon_0 kT_e}\right)^{1/2}, \quad M = \frac{v_0}{\left(kT_e/m\right)^{1/2}} \tag{B.5}$$

one can write equation (B.4) as:

$$\chi'' = \left(1 + \frac{2\chi}{M^2}\right)^{-1/2} - e^{-\chi} \tag{B.6}$$

where the $'$ denote differentiation with respect to $\xi$. Equation (B.6) can be integrated once simply by multiplying both sides by $\chi'$ and setting $\chi = 0$ at $\xi = 0$, obtaining:

$$\frac{1}{2}\left(\chi'^2 - \chi_0'^2\right) = M^2\left[\left(1 + \frac{2\chi}{M}\right)^{1/2} - 1\right] + e^{-\chi} - 1 \tag{B.7}$$

A second integration to find $\chi$ is not possible analytically. However, important considerations can be made by noting that the RHS of this equation must be positive for all value of $\chi$. In particular, for $\chi \ll 1$, one can expand the RHS in Taylor series and obtain the following inequality:

$$M^2 \geq 1 \tag{B.8}$$

This inequality is called the **Bohm sheath criterion**. It tells that the ions must enter the sheath with a velocity greater or equal than the acoustic velocity (cfr. equation (B.5)). It is of particular relevance in edge plasma modelling. Indeed, in edge plasma modelling the boundary conditions to be applied when the plasma touches a solid surfaces are not known, due to the development of the sheath. Since the characteristic dimension of the sheath is very small (some Debye lengths), a fluid description of the plasma cannot be applied here. Rather, one takes the sheath entrance as the boundary and imposes here the bondunary conditions.

Up to now, we have analysed in some details the case of a plasma in absence of externally imposed magnetic field. The same considerations, as already stated, applies also for the case of a magnetised plasma were the magnetic field intersect at normal incidence. This is, however, not the case of interest in tokamaks, were the magnetic field direction can be almost tangent to the solid surface [151]. In this case, additional considerations need to be made, as clearly described by Chodura [15]. In particular, in the pre-sheath were the electric fields are small and so the motion of the charge particles occurs almost parallel to the magnetic field. The former, if the wall is a pure conductor, is parallel to the surface normal and, therefore, it is in general oblique to the magnetic field. The intensity of the electric field can become dominant when the plasma ions reaches the sheath entrance and it bends their trajectory from the parallel-to-B direction towards the surface normal. These physical processes are clearly visualised in figure B.1. Therefore,

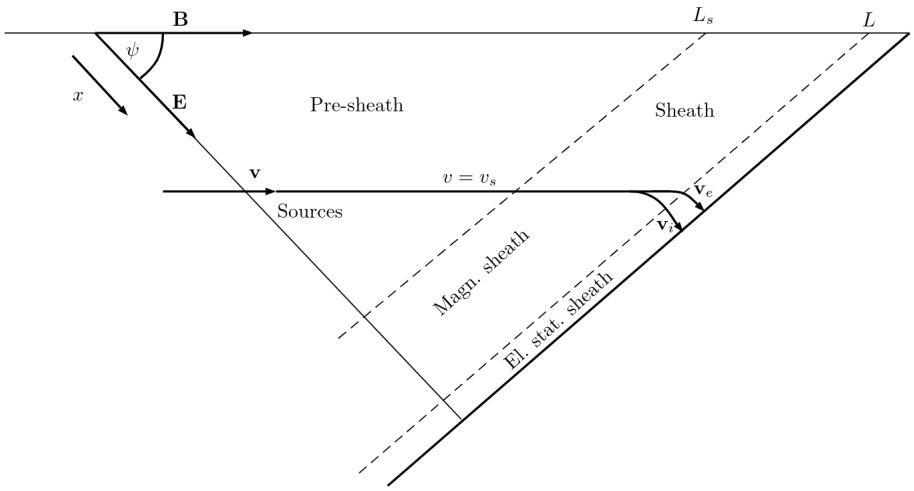


**Figure B.1:** *Schematic view of the pre-sheath and sheath in the case of an oblique magnetic field. From [15].*

in the case of an inclined magnetic field with respect to the wall normal, the sheath develops an additional zone, called the **magnetic pre-sheath**, located before the electrostatic sheath and characterised by globally neutral flows [15, 151]. By considerations similar to those leading to (B.8), it is possible to show that, in addition to the Bohm criterion, the ion velocity in the direction parallel to the magnetic field at the entrance of the magnetic pre-sheath must satisfy the following inequality [15]:

$$M_{\parallel} \geq 1 \tag{B.9}$$

where $M_{\parallel}$ denotes the parallel Mach number.

APPENDIX C

# Python code for mesh construction in LPDs

This Appendix aims to briefly describe the Python code which was developed during this Ph.D. project for constructing a field aligned quadrilateral grid for SOLPS-ITER modelling of LPDs. It should be noted that no specifical code need to be developed for building the triangular mesh needed by EIRENE. Indeed, recalling the discussion made in § 3.2, the latter is an unstructured grid, for which the standard **Triang** tool available with the SOLPS-ITER code package can be straightforwardly applied also for LPDs.
Under the assumption of axisymmetry, the computation of the magnetic field in a tokamak or a LPD can be easily computed solving the Grad-Shafranov equation [121]:

$$\Delta^* \psi = -\mu_0 R J_\varphi \tag{C.1}$$

In this equation, $\Delta^*$ is the Stokes operator defined as

$$\Delta^* = R\partial_R \left( \frac{1}{R} \partial_R \psi \right) + \partial_Z^2 \psi, \tag{C.2}$$

$\mu_0$ the vacuum magnetic permeability and $J_\varphi$ the toroidal currents. These include contributions either coming from the plasma itself or those due to external coils. For a linear plasma device, the former can in general be neglected. The $\psi$ function plays the role of a stream-function: its level set contains the magnetic field lines. Indeed, the latter can be simply compute as

$$B_R = \frac{1}{R}\frac{\partial \psi}{\partial Z} \tag{C.3}$$

$$B_Z = -\frac{1}{R}\frac{\partial \psi}{\partial R} \tag{C.4}$$

Solution of equation (C.1) can be based on several approaches. One of the possibility involves the Green's function for the Stokes operator, that is the solution of (C.1) can be written as

$$\psi\left(R, Z\right) = \iint G\left(R, Z; R', Z'\right) J_\varphi\left(R', Z'\right) \mathrm{d}R' \mathrm{d}Z' \tag{C.5}$$

with

$$G\left(R, Z; R', Z'\right) = \frac{\mu_0}{2\pi}\frac{\sqrt{RR'}}{k}\left[\left(2 - k^2\right) K\left(k\right) - \right.$$
$$\left. - 2E\left(k\right)\right]$$
$$k^2 = \frac{4RR'}{\left(R + R'\right) + \left(Z - Z'\right)^2}$$

In this expression, $K\left(k\right)$ and $E\left(k\right)$ are the elliptic integrals of the first and second kind, respectively. In the remaining of this section, we shall describe the Python code developed for the construction of the equilibrium magnetic field. The code rely on the Python library `numpy` and `scipy`, as it will be described in the following. For the computation of the integral in (C.1) knowledge of the position of the different coils and their current density is needed. Coils information are stored in the Python class `Coils`. The `__init__` method first ask for a .txt file where the geometrical information of the coils and the current flowing in each of the windings are stored. The method `ComputeCurrents` then computes the current density, simply dividing the current by the cross-sectional area (a rectangle) of each coil and storing the information in the variable `Jc`.
Once the relevant geometrical and physical information of the external current coils are known, one can compute the equilibrium solving the Grad-Shafranov equation (C.1) or, equivalently, the integral form (C.5). This is

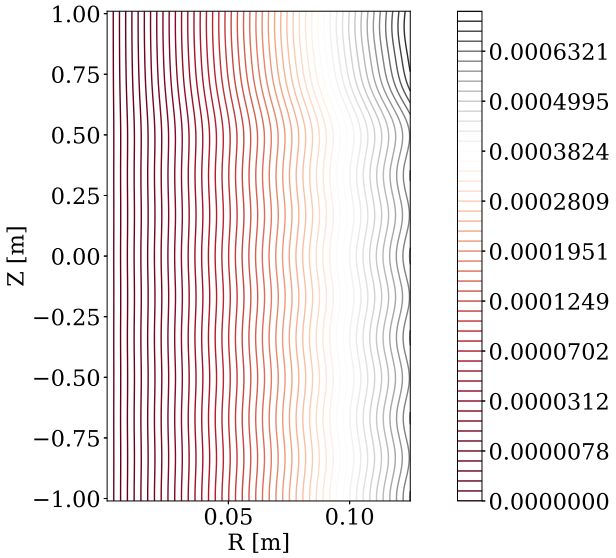


**Figure C.1:** *Contour lines of the stream function $\psi$ for the standard magnetic configuration of the GyM LPD.*

done the class `Equilibrium`. The `__init__` method take as an input six parameters, `def __init__(self, r1, r2, z1, z2, Nr, Nz, Nc = 10)`, which define the extension of the square computational domain where the equilibrium is to be computed as well as its resolution (the number of points in the radial, `Nr`, and axial, `Nz`) direction). The seventh argument, `Nc=10` is optional and it is related to the discretisation of the square domain defining the cross-sectional area of each of the magnetic field coils. The core of the computation occurs in the `ComputePsi` method. Three nested loop are used to compute the Green function for the GS operator, which is first initialised as a $4D$ numpy array. The first **`for`** loop ranges over the number of external magnetic field coils, `Ncoil`. The remaining two over the square domain, `Nc`×`Nc`, defining the coils extension. The elliptic integrals of the first and second kind are computed with the `ellipk` and `ellipe` functions in `scipy`. Integration of equation C.5 is then performed thanks to the trapeziodal method `trapz` in `numpy` and the result stored in the $3D$ numpy array `psi_coil`. Finally, the contribution from each of the external magnetic field coil is summed over and the result is stored into the $2D$ numpy array `psi`. Once the information of the $\psi$ function is known over

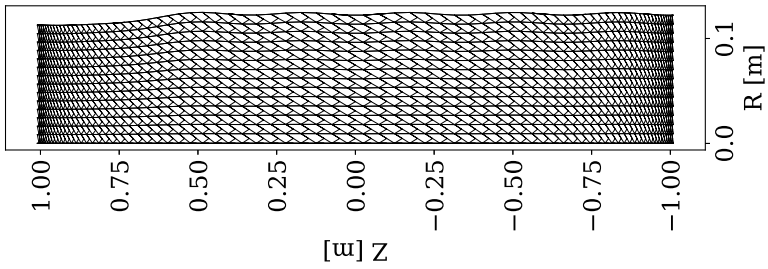


**Figure C.2:** *Quadrilateral, field-aligned grid constructed with the Python code presented in the text. The grid refers to the stadandard magnetic configuration of the GyM LPD (see § 3.4.3).*

all the `Nr`$\times$ `Nz`, one can compute the two component of the magnetic field $B_R, B_Z$ using equations (C.3) and (C.4). This is numerically performed in the method `ComputeField` of the class `Equilibrium` using a standard finite difference scheme and the result is stored in the two $2D$ numpy array `Br,Bz`. As an example, we show in figure C.1 the contour lines of the $\psi$ function for the standard magnetic configuration of the GyM device. The construction of this type of grid is performed in the class `Mesh`. The constructor method takes as input four quantities, namely the equilibrium (`Eq`), the number of grid points in the radial direction (`m`), the number of grid points in the axial direction (`n`) and the position of the vessel vacuum chamber (`Rlim`). Additionally, two hidden properties of the `Mesh` class are also defined, namely `Ncont` and `LowerPsiValue`, whose role will be described in the following. The constructor first computes the last magnetic field lines before intersection of the level-set of $\psi$ with the vacuum vessel position (specified by `Rlim`) occurs. This is done in the `ComputeLastPsi` method. Here a `numpy` array , `ContourLevels`, of dimension `Ncont` is first defined, ranging from `LowerPsiValue` and `psi.max()`. The contour lines of $\psi$ are then computed and the result stored in `Cnt`. Then, an empty list `lines` is defined. A **`for`** loop cycles over the dimension of `ConourLevels` (i.e., `Ncont`). An inner **`for`** loop is then performed, which cycles over all the computed contour lines (`Cnt.collections[it].get_paths()`). The vertices ($(x, y)$ coordinates) defying each level set are then appended to the list `lines`. Finally, the difference between the maximum of each radial coordinate of these contour lines and the radial position of the vessel vacuum chamber is computed. If the difference is positive or equal to zero, the code prints out

a message and the last value of the $\psi$ function stored in `PsiLim`.
The core of the computation occurs in the `ComputeGrid` method. First, a `numpy` array `ContourLevels` having dimension `m` is defined, ranging from `LowerPsiValue` to `PsiLim`. Mesh refinement is needed at every the points where the plasma touches solid surfaces, since strong gradients exist there. To this end, a $\tanh$ function is used to satisfy this requirement. These points are then stored in a `numpy` array (`zQuery`), having dimension `n`, that is the number of grid points in the axial direction. The $\psi$ function need then to be interpolated over these new grid points. This is done in the method `InterpolatePsi`, where a spline function (relying on the `scipy` library) is used to interpolate the values of $\psi$ over the new grid points, `zQuery`. The result is then stored into a $2D$ `numpy` array `InterpPsi`, having dimensions `n`$\times$`m`. This array is then use, together with `zQuery` in order to build each of the quadrilateral cells that makes the computational grid. Small guard cells are also added and treated as guard cells for the boundary conditions. Finally, each of the cells' vertex are assembled in a `numpy` array `MESH`. The dimension of this array are code-specific. For SOLPS, the structure of the array is the following. The number of columns is fixed to fifteen. The first two columns are the cell indicator; that is, each of the grid cell is assigned a unique couple of numbers. The successive ten entries are the radial and axial position of the five vertices (including also the cells' center vertices) that make up the quadrilaterals. Finally, the remaining two entries specify the magnetic field components (radial and axial) at each of the quadrilateral cell center. Again, since the magnetic field is known on a rectangular grid, an interpolation procedure is first performed in the method `InterpolateField`. Here we used the `scipy` module and, in particular, the `RectBivariateSpline` function.
We illustrate the construction of the mesh corresponding to the standard magnetic configuration of the GyM LPD, whose $\psi$ function has been reported in figure C.1. The grid is displayed in figure C.2. It should be noted that the grid has been rotated by $90^\circ$ for typographic purposes.

# List of Figures

# List of Tables

# Bibliography


[1] Iter: the way to new energy.

[2] Psi-2 linear plasma device.

[3] R. Schneider A. Mutzke and G. Bandelow. Sdtrimsp-2d: Simulation of particles bombarding on a two dimensional target-version 2.0. 2013.

[4] P. Alexandroff and H. Hopf. *Topologie I: Erster Band. Grundbegriffe der Mengentheoretischen Topologie Topologie der Komplexe· Topologische Invarianzsätze und Anschliessende Begriffsbildungen· Verschlingungen im n-Dimensionalen Euklidischen Raum Stetige Abbildungen von Polyedern*. Springer-Verlag, 2013.

[5] S. Atzeni and J. Meyer ter Vehn. *The Physics of Inertial Fusion: BeamPlasma Interaction, Hydrodynamics, Hot Dense Matter*, volume 125. OUP Oxford, 2004.

[6] M. Baelmans. Code improvements and applications of a two-dimensional edge plasma model for toroidal fusion devices. 1993.

[7] M. J. Baldwin and R. P. Doerner. Helium induced nanoscopic morphology on tungsten under fusion relevant plasma conditions. *Nuclear Fusion*, 48(3):035001, 2008.

[8] R. Balescu. Transport processes in plasmas. 1988.

[9] R. Betti and O. A. Hurricane. Inertial-confinement fusion with lasers. *Nature Physics*, 12(5):435–448, May 2016.

[10] T. R. Boehly. Initial performance results of the omega laser system. *Optics communications*, 133(1-6):495–506, 1997.

[11] R. Mark Bradley and James M. E. Harper. Theory of ripple topography induced by ion bombardment. *Journal of Vacuum Science & Technology A: Vacuum, Surfaces, and Films*, 6(4):2390–2395, July 1988.

[12] S. I. Braginskii. Transport phenomena in a completely ionized two-temperature plasma. *Sov. Phys. JETP*, 6(33):358–369, 1958.

[13] M. E. Campbell and J. W. Hogan. The national ignition facility-applications for inertial fusion energy and high-energy-density science. *Plasma Physics and Controlled Fusion*, 41(12B):B39, 1999.

[14] C. Cercignani. *The Boltzmann Equation and Its Applications*. Applied Mathematical Sciences. Springer New York, 2012.

[15] R. Chodura. Plasma flow in the sheath and the presheath of a scrape-off layer. In *Physics of plasma-wall interactions in controlled fusion*, pages 99–134. Springer, 1986.

[16] R. Clark. *Nuclear fusion research: understanding plasma-surface interactions*, volume 78. Springer Science & Business Media, 2005.

[17] W. Eckstein. Energy distributions of sputtered particles. *NIMPB*, 18(1):344–348, 1986.

[18] W. Eckstein. Sputtering yields. *Vacuum*, 82(9):930–934, May 2008.

[19] A. Eksaeva. Effect of surface morphology on erosion of metallic plasma-facing materials modelled with the 3d monte-carlo code ero. 2020.

[20] A. Baron-Wiechec et al. First dust study in jet with the iter-like wall: sampling, analysis and classification. *Nuclear Fusion*, 55(11):113033, 2015.

[21] A. Decoster et al. *Modeling of collisions*, volume 2. Elsevier, 1998.

[22] A. Eksaeva et al. Ero modeling of cr sputtering in the linear plasma device psi-2. *Physica Scripta*, 2017(T170):014051, 2017.

[23] A. Eksaeva et al. ERO modelling of tungsten erosion in the linear plasma device PSI-2. *Nuclear Materials and Energy*, 12:253–260, August 2017.

[24] A. Eksaeva et al. Ero2. 0 modelling of the effects of surface roughness on molybdenum erosion and redeposition in the psi-2 linear plasma device. *Physica Scripta*, 2020(T171):014057, 2020.

[25] A. Kallenbach et al. Impurity seeding for tokamak power exhaust: from present devices via ITER to DEMO. *Plasma Physics and Controlled Fusion*, 55(12):124041, November 2013.

[26] A. Litnovsky et al. Investigations of single crystal and polycrystalline metal mirrors under erosion conditions in textor. *Fusion engineering and design*, 82(2):123–132, 2007.

[27] A. Manhard et al. Blister formation on rough and technical tungsten surfaces exposed to deuterium plasma. *Nuclear Fusion*, 57(12):126012, 2017.

[28] B. M. Berger et al. Transient effects during erosion of wn by deuterium ions studied with the quartz crystal microbalance technique. *Nuclear Instruments and Methods in Physics Research Section B: Beam Interactions with Materials and Atoms*, 382:82–85, 2016.

[29] C. H. Linsmeier et al. Material testing facilities and programs for plasma-facing component testing. *Nuclear Fusion*, 57(9):092012, 2017.

[30] C. Pardanaud et al. Post-mortem analysis of tungsten plasma facing components in tokamaks: Raman microscopy measurements on compact, porous oxide and nitride films and nanoparticles. *Nuclear Fusion*, 2020.

[31] C. Ruset et al. Tungsten coatings deposited on cfc tiles by the combined magnetron sputtering and ion implantation technique. *Physica Scripta*, 2007(T128):171, 2007.

[32] C. Ruset et al. Development of w coatings for fusion applications. *Fusion Engineering and Design*, 86(9-11):1677–1680, October 2011.

[33] D Alegre et al. A parametric study of helium retention in beryllium and its effect on deuterium retention. *Physica Scripta*, T170:014028, oct 2017.

[34] D. Borodin et al. Modelling of impurity transport in the linear plasma devices pisces-b and pilot-psi using the monte-carlo code ero. *Contributions to Plasma Physics*, 50(3-5):432–438, 2010.

[35] D. Borodin et al. Simulation of be–c interaction dynamics in mixed be/c layers formed in experiments at pisces-b. *Journal of nuclear materials*, 415(1):S219–S222, 2011.

[36] D. Dellasega et al. Nanostructured and amorphous-like tungsten films grown by pulsed laser deposition. *Journal of Applied Physics*, 112(8):084328, 2012.

[37] D. Dellasega et al. Tungsten oxide nanowires grown on amorphous-like tungsten films. *Nanotechnology*, 26(36):365601, aug 2015.

[38] D. R. Zhang et al. Self-consistent simulation of transport and turbulence in tokamak edge plasma by coupling solps-iter and bout++. *Physics of Plasmas*, 26(1):012508, 2019.

[39] D.Naujoks et al. Material transport by erosion and redeposition on surface probes in the scrape-off layer of jet. *Nuclear fusion*, 33(4):581, 1993.

[40] E. Besozzi et al. Coefficient of thermal expansion of nanostructured tungsten based coatings assessed by substrate curvature method. *Materials & Design*, 137:192–203, 2018.

[41] E. Marenkov et al. Modeling of tungsten transport in the linear plasma device psi-2 with the 3d monte-carlo code ero. *Journal of Nuclear Materials*, 463:268–271, 2015.

[42] E. Marenkov et al. Modeling of tungsten transport in the linear plasma device PSI-2 with the 3D Monte-Carlo code ERO. *Journal of Nuclear Materials*, 463:268–271, August 2015.

[43] E. Sytova et al. Impact of a new general form of friction and thermal forces on solps-iter modelling results. *Contributions to Plasma Physics*, 58(6-8):622–628, 2018.

[44] G. Antar et al. The properties of the tungsten coating on fine grain graphite using pulsed laser deposition. *Fusion Engineering and Design*, 148:111261, November 2019.

[45] G. M. Wright et al. Tungsten nano-tendril growth in the alcator c-mod divertor. *Nuclear Fusion*, 52(4):042003, 2012.

[46] H. Bufferand et al. Numerical modelling for divertor design of the west device with a focus on plasma–wall interactions. *Nuclear Fusion*, 55(5):053025, 2015.

[47] H. Bufferand et al. Implementation of drift velocities and currents in soledge2d–eirene. *Nuclear Materials and Energy*, 12:852–857, 2017.

[48] H. Bufferand et al. Three-dimensional modelling of edge multi-component plasma taking into account realistic wall geometry. *Nuclear Materials and Energy*, 18:82–86, 2019.

[49] H. Y. Xu et al. Observations of orientation dependence of surface morphology in tungsten implanted by low energy and high flux d plasma. *Journal of nuclear materials*, 443(1-3):452–457, 2013.

[50] H.Y. Xu et al. Enhanced modification of tungsten surface by nanostructure formation during high flux deuterium plasma exposure. *Journal of Nuclear Materials*, 447(1-3):22–27, apr 2014.

[51] J. F. Ziegler et al. Srim–the stopping and range of ions in matter (2010). *Nuclear Instruments and Methods in Physics Research Section B: Beam Interactions with Materials and Atoms*, 268(11-12):1818–1823, 2010.

[52] J. Nuckolls et al. Laser compression of matter to super-high densities: Thermonuclear (CTR) applications. *Nature*, 239(5368):139–142, September 1972.

[53] J. Ongena et al. Magnetic-confinement fusion. *Nature Physics*, 12(5):398–410, 2016.

[54] J. Rapp et al. Transport simulations of linear plasma generators with the B2.5-EIRENE and EMC3-EIRENE codes. *Journal of Nuclear Materials*, 463:510–514, August 2015.

[55] J. Roth et al. Recent analysis of key plasma wall interactions issues for iter. *Journal of Nuclear Materials*, 390:1–9, 2009.

[56] J. Xiong et al. Effect of processing conditions and methods on residual stress in CeO2 buffer layers and YBCO superconducting films. *Physica C: Superconductivity*, 442(2):124–128, aug 2006.

[57] K. Ješko et al. Soledge2d-EIRENE simulations of the pilot-PSI linear plasma device compared to experimental data. *Contributions to Plasma Physics*, 58(6-8):798–804, April 2018.

[58] K. Ješko et al. Studying divertor relevant plasmas in the pilot-PSI linear plasma device: experiments versus modelling. *Plasma Physics and Controlled Fusion*, 60(12):125009, November 2018.

[59] K. Nordlund et al. Multiscale modelling of plasma–wall interactions in fusion reactor conditions. *Journal of Physics D: Applied Physics*, 47(22):224018, 2014.

[60] K. Ouaras et al. Tungsten blister formation kinetic as a function of fluence, ion energy and grain orientation dependence under hydrogen plasma environment. *Journal of Fusion Energy*, 37(2-3):144–153, 2018.

[61] K. Song et al. Temperature dependence of retarded recrystallisation in helium plasma-exposed tungsten. *Nuclear Fusion*, 59(9):096031, 2019.

[62] L. Dong et al. Influence of impurity seeding on the plasma radiation in the EAST tokamak. *Plasma Science and Technology*, 20(6):065102, April 2018.

[63] L W Owen et al. B2.5-EIRENE modeling of radial transport in the MAGPIE linear plasma device. *Plasma Sources Science and Technology*, 26(5):055005, March 2017.

[64] L. W. Owen et al. Transport modeling of convection dominated helicon discharges in proto-MPEX with the B2.5-EIRENE code. *Physics of Plasmas*, 24(11):112504, November 2017.

[65] M. B. Berger et al. Sputtering measurements using a quartz crystal microbalance as a catcher. *Nuclear Instruments and Methods in Physics Research Section B: Beam Interactions with Materials and Atoms*, 406:533–537, 2017.

[66] M. Baeva et al. B2-EIRENE simulation of plasma and neutrals in MAGNUM-PSI. *Journal of Nuclear Materials*, 363-365:330–334, June 2007.

[67] M. Kang et al. Formation and evolution of ripples on ion-irradiated semiconductor surfaces. *Applied Physics Letters*, 104(5):052103, February 2014.

[68] M. Mayer et al. Strongly reduced penetration of atomic deuterium in radiation-damaged tungsten. *Physical review letters*, 111(22):225001, 2013.

[69] M. Mayer et al. Tungsten surface enrichment in EUROFER and fe-w model systems studied by high-resolution time-of-flight rutherford backscattering spectroscopy. *Nuclear Materials and Energy*, 17:147–151, dec 2018.

[70] M. Miyamoto et al. Systematic investigation of the formation behavior of helium bubbles in tungsten. *Journal of Nuclear Materials*, 463:333–336, 2015.

[71] M. Passoni et al. Nanostructured rhodium films produced by pulsed laser deposition for nuclear fusion applications. *Journal of nuclear materials*, 404(1):1–5, 2010.

[72] M. Rasinski et al. High resolution scanning transmission electron microscopy (hr stem) analysis of re-deposited layer on asdex upgrade tile. *Fusion engineering and design*, 86(9-11):1753–1756, 2011.

[73] M. Sala et al. Exposures of bulk w and nanostructured w coatings to medium flux d plasmas. *Nuclear Materials and Energy*, page 100779, 2020.

[74] M. Sala et al. Simulations of argon plasmas in the linear plasma device gym with the solps-iter code. *Plasma Physics and Controlled Fusion*, 62(5):055005, 2020.

[75] M. Shoji et al. Studies of dust transport in long pulse plasma discharges in the large helical device. *Nuclear Fusion*, 55(5):053014, 2015.

[76] M. Wischmeier et al. High density operation for reactor-relevant power exhaust. *Journal of Nuclear Materials*, 463:22–29, 2015.

[77] M. Y. Ye et al. Blister formation on tungsten surface under low energy and high flux hydrogen plasma irradiation in nagdis-i. *Journal of nuclear materials*, 313:72–76, 2003.

[78] N. Kafle et al. Plasma flow measurements in the prototype-material plasma exposure eXperiment (proto-MPEX) and comparison with B2.5-EIRENE modeling. *Physics of Plasmas*, 25(5):052508, May 2018.

[79] N. Mellet et al. Multiscale modelling of sheath physics in edge transport codes. In *26th IAEA Fusion Energy Conference*, oct 2016.

[80] N. Ohno et al. Influence of crystal orientation on damages of tungsten exposed to helium plasma. *Journal of Nuclear Materials*, 438:S879–S882, 2013.

[81] Noriyasu Ohno et al. Influence of crystal orientation on damages of tungsten exposed to helium plasma. *Journal of Nuclear Materials*, 438:S879–S882, July 2013.

[82] O. A. Hurricane et al. Fuel gain exceeding unity in an inertially confined fusion implosion. *Nature*, 506(7488):343–348, 2014.

[83] O. V. Ogorodnikova et al. Deuterium retention in dense and disordered nanostructured tungsten coatings. *Journal of Nuclear Materials*, 507:226–240, 2018.

[84] P. Ström et al. Sputtering of polished eurofer97 steel: Surface structure modification and enrichment with tungsten and tantalum. *Journal of Nuclear Materials*, 508:139–146, 2018.

[85] P. Wang et al. Deuterium retention in tungsten films deposited by magnetron sputtering. *Physica Scripta*, 2014(T159):014046, 2014.

[86] R. A. Pitts et al. Physics basis for the first iter tungsten divertor. *Nuclear Materials and Energy*, 20:100696, 2019.

[87] R. Albanese et al. DTT: a divertor tokamak test facility for the study of the power exhaust issues in view of DEMO. *Nuclear Fusion*, 57(1):016010, oct 2016.

[88] R. Behrisch et al. Material erosion at the vessel walls of future fusion devices. *Journal of Nuclear Materials*, 313-316:388–392, mar 2003.

[89] R. C. Wieggers et al. B2. 5-eunomia simulations of pilot-psi plasmas. *Journal of Nuclear Materials*, 438:S643–S646, 2013.

[90] R. Caniello et al. Erosion yield and w surface enrichment of fe-w model system exposed to low flux deuterium plasma in the linear device GyM. *Nuclear Materials and Energy*, 10:9–16, jan 2017.

[91] R. Mateus et al. Helium load on wo coatings grown by pulsed laser deposition. *Surface and Coatings Technology*, 355:215–221, 2018.

[92] R. Sakamoto et al. Surface morphology of tungsten exposed to helium plasma at temperatures below fuzz formation threshold 1073 k. *Nuclear Fusion*, 57(1):016040, 2016.

[93] R. Schneider et al. Plasma edge physics with b2-eirene. *Contributions to Plasma Physics*, 46(1-2):3–191, 2006.

[94] R. Stadlmayr et al. Fluence dependent changes of surface morphology and sputtering yield of iron: comparison of experiments with sdtrimsp-2d. *Nuclear Instruments and Methods in Physics Research Section B: Beam Interactions with Materials and Atoms*, 430:42–46, 2018.

[95] S. K. Krane et al. *Introductory nuclear physics*. 1987.

[96] S. Kajita et al. Formation process of tungsten nanostructure by the exposure to helium plasma under fusion relevant plasma conditions. *Nuclear Fusion*, 49(9):095005, 2009.

[97] S. Kajita et al. Measurement of heat diffusion across fuzzy tungsten layer. *Results in physics*, 6:877–878, 2016.

[98] S. Kajita et al. Fuzzy nanostructure growth on precious metals by he plasma irradiation. *Surface and Coatings Technology*, 340:86–92, 2018.

[99] S. Takamura et al. Formation of nanostructured tungsten with arborescent shape due to helium plasma irradiation. *Plasma and fusion research*, 1:051–051, 2006.

[100] T. J. Petty et al. Tungsten fuzz growth re-examined: the dependence on ion fluence in non-erosive and erosive helium plasma. *Nuclear Fusion*, 55(9):093033, 2015.

[101] T. Škereň et al. Ion-induced roughening and ripple formation on polycrystalline metallic films. *New Journal of Physics*, 15(9):093047, 2013.

[102] V. A. Rozhansky et al. Simulation of tokamak edge plasma including self-consistent electric fields. *Nuclear Fusion*, 41(4):387, 2001.

[103] V. Kh. Alimov et al. Temperature dependence of surface topography and deuterium retention in tungsten exposed to low-energy, high-flux d plasma. *Journal of Nuclear Materials*, 417(1-3):572–575, 2011.

[104] V. Kotov et al. Numerical study of the iter divertor plasma with the b2-eirene code package. 2007.

[105] V. Rozhansky et al. New b2solps5. 2 transport code for h-mode regimes in tokamaks. *Nuclear fusion*, 49(2):025007, 2009.

[106] V.Kh. Alimov et al. Depth distribution of deuterium in single- and polycrystalline tungsten up to depths of several micrometers. *Journal of Nuclear Materials*, 337-339:619–623, mar 2005.

[107] W. Eckstein et al. Sdtrimsp: A monte-carlo code for calculating collision phenomena in randomized targets. *Report IPP*, 12(3), 2007.

[108] Y. Liu et al. Hydrogen diffusion in tungsten: A molecular dynamics study. *Journal of Nuclear Materials*, 455(1-3):676–680, 2014.

[109] Y. Marandet et al. Assessment of tungsten sources in the edge plasma of WEST. *Journal of Nuclear Materials*, 463:629–633, aug 2015.

[110] Y. Ueda et al. PSI issues at plasma facing surfaces of blankets in fusion reactors. *Journal of Nuclear Materials*, 313-316:32–41, March 2003.

[111] Y.Z. Jia et al. Nanostructures and pinholes on w surfaces exposed to high flux d plasma at high temperatures. *Journal of Nuclear Materials*, 463:312–315, August 2015.

[112] Y.Z. Jia et al. Subsurface deuterium bubble formation in w due to low-energy high flux deuterium plasma exposure. *Nuclear Fusion*, 57(3):034003, December 2016.

[113] K. D. Hammond F. Ferroni and B. D. Wirth. Sputtering yields of pure and helium-implanted tungsten under fusion-relevant conditions calculated using molecular dynamics. *Journal of Nuclear Materials*, 458:419–424, 2015.

[114] E Fortuna-Zalesna, M Andrzejczuk, L Ciupinski, K Rozniatowski, K Sugiyama, M Mayer, KJ Kurzydlowski, and ASDEX Upgrade Team. Post mortem analysis of a tungsten coated tile from the outer divertor strike point region of asdex upgrade. *Nuclear Materials and Energy*, 9:128–131, 2016.

[115] T. Hirai G. De Temmerman and R. A. Pitts. The influence of plasma-surface interaction on the performance of tungsten at the iter divertor vertical targets. *Plasma Physics and Controlled Fusion*, 60(4):044018, 2018.

[116] W. M. Shu G-N Luo and M. Nishi. Incident energy dependence of blistering at tungsten irradiated by low energy high flux deuterium plasma beams. *Journal of nuclear materials*, 347(1-2):111–117, 2005.

[117] Wolfram G. Radons, W. Just and P. Häussler. *Collective Dynamics of Nonlinear and disordered systems*. Springer, 2005.

[118] R.J. Goldston. Heuristic drift-based model of the power scrape-off width in low-gas-puff h-mode tokamaks. *Nuclear Fusion*, 52(1):013009, dec 2011.

[119] F. Hecht. New development in freefem++. *J. Numer. Math.*, 20(3-4):251–265, 2012.

[120] K. Heinola and T. Ahlgren. Diffusion of hydrogen in bcc tungsten studied with first principle calculations. *Journal of Applied physics*, 107(11):113531, 2010.

[121] P. Helander and D. J. Sigmar. *Collisional transport in magnetized plasmas*, volume 4. Cambridge university press, 2005.

[122] C. Herring. Effect of change of scale on sintering phenomena. *Journal of Applied Physics*, 21(4):301–303, April 1950.

[123] N. Ishida and V. S. J. Craig. Direct measurement of interaction forces between surfaces in liquids using atomic force microscopy. *KONA Powder and Particle Journal*, 36:187–200, 2019.

[124] M. Itskov. *Tensor algebra and tensor analysis for engineers*. Springer, 2007.

[125] L. Spitzer Jr. The stellarator concept. *The Physics of Fluids*, 1(4):253–264, 1958.

[126] S. Kajita. Sub-ms laser pulse irradiation on tungsten target damaged by exposure to helium plasma. *Nuclear fusion*, 47(9):1358, 2007.

[127] H. Kastelewicz and G. Fussmann. Plasma modelling for the PSI linear plasma device. *Contributions to Plasma Physics*, 44(4):352–360, July 2004.

[128] B. Kueppers.

[129] J. D. Lawson. Some criteria for a power producing thermonuclear reactor. *Proceedings of the physical society. Section B*, 70(1):6, 1957.

[130] R. Cuerno M. A. Makeev and A. L. Barabasi. Morphology of ion-sputtered surfaces. *Nuclear Instruments and Methods in Physics Research Section B: Beam Interactions with Materials and Atoms*, 197(3-4):185–227, 2002.

[131] C. Sella M. Navez and D D. Chaperot. Investigation of the attack on glass by ion bombardment. *C. R. Acad. Sci. Paris*, 254:240–244, 1962.

[132] R. Marchang and M. Dumberry. Carre: a quasi-orthogonal mesh generator for 2d edge plasma modelling. *Computer Physics Communications*, 96(2-3):232–246, 1996.

[133] Yu V Martynenko and M Yu Nagel. Model of fuzz formation on a tungsten surface. *Plasma physics reports*, 38(12):996–999, 2012.

[134] W. W. Mullins. Theory of thermal grooving. *Journal of Applied Physics*, 28(3):333–339, March 1957.

[135] D. Naujoks. *Plasma-material interaction in controlled fusion*, volume 39. Springer Science & Business Media, 2006.

[136] D. Nishijima. Sputtering properties of tungsten fuzzy surfaces. *Journal of nuclear materials*, 415(1):S96–S99, 2011.

[137] D Nishijima, H Iwakiri, K Amano, M.Y Ye, N Ohno, K Tokunaga, N Yoshida, and S Takamura. Suppression of blister formation and deuterium retention on tungsten surface due to mechanical polishing and helium pre-exposure. *Nuclear Fusion*, 45(7):669–674, jun 2005.

[138] Andrea Pezzoli. *Tungsten-based coatings for magnetic fusion research: damage and hydrogen retention*. PhD thesis, 2017.

[139] L. P. Pitaevskii and E. M. Lifshitz. *Physical Kinetics: Volume 10*, volume 10. Butterworth-Heinemann, 2012.

[140] J. Rapp. Addressing research and development gaps for plasma-material interactions with linear plasma devices. Technical report, Oak Ridge National Lab.(ORNL), Oak Ridge, TN (United States), 2018.

[141] T. D. Rognlien. Understanding of edge plasmas in magnetic fusion energy devices. *Plasma physics and controlled fusion*, 47(5A):A283, 2005.

[142] J. Romazanov. 3d simulation of impurity transport in a fusion edge plasma using a massively parallel monte-carlo code. Technical report, Plasmaphysik, 2018.

[143] T.G. Cowling S. Chapman and D. Burnett. *The mathematical theory of non-uniform gases: an account of the kinetic theory of viscosity, thermal conduction and diffusion in gases*. Cambridge university press, 1990.

[144] C. Boragno S. Rusponi and U. Valbusa. Ripple structure on ag(110) surface induced by ion sputtering. *Physical Review Letters*, 78(14):2795–2798, April 1997.

[145] Ryuichi Sakamoto, Elodie Bernard, Arkadi Kreter, and Naoaki Yoshida. Surface morphology of tungsten exposed to helium plasma at temperatures below fuzz formation threshold 1073 k. *Nuclear Fusion*, 57(1):016040, December 2016.

[146] A. D. Sakharov. Theory of the magnetic thermonuclear reactor, part ii. *Soviet Physics Uspekhi*, 34(5):378, 1991.

[147] P. Sigmnund. Theory of sputtering. i. sputtering yield of amorphous and polycrystalline targets. *Physical review*, 184(2):383, 1969.

[148] A. N. Simakov and P. J. Catto. Drift-ordered fluid equations for field-aligned modes in low-$\beta$ collisional plasma with equilibrium pressure pedestals. *Physics of Plasmas*, 10(12):4744–4757, 2003.

[149] V. P. Smirnov. Tokamak foundation in ussr/russia 1950–1990. *Nuclear fusion*, 50(1):014003, 2009.

[150] R. Smith. Ripple structures on ion bombarded surfaces arising from the sputter yield dependence on incidence angle. *Nuclear Instruments and Methods in Physics Research Section B: Beam Interactions with Materials and Atoms*, 352:213–216, 2015.

[151] P. C. Stangeby. *The plasma boundary of magnetic fusion devices*, volume 224. Institute of Physics Pub. Philadelphia, Pennsylvania, 2000.

[152] K. Sugiyama, K. Schimd, and W. Jacob. Sputtering of iron, chromium and tungsten by energetic deuterium ion bombardment. *Nuclear Materials and Energy*, 8:1–7, 2016.

[153] P. H. Summers and MG M. G. O Mullane. The atomic data and analysis structure. In *AIP Conference Proceedings*, volume 543, pages 304–312. American Institute of Physics, 2000.

[154] M.H.J. 't Hoen et al. Surface morphology and deuterium retention of tungsten after low- and high-flux deuterium plasma exposure. *Nuclear Fusion*, 54(8):083014, June 2014.

[155] M.H.J. 't Hoen et al. Deuterium retention and surface modifications of nanocrystalline tungsten films exposed to high-flux plasma. *Journal of Nuclear Materials*, 463:989–992, August 2015.

[156] C. Boragno U. Valbusa and F. B. De Mongeot. Nanostructuring surfaces by ion sputtering. *Journal of Physics: Condensed Matter*, 14(35):8153, 2002.

[157] J. Roth V. Kh. Alimov and M. Mayer. Depth distribution of deuterium in single-and polycrystalline tungsten up to depths of several micrometers. *Journal of Nuclear Materials*, 337:619–623, 2005.

[158] B. D. Wirth. Fusion materials modeling: challenges and opportunities. 2011.

[159] F. Sardei Y. Feng and J. Kisslinger. 3d fluid modelling of the edge plasma by means of a monte carlo technique. *Journal of nuclear materials*, 266:812–818, 1999.

[160] V. M. Zhdanov. Transport processes in multicomponent plasma. *Plasma Physics and Controlled Fusion*, 44(10):2283, 2002.